

**New Microtubule-destabilizing Agents –
Optimization of their Anti-angiogenic,
Vascular-disruptive, and Anti-metastatic
Activity**

DISSERTATION

zur Erlangung des akademischen Grades eines
Doktors der Naturwissenschaften (Dr. rer. nat.)
an der Fakultät für Biologie, Chemie und Geowissenschaften
der Universität Bayreuth

vorgelegt von

Florian Schmitt

aus Kronach

Bayreuth, 2018



UNIVERSITÄT
BAYREUTH



UNIVERSITÄT
BAYREUTH

- Lehrstuhl für Organische Chemie –

Fakultät für Biologie, Chemie und Geowissenschaften

Universität Bayreuth

**New Microtubule-destabilizing Agents – Optimization of
their Anti-angiogenic, Vascular-disruptive, and Anti-
metastatic Activity**

-

**Neuartige Mikrotubuli-destabilisierende Agenzien –
Optimierung ihrer anti-angiogenen, vaskular-disruptiven
und anti-metastatischen Aktivität**

Dissertation

Zur Erlangung des akademischen Grades

Doktor der Naturwissenschaften

(Dr. rer. nat.)

vorgelegt von

Florian Schmitt

aus Kronach

Bayreuth 2018

Die vorliegende Arbeit wurde im Zeitraum von Juni 2014 bis Dezember 2017 in Bayreuth am Lehrstuhl für Organische Chemie I (OC I) unter Betreuung von Prof. Dr. Rainer Schobert angefertigt.

Dissertation eingereicht am:	27.06.2018
Zulassung durch die Promotionskommission:	04.07.2018
Wissenschaftliches Kolloquium:	06.12.2018

Amtierender Dekan: Prof. Dr. Stefan Peiffer

Prüfungsausschuss:

Prof. Dr. Rainer Schobert (Gutachter)

Prof. Dr. Klaus Ersfeld (Gutachter)

Prof. Dr. Rhatt Kempe (Vorsitz)

Prof. Andreas Möglich

Inhaltsverzeichnis

Inhaltsverzeichnis	i
Abkürzungsverzeichnis	iii
Summary	- 1 -
Zusammenfassung	- 3 -
1 Einleitung	- 6 -
1.1 Krebs.....	- 6 -
1.2 Tumolvaskulatur - Ausbildung und Eigenschaften	- 8 -
1.2.1 Angiogenese	- 8 -
1.2.2 Tumorale Angiogenese - der <i>Angiogenic Switch</i>	- 8 -
1.2.3 Tumolvaskulatur – Eigenschaften und Struktur.....	- 9 -
1.3 Die Invasierungs-Metastasierungs-Kaskade.....	- 11 -
1.4 Das Zytoskelett	- 13 -
1.4.1 Das Aktinzytoskelett	- 13 -
1.4.2 Die Mikrotubuli.....	- 15 -
1.5 Mikrotubuli als Target in der Krebstherapie	- 17 -
1.5.1 Tubulinbindende Wirkstoffe	- 17 -
1.5.2 Mikrotubuli-destabilisierende Agenzien	- 17 -
1.5.3 Der Wirkmechanismus Mikrotubuli-destabilisierender Agenzien.....	- 20 -
1.5.4 Probleme Mikrotubuli-destabilisierender Agenzien	- 22 -
1.6 Metallkomplexe in der Krebsforschung	- 23 -
1.6.1 Cisplatin – vom Unfall zum Goldstandard.....	- 23 -
1.6.2 Ruthenium-Komplexe als potentielle Chemotherapeutika	- 24 -
1.7 Histondeacetylase-Inhibitoren	- 26 -
1.7.1 Histondeacetylasen – Vorkommen und Kategorisierung.....	- 26 -
1.7.2 Substrate und Funktionen der Histondeacetylasen.....	- 26 -
1.7.3 Inhibitoren der Zink-abhängigen Histondeacetylasen.....	- 29 -
2 Zielsetzung	- 32 -
3 Synopsis	- 33 -
3.1 Übersicht der Teilprojekte	- 33 -
3.2 Halogenierte Naphthochalkone und strukturverwandte Naphthopyrazoline mit anti-tumoraler Aktivität	- 35 -
3.3 LY290181-abgeleitete Analoga als Mikrotubuli-destabilisierende Agenzien	- 37 -

3.3.1	Neue Naphthopyrananaloga von LY290181 als potentiell vaskular-disruptive Wirkstoffe	- 37 -
3.3.2	Neue (Aren)Ruthenium(II)-Komplexe von 4-Aryl-4H-Naphthopyranen mit anti-tumoraler und anti-vaskularer Aktivität	- 40 -
3.4	Oxazol-verbrückte Combretastatin A-4 Derivate mit Alkyl-Hydroxamsäure Seitenkette: Struktur-Aktivitätsbeziehungen neuer dualer Inhibitoren der HDAC- und Tubulinfunktion	- 42 -
4	Literaturverzeichnis	- 44 -
5	Publikationen.....	- 55 -
5.1	Darstellung des Eigenanteils	- 55 -
5.1.1	Eigenanteil: Publikation I.....	- 56 -
5.1.2	Eigenanteil: Publikation II	- 57 -
5.1.3	Eigenanteil: Publikation III	- 58 -
5.1.4	Eigenanteil: Manuskript IV	- 59 -
5.2	Publikation I	- 60 -
5.3	Publikation II	- 73 -
5.4	Publikation III.....	- 127 -
5.5	Manuskript IV.....	- 149 -
6	Liste weiterer Publikationen im Rahmen der Dissertation.....	- 181 -
7	Danksagung	- 187 -
8	Eidesstattliche Versicherung und Erklärungen des Verfassers	- 189 -

Abkürzungsverzeichnis

ABC	<i>ATP binding cassette</i>
ATP	Adenosintriphosphat
Bad	<i>Bcl-2-antagonist of cell death</i>
Bak	<i>Bcl-2 homologous antagonist killer</i>
Bax	<i>Bcl-2-associated X protein</i>
Bcl-2	<i>B-cell lymphoma 2</i>
BCRP	<i>Breast cancer resistance protein</i>
Bim	<i>Bcl-2 interacting mediator</i>
Bmf	<i>Bcl-2 modifying factor</i>
CAM	Chorioallantoismembran
CA-4	Combretastatin A-4
Cdc42	<i>Cell division control protein 42 homolog</i>
CDDP	cis-Diammindichloroplatin(II)
DNA	<i>Desoxyribonucleic acid</i>
ECM	extracellular matrix
EGF	<i>Epidermal growth factor</i>
EMT	Epitheliale Mesenchymale Transition
EMSA	<i>Electrophoretic Mobility Shift Assay</i>
ERK	<i>Extracellular signal-regulated kinases</i>
F-Aktin	filamentäres Aktin
FAK	<i>Focal adhesion kinase</i>
FGF	<i>Fibroblast growth factor</i>
G-Aktin	globuläres Aktin
GTP	Guanosintriphosphat
HAT	Histonacetyltransferase
HDAC	Histondeacetylase
HDACi	Histondeacetylaseinhibitoren
HGF	<i>Hepatocyte growth factor</i>
HIF1	<i>Hypoxia-inducible factor 1</i>

IC ₅₀	halbmaximale, inhibitorische Konzentration; Maß für die anti-proliferative/zytotoxische Wirkung von Wirkstoffen
JNK	<i>c-Jun N-terminal kinases</i>
MAP	<i>Microtubule-associated protein</i>
MAPK	<i>Mitogen-activated protein kinase</i>
Mcl-1	<i>Induced myeloid leukemia cell differentiation protein</i>
MDA	<i>Microtubule disrupting agents</i>
mDia1/2	<i>Diaphanous-related formin-1</i>
MMP	Matrixmetalloproteinase
mRNA	<i>Messenger ribonucleic acid</i>
MTA	<i>Microtubule targeting agents</i>
MTOC	<i>Microtubule organizing center</i>
MTT	3-(4,5-Dimethylthiazol-2-yl)-2,5-diphenyltetrazoliumbromid
NAD	Nicotinamid-Adenin-Dinukleotid
NAMI-A	<i>“New anti-tumor metastasis inhibitor”</i>
Nf-κB	<i>Nuclear factor kappa-light-chain-enhancer of activated B-cells</i>
P-gp	P-Glykoprotein
P38	<i>p38 mitogen-activated protein kinases</i>
PDGF	<i>Platelet-derived growth factor</i>
PIGF	<i>Placental growth factor</i>
PTN	Pleiothropin
PUMA	<i>p53 upregulated modulator of apoptosis</i>
RhoA	<i>Ras homolog gene family, member A</i>
ROCK	<i>Rho-associated protein kinase</i>
ROS	reaktive Sauerstoffspezies
SAHA	<i>Suberanolhydroxamic acid</i>
SIV	<i>Subintestinal veins</i>
STAT	<i>Signal transducers and activators of transcription</i>

Abkürzungsverzeichnis

TGF- β	<i>Transforming growth factor β</i>
TRAIL	<i>Tumor necrosis factor related apoptosis inducing ligand</i>
TUNEL	<i>Terminal desoxynucleotidyl transferase-mediated dUTP-biotin nick end labeling</i>
VDA	<i>Vasculature disrupting agent</i>
VEGF	<i>Vascular endothelial growth factor</i>
VEGFR	<i>Vascular endothelial growth factor receptor</i>
VTA	<i>Vasculature targeting agent</i>

Bei allen weiteren Abkürzungen handelt es sich um gängige Abkürzungen und SI-Einheiten, welche laut ihrer Definition verwendet wurden.

Summary

The development of an intratumoral vasculature is essential for tumor growth, progression and metastasis. Hence, tumor vasculature represents an attractive target for chemotherapy. While anti-angiogenic agents exert their effect by inhibition of blood vessel development, vascular-disruptive compounds act by the destruction of already established tumor vasculature. Microtubule-destabilizing agents such as the ones discussed in this thesis are known to influence tumor vasculature in both ways. By deregulation of microtubule dynamics various signaling pathways and the intracellular transport are altered which effects migration and angiogenesis. Especially, the endothelial cells within the tumor vasculature are sensitive towards the treatment with microtubule destabilizing agents. By alterations of their cytoskeletal organization, the already fragile and abnormally permeable tumor vasculature is further destabilized. Hence, the tumor vasculature is disrupted causing necrosis of the tumor. By subtly modifying the chemical structures of known microtubule-destabilizing agents the shortcomings of this class of compounds such as their small therapeutic window and their susceptibility towards multi-drug resistance were to be remedied. In unison, their anti-vascular and anti-metastasis activity were to be optimized. The aim of this work was to evaluate compounds and their mode of action by using various *in vitro* and *in vivo* assays in order to identify potential new drug candidates.

Reference compounds and their derivatives were evaluated in preclinical studies for their cytotoxic and anti-proliferative activity in cultivated cancer cell lines of various entities. Moreover, the effect of the new compounds on diverse cellular components, processes and signaling pathways was investigated by biochemical and immunological methods. The anti-migratory and anti-angiogenic activity of the best compounds were determined by using *in vitro* assay systems. While the vascular disrupting activity of these compounds was evaluated by monitoring their effect on the developing blood vessels of the avian chorioallantois membrane, their anti-angiogenic activity was determined by analysis of the subintestinal veins in zebrafish embryos.

First the anti-proliferative effects and alterations of tubulin dynamics were proved for a series of chalcones and related pyrazolines. These derivatives induce apoptosis and alter the actin cytoskeleton causing reduced migration. Moreover, the investigated derivatives are able to circumvent multidrug resistance by inhibition of ABC efflux transports.

The second part of this work is dealing with the optimization of the effects of the strongly anti-proliferative naphthopyran LY290181. The effects of new derivatives of LY290181 strongly depend on their substitution pattern. Beside the augmented destabilization of microtubules the new compounds initiate a pronounced formation of actin stress fibres causing reduced migration of tumor cells and anti-angiogenic effects. These studies proved the vascular-disruptive activity *in vivo* for the first time for this specific class of compounds. The best analogue of LY290181 convinced with its excellent therapeutic window and by inhibition of tumor growth in mice bearing xenograft tumors. For a second generation of (arene)ruthenium(II) complexes bearing naphthopyrans, additive effects of naphthopyran and ruthenium fragment properties were observed. Beside the alterations of cytoskeletal components, DNA binding was proven. The anti-angiogenic activity of these compounds, typical of both ruthenium complexes and microtubule-destabilizing agents, were confirmed *in vivo* in zebrafish embryos.

The third part of this work deals with a series of compounds which are derived from the known microtubule-destabilizing natural compound combretastatin A-4. The bioactive cis-configuration of combretastatin A-4 was chemically stabilized in these new compounds. By adding tethered hydroxamic acids of different length to the derivatives, the resulting compounds were supposed to combine the combretastatin A-4 mediated inhibition of microtubule dynamics with the inhibition of histone deacetylases. The hydroxamic acid is crucial for the anti-proliferative activity of these hybrid compounds which showed a distinct selectivity for cancer cells over non-malignant fibroblasts. In addition, it was found that the activity of the test compounds strongly depends on the length of the linker between the combretastatin A-4 backbone and the hydroxamic acid. While the anti-proliferative and microtubule-destabilizing activities grow with decreasing linker length, the compounds inhibit histone deacetylases more effectively the shorter their linker is. Those compounds bearing short linkers and having the highest effect on microtubule dynamics induce the arrest of the cell cycle progression at G2/M. On contrary, the most potent histone deacetylase inhibitor with the longest linker caused the accumulation of cells at the G1 phase. However, alterations of the actin cytoskeleton are independent of the linker length. The enhanced formation of actin stress fibres indicates a reduced migration of treated cells.

Zusammenfassung

Für den Wachstum, die Progression und Metastasierung eines Primärtumors ist die Ausbildung eines intratumoralen Blutgefäßsystems essentiell. Aus diesem Grund stellt die Tumolvaskulatur ein attraktives Ziel (Target) bei der Chemotherapie dar. Während anti-angiogene Agenzien ihre Wirkung durch Hemmung der Blutgefäßausbildung erzielen, agieren vaskular-disruptive Wirkstoffe, indem sie bereits bestehende Blutgefäße im Tumor zerstören. Mikrotubuli-destabilisierende Agenzien, wie sie im Rahmen der vorliegenden Arbeit getestet wurden, sind dafür bekannt auf beiden Wegen Einfluss auf die Tumolvaskulatur nehmen zu können. Durch die Deregulierung der Mikrotubulidynamik werden zahlreiche Signalwege sowie der intrazelluläre Transport verändert, wodurch Migration und Angiogenese beeinflusst werden. Besonders sensibel reagieren Endothelzellen innerhalb der Tumolvaskulatur auf die Behandlung mit Mikrotubuli-destabilisierenden Agenzien. Durch die Zerstörung des Zytoskeletts dieser Zellen wird die ohnehin schon instabile und ungewöhnlich permeable Tumolvaskulatur weiter destabilisiert. In Folge kommt es zur Zerstörung der Blutgefäße, wodurch Tumornekrose ausgelöst wird. Durch geschickte Modifizierung bekannter Mikrotubuli-destabilisierender Agenzien sollten die Schwachstellen dieser Verbindungsklasse, wie deren geringe therapeutische Breite und deren Anfälligkeit für Multiresistenzen, behoben werden. Gleichzeitig galt es aber deren anti-vaskuläre und anti-metastatische Aktivität zu optimieren. Ziel dieser Arbeit war es unter Verwendung diverser *in vitro* und *in vivo* Testsysteme Testverbindungen und deren Wirkmechanismen zu evaluieren, um geeignete Wirkstoffkandidaten zu finden, die diese Kriterien erfüllen.

Zunächst wurde im Rahmen der präklinischen Untersuchungen der Referenzverbindungen sowie von deren Derivaten, deren zytotoxische und anti-proliferative Aktivität in kultivierten Krebszelllinien diverser Entitäten bestimmt. Überdies wurden die Auswirkungen der neuen Verbindungen auf etliche zelluläre Komponenten, Vorgänge und Signalwege biochemisch/zellbiologisch evaluiert. Die anti-migrative und anti-angiogene Aktivität ausgewählter Verbindungen wurde *in vitro* mittels diverser Assaysysteme an verschiedenen Zelltypen getestet. *In vivo* wurde die vaskular-disruptive Aktivität bestimmter Derivate auf die sich entwickelnden Blutgefäßen der Chorionallantoismembran in Hühnereiern untersucht während die anti-angiogene Aktivität anhand der Entwicklung der subintestinalen Venen im Zebrafischembryo bestimmt wurde.

Im ersten Teil dieser Arbeit wurden für eine Serie von Chalkon- und strukturverwandten

Pyrazolinderivaten anti-proliferative Effekte sowie Veränderungen der Tubulindynamik belegt. Neben der Induktion von Apoptose lösen die Derivate Veränderungen des Aktinzytoskeletts aus, wodurch die Migrierfähigkeit der Zellen herabgesetzt wird. Hinzu kommt, dass die getesteten Derivate die Fähigkeit besitzen über die Inhibition von ABC Efflux-Transportern Wirkstoffresistenzmechanismen von Krebszellen zu umgehen.

Der zweite Teil dieser Arbeit befasst sich mit der Optimierung der Wirkung des stark anti-proliferativen Naphthopyrans LY290181. Die Wirkung von Derivaten von LY290181 hängt dabei stark von deren Substitutionsmuster ab. Neben der vermehrten Destabilisierung der Mikrotubuli, initiieren die Naphthopyranderivate eine verstärkte Ausbildung von Aktin *Stress Fibres*. Daraus resultieren die Verringerung der Migrierfähigkeit von Tumorzellen und die anti-angiogene Wirkung dieser Verbindungen. Erstmals konnten für Derivate dieser Verbindungsklasse vaskular-disruptive Effekte auch *in vivo* nachgewiesen werden. Im Gegensatz zu vielen weiteren Mikrotubuli-destabilisierenden Agenzien konnte ein Analogon von LY290181 gefunden werden, das durch eine gute therapeutische Breite besticht, so dass das Tumorstadium in Xenograft-Mäusen gehemmt wurde. Indem Naphthopyrane als Liganden an (Aren)Ruthenium(II)-Fragmente koordiniert wurden, konnten additive Effekte aus der Wirkung des Naphthopyrans und der des Rutheniumfragments erzielt werden. So wurde neben den Veränderungen der Zytoskelettkomponenten auch DNA Bindung festgestellt. Die anti-angiogene Aktivität der Verbindungen, die sowohl als Eigenschaft von Rutheniumkomplexen als auch von Mikrotubuli-destabilisierenden Agenzien bekannt ist, konnte *in vivo* im Zebrafischembryo belegt werden.

Der dritte Teil dieser Arbeit behandelt eine Serie von Verbindungen, die vom Mikrotubuli-destabilisierenden Naturstoff Combretastatin A-4 abgeleitet ist. Neben der chemischen Stabilisierung von dessen bioaktiver *cis*-Form wurden die neuen Verbindungen mit Alkylhydroxamsäureresten unterschiedlicher Länge versehen. Dadurch sollten die Derivate neben der Combretastatin A-4 vermittelten Hemmung der Mikrotubuli-Dynamik noch als Histondeacetylaseinhibitoren fungieren. Für die anti-proliferative Wirkung dieser hochselektiv an Krebszellen wirkenden Hybridverbindungen ist die Hydroxamsäurefunktion essentiell. Weiterhin wurde gezeigt, dass die Länge des Verbindungsstücks (Linker) zwischen dem Combretastatin A-4 Grundgerüst und der Hydroxamsäure die Wirkung der Verbindungen stark beeinflusst. Tendenziell steigen die anti-proliferative sowie die Mikrotubuli-destabilisierende Wirkung je kürzer der Linker gewählt wird. Im Gegensatz dazu inhibieren die Verbindungen Histondeacetylase umso besser je länger deren Linkerfunktion ist. Während die kurzkettigen

Derivate mit starkem Einfluss auf die Mikrotubuli zur Arretierung des Zellzyklus in der G2/M Phase führen, induziert der beste Histondeacetylaseninhibitor mit dem längsten Linker zu einem Arrest in der G1 Phase. Unabhängig von der Linkerlänge führen die Combretastatin A-4 Derivate zu Veränderungen des Aktinzytoskeletts. Die vermehrte Ausbildung von Aktin Stress Fibres führt dazu, dass die Migrierfähigkeit der behandelten Zellen herabgesetzt wird.

1 Einleitung

1.1 Krebs

Krebs ist nach Erkrankungen des Herz-Kreislaufsystems die zweithäufigste Todesursache in Deutschland.¹ Laut einer aktuellen Studie des *Robert Koch Instituts* erkranken jedes Jahr alleine in Deutschland in etwa 480.000 Menschen neu an Krebs und etwa 220.000 Todesfälle werden jährlich mit einer Krebserkrankung assoziiert.² Da die Wahrscheinlichkeit an Krebs zu erkranken mit zunehmenden Alter exponentiell zunimmt, hat unter anderem die steigende Lebenserwartung in Deutschland dazu beigetragen, dass sich die Anzahl der Krebsneuerkrankungen seit Beginn der 1970er in etwa verdoppelt hat und auch in Zukunft ein weiterer Anstieg prognostiziert wird.²⁻⁴ Hoffnung macht hingegen der Rückgang der Krebssterblichkeit, der seit Anfang der 1990er Jahre beobachtet wird.³



Abbildung 1. Freie Interpretation der erweiterten „Hallmarks of Cancer“ nach Hanahan und Weinberg 2011.⁵

Der Terminus Krebs wird umgangssprachlich als Sammelbegriff für maligne Neoplasien verwendet und umfasst dabei etliche ausgesprochen heterogene Krankheitsformen.³ Nach über einem Jahrhundert an Forschung zu diesem Thema konnte zwar eine Fülle an Wissen zu dieser „Krankheit“ generiert werden. Diese zeigte jedoch lediglich wie divers, komplex und

vielschichtig Krebs ist. Der Versuch von Hanahan *et al.* aus dem Jahr 2000 die Kennzeichen von Krebszellen auf sechs sogenannte *Hallmarks* zu reduzieren, ist bis heute weitestgehend akzeptiert und wahrscheinlich die häufigst zitierte Literaturquelle zu diesem Thema (siehe Abb. 1).⁶ Die sechs Kennzeichen (*Hallmarks*) von Krebszellen sind demnach deren unbegrenztes Teilungspotential (1), ihre Unempfindlichkeit gegenüber wachstumshemmender Stimuli (2), ihre Fähigkeit Apoptose zu umgehen (3), sowie dauerhaft Angiogenese zu induzieren (4), ihre autarke Versorgung mit Wachstumsfaktoren (5) und ihre Fähigkeit invasiv in Gewebe vorzudringen und zu metastasieren (6).⁶ Im Jahr 2011 ergänzten Hanahan *et al.* hierbei noch die Fähigkeit der Krebszellen den Energiemetabolismus zu reprogrammieren (7) sowie den Angriffen des Immunsystems auszuweichen (8).⁵ Als förderliche Charakteristika wurden außerdem tumorfördernde Entzündungen (9), die Instabilität des Genoms sowie Mutationen (10) eingestuft.^{5,6} Jedoch riet man schon im Jahr 2000 davon ab Tumore auf eine Ansammlung von relativ homogenen Zellen zu reduzieren, sondern diese vielmehr als eine Art komplexes Organ zu betrachten, welches aus individuell spezialisierten Zelltypen besteht und in einem eigens konzipierten Tumormikroumfeld fungiert. Erst unter Berücksichtigung dessen könne es laut Hanahan *et al.* möglich sein die Biologie eines Tumors ansatzweise zu verstehen und diesen erfolgreich zu behandeln.^{6,7} Auch wenn Krebsentstehung und –ausbreitung in ihrer Komplexität die starke Vereinfachung auf die wenigen *Hallmarks* bei weitem übersteigt, bildet das Konzept nach wie vor eine wichtige Grundlage in der Krebs- und Wirkstoffforschung.

Da nicht der Primärtumor, sondern vielmehr die durch Metastasen ausgelösten Folgeschäden das Gros der Krebspatienten tötet, treten anti-metastatische Wirkstoffe immer weiter in den Fokus der Forschung.⁸ Überdies bilden sogenannte VTAs (*vasculature-targeting-agents*) eine vielversprechende Wirkstoffklasse, die entweder die Ausbildung der Tumolvaskulatur hemmen (anti-angiogene Verbindungen) oder selektiv die bereits bestehende Tumolvaskulatur zerstören (vaskular-disruptive Verbindungen).⁹ Die VTAs üben neben der direkten Hemmung des Tumorwachstums über die Veränderung der Tumolvaskulatur auch anti-metastatische Wirkung aus.⁹

Im Folgenden sollen deshalb nun die tumorinduzierte Angiogenese, die aus dieser resultierende tumorale Vaskulatur, sowie der Metastasierungsprozess und die dafür relevanten Signalwege näher beschrieben werden. Besonderes Augenmerk soll dabei auf der Rolle der Zytoskelettkomponenten Aktin und Tubulin im Rahmen dieser Prozesse liegen.

1.2 Tumervaskulatur - Ausbildung und Eigenschaften

1.2.1 Angiogenese

Unter Angiogenese versteht man die Blutgefäßbildung durch Sprossung aus bereits bestehenden Blutgefäßen.¹⁰ Im Gegensatz dazu wird die *de novo* Blutgefäßbildung im Embryo aus Angioblasten, den Vorläufern der Endothelzellen, als Vaskulogenese bezeichnet.^{10,11} Aus diesem durch Vaskulogenese gebildeten, ersten primitiven vaskulären Labyrinth kann dann durch Sprossung (Angiogenese) ein komplexeres Netzwerk aus Epithelröhren entstehen, aus welchem dann Arterien und Venen hervorgehen.¹² Im erwachsenen Menschen ist die Angiogenese weitestgehend inaktiv.¹³ In Ausnahmefällen, wie während der Wundheilung oder während des weiblichen Monatszyklus wird sie jedoch zeitweilig angeregt.¹³ Zudem kommt es während des Tumorwachstums zum sogenannten „*Angiogenic Switch*“, wodurch die Angiogenese dauerhaft aktiviert wird, um die Nähr- und Sauerstoffversorgung des Tumors zu garantieren.¹⁴

1.2.2 Tumorale Angiogenese - der *Angiogenic Switch*

Judah Folkman postulierte schon 1971, dass ein Tumor ab einer gewissen Größe eine eigenständige Blutversorgung benötigt, um überleben und wachsen zu können, und dass eben diese Abhängigkeit von der Angiogenese als therapeutisches Target verwendet werden könnte.¹⁵ Diese Hypothese konnte in den Folgejahren mittels verschiedener Tiersysteme bestätigt werden. Diese zeigten, dass erst zu dem Zeitpunkt der Neovaskularisierung der implantierten Tumorzellen ein Wachstum über einen bestimmten Schwellenwert hinaus möglich ist.¹⁶⁻²¹ Falls diese Vaskularisierung ausbleibt, können die Tumorzellen nicht ausreichend mit Sauerstoff und Nährstoffen versorgt werden und es wird Apoptose bzw. Nekrose eingeleitet, wodurch es zum Stillstand des Tumorwachstums kommt.²²

Vaskularisierung erfolgt im Allgemeinen in vier Stufen. Zu Beginn muss die extrazelluläre Matrix (ECM) lokal so verdaut werden (1), dass die durch Wachstumsfaktoren aktivierten Endothelzellen durch diese migrieren können (2).²² Die Endothelzellen proliferieren und werden stabilisiert (3).²² Der weitere Angiogenese Prozess wird über das Gleichgewicht von pro- und anti-angiogenen Faktoren beeinflusst (4).²² Da sich Endothelzellen unter normalen Umständen nur etwa alle 1000 Tage teilen, bedarf es im direkten Tumorumfeld einer starken Deregulierung dieses Gleichgewichts um die Angiogenese dauerhaft aktiv zu halten.²³ Diese Veränderung des Gleichgewichts wird als „*Angiogenic Switch*“ bezeichnet. Neben der

Erhöhung des Levels der pro-angiogenen Faktoren kommt es in Folge dessen auch zur Absenkung des Levels der anti-angiogenen Faktoren.²⁴ Die Aktivität sowohl der pro- als auch der anti-angiogenen Faktoren wird durch den Grad der Genexpression, Sekretion und proteolytischen Aktivierung reguliert.²⁴ Die Expression der pro-angiogenen Faktoren kann direkt durch Onkogene aktiviert oder durch den Verlust der Funktion von Tumorsuppressorgenen begünstigt werden.²⁴ Auch Umwelteinflüsse, wie Hypoxie, die Bildung von reaktiven Sauerstoffspezies (ROS), zelluläre Azidose oder Glukose- und Eisenmangel, können die Expression dieser Faktoren induzieren.²⁵ Dabei gilt es allerdings zu beachten, dass der Stimulus nicht alleine von den Tumorzellen ausgeht, sondern dass auch den Tumor infiltrierende Entzündungszellen an der Angiogenese beteiligt sind.²⁶

Zu den pro-angiogenen Wachstumsfaktoren zählen unter anderem VEGF-A (*vascular endothelial growth factor A*), FGF (*fibroblast growth factor*), PlGF (*placenta growth factor*), PDGF (*platelet-derived growth factor*), und PTN (Pleiothropin).^{24,27,28} Weiterhin ist eine ganze Reihe Proteasen und Glykosidasen, wie beispielsweise MMP-9 (*matrix metalloproteinase-9*), Heparanase und Cathepsin an der Regulierung der Angiogenese beteiligt.²⁹⁻³¹ Durch deren Verdauung sinkt die Proteindichte innerhalb der ECM (*extracellular matrix*), was sich förderlich auf die Migrationsfähigkeit der Endothelzellen auswirkt.³² Weiterhin werden durch den Proteaseverdau vorher unzugängliche, migrationsfördernde Bindestellen an Matrixproteinen freigelegt und matrixgebundene Wachstumsfaktoren, wie beispielsweise FGF freigesetzt.^{32,33}

1.2.3 Tumervaskulatur – Eigenschaften und Struktur

Die durch die dauerhaft aktivierte Angiogenese resultierenden tumoralen Blutgefäße besitzen auf Grund der fehlenden Regulation eine abnormale, chaotische Strukturierung und zeichnen sich durch eine übermäßig hohe Durchlässigkeit aus (siehe Abb. 2).^{10,34} Durch die unregelmäßige Gefäßverteilung, Gefäßdicke und Struktur der Tumervaskulatur ist auch die Versorgung der Tumore mit Nährstoffen und Sauerstoff unausgewogen.^{10,35} Aus dieser häufig auftretenden Mangelversorgung resultiert eine weitere Erhöhung der pro-angiogenen Faktoren, wodurch die Fehlregulation lediglich verstärkt wird. Weiterhin haben die Basalmembranen der Tumorblutgefäße eine anormale Zusammensetzung und Dicke.¹⁰ Auch das häufige Fehlen der Perizyten-schicht und die weniger starke Verbindung mit den die Epithelröhre umgebenden muralen Zellen führen dazu, dass die tumoralen Blutgefäße ungewöhnlich permeabel sind.³⁶⁻³⁸

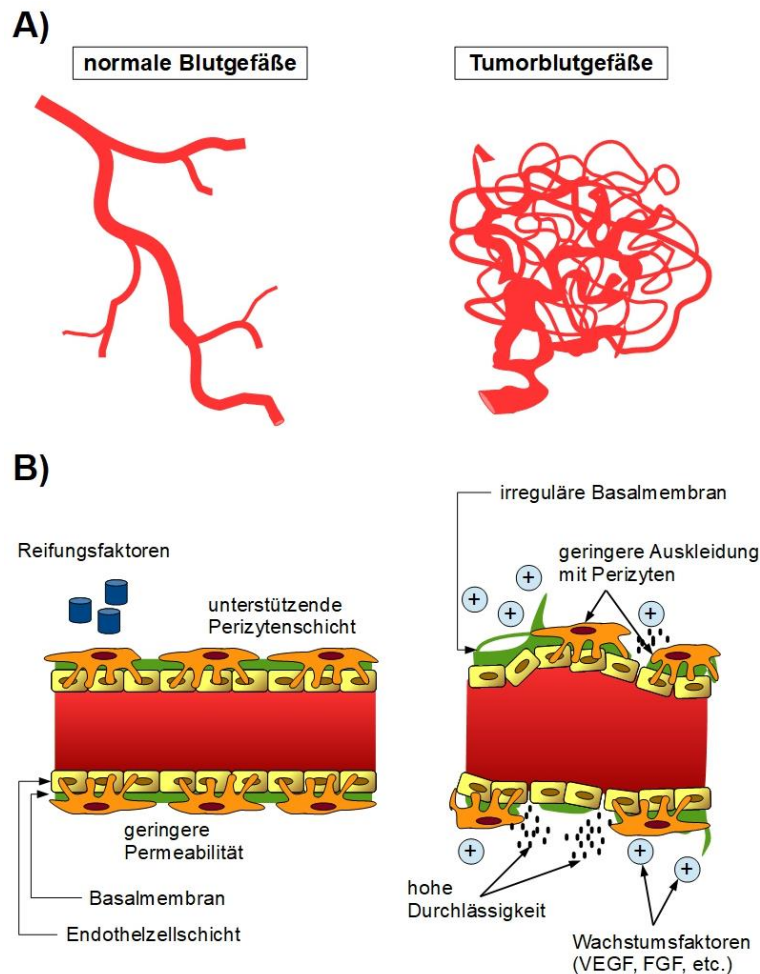


Abbildung 2. Schematischer Vergleich gesunder Blutgefäße mit Tumorblutgefäßen. A) Unter gesunden Umständen verlaufen die Blutgefäße strukturiert und fein abgestimmt. Ihr Durchmesser ist dabei wohl reguliert. Im Gegensatz dazu ist der Verlauf der tumoralen Blutgefäße chaotisch und verworren. Auch die Dicke der Blutgefäße ist unregelmäßig. B) Aufbau der Blutgefäße unter normalen Umständen sowie im Tumorumfeld. Normale Blutgefäße reifen nach der endothelialen Sprossung zu stabilen, wohl regulierten Gefäßsystemen. Dabei ist die Endothelzellschicht ausgewogen von einer Basalmembran umgeben. Stabilisierend wirkt zudem die Auskleidung der Gefäßwände mit Perizyten. Im Gegensatz dazu fehlt bei Tumorblutgefäßen auf Grund der raschen Entstehung der wohlregulierten Reifungsprozess. Ihre Dicke ist unausgewogen und auch die Endothelzellen sind weniger stark miteinander verknüpft. Die Basalmembran fällt auf durch Unterbrechungen, ist teilweise doppelschichtig und zeigt ungewöhnliche Sprossungen. Zudem sind die tumoralen Blutgefäße weniger stark mit Perizyten ausgekleidet. Folge dessen ist eine ungewöhnliche Instabilität und Durchlässigkeit. Weiterhin sind die Blutgefäße durch stetige Erhöhung der Wachstumsfaktoren dauerhafter Angiogenese ausgesetzt.[Eigene Darstellung nach Sund *et al.* 2005 und Cao 2009^{39,40}]

Diese Instabilität der Blutgefäße gepaart mit deren unregelmäßigem Blutfluss führt bei steigender Tumormasse zur Erhöhung des interstitiellen Drucks, der zu Hämorrhagien sowie zum kompletten Kollabieren bestimmter Blutgefäße führen kann.^{10,41} Die brüchigen Gefäßwände erleichtern weiterhin die Intravasation und Dissemination der Tumorzellen und erschweren gleichzeitig die gleichmäßige Verteilung von Chemotherapeutika innerhalb des Tumors.¹⁰

1.3 Die Invasierungs-Metastasierungs-Kaskade

Im Gegensatz zu Primärtumoren, die man mittlerweile durch operative Entfernung, Bestrahlung oder Chemotherapie häufig gut bekämpfen kann, stellen die aus diesen Primärtumoren entstandenen Metastasen nach wie vor meist ein Todesurteil dar.⁸ Besonders Resistenzen und die mangelnde Möglichkeit diese häufig weit gestreuten Metastasen adressieren zu können, erweisen sich bei deren Behandlung als problematisch.⁸ So ist es nicht verwunderlich, dass mehr als 90% der krebsbedingten Todesfälle eben nicht durch den Primärtumor, sondern vielmehr durch Metastasen verursacht werden.^{8,42,43} Auch wenn man in den letzten Jahrzehnten große Fortschritte im Verständnis der Invasierungs-Metastasierungskaskade gemacht hat, sind noch immer diverse Details unklar. Unverändert hoch ist jedoch die Wichtigkeit mehr Einblick in diesen Prozess zu erlangen, um Wege zu finden diesen zu verhindern oder eventuell sogar umkehren zu können.⁸

Damit aus den Epithelzellen eines Primärtumors Metastasen gebildet werden können, müssen diese Zellen folgende Schritte innerhalb der Invasierungs-Metastasierungskaskade durchlaufen (siehe Abb. 3). Der erste Schritt wird als Invasion (1) bezeichnet, bei dem sich Tumorzellen aus dem Zellverband des Primärtumors lösen und in die sie umgebende extrazelluläre Matrix und die stromalen Zellschichten eindringen.⁸ Nachdem die Zellen durch Intravasation (2) in die Blutgefäße invadiert sind, müssen sie als zirkulierende Tumorzellen den Transport (3) durch Blut- oder Lymphgefäße überstehen, um sich nach der Extravasation (4) durch die Blutgefäßwände im umliegenden Gewebe anlagern zu können.^{8,43-46} Doch nur die Zellen, die durch Adaption innerhalb des fremden Milieus überleben (5), sind in der Lage dort sogenannte Mikrometastasen zu bilden. Durch Wiederaufnahme der Proliferation, sowie durch Initiation von Angiogenese und Invasion in neues Gewebe besitzen diese die Möglichkeit zu klinisch nachweisbaren Makrometastasen (6) heranzuwachsen.^{8,45}

Epithelgewebe, welches zu einem Großteil den Ursprung solider Tumore darstellt, hat von Haus aus stationäre Eigenschaften und bildet durch interzelluläre Adhäsionen (*aherens junctions*, *tight junctions*, und *gap junctions*) einen starken Verbund.^{8,42,47} In den Epithelzellschichten werden diese interzellulären Verbindungen überwiegend mit Hilfe von N-Cadherin/ β -Catenin-Komplexen gebildet, welche über β -Catenin am Aktinzytoskelett verankert sind.^{48,49} Damit sich diese Tumorzellen aus dem Tumorverband lösen und durch Gewebe wandern können, müssen sich die Eigenschaften dieser Zellen umfassend ändern. Der zugrunde liegende Prozess wird als sogenannte Epithelial-Mesenchymale-Transition (EMT) bezeichnet.^{50,51} Dabei verändern

Epithelzellen ihre Morphologie, verlieren typische Eigenschaften und verwandeln sich in Zellen mit mesenchymalen Charakter.⁵⁰

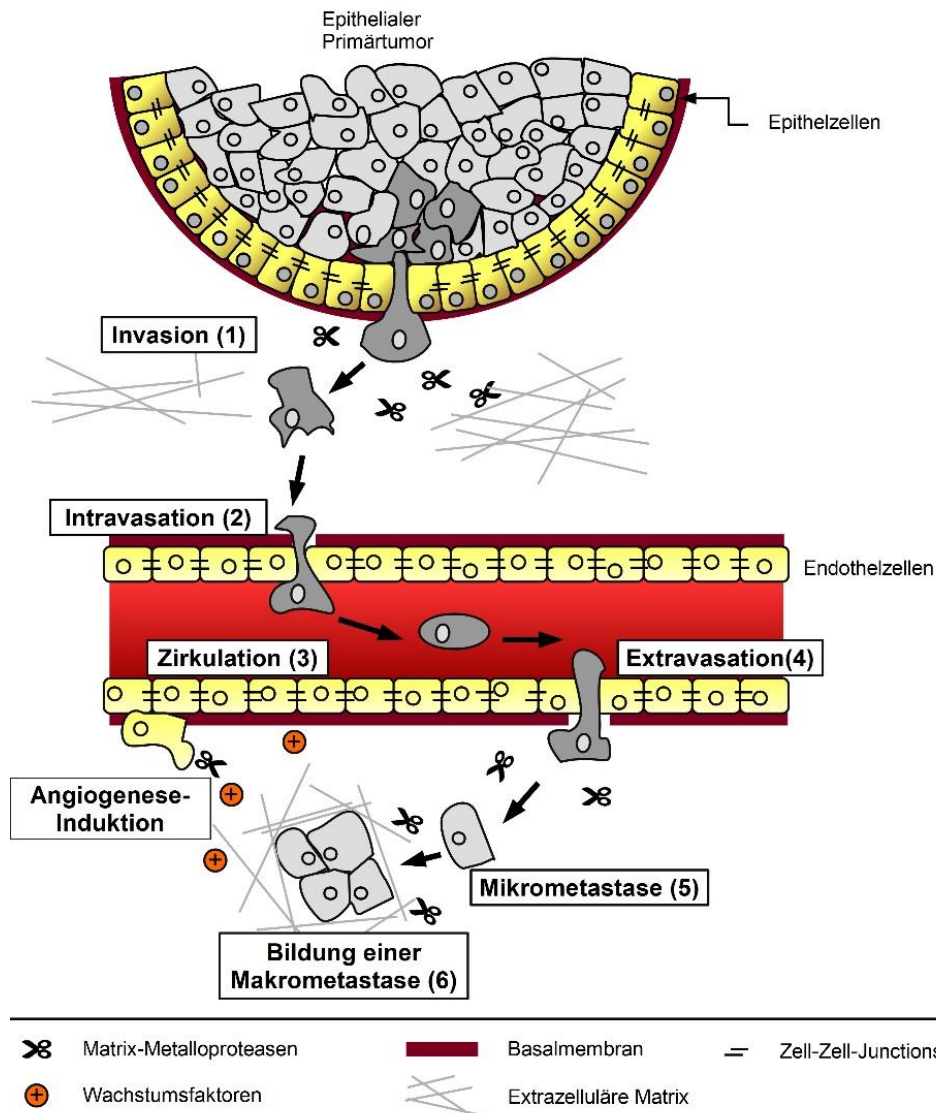


Abbildung 3. Schematische Darstellung der Metastasierungskaskade am Beispiel eines Epithelkarzinoms. Nachdem die epithelialen Tumorzellen die Transition zu Tumorzellen mit mesenchymalen Eigenschaften durchlaufen haben, dringen die Zellen per gerichteter Migration aktiv in das umliegende Gewebe ein (Invasion). Essentiell dafür ist deren Fähigkeit physiologische Barrieren, wie die Epithelzellschicht, die Basalmembran, die extrazelluläre Matrix oder die Endothelzellschicht zu überwinden. Nach dem Eindringen in die Blutgefäße (Intravasation) müssen die Tumorzellen die Zirkulation im Blutkreislauf überstehen, um dann nach dem Anheften an die Gefäßwand wieder aus den Blutgefäßen entkommen zu können (Extravasation). Nur die Tumorzellen, die in der Lage sind sich in der neuen Umgebung durch geschickte Anpassung zu behaupten, können dort Mikrometastasen bilden. Diese wiederum können durch Umstrukturierung der extrazellulären Matrix (u.a. durch Matrixmetalloproteinasen) zu größeren malignen Neoplasien heranwachsen, die mittels der Ausschüttung von Wachstumsfaktoren die Blutgefäßbildung anregen. [Eigene Darstellung nach K. Mahal 2015, A.M Alizadeh, S. Shiri, und S. Farsinejad 2014, sowie X. Guan 2015. ^{44,46,48}]

Im Gegensatz zu Endothelzellen verfügen Mesenchymalzellen über keine Zellpolarität und es fehlen ihnen feste Zell-Zellverbindungen.⁴⁷ Außerdem unterscheiden sie sich durch ihre höhere Motilität sowie durch ihre spindelförmige Morphologie von Epithelzellen.^{45,48} Während der EMT verlieren maligne Epithelzellen neben ihrer Polarität auch durch das Auflösen der Zell-Zell-Adhäsionen die Verbindung zum epithelialen Zellverbund. Dadurch wird das Ablösen dieser Zellen vom Verbund begünstigt. Eine zentrale Rolle nimmt dabei die Herunterregulation der E-Cadherin Expression ein.⁵⁰ In Folge wird β -Catenin aus den E-Cadherin/ β -Catenin-Komplexen ins Zytosol freigesetzt und es kommt zu dessen Translokation in den Zellkern.^{42,46,48} Dort fungiert β -Catenin mit Hilfe der Bindung an Co-Faktoren als Transkriptionsfaktor, der die Expression von Genen induziert, welche die EMT weiter fördern.^{47,49} Dazu zählen mesenchymal-typische Proteine wie N-Cadherin, Vimetin oder diverse Zytokeratine, die neben der Erhöhung der Motilität auch für die Interaktion mit der ECM verantwortlich sind.^{8,45,48} Auch werden in Folge der EMT die Expression und Sekretion von MMPs begünstigt, die den Abbau der ECM bewirken und dabei Wachstumsfaktoren proteolytisch freisetzen.⁵¹

In vielen Fällen wird die EMT durch Signalmoleküle (u.a. HGF, EGF, PDGF, und TGF- β) aus dem tumorassozierten Stroma induziert.⁵⁰ Weiterhin kann die EMT auch durch Hypoxie ausgelöst werden.⁵²

1.4 Das Zytoskelett

Zu den drei Hauptkomponenten des Zytoskeletts der Zelle gehören die Mikrofilamente (Aktinproteine), die Intermediärfilamente und die Mikrotubuli (Tubulinproteine).⁵³ Diese hochdynamischen auf- und abbaubaren Biopolymere bilden Fasern oder Filamente, die neben der mechanischen Stabilisierung und Formgebung der Zelle auch für deren Motilität, sowie für Transport und Bewegung innerhalb der Zelle verantwortlich sind.⁵³ Im Folgenden wird die Rolle des Aktin- und des Tubulinzytoskeletts in der Zelle, sowie die Möglichkeit diese beiden als Target für die Krebsbehandlung zu nutzen, näher erläutert.

1.4.1 Das Aktinzytoskelett

Den Großteil der Mikrofilamente bildet filamentäres Aktin (F-Aktin), welches durch Polymerisierung aus dem globulären Monomer G-Aktin entsteht.⁵⁴ Neben der mechanischen Stabilisierung der Zelle und intrazellulären Transportvorgängen, haben die Mikrofilamente eine

tragende Rolle für die Motilität und Polarisierung der Zelle.⁵⁴⁻⁵⁷ Die Gestalt der Filamente kann von verzweigten und quervernetzten Netzwerken, über parallele Bündel, zu anti-parallelen kontraktilen Strukturen variieren.⁵⁵ Während die Struktur der Zelle durch den Kortex, eine dünne Schicht aus Aktin, bestimmt wird, ist das gut regulierte Zusammenspiel verschiedener Gestalten der Mikrofilamente für die Zellmigration von essentieller Bedeutung (siehe Abb. 4).⁵⁵ Der Migrationszyklus beginnt mit der gezielten Polymerisierung der Filamente gegen die Zellmembran, wodurch diese in Migrationsrichtung ausgebeult wird (Zellprotrusion). Dies geschieht am sogenannten Lamellipodium, einem quasi zweidimensionalen Blatt, welches aus einem verzweigten Netzwerk an Filamenten besteht.⁵⁵

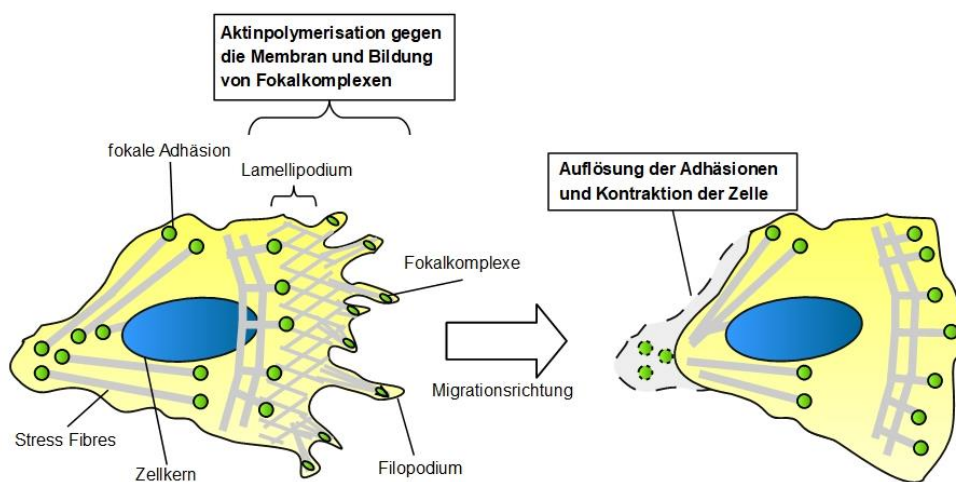


Abbildung 4. Schematische Darstellung der Aktin-Filamente sowie der fokalen Adhäsionen in migrierenden Zellen. Innerhalb der Lamellipodien, einer nahezu zweidimensionalen Struktur, finden sich quervernetzte Mikrofilamente, die durch Polymerisation gegen die Zellmembran diese in Richtung der Migration ausbeulen und so in neue Regionen vorstoßen. In den Lamellipodien fungieren die Filopodien, die aus parallel angeordneten Mikrofilamenten bestehen, als eine Art Vorhut um die Stimuli in der jeweiligen Richtung zu testen. *Stress Fibres* sind kontraktile Bündel aus Mikrofilamenten, die sich parallel zur Migrationsrichtung über den Zellkörper spannen. Über fokale Adhäsionen sind sie mit der extrazellulären Matrix verbunden und vermitteln über ihre Kontraktion das Vorwärtsbewegen der Zelle. [Eigene Darstellung nach L. Blanchoin *et al.* 2014 und Klaile 2015.^{55,58}]

Als eine Vorhut innerhalb dieses Blattes, die das Mikroumfeld an der sogenannten *Leading Edge* untersuchen, dienen die dünnen fingerartigen Filopodia.⁵⁹ Diese bestehen aus parallelen Bündeln von F-Aktin.⁵⁹ Durch Ausbildung von Ankerpunkten (fokalen Komplexen), die das Aktin-Zytoskeletts mit der ECM verbinden, können diese Ausstülpungen stabilisiert werden.⁵⁹ Diese ersten Fokalkomplexe werden durch transmembrane Integrine vermittelt, die auf zytoplasmatischer Seite über Proteine wie Talin, α -Actinin und Vinculin mit dem Aktinzytoskelett interagieren, während sie auf extrazellulärer Seite an Komponenten aus der

ECM (z.B. Kollagen, Laminin, oder Fibronectin) binden.⁶⁰ Während diese ersten Fokalkomplexe zu stabilen Fokaladhäsionen reifen, wird eine ganze Reihe strukturgebender sowie signalübertragender Proteine, wie Paxillin, Vinculin, c-Scr, FAK (*focal adhesion kinase*), oder Zyxin, rekrutiert.⁶¹ Die Fokaladhäsionen sind mit den sogenannten *Stress Fibres*, die aus kontraktile Filamentbündeln und Myosin bestehen, verknüpft.⁶² Während die Fokaladhäsion an der *Leading Edge* verstärkt werden, beginnen sich die an der gegenüberliegenden Seite zu lösen. Durch Kontraktion der *Stress Fibres* kommt es so zur Bewegung der Zelle.⁶²

Eine tragende Rolle in der Steuerung des Migrationsprozesses kommt RhoA, Rac1, und Cdc42 zu, drei Vertretern der Familie der Rho-GTPasen.⁶³ Während die zielgerichtete Aktin-Polymerisierung innerhalb des Lamellipodiums vor allem durch Rac1 reguliert wird, ist Cdc42 hauptsächlich für die Filopodiaausbildung verantwortlich.^{59,63-65} Durch RhoA-bedingte Aktivierung von Effektoren wie mDia1/2 und ROCK wird erst die Ausbildung von ausgereiften fokalen Adhäsionen an der *Leading Edge* und später die Aktin-Myosin Kontraktion induziert, während im der Migration abgewandten Teil der Zelle die Auflösung der Fokaladhäsionen bewirkt wird.^{61,62}

1.4.2 Die Mikrotubuli

Die Mikrotubuli sind hochdynamische Filamente, die fortwährend einem wohlregulierten Auf- und Abbau unterworfen sind. Heterodimere aus α - und β -Tubulin Monomeren lagern sich zu sogenannten Protofilamenten zusammen.⁶⁶ Durch seitliche Verknüpfung von meist 13 dieser Protofilamente werden wiederum die helikalen, hohlzylindrischen Mikrotubuli gebildet (siehe Abb. 5 A).⁶⁷ Die Enden von α - und β -Tubulin weisen innerhalb der Mikrotubuli verschiedene Ladungen auf. Während die von α -Tubulin negativ geladen sind, tragen die von β -Tubulin positive Ladungen.⁶⁶ Daraus resultiert, dass Mikrotubuli über ein Minus- und ein Plusende verfügen, wobei diese Polung ausschlaggebend für deren biologische Funktion ist.⁶⁶ In der Zelle erfolgt die Bildung der Mikrotubuli ausgehend vom MTOC (*microtubule-organizing center*).⁶⁸ Dabei ist das Minusende der Mikrotubuli in das MTOC eingebettet während die Polymerisierung am Plusende erfolgt (vgl. Abb. 5 B).^{68,69} Die Dynamik der Polymerisierung und Depolymerisierung wird dabei sowohl von intrinsischen wie extrinsischen Prozessen sowie von der posttranslationalen Modifizierung der Mikrotubuli reguliert.⁶⁸ Zur intrinsischen Kontrolle zählt das Vorhandensein von GTP-Caps oder –Inseln, wobei die extrinsischen Regulierung vor allem durch die MAPs (*microtubule-associated proteins*) und im Speziellen durch die Proteine, welche an die Plusenden der Mikrotubuli binden, bestimmt wird.⁶⁸

Die Rolle der Mikrotubuli für die Zelle ist fundamental. Unter anderem sind sie elementar für die Proliferation, die Formgebung der Zelle, die Migration und die Vaskularisierung.⁶⁸ Essentiell sind die Mikrotubuli auch für die Zellteilung, da sie während der Mitose den Spindelapparat ausbilden, welcher für die akkurate Aufteilung der Chromosomen auf die beiden entstehenden Tochterzellen verantwortlich ist.⁷⁰ Auch der intrazelluläre Transport verschiedenster Zellkomponenten kann nur mit Hilfe der Mikrotubuli gewährleistet werden.⁶⁶ Durch die hohe Steifheit der Mikrotubuli wird die Zelle mechanisch stabilisiert und somit deren Morphologie erhalten. Weiterhin sind die Mikrotubuli bei einer Vielzahl von Signalwegen involviert. Unter anderem besteht eine wechselseitige Regulierung zwischen den Mikrotubuli und den MAPKs (*mitogen-activated protein kinases*), die zelluläre Prozesse wie die Gentranskription, die Proteinbiosynthese, den Zellzyklus, Apoptose, oder Differenzierung organisieren.^{71,72}

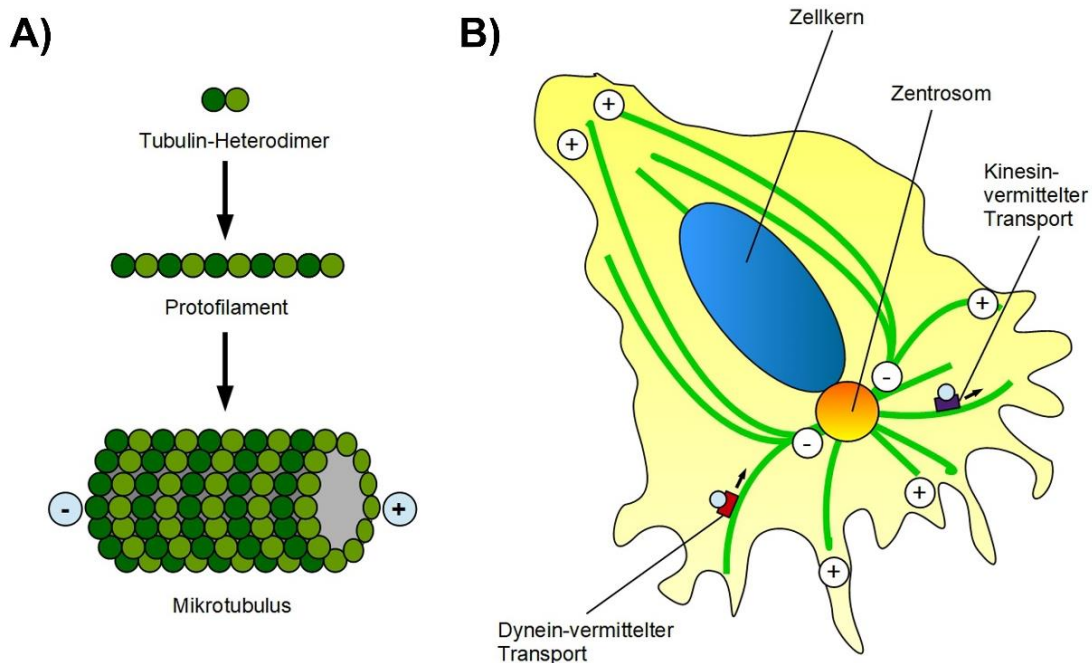


Abbildung 5. Schematische Darstellung der Mikrotubuli. A) Aufbau der Mikrotubuli aus α - und β -Tubulin Heterodimeren über die zylindrische Anordnung von 13 Protofilamenten. B) Ausgehend vom Minusende am Zentrosom polymerisieren die Mikrotubuli am Plusende. Der Kinesin-vermittelte Transport erfolgt entlang der Mikrotubuli in Richtung des Plusendes, wohingegen der Dynein-vermittelte Transport in Richtung des Minusendes gerichtet ist. [Eigene Darstellung nach Akhmanova und Steinmetz 2015, Small *et al.* 2002, und Alberts *et al.* „Molecular biology of the cell“ 5. Edition; 2008; Abb.16-104; ^{66,69,73}]

Überdies wird die Migration und Wundheilung auch mittels der Interaktion zwischen Aktin und Tubulin gesteuert.^{54,74} So beeinflusst die Mikrotubulipolymerisierung die Aktivierung der Rho

GTPasen Rac1 und Cdc42, wodurch wiederum die Aktin-vermittelte Zellprotrusion angeregt wird.⁷⁵ Im Gegensatz dazu löst die lokale Mikrotubulidepolymerisierung die Aktivierung von RhoA aus, worüber die Bildung der Aktin-*Stress Fibers* und deren Kontraktion induziert werden.⁷⁶ Auch deuten verschiedene Studien daraufhin hin, dass über die Regulation der Mikrotubulidynamik auch die Auflösung von fokalen Adhäsionen gesteuert wird.⁷⁷⁻⁸⁰ Zu guter Letzt ist der intrazelluläre Transport von Proteinen, Organellen und Vesikeln, welcher von Motorproteinen aus der Kinesin- und Dyneinfamilie entlang der Mikrotubuli ausgeführt wird, eine bedeutende Funktion dieser Zytoskelettkomponente.^{54,74} Dabei ist für die Migration im Speziellen, der Transport von post-Golgi *Carriern*, von mRNA, und der von Recycling-Endosomen zu den *Leading Edges* der Zellprotrusion wichtig.⁷⁵

1.5 Mikrotubuli als Target in der Krebstherapie

1.5.1 Tubulinbindende Wirkstoffe

Tubulinbindende Wirkstoffe, auch *Microtubule-targeting Agents* (MTA), wurden in der Chemotherapie schon eingesetzt bevor ihr Zielmolekül Tubulin 1967 überhaupt das erste Mal isoliert und charakterisiert werden konnte.⁸¹⁻⁸³ Die weitreichenden Folgen, die die Behandlung mit diesen Verbindungen auf zellulärer Ebene auslösen, waren zum damaligen Zeitpunkt noch größtenteils unbekannt. Wie bereits beschrieben, ist die Polymerisierung und Depolymerisierung der Mikrotubuli ein Prozess, der zahlreiche elementare Funktionen besitzt. Die Störung dieses hochdynamischen Gleichgewichts ist der Ansatzpunkt der MTA.⁸⁴ Grundsätzlich können diese in zwei Kategorien eingeteilt werden. Auf der einen Seite stehen die Vertreter, die ihre Wirkung durch die Stabilisierung der Mikrotubuli erzielen.⁸⁴ Zu dieser Gruppe zählen unter anderem Paclitaxel, Docetaxel, Epothilone oder Discodermolid.⁸⁵ Die andere Gruppe wird von Verbindungen gebildet, die eine destabilisierende Wirkung auf die Mikrotubuli besitzen (vgl. Abb. 6). Dazu zählen beispielsweise Vinca-Alkaloide, Colchicin oder Combretastatin A-4.⁷⁴ Im Folgenden soll die Wirkweise dieser Mikrotubuli-destabilisierenden Agenzien (MDA) und deren Folgen näher beschrieben werden.

1.5.2 Mikrotubuli-destabilisierende Agenzien

Der Großteil der MDA führt zur Destabilisierung der Mikrotubuli, indem die Tubulinpolymerisierung durch deren Bindung an die Colchicin- oder die Vinca-Bindestelle gehemmt wird. Vinblastin und Vincristin, beide aus dem Tropischen Madagaskar-Immergrün

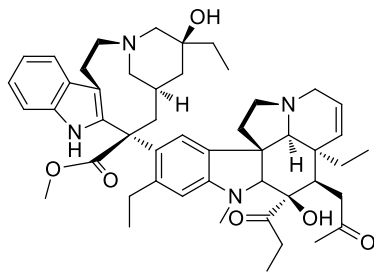
(*Vinca rosea* L.), sind die wohl bekanntesten Vertreter der Vinca-Alkaloide, die in der Tumorthherapie Anwendung finden und namensgebend für die Bindestelle sind. Diese befindet sich zwischen den α - und β -Tubulin Untereinheiten von zwei unterschiedlichen, longitudinal verbundenen Dimeren.⁶⁹ Diese MDA erzielen ihre Wirkung, indem sie als eine Art Keil zwischen diesen verschiedenen Dimeren fungieren.⁶⁹ Sie werden meist in einer Polychemotherapie bei verschiedenen malignen Erkrankungen (z.B. Hodgkin Lymphom) in Kombination mit anderen Chemotherapeutika eingesetzt.⁸⁶

Im Gegensatz zur Vinca-Bindestelle, befindet sich die Colchicin-Domäne zwischen den α - und β -Tubulin Untereinheiten innerhalb eines Heterodimers.⁶⁹ Die MDA, die an die Colchicin-Bindestelle binden, führen zur Destabilisierung der Mikrotubuli, indem sie den sogenannten „*curved-to-straight*“ Konformationsübergang bei der Mikrotubulibildung verhindern.^{67,69} Namensgeber ist Colchicin, ein toxisches Alkaloid aus der Herbstzeitlosen (*Colchicum autumnale* L.).⁸⁷ Für die Interaktion zwischen Colchicin und dessen Bindestelle am Tubulin spielt auf struktureller Ebene besonders die Anordnung der Ringsysteme sowie das sogenannte Trimethoxymotiv im A-Ring von Colchicin eine tragende Rolle.^{88,89} Dieses Trimethoxymotiv tritt über Colchicin hinaus in einer Reihe weiterer MDA auf. Im Fall von Colchicin verhinderten jedoch dessen geringe therapeutische Breite sowie seine fatalen Nebenwirkungen einen Einsatz in der Krebstherapie.⁹⁰ Auch für das wasserlösliche ZD6126, ein *Phospho-Prodrug* von N-Acetylcolchinol, welches strukturell eng mit Colchicin verwandt ist, wurde auf Grund von dessen starker Kardiotoxizität ein Abbruch der klinischen Studien beschlossen.⁹⁰

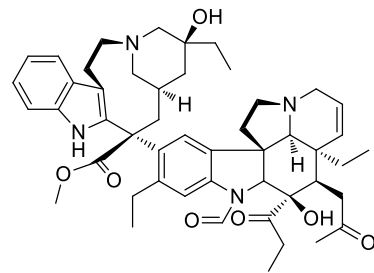
Strukturell eng mit Colchicin verwandt ist auch Combretastatin A-4 (CA-4), ein *cis*-Stilben mit dem charakteristischen Trimethoxymotiv im A-Ring, welches aus der Rinde der afrikanischen Buschweide (*Combretum caffrum*) isoliert wurde.⁹¹ Anders als bei Colchicin scheint die Zulassung verschiedener CA-4 Analoga durchaus vielversprechend. Besonders bewährt haben sich dabei die Derivatisierung zu wasserlöslichen *Phospho-Prodrugs* (z.B. Fosbretabulin, Oxi4503) und die Stabilisierung der bioaktiven *cis*-Konfiguration durch chemische Modifikation (z.B. Ombrabulin, und Phenstatin).⁹⁰

Eine Vielzahl an weiteren Verbindungen/Verbindungsklassen erzielt ihren anti-tumoralen Effekt durch die Destabilisierung der Mikrotubuli. An dieser Stelle soll lediglich die Verwendung von Vertretern der Verbindungsklassen der Chalkone und Naphthopyrane als MDA erwähnt werden.⁹²⁻⁹⁵

Vinca Alkaloide

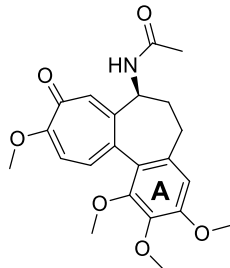


Vinblastin

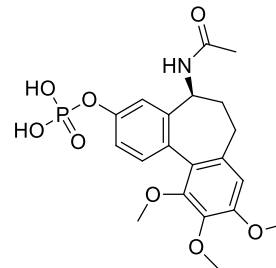


Vincristin

Colchicin und Analoga

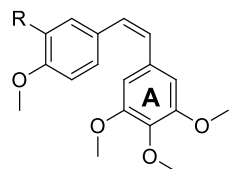


Colchicin

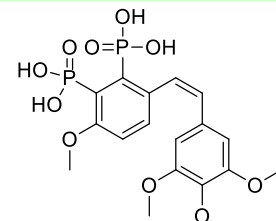


ZD6125

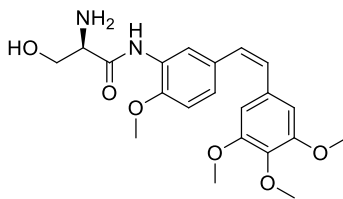
Combretastatin und Analoga



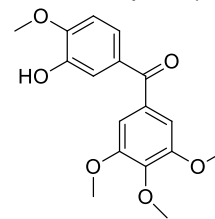
Combretastatin A-4: R = OH
Fosbretabulin: R = OPO₃H₂



Combretastatin A-1-Phosphat (Oxi4503)

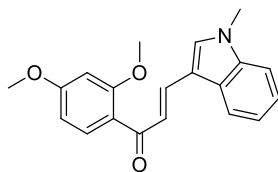


Ombrabulin

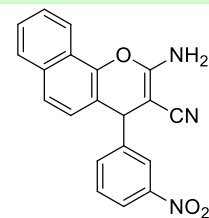


Phenstatin

Sonstige MDA



IPP51 (Chalkon)



LY290181 (Naphthopyran)

Abbildung 6. Beispiele für Mikrotubuli-destabilisierende Agenzien (MDA). Vinca-Alkaloide wie Vinblastin oder Vincristin interagieren mit Tubulin an der sogenannten Vinca-Bindestelle und führen so ihren Mikrotubuli-destabilisierenden Effekt aus. Colchicin und Combretastatin A-4 (CA-4) mit ihrem charakteristischen Trimethoxymotiv im A-Ring binden dagegen am Tubulin an der sogenannten Colchicin Bindestelle und führen so zur Destabilisierung der Mikrotubuli. Weitere MDAs: Das Colchicinderivat ZD6125, die Combretastinderivate Fosbretabulin, Oxi4503, Ombrabulin, Phenstatin, das Chalkon IPP51, sowie das Naphthopyran LY290181.

1.5.3 Der Wirkmechanismus Mikrotubuli-destabilisierender Agenzien

So elementar die Funktionen der Mikrotubuli in der Zelle sind, so umfassend wirkt sich auch die Störung der Mikrotubulidynamik auf die Zelle aus (vgl. Abb. 7). Am besten charakterisiert ist wohl die anti-mitotische Aktivität der MDA. Durch die Inhibition der Tubulinpolymerisierung wird die korrekte Ausbildung des mitotischen Spindelapparats unterbunden, was bei Zellen, die sich in der Mitose befinden oder in diese eintreten, zur Arretierung des Zellzyklus führt.⁹⁶ Bleibt der Zellzyklus auf Dauer unvollständig wird von diversen Regulationsproteinen an den Kontrollpunkten des Zellzyklus Apoptose eingeleitet.⁷⁴ Dass MDA auch auf anderen Wegen Apoptose auslösen können, belegt deren Fähigkeit, dass sie diese auch in nicht-mitotischen Zellen und bei Konzentrationen, die noch keinen Mitosearrest auslösen, induzieren.⁷⁴

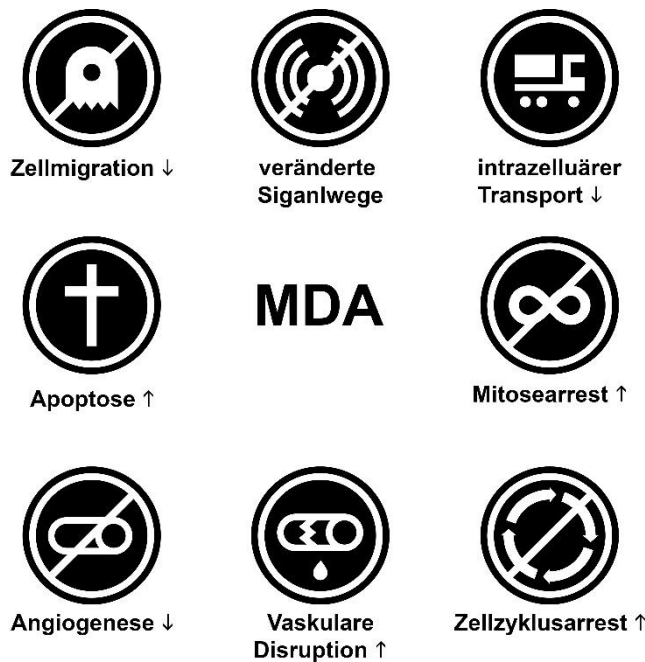


Abbildung 7. Vereinfachte Darstellung der Effekte der MDA. Bekannt sind MDA durch ihre Wirkung als Mitosegift, indem sie die korrekte Ausbildung der Mitosespindel inhibieren. Überdies induzieren sie den Arrest des Zellzyklus und beeinflussen diverse Signalwege. Als Folge dessen kommt es in MDA-behandelten zur Induktion von Apoptose. Durch die Zerstörung der Mikrotubuli werden weiterhin die Dynein- bzw. Kinesin-vermittelten Transportvorgänge innerhalb der Zelle gehemmt. Besonders über ihren Einfluss auf Migration und Angiogenese können MDA den Tumorwachstum sowie auch die Metastasierung reduzieren. Als einer der wichtigsten Sekundäreffekte, der von MDA vermittelt wird, gilt die selektive Zerstörung von tumoralen Blutgefäßen (vaskular-disruptive Aktivität).

Eine tragende Rolle bei der MDA-induzierten Apoptose spielt dabei die Verschiebung des Gleichgewichts aus pro- und anti-apoptotischen Faktoren aus der Bcl-2 Familie zu Gunsten der Apoptoseinduktion. Zum einen werden die Expression sowie die Aktivität der pro-apoptotischen Vertreter Bad, PUMA, Bax und/oder Bak hochreguliert.⁷⁴ Zum anderen kommt es zur Inaktivierung anti-apoptotischer Vertreter, wie beispielsweise Bcl-2, Bcl-XL, und Mcl-1, durch deren Hyperphosphorylierung.^{74,84,97} Zudem kann Apoptose durch die pro-apoptotischen Faktoren Bim und Bmf ausgelöst werden. Unter normalen Umständen liegen

diese in der Zelle gebunden an Dyneinproteine vor, welche wiederum an das Zytoskelett der Zelle binden.^{74,98} Als Folge der Zerstörung der Mikrotubuli werden diese pro-apoptotischen Faktoren vom Zytoskelett freigesetzt und regen den kontrollierten Zelltod an.^{74,98} Die Bcl-2-assoziierte Apoptoseinduktion kann auch durch die von MDA verursachten Veränderungen der MAPK-Signalwege ausgelöst werden.⁷⁴ So wird durch Behandlung mit MDA die dauerhafte Aktivierung des JNK (*c-Jun-terminal kinases*) Signalwegs induziert.^{99–104} Eine derart starke Aktivierung dieses Signalwegs löst Apoptose nicht nur über veränderte Genexpression, sondern auch transkriptionsunabhängig durch Phosphorylierung von Vertretern der Bcl-2 Proteinfamilie aus.¹⁰⁵ Auch weitere MAPK-Signalwege [z.B. ERK1/2 (*extracellular signal-regulated kinases*) und p38] werden durch die Behandlung mit MDA beeinflusst. Allerdings unterscheiden sich die Beeinflussungen dieser Signalwege zwischen den verschiedenen bekannten MDA. So führt beispielsweise die Behandlung mit CA-4 zu Erhöhung der Menge an phospho-p38 und der ERK-Aktivität, wohingegen durch die Behandlung mit Colchicin beides verringert wird.⁷⁴

Neben Apoptoseinduktion, Zellzyklus- und Mitosearrest üben MDA auch Einfluss auf Migration, Metastasierung und Angiogenese aus.⁷⁴ Besonders über die Interaktion mit dem Aktinzytoskelett sowie über die Kinesin/Dynein-vermittelten Transportvorgänge entlang der Mikrotubuli beeinflusst das Tubulinzytoskelett diese Vorgänge. Wie bereits beschrieben, induziert die Depolymerisierung der Mikrotubuli die Aktivierung von RhoA, wodurch das Aktinzytoskelett und daraus resultierend auch die Morphologie der Zelle verändert werden.⁷⁶ Durch die Aktivierung von RhoA kommt es zur erhöhten Bildung von Aktin *Stress Fibres* und von fokalen Adhäsionen.^{76,106} Außerdem sind vermehrte Aktomyosinkontraktionen die Folge.¹⁰⁷ Insgesamt gesehen wird durch diese Stabilisierung der Mikrofilamente die Motilität der Zelle herabgesetzt, wodurch Prozesse wie Angiogenese oder Metastasierung beeinflusst werden. Überdies wird durch die Destabilisierung der Mikrotubuli der intrazelluläre Transport gestört. Unter anderem wird so der Dynein-vermittelte Transport von HIF-1 α (*Hypoxia-inducible factor 1 α*) in Richtung des Zellkerns unterbunden, wodurch dessen transkriptionelle Aktivität und daraus resultierend auch Prozesse wie Angiogenese reduziert werden.^{108,109}

Besonders sensitiv reagieren Endothelzellen auf die Behandlung mit MDA. Neben der bereits beschriebenen Umgestaltung der Zellmorphologie führen dabei auch die MDA-induzierten Änderungen der interzellulären durch β -Catenin/N-Cadherin vermittelten Verknüpfungen zur Erhöhung der Permeabilität von Endothelschichten.¹¹⁰ Zudem bewirken auch das abnormale Aktinzytoskelett sowie der gestörte intrazelluläre Transport entlang der Mikrotubuli, dass bereits geknüpfte Zell-Zellverbindungen gelöst werden und die Ausbildung neuer fehlreguliert

ist.^{49,111-115} Folglich verliert die Endothelauskleidung der Blutgefäße an Integrität und ist instabiler und stärker permeabel. Insbesondere in Tumorblutgefäßen hat dies gravierende Folgen. Zusätzlich zu den Veränderungen der Endothelzellschicht führen der hohe interstitielle Druck sowie der von Haus aus schon fehlerhafte Aufbau der Tumorblutgefäßwände dazu, dass die Blutgefäße des Tumors kollabieren.³⁵ In Folge dieser sogenannten vaskular-disruptiven Effekte treten Einblutungen im Tumor auf. Durch die ausbleibende Blutversorgung werden weite Teile des Tumors auf Grund des Nähr- und Sauerstoffmangels nekrotisch.¹¹⁶ Lediglich die Rinde des Tumors kann durch Diffusion aus dem umliegenden nicht-malignen Gewebe versorgt werden und bleibt folglich vital.⁴¹ Neben den direkten Folgen der vaskular-disruptiven Effekte, wird über diese auch indirekt Einfluss auf die Angiogenese genommen, da sie durch die Zerstörung der Tumolvaskulatur, dem Tumor das Grundgerüst, das zur Sprossung neuer Kapillare notwendig ist, berauben.¹¹⁷ Auch geht man davon aus, dass MDA über die veränderten Zell-Zellkontakte die Hemmung der Angiogenese bewirken.¹¹⁷

Insgesamt sind MDA also weit mehr als Mitosegifte. Ihre Möglichkeit Einfluss auf Zellwachstum, Apoptose, Metastasierung und Angiogenese zu nehmen, macht sie genau wie ihre vaskular-disruptive Aktivität hochinteressant für die Krebstherapie.

1.5.4 Probleme Mikrotubuli-destabilisierender Agenzien

Auch wenn MDA eine Vielzahl positiver Wirkungen und Aktivitäten auf zellulärer Ebene und überdies hinaus positive Sekundäreffekte auslösen, haben sie in puncto Nebenwirkungen und Resistenzen definitiv Verbesserungsbedarf. Besonders das kleine therapeutische Fenster vieler MDA verhinderte deren Zulassung. Als Nebenwirkungen treten bei der Behandlung mit MDA unter anderem Cardio-, Neurotoxizität, Veränderungen des Blutbilds, Knochenmarkschädigungen und starke Durchfälle als Folge der Schädigung des Darmepithels, auf.^{84,118,119}

Neben der Überexpression von β III-Tubulin oder von anti-apoptotischen Faktoren (z.B. Bcl-2), können auch über die Bindung der MDA durch MAPs (*microtubule-associated proteins*) oder Veränderungen des Aktinzytoskeletts, die Resistenz von Tumoren gegen MDA begünstigt werden.¹²⁰ Multiresistenzen können auch durch die Überexpression von ABC (*ATP-binding cassette*) Efflux-Transportern entstehen. Diese schleusen unter ATP-Verbrauch Xenobiotika über die Zellmembran aus der Zelle aus.¹²⁰⁻¹²³ Einer dieser ABC-Transporter ist die promiske Effluxpumpe P-gp (*P-glyco protein*), deren Überexpression durch MDA-Behandlung ausgelöst

werden kann.¹²⁴ Da neben MDA auch andere Zytostatika zu deren Substraten gehören, kann für Folgetherapien nicht nur der erneute Einsatz von MDA, sondern auch der von etlichen weiteren Chemotherapeutika ineffektiv werden.^{120,123}

Generell können MDA, die ihren anti-tumoralen Effekt vor allem durch ihre anti-vaskuläre Aktivität erzielen, nicht in Monochemotherapien eingesetzt werden, da diese durch die Zerstörung der Tumorblutgefäße meist nur zu Nekrosen im Inneren eines Tumors führen, während die Tumorrinde von der Behandlung unberührt bleibt.⁴¹ Deshalb können diese Wirkstoffe nur effektiv in Kombination mit anderen Zytostatika in einer Polychemotherapie verwendet werden.

Insgesamt gesehen besteht also weiterhin der Bedarf an neuen Mikrotubuli-destabilisierenden Verbindungen, die auf der einen Seite die Möglichkeit besitzen Wirkstoffresistenzen zu umgehen und auf der anderen Seite effektiver und selektiver wirken, um so die Nebenwirkungen zu reduzieren und das therapeutische Fenster zu vergrößern.

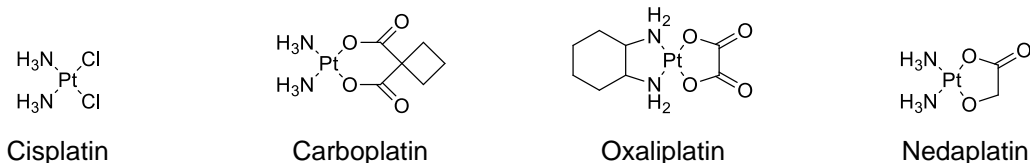
1.6 Metallkomplexe in der Krebsforschung

1.6.1 Cisplatin – vom Unfall zum Goldstandard

Das 1965 von Rosenberg *et al.* durch Zufall entdeckte Cisplatin [cis-Diammindichloroplatin(II)] ist bis heute der Goldstandard der metallbasierten Zytostatika.¹²⁵ Interessanterweise wurde erst nach seiner Zulassung für die Behandlung von diversen Krebsentitäten der zugrundeliegende Wirkmechanismus aufgeklärt.¹²⁶ Nach der Anreicherung des Komplexes in der Zelle kommt es aufgrund des Chloriddefizits innerhalb der Zelle zum Austausch der Chloridliganden gegen Wassermoleküle.¹²⁶ Die entstandene Diaquaverbindung kann dann wiederum an die Nukleinbasen Guanin und Adenin in der DNA binden.¹²⁷ Dadurch entstehen Inter- und Intrastrang-Quervernetzungen, die zur Spaltung und zum Abknicken der DNA-Doppelhelix führen.¹²⁷ Diese Schädigung der DNA induziert, neben der Inhibition der Transkription und DNA-Reparaturmechanismen den Arrest des Zellzyklus und letztendlich Apoptose.¹²⁷ Auch wenn Cisplatin bis heute standardmäßig in der Chemotherapie eingesetzt wird, haben die immensen Nebenwirkungen, wie beispielsweise Nephro-, Oto-, und Neurotoxizität sowie die Entwicklung von Resistenzen, einen negativen Einfluss auf dessen Effizienz.¹²⁶ Grund für die Resistenzen können die Verringerung der zellulären Aufnahme, die Erhöhung des Efflux, die Intensivierung der DNA-Reparaturmechanismen, oder die Entgiftung

durch Bindung an Glutathione und Metallothione sein.¹²⁶ Als Folge dieser Nachteile von Cisplatin wurde eine Reihe weiterer platinbasierter Metallkomplexe für die Krebstherapie entwickelt (u.a. Carboplatin, Oxaliplatin, Nedaplatin; vgl. Abb. 8).¹²⁶ Neben den Platin-Therapeutika wurden zudem sehr vielversprechende Fortschritte bei der Verwendung von weiteren Metallen, wie Gold, Ruthenium, Iridium und Kupfer gemacht.^{126,128–131} Im Folgenden soll jedoch speziell auf den potentiellen Einsatz von Ruthenium-Komplexen in der Krebstherapie eingegangen werden.

Platin-Komplexe



Ruthenium-Komplexe

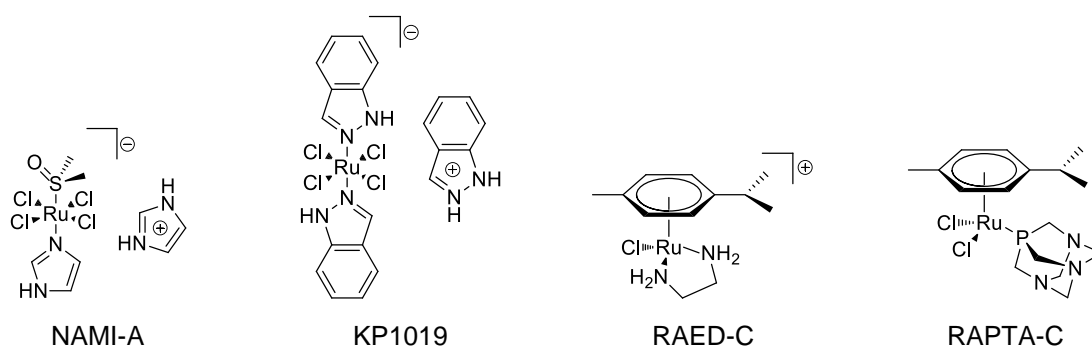


Abbildung 8. Beispiele für Platin-, und Ruthenium-Komplexe. Neben dem wohl bekanntesten Vertreter der Metallkomplexe in der Chemotherapie Cisplatin (CDDP), finden sich hier weitere bekannte *cis*-Platinkomplexe wie Carboplatin, Oxaliplatin oder Nedaplatin. Auf dem Gebiet der Ruthenium-Komplexe sind neben den Ruthenium(III)-Komplexen NAMI-A und KP1019 besonders (Aren)Ruthenium(II)-Komplexe wie RAED-C und RAPTA-C von Bedeutung.

1.6.2 Ruthenium-Komplexe als potentielle Chemotherapeutika

Neben Gold- und Platinkomplexen sind auch Ruthenium(II)- und (III)-Komplexe in der Krebsforschung von Bedeutung. Sie sind auf Grund ihrer vielseitigen anti-tumoralen Aktivitäten und vor allem auch wegen ihrer deutlich geringeren Nebenwirkungen interessant für die Chemotherapie (vgl. Abb. 9). Einige Ruthenium(III)-Komplexe, wie NAMI-A oder KP1019 (vgl. Abb. 8) haben sogar den Weg in klinische Studien geschafft.^{132,133} Sie bestehen dadurch, dass die inerten Verbindungen im Blut stabil zirkulieren können.¹²⁶ Man geht davon aus, dass der selektive Transport der Komplexe mit Hilfe von Transferrin zur Erhöhung der Aufnahme und der Akkumulierung in Krebszellen führt. Erst im Milieu der Krebszelle passiert

dann vermutlich die sogenannte Aktivierung-durch-Reduktion zur biologisch aktiven Ruthenium(II)-Verbindung.¹²⁸ Besonders vielversprechend ist dabei der Ruthenium(III)-Komplex NAMI-A, welcher *in vitro* keine Zytotoxizität aufweist *in vivo* jedoch über einen noch nicht im Detail verstandenen Mechanismus die Metastasierung und Progression bereits bestehender Metastasen hemmt.¹³⁴

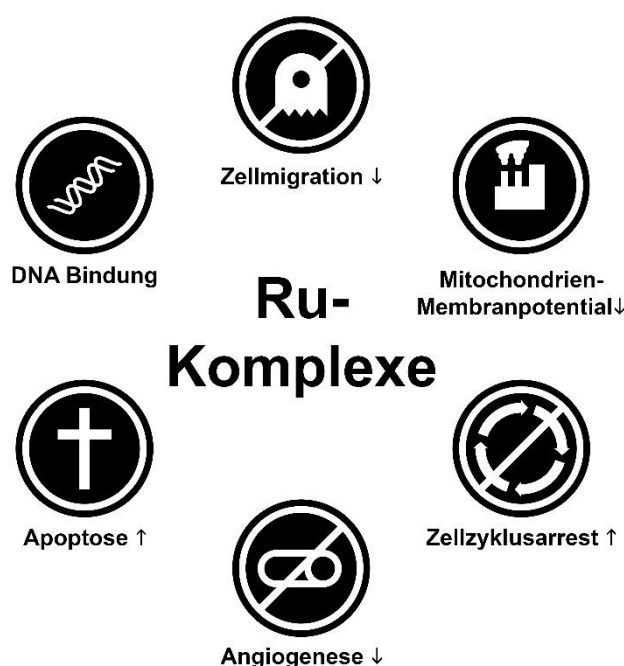


Abbildung 9. Vereinfachte Darstellung der möglichen Effekte von Ruthenium(II/III)-Komplexen. Während einige Rutheniumverbindungen ähnlich wie Cisplatin durch die Bindung an DNA die Arretierung des Zellzyklus und die Induktion von Apoptose verursachen, agieren andere Komplexe indem sie durch Absenkung des Mitochondrien-Membranpotentials zur Aktivierung der Apoptosekaskade über den intrinsischen Weg führen. Weiterhin verfügen andere Ruthenium-Komplexe über die Fähigkeit die Migrierfähigkeit von Zellen herabzusetzen. So kann die Metastasenbildung reduziert werden. Zudem wird durch diese anti-migrative Aktivität auch die Blutgefäßbildung durch Angiogenese reduziert. Dadurch wird neben der Hemmung des Tumorwachstums auch das Metastasierungspotential herabgesetzt.

Um den Aktivierungsschritt bei der Aktivierung-durch-Reduktion zu umgehen, wurde intensiv nach stabilen Ruthenium(II)-Komplexen geforscht. Bemerkenswert ist hier die Klasse der (Aren)Ruthenium(II)-Komplexe, deren sogenannte „half-sandwich piano-stool“ Struktur die Komplexe in der bioaktiven Ruthenium(II) Form hält.¹³⁵ Die Wirkmechanismen dieser Art von Komplexen sind vielfältig und können sich von Komplex zu Komplex unterscheiden. Einige weisen eine ähnliche Wirkung wie NAMI-A auf, wohingegen andere wie Cisplatin an das Target DNA (z.B. RAED-C) binden, ohne dabei Kreuzresistenzen zu zeigen.^{126,135–137} Wiederum andere zeigen anti-proliferative Aktivität, indem sie den Arrest des Zellzyklus verursachen und Apoptose induzieren.¹³⁸ Neben einigen anti-metastatischen Komplexen wurde, wie im Beispiel von RAPTA-C, auch schon anti-angiogene Aktivität beobachtet.¹³⁹ Dabei scheint auch die Interaktion dieser Verbindungen mit verschiedenen Proteinen, u.a. mit dem Histonkern der Chromatine, oder Cathepsin B, eine gewisse Rolle zu spielen.^{136,139,140} Allerdings ist wie im Fall von NAMI-A der detaillierte Wirkmechanismus von RAPTA-C bisher noch nicht vollständig verstanden.

1.7 Histondeacetylase-Inhibitoren

1.7.1 Histondeacetylasen – Vorkommen und Kategorisierung

Die Acetylierung ist eine der wichtigsten posttranslationalen Proteinmodifikationen in der Zelle und hat immensen Einfluss auf die Transkription, die Enzymaktivität und das Metabolom.¹⁴¹ Neben der Acetylierung des N-Terminus der Proteine spielt vor allem die Acetylierung der Lysinseitenketten eine wichtige Rolle.¹⁴¹ Die strikte Regulation des Anfügens von Acetylgruppen durch Histonacetyltransferasen (HAT) und des Entfernens durch Histondeacetylasen (HDAC) ist essentiell für diverse Prozesse in der Zelle.^{141,142} Anders als der Name Histondeacetylase es vermuten lässt, zählen zu deren Substratproteinen aber nicht nur Histone, sondern auch eine Reihe weiterer Proteine, unter anderem Tubulin, Transkriptionsfaktoren, Signaltransducer, und Proteine, die in zelluläre Prozesse wie Angiogenese, Migration und den Zellzyklus involviert sind (vgl. Abb 10).^{142,143} Im Menschen gibt es 18 verschiedene HDACs, die die Deacetylierung entweder über einen Zink- oder über einen NAD⁺-abhängigen Mechanismus vermitteln.¹⁴² Die HDACs sind in vier Subklassen (I, IIa, IIb, III, und IV) kategorisiert und unterscheiden sich in ihrer Struktur, enzymatischen Funktion und ihrer subzellulären Lokalisierung und Expression.¹⁴⁴ Neben den HDACs aus Subklasse I [HDAC1, HDAC2, HDAC3, HDAC8] und IIa [HDAC4, HDAC5, HDAC7, HDAC9] sind auch die HDACs aus Subklasse IIb [HDAC6, HDAC10] Zink-abhängige Histondeacetylasen.¹⁴⁴ Eine eigenständige Subklasse bildet dabei HDAC11, das auf Grund seiner Struktur der Klasse IV zugeordnet wird. Die Klasse III unterscheidet sich dabei stark vom Rest und wird der Klasse der III-Sirtuine (Sirt1-7) zugeordnet, welche die Deacetylierung über einen NAD⁺-abhängigen Mechanismus vermitteln.¹⁴⁵ Im Weiteren soll sich bei der Inhibition der Deacetylasen aber nur auf die Zink-abhängigen HDACs beschränkt werden.

1.7.2 Substrate und Funktionen der Histondeacetylasen

Histondeacetylasen als Target in der Krebstherapie zu nutzen, hat sich in den letzten Jahren als ein vielversprechender Ansatz herausgestellt. HDACs sind unter anderem an der Regulation von Apoptose, Zellzyklus, Angiogenese, Migration, Signaltransduktion und Transkription beteiligt (vgl. Abb. 11).¹⁴⁶ Die HDACs spielen demnach eine wichtige Rolle bei der Initiation und der Progression maligner Erkrankungen, die eine Folge der Fehlregulierung dieser Prozesse sind.¹⁴⁶ Bestimmte HDACs agieren neueren Erkenntnissen zu Folge selbst als Onkogene und liegen überexprimiert in verschiedenen soliden Tumoren vor.^{147,148} Weiterhin variiert die

Expression verschiedener HDAC Subtypen in einigen Fällen je nach Tumorsubtyp.¹⁴⁸ Es ist jedoch schwierig eine Korrelation zwischen dem Grad der Expression einzelner HDAC Subtypen und deren Folgen herzustellen.¹⁴⁸ Im Folgenden sollen nun die Substrate bestimmter HDACs näher beleuchtet werden, wobei ein besonderes Augenmerk auf jene gelegt werden soll, die Einfluss auf Angiogenese und Metastasierung ausüben (siehe Abb. 10).

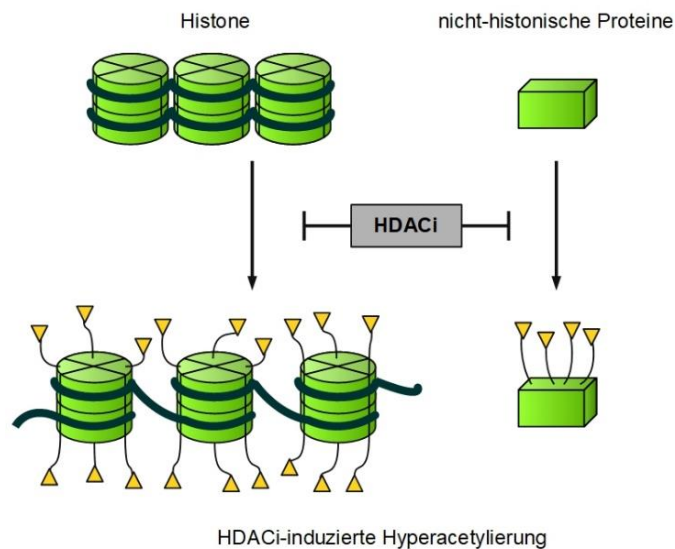


Abbildung 10. Vereinfachte Darstellung der Histondeacetylase-Inhibitor-vermittelten Hyperacetylierung. Durch die Hemmung der Deacetylierung von Histonen wird vereinfacht gesagt die Attraktion zwischen Histonen und DNA verringert, was zu veränderter Genexpression führt. Über die Histone hinaus gehören eine Reihe weiterer nicht-Histon-Proteine zu den Substraten der HDACs. Deren Hyperacetylierung beeinflusst eine ganze Palette an zellulären Prozessen, wie Migration, Angiogenese oder die Dynamik der Mikrotubuli. [Eigene Darstellung nach Do und Rizvi 2011.¹⁴⁹]

Namensgeber dieser Enzyme sind die Histonproteine. Ein Histonoktamer, bestehend aus jeweils zwei Kopien der Histone H2A, H2B, H3, und H4, bildet zusammen mit einer um sie gewundenen DNA-Sequenz das sogenannte Nukleosom.¹⁵⁰ Dieses wiederum ist elementarer Bestandteil des Chromatins. Auf epigenetischer Ebene haben die Histone große Bedeutung, da über deren Modifizierung Genexpression und –silencing reguliert werden können.¹⁵¹ Durch die von HAT vermittelte Acetylierung von Lysinen innerhalb der Histone, werden vereinfacht gesagt, die elektrostatischen Wechselwirkungen zwischen DNA und den Lysinen verringert.¹⁵² Die daraus resultierende Öffnung der Chromatinkonfiguration begünstigt das Binden sowohl von Transkriptionsfaktoren als auch von den Multiproteinkomplexen der Transkriptionsmaschinerie, wodurch die Transkription erhöht wird.^{153,154} Umgekehrt kommt es in Folge der HDAC-vermittelten Deacetylierung zur Erhöhung der Attraktionen zwischen Lysinen und der

DNA, woraus ein kompakteres Chromatin resultiert, was letzten Endes die Interaktion mit Proteinen erschwert und so zur Repression der Genexpression führt.¹⁵⁰

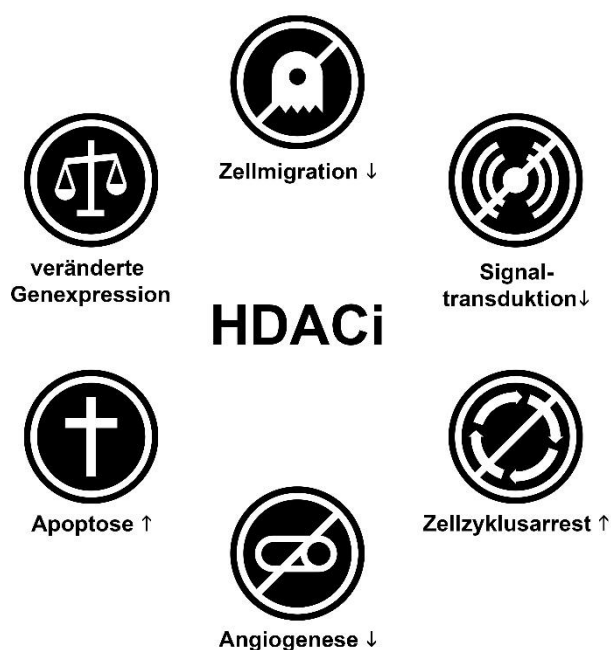


Abbildung 11. Vereinfachte Darstellung der von HDACi-vermittelten Effekte. Die HDACi hemmen die Deacetylierung von Histonen, sowie von weiteren nicht-Histon-Proteinen. In Folge dieser Inhibition kommt es zur Hyperacetylierung dieser Targetmoleküle, woraus eine veränderte Expression diverser Gene resultiert. Weiterhin werden durch die Inhibition der HDACs etliche Signalwege beeinflusst. So können HDACi unter anderem die Arretierung des Zellzyklus bewirken, infolgedessen auch Apoptose induziert werden kann. Weiterhin wird als Folge der Inhibition der HDACs das Aktinzytoskelett so beeinflusst, dass die Migrierfähigkeit der behandelten Zellen herabgesetzt wird. Neben der Senkung des Metastasierungspotentials kommt es so auch zur Hemmung der Angiogenese.

Neben diesen namensgebenden Substraten, gehören auch noch eine Vielzahl weiterer nicht-historischer Proteine zu den Substraten der HDACs. Zu diesen Substraten gehören unter anderem der Tumorsuppressor p53, sowie der Estrogenrezeptor ER α , beides Transkriptionsfaktoren, die an der Regulation des Zellzyklus und von Apoptose beteiligt sind.^{142,150,153,155,156} Weiterhin beeinflussen HDACs auch die Aktivierung und Expression des Oncoproteins c-MYC. So führt die Hyperacetylierung in Folge der HDAC-Inhibition zur Senkung der c-MYC Expression, wodurch es zur Aktivierung des TRAIL Signalwegs und zur Apoptoseinduktion kommt.^{150,157} Zudem werden durch (De-)Acetylierung auch die Transkriptionsfaktoren Nf- κ B und jene der STAT Familie reguliert. Diese wiederum sind über die dazugehörigen Signalwege unter anderem an Apoptoseinduktion, Proliferation, und Angiogenese beteiligt.^{150,158–163} Überdies wird mit Hilfe der HDACs die Stabilität des Transkriptionsfaktors HIF-1 α und darüber dessen Aktivierung gesteuert.^{150,164,165} Da HIF-1 α unter anderem auch die Ausschüttung von VEGF und von Matrixmetalloproteinasen induziert, haben HDACs großen Einfluss auf Angiogenese und Metastasierung.^{165–168} Weiterhin wirken HDACs auch auf das Zytoskelett und dessen Funktionen ein.¹⁶⁹ So wird über die (De-)Acetylierung von Tubulin die Dynamik der Mikrotubuli beeinflusst und die Stabilität, der intrazelluläre Transport und, durch die Interaktion mit dem Aktinzytoskelett, auch die Motilität

der Zelle verändert.¹⁶⁹ Über diese Tubulin-vermittelten Veränderungen des Aktinzytoskeletts hinaus, sind HDACs auch über ihr Substrat Cortactin an der Regulierung des Aktinzytoskeletts beteiligt und beeinflussen so Migration und Angiogenese.¹⁶⁹

1.7.3 Inhibitoren der Zink-abhängigen Histondeacetylasen

Der enorme Einfluss, den HDACi auf die Gentranskription ausüben, zeigt sich wohl schon daran, dass bis zu 20% aller bekannten Gene davon betroffen sind, wobei sich die Hoch- und Herunterregulierung in etwa die Waage halten.¹⁵⁰ Die enzymatische Aktivität der HDACs der Subklassen I, II, und IV läuft, wie bereits beschrieben, über einen Zink-abhängigen Mechanismus. Generell agieren HDACi, indem sie als Mimikry des endogenen Liganden Acetyllysin in das aktive Zentrum eindringen und dort an die Zn^{2+} -Ionen binden, was die Inhibition der enzymatischen Funktion zur Folge hat.¹⁷⁰

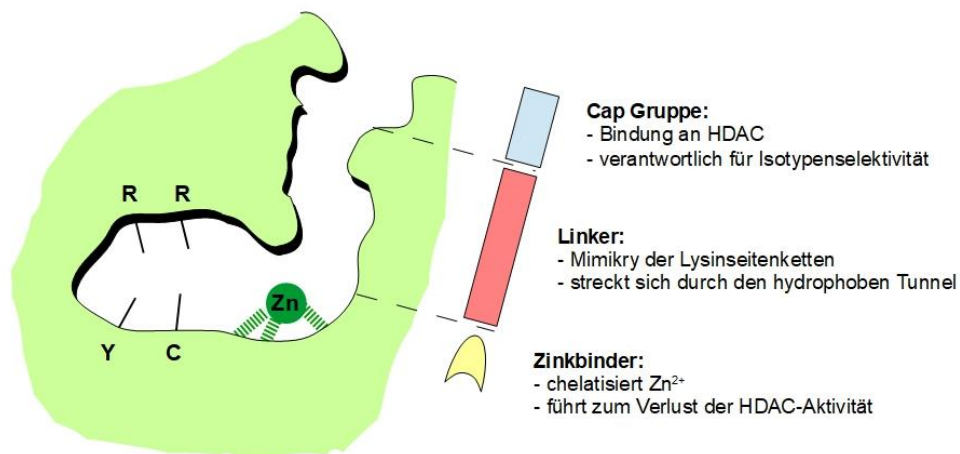
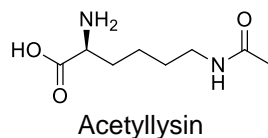


Abbildung 12. Grafisch vereinfachte Darstellung des aktiven Zentrums, und dessen Zugang wie er klassischerweise bei zinkabhängigen Histondeacetylasen vorliegt. Das Pharmakophormodell von klassischen HDACi, welches aus Cap-Gruppe, Linker sowie einer Zinkbindenden Funktion besteht, zeigt wie die einzelnen Untereinheiten in dieser Bindetasche liegen und welche Aufgaben sie dort erfüllen. [Eigene Darstellung nach Hancock *et al.* 2012.¹⁷¹]

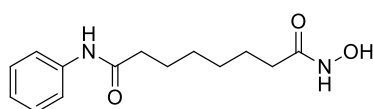
Sie bestehen im Allgemeinen aus einer sogenannten Cap-Gruppe, die über einen Linker mit einer zinkbindenden Gruppe verbunden ist (vgl. Abb. 12).¹⁷¹ Die Cap-Gruppe ist dabei relativ variabel und verantwortlich für die Bindung des Moleküls an die HDAC. Zudem kann über die Wahl der Cap-Gruppe vermutlich die Subtypselektivität gesteuert werden.¹⁷¹ Der Linker imitiert die Lysinseitenkette und ragt über einen „schmalen“, hydrophoben Tunnel in das aktive Zentrum hinein.¹⁷¹ Folglich sind besonders hydrophobe, wenig sperrige Linker von Vorteil, die zudem eine bestimmte Länge besitzen sollten.¹⁷¹ An diesen Linker ist eine zinkbindende

Gruppe geknüpft. Über die Wahl der zinkbindenden Gruppe sind die HDACi in die Hauptkategorien Hydroxamsäuren, Benzamide, elektrophile Ketone, zyklische Tetrapeptide und kurzkettige Fettsäuren eingeteilt (vgl. Abb. 13).¹⁴⁶

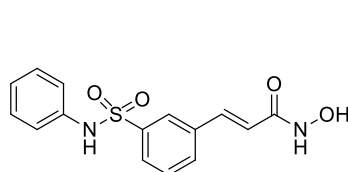
Endogenes Substrat



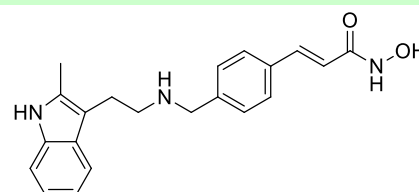
Hydroxamsäuren als HDACi



SAHA/Vorinostat

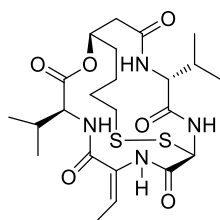


Belinostat

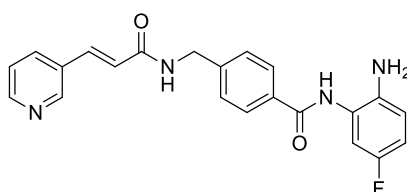


Panobinostat

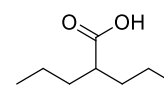
weitere HDACi



Romidepsin
(Tetrapeptid)



Chidamide
(Benzamid)



Valproinsäure
(kurzkettige Fettsäure)

Abbildung 13. Struktur des endogenen Substrats Acetyllysins, sowie Beispiele für Histondeacetylase-Inhibitoren (HDACi). Bei den zugelassenen HDACi Vorinostat (*suberoylanilide hydroxamic acid*, SAHA), Belinostat, und Panobinostat handelt es sich um Hydroxamsäuren, die mittels dieser funktionellen Gruppe das Zn^{2+} im aktiven Zentrum der HDACs chelatisieren. Weitere HDACi: das Tetrapeptid Romidepsin (in den USA zugelassen), das Benzamidderivat Chidamide (in China zugelassen), sowie die kurzkettige Fettsäure Valproinsäure (klinische Studien Phase III).

Neben den bereits in den USA zugelassenen Hydroxamsäurederivaten Vorinostat, Belinostat und Panobinostat und dem zyklischen Tetrapeptid Romidepsin, ist seit 2015 auch das erste Benzamidderivat Chidamide in China zugelassen.^{172–176} Überdies befinden sich einige weiterer HDACi, wie die kurzkettige Fettsäure Valproinsäure, in fortgeschrittenen klinischen Studien (Phase III).^{177–180} Neben diesen pan-spezifischen HDAC Inhibitorderivaten wurden in den vergangenen Jahren auch große Fortschritte in der Entwicklung Isotypen- oder Subklassenspezifischer HDACi gemacht.^{181–185} Bisherige Studien zu diesen selektiveren HDACi zeigten in puncto klinischer Aktivität und Nebenwirkungen aber keine Unterschiede zu den pan-

HDACi.¹⁷⁹ Ob die Hypothese stimmt, dass selektive HDACi im Vergleich zu pan-HDACi bessere Aktivität gepaart mit einem verbesserten Toxizitätsprofil aufweisen, muss somit erst noch gezeigt werden.¹⁷⁹

Neben der Überwindung der Nebenwirkungen (u.a. Fatigue, Diarrhö, Thrombozytopenie, Kardio- und Knochenmarkstoxizität) sowie der Umgehung von Wirkstoffresistenzmechanismen, besteht nach wie vor der Bedarf an effektiveren und selektiveren HDACi.^{148,179,186}

2 Zielsetzung

Nachdem über Jahre nach einer „*magic bullet*“ zur Bekämpfung von Krebs gesucht wurde, wird mittlerweile vielmehr die Individualisierung der Therapie für den jeweiligen Patienten, dessen Tumor und dessen Mikroumfeld präferiert.⁷ Besonders über die Kombination effektiver Wirkstoffe oder von Pharmakophoren innerhalb eines Moleküls könnte so spezifisch für jeden Patienten die optimale Therapie gewählt werden. Aus diesem Grund ist der Bedarf an neuen Verbindungen ungebrochen hoch, die neben verbesserter zytotoxischer Wirkung sowie der Möglichkeit Wirkstoffresistenzen umgehen zu können, auch anti-vaskuläre und anti-metastatische Eigenschaften besitzen, um Tumorprogression, Rezidive und Metastasierung unterbinden zu können.

Im Rahmen dieser Arbeit werden neue potentielle Wirkstoffe auf deren Wirkung sowie auf Strukturwirkbeziehungen präklinisch untersucht. Bei den evaluierten Substanzen handelt es sich um Derivate des Naturstoffs Combretastatin A-4, um Analoga des synthetisch hergestellten 4-Aryl-4*H*-Naphthopyrans LY290181 sowie um eine Serie von Verbindungen mit Chalkongrundgerüst. Alle drei Verbindungsklassen eint deren Potential durch die Destabilisierung der Mikrotubuli Einfluss auf diverse zelluläre Komponenten, Vorgänge und Signalwege zu nehmen und dadurch womöglich anti-vaskuläre und anti-metastatische Effekte auszulösen. Weiterhin wird untersucht, wie die Kombination mit weiteren Pharmakophoren (z.B. mit (Aren)Ruthenium(II)-Fragmenten oder Hydroxamsäuren) den Wirkmechanismus der neuen potentiellen Therapeutika beeinflusst.

Die anti-tumorale Effektivität und Selektivität der neuen Verbindungen sowie die Aufklärung ihrer Wirkmechanismen erfolgt dabei in Experimenten an humanen Zelllinien verschiedener Entitäten. Für die Aufklärung der Wirkung der Verbindungen auf Angiogenese, Metastasierung und Vaskulatur wird neben *in vitro* Tests auch auf *in vivo* Modellsysteme (z.B. Hühnerei und Zebrafischembryo) zurückgegriffen.

Besonderes Augenmerk wird in dieser Arbeit auf den Einfluss der zu testenden Wirkstoffe auf die Zytoskelettkomponenten Aktin und Tubulin gelegt. Im Speziellen wurden die Folgen der zytoskelettalen Veränderungen auf Prozesse wie Angiogenese und Metastasierung, sowie auf die Beschaffenheit der Tumervaskulatur erforscht. Die Erkenntnisse aus diesen präklinischen Evaluationen sollen die Grundlage bei der Entwicklung und Optimierung neuer, potentieller Wirkstoffkandidaten für die Chemotherapie bilden.

3 Synopsis

3.1 Übersicht der Teilprojekte

Die vorliegende kumulative Dissertation beinhaltet vier Publikationen bzw. Manuskripte, in denen die Wirkmechanismen neuer zytotoxischer Verbindungen aus der Klasse der *small molecules*, charakterisiert werden (vgl. Abb. 14). Dazu zählen neben halogenierten Naphthochalkonen und deren strukturverwandten Naphthopyrazolinen, auch eine ganze Bibliothek von Derivaten des 4-Aryl-4*H*-Naphthopyrans LY290181, die destabilisierend auf die Dynamik der Mikrotubuli einwirken. Als Weiterentwicklung dieser Substanzklasse wird im Folgenden eine Serie von (Aren)Ruthenium(II)-Komplexen mit Naphthopyranliganden gezeigt. Diese vereinen Naphthopyran-typische Eigenschaften, wie tubulinbindende, vaskular-disruptive und anti-angiogene Aktivität mit solchen, die auf das Rutheniumzentrum der Komplexe zurückzuführen sind. Zudem wird bei einer Serie von Combretastatin A-4 abgeleiteten Oxazol-Derivaten mit Alkyl-Hydroxamsäuren-Seitenkette gezeigt, wie sich die Veränderung der Struktur dieser Verbindungen auf die Bindung an Tubulin sowie die Inhibition von Histondeacetylasen auswirkt.

Alle im Rahmen dieser Arbeit untersuchten Testsubstanzen wurden am Lehrstuhl für Organische Chemie I der Universität Bayreuth hergestellt. Zum Teil wurden die Untersuchungen der Wirkmechanismen der getesteten Verbindungen in Kooperation mit dem Institut für Innere Medizin IV, Onkologie/Hämatologie der Martin Luther-Universität Halle-Wittenberg, dem Lehrstuhl für Entwicklungsbiologie der Universität Bayreuth, dem Institut Biophysik der *Academy of Science of the Czech Republic* in Brünn (Tschechien), dem Lehrstuhl für Biophysik der Wissenschaftlichen Fakultät der Palacky Universität Olmütz (Tschechien), dem *Research Center for Integrated Analysis and Territorial Management* der Universität Bukarest (Rumänien) und dem Institut für Physiologie der Charité-Universitätsmedizin Berlin durchgeführt.

Synopsis

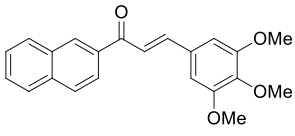
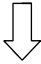
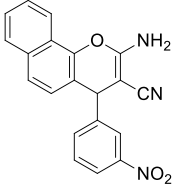
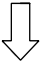
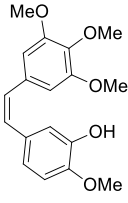
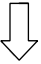
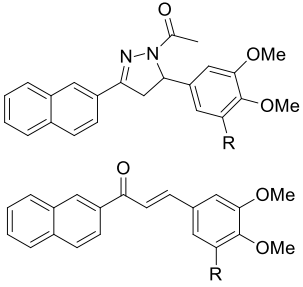
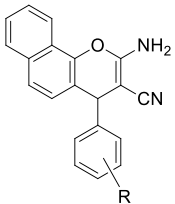
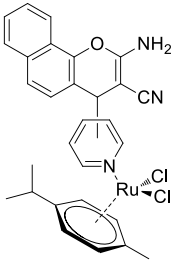
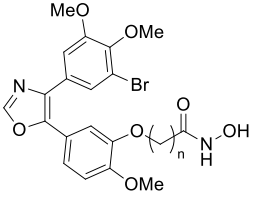
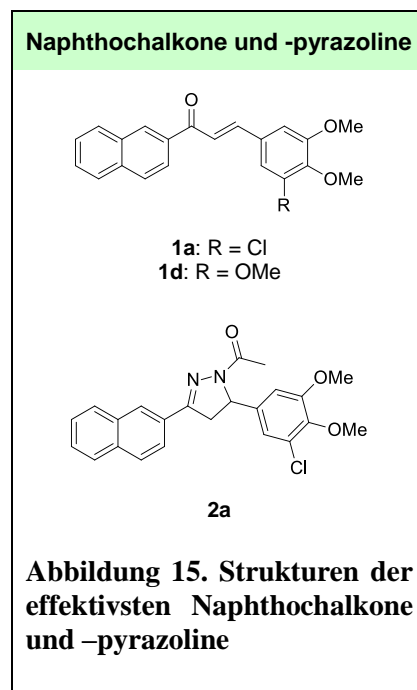
 Naphthochalkon 	 LY290181 	 Combretastatin A-4 	
Chalkon-Analoga	Naphthopyran-Analoga		Combretastatin A-4 Hydroxamsäure-Konjugate
			
Mikrotubuli-Destabilisierende Agenzien (MDA)	MDA/Metallkomplex	MDA/HDACi	
Publikation I Halogenated naphthochalcones and structurally related naphthopyrazolines with antitumor activity. <i>Bioorg. Med. Chem. Lett.</i> 2016	Publikation II New Naphthopyran Analogues of LY290181 as Potential Tumor Vascular-Disrupting Agents. <i>Eur. J. Med. Chem.</i> 2019	Publikation III New (arene)ruthenium(II) complexes of 4-aryl-4H-naphthopyrans with anticancer and anti-vascular activities <i>J. Inorg. Biochem.</i> 2018	Manuskript IV Oxazole-bridged combretastatin A-4 derivatives with tethered hydroxamic acids: Structure-activity relations of new dual inhibitors of HDAC and tubulin function <i>to be submitted</i>

Abbildung 14. Übersicht der untersuchten Wirkstoffklassen und Zuordnung zu den jeweiligen Einzelarbeiten. Im Rahmen dieser Arbeit wurden ein Naphthochalkon, das anti-proliferative, Mikrotubuli-destabilisierende Naphthopyran LY290181, sowie das vaskular-disruptive Combretastatin A-4 als Leitstrukturen verwendet (obere Reihe). Davon wurden die im Rahmen dieser Arbeit evaluierten Verbindungen abgeleitet (mittlere Reihe). Nach ihrer Wirkung werden die Derivate den MDA zugeordnet, die zudem durch die Komplexierung an Ruthenium (zweite von rechts) oder durch Konjugation mit Histondeacetylase (HDAC)-Inhibitoren (ganz rechts) mit zusätzlichen Wirkungen versehen wurden. Übersicht der Publikationen und Manuskripte (untere Reihe).

3.2 Halogenierte Naphthochalkone und strukturverwandte Naphthopyrazoline mit anti-tumoraler Aktivität

Der erste Artikel zu Mikrotubuli-destabilisierenden Agenzien behandelt eine Serie von Derivaten eines Naphthochalkons mit Trimethoxymotiv (**1d**), das erstmals von Ethiraj *et al.* synthetisiert wurde (vgl. Abb. 15).¹⁸⁷ Das ursprüngliche Trimethoxymotiv, welches in einer Reihe von MDA auftritt, wurde für die im Rahmen dieser Arbeit durchgeführte Studie in *meta*-Position durch Halogen-Substituenten derivatisiert, da sich dies bei etlichen Combretastatin A-4 (CA-4) Derivaten positiv auf deren Effektivität auswirkte. Weiterhin wurden die strukturell verwandten Naphthopyrazoline dieser Verbindungen getestet. IC₅₀-Werte (halbmaximale, inhibitorische Konzentration; Maß für die anti-proliferative/zytotoxische Wirkung von Wirkstoffen) im zweistellig mikromolaren Bereich spiegeln die eher moderate *in vitro* Toxizität der Naphthochalkone wider. Um einiges effektiver wirkten die Naphthopyrazoline, die IC₅₀-Werte im einstellig mikromolaren Bereich zeigten.

Sowohl die Naphthochalkone als auch die -pyrazoline scheinen durch, wenn auch im Vergleich zu CA-4 oder Colchicin nur moderate, Interaktion mit Tubulin die Dynamik der Mikrotubuli zu beeinflussen. Als Folge konnte eine vermehrte Bildung von Aktin-*Stress Fibres* in 518A2 Melanomzellen beobachtet werden (siehe Abb. 16). Diese Veränderungen des Aktin-Zytoskeletts sind Indiz für die herabgesetzte Fähigkeit der Zellen zu migrieren. Weiterhin wurde der für Mikrotubuli-destabilisierende Verbindungen typische Arrest des Zellzyklus in der G₂/M Phase gezeigt, welcher aus der Hemmung des Aufbaus der mitotischen Spindel resultiert. Die Chalkone, die im Gegensatz zu den Pyrazolinen bereits nach einer Behandlung von nur 24 h Apoptose in 518A2 Melanomzellen ausgelöst hatten, scheinen neben Tubulin noch auf weitere Targets Einfluss zu nehmen. Es wird davon ausgegangen, dass wie für strukturverwandte Derivate mit anderem Substituenten belegt, die Behandlung der Zellen zu Veränderungen der zellulären Level der Proteine aus der Bcl-2 Familie führt und so Apoptose über den intrinsischen Weg induziert wird.



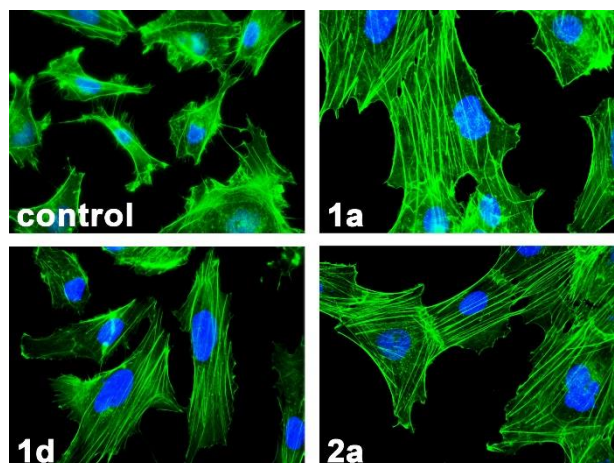


Abbildung 16. Effekte der Naphthochalkone (1a und 1d) sowie des Pyrazolins (2a) auf das Aktin-Zytoskelett in 518A2 Melanomzellen. Durch die Destabilisierung der Mikrotubuli, kommt es in den behandelten Zellen zur vermehrten Bildung sogenannter Aktin *Stress Fibrines*. Die Veränderungen des Aktin-Zytoskeletts sind ein Indiz dafür, dass die Migrierfähigkeit der behandelten Zellen im Gegensatz zu den unbehandelten herabgesetzt ist. [Reprinted with permission from F. Schmitt, H. Draut, *et al.* *Bioorg. Med. Chem. Lett* 26, 5168-5171, doi 10.1016/j.bmcl.2016.09.076. Copyright 2016, Elsevier Ltd.]

Besonders bestachen diese neuen Verbindungen durch ihre Fähigkeit die Resistenz multi-resistenter Zelllinien zu überwinden. ABC-Transporter, welche häufig überexprimiert in multiresistenten Tumoren vorliegen und über die Ausschleusung der Xenobiotika Chemotherapien stark einschränken können, wurden von den Testverbindungen inhibiert. Folglich zeigten diese auch in den Zytotoxizitätsstudien mit multiresistenten MCF-7^{Topo} Mammakarzinomzellen und KB-V1^{Vbl} Gebärmutterhalskrebszellen gute Ergebnisse. Während die Pyrazoline sowohl die ABC-Transporter BCRP als auch P-gp inhibierten, wirken die halogenierten Chalkone selektiv nur bei BCRP.

Weitere Details in: F.Schmitt, H. Draut, B. Biersack, R. Schobert.

Halogenated naphthochalcones and structurally related naphthopyrazolines with antitumor activity.

Bioorg. Med. Chem. Lett. **2016** 26, 5168-5171.

[Publikation I]

3.3 LY290181-abgeleitete Analoga als Mikrotubuli-destabilisierende Agenzien

3.3.1 Neue Naphthopyrananaloga von LY290181 als potentiell vaskular-disruptive Wirkstoffe

Diese Publikation behandelt eine Serie von Derivaten des 4-Aryl-4*H*-Naphthopyrans LY290181 (**2a**; siehe Abb. 17). Diese stark anti-proliferative, Tubulin-bindende Verbindung, die erstmalig 1996 in einer Publikation von Wiernicki *et al.* Erwähnung findet, wurde ursprünglich eher auf die Verhinderung von Restenosen sowie in der Behandlung von Diabetes getestet.¹⁸⁸ Für einige struktur-

verwandte Verbindungen wurden *in vitro* bereits Sekundäreffekte der Destabilisierung der Mikrotubuli beobachtet (z.B. die Arretierung des Zellzyklus in G2/M, Induktion von Apoptose oder vaskular-disruptive Effekte), die für die Krebstherapie interessant

sein könnten. Aus diesem Grund wurde die Mutterverbindung LY290181 an dessen Phenylring mit verschiedenen Substituenten variiert, um so Beziehungen zwischen Struktur und Aktivität herstellen zu können und darauf aufbauend die Verbindungen hinsichtlich ihrer Aktivität zu optimieren.

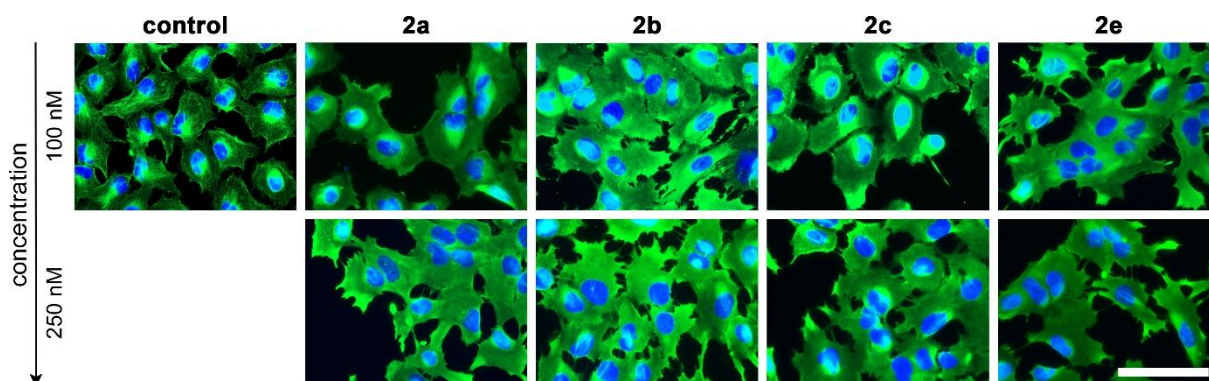
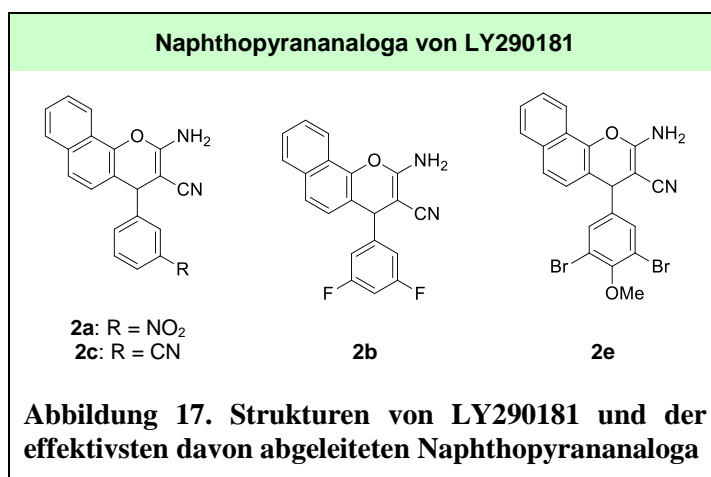


Abbildung 18. Effekte von LY290181 (2a) und seiner Analoga (2b, 2c, und 2e) auf die Organisation des Tubulin-Zytoskeletts (grün) in 518A2 Melanomzellen. Im Gegensatz zu den hochkomplexen, filamentösen Strukturen des Tubulin-Zytoskeletts in den Kontrollzellen, liegt das Tubulin in den behandelten Zellen nur noch diffus verteilt vor. Maßstabsbalken: 50 µm. [Reprinted with permission from F. Schmitt, M. Gold, *et al.* Eur. J. Med. Chem. 163, 160-168, doi 10.1016/j.ejmech.2018.11.055. Copyright 2018, Elsevier Ltd.]

Tatsächlich wurde in Zytotoxizitätsstudien mit einer ganzen Reihe an Derivaten von LY290181 gezeigt, dass die Aktivität dieser Verbindungen stark durch deren Substitutionsmuster beeinflusst wird. Hierbei wurde eine Reihe an Verbindungen identifiziert, die ähnlich stark oder sogar stärker als LY290181 wirken. Für eine Auswahl der effektivsten Derivate wurde daraufhin die Mikrotubuli-destabilisierende Wirkung in 518A2 Melanomzellen belegt (vgl. Abb. 18). Zudem wurde der MDA-typische G2/M Arrest beobachtet, der auf der Hemmung der Ausbildung des mitotischen Spindelapparats basiert.

Die Arretierung des Zellzyklus sowie womöglich auch die Beeinflussung weiterer Signalwege und Regulatoren führen überdies zur Einleitung der Apoptose. Zudem konnte mittels Immunfluoreszenz-Mikroskopie auch die vermehrte Bildung von Aktin-*Stress Fibres* detektiert werden, wodurch die Motilität der behandelten Zellen reduziert wird. Neben dem Einfluss der Behandlung auf Zellmigration konnten so auch anti-angiogene Effekte *in vitro* beobachtet werden.

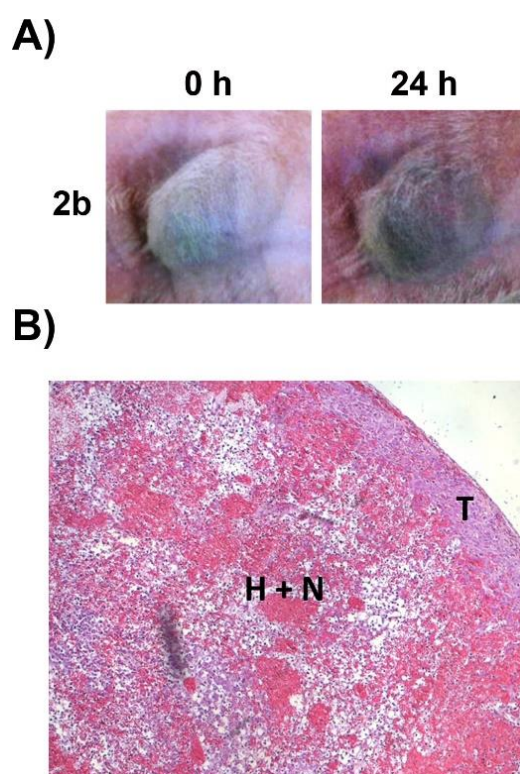


Abbildung 19. Auswirkungen der Behandlung mit Naphthopyran 2b auf Xenograft-Tumore in Mäusen. (A) Dokumentation der vaskular-disruptiven Aktivität von 2b in einem Tumor, der sich auf Grund der Einblutungen dunkel verfärbt hat. Gewebeschnitt eines Tumors (B) in dessen Kern Hämorrhagien (H) und Nekrosen (N) auftreten, wohingegen die Tumorrinde (T) vital bleibt. [Reprinted with permission from F. Schmitt, M. Gold, *et al.* Eur. J. Med. Chem. 163, 160-168, doi 10.1016/j.ejmech.2018.11.055. Copyright 2018, Elsevier Ltd.]

In ersten vorläufigen *in vivo*-Untersuchungen zur Auswirkung der Behandlung auf die Blutgefäße der Chorioallantoismembran in befruchteten Hühnereiern konnte die vaskular-disruptive Aktivität der Verbindungen belegt werden. Diese führte zur sehr effektiven Zerstörung speziell kleinerer Blutgefäße nach nur 6 h Behandlung, erlaubte jedoch die Regeneration nach 24 h. Neben der Muttersubstanz zeigte bei diesem Assay besonders das difluorierte Derivat **2b** gute Aktivität. Im Gegensatz dazu führte die Behandlung der CAM mit dem Dibromo-Methoxy Derivat **2e** zur Reizung der gesamten Membran, was ein Indiz für dessen generelle Toxizität ist.

Bei weiterführenden *in vivo* Studien an Mäusen mit hoch-vaskularisierten Xenograft-Tumoren konnte bei LY290181 auch bei sehr hoher Dosierung kein Effekt auf die Tumorvaskulatur ausgemacht werden. Wie bereits in den CAM Assays vermutet, fiel auch das Dibromo-Methoxy Derivat auf Grund seiner geringen therapeutischen Breite durch, wohingegen das Derivat **2b** zu den für vaskular-disruptive Verbindungen typischen Verfärbung des Tumors führte, welche auf intratumorale Hämorrhagien zurückzuführen ist (vgl. Abb 19 A). Neben diesen Hämorrhagien innerhalb des Tumors wurden in histologischen Untersuchungen der Tumorgewebeschnitte zudem die für VDA-typischen nekrotischen Bereiche im Kern des Xenografts sowie die intakte Tumorrinde mit vitalen Tumorzellen nachgewiesen (vgl. Abb. 19 B). Weiterhin wurde in einer Studie an Mäusen mit Cisplatin-resistenten Xenograft-Tumoren ein signifikant geringeres Tumorstadium gegenüber den Kontrolltieren festgestellt.

Anhand dieses Beispiels von verschiedenen Naphthopyran-Derivaten konnte demonstriert werden, wie durch geschickte Substitution zum Einen die Wirkung optimiert, aber zum Anderen auch Nebenwirkungen bzw. die generelle Toxizität beeinflusst werden können.

Weitere Details: F. Schmitt, M. Gold, M. Rothmund, I.C. Andronache, B. Biersack, R. Schobert, T. Mueller.

New Naphthopyran Analogues of LY290181 as Potential Tumor Vascular-Disrupting Agents

Eur. J. Med. Chem. **2019** 163, 160-168.

[Publikation II]

3.3.2 Neue (Aren)Ruthenium(II)-Komplexe von 4-Aryl-4H-Naphthopyranen mit anti-tumoraler und anti-vaskularer Aktivität

Durch die Koordination von 4-Aryl-4H-Naphthopyranliganden an (Aren)Ruthenium(II)-Fragmente sollten neben der Verbesserung der Löslichkeit, Synergien bzw. additive Effekte erzielt werden (vgl. Abb. 20). Die neuen Rutheniumkomplexe mit Naphthopyranliganden wirken außergewöhnlich stark anti-proliferativ, was wohl vor allem auf die Naphthopyranliganden zurückzuführen ist. Zudem verfügen die Verbindungen über eine außerordentlich gute Selektivität für Tumorzellen gegenüber nicht-malignen Fibroblasten. Die Verbindungen konnten weiterhin die Resistenzmechanismen multiresistenter Zelllinien umgehen. In verschiedenen zellfreien Assay-Systemen wurde belegt, dass die (Aren)Ruthenium(II)-Komplexe an DNA binden. Die Bindung erfolgt dabei circa 10-mal rascher als bei Cisplatin. Weiterhin beeinflussen die Verbindungen die Dynamik der Mikrotubuli. Infolge der Behandlung mit hohen Konzentrationen der Testsubstanzen werden die Zellen in der Mitose arretiert, was zu Apoptoseinduktion führt. In MCF-7^{Topo} Brustkrebszellen lösen niedrige Konzentrationen hingegen einen postmitotischen G1 Arrest aus, der womöglich auf eine p53-abhängige Aktivierung zurückzuführen ist.

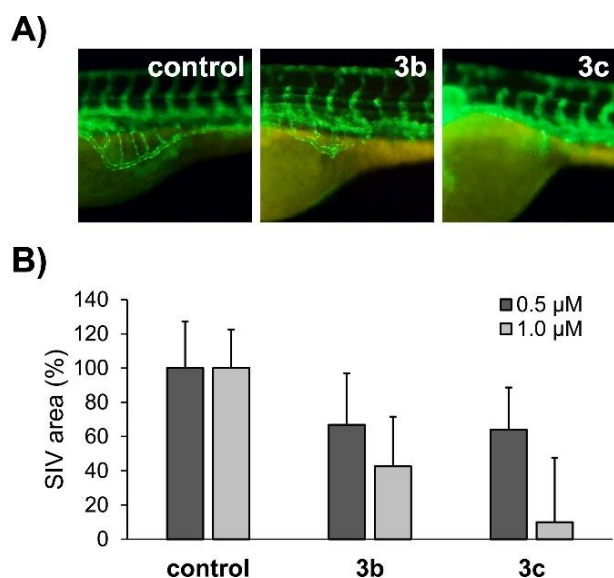
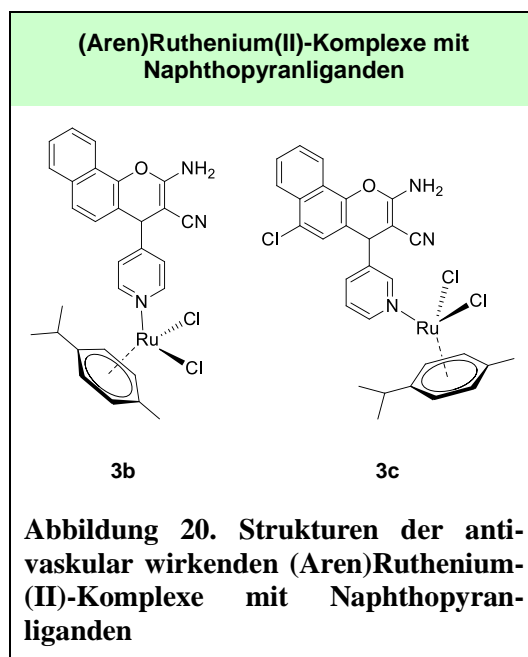


Abbildung 21. Anti-angiogene Aktivität der (Aren)Ruthenium(II)-Komplexe (3b und 3c) im Zebrafischembryo. Als Marker für die anti-angiogene Aktivität wird in diesem Assay-system die Entwicklung der subintestinalen Venen (SIV) verwendet. (A) Während die Entwicklung der SIV in den Kontrolltieren normal verlaufen ist und die gewöhnliche sinoidale Form ausgebildet wurde, sind diese Blutgefäße in den behandelten Tieren weniger stark ausgeprägt. (B) Die Quantifizierung der Fläche der SIV zeigt, wie stark die anti-angiogene Wirkung der (Aren)Ruthenium(II)-Komplexe ist. [Reprinted with permission from F. Schmitt *et al.* J. Inorg. Biochem 184, 69-78, doi. 10.1016/j.inorgbio.2018.03.013. Copyright 2018, Elsevier Ltd.]

Die beiden am besten löslichen Komplexe **3b** und **3c** üben zudem starken Einfluss auf die Vaskulatur und deren Entstehung aus. Neben vaskular-disruptive Effekten, die *in vivo* auf der Chorioallantoismembran befruchteter Hühnereier nachgewiesen werden konnten (vgl. Abb. 22 B), wurde *in vitro* die Ausbildung von Blutgefäß-ähnlichen Systemen durch Tumorzellen über sogenanntes Vasculäres Mimikry von den Testverbindungen inhibiert (vgl. Abb. 22 A). Zudem konnte die anti-angiogene Aktivität dieser Verbindungen *in vivo* unter Verwendung von genveränderten Zebrafischembryonen belegt werden (siehe Abb. 21).

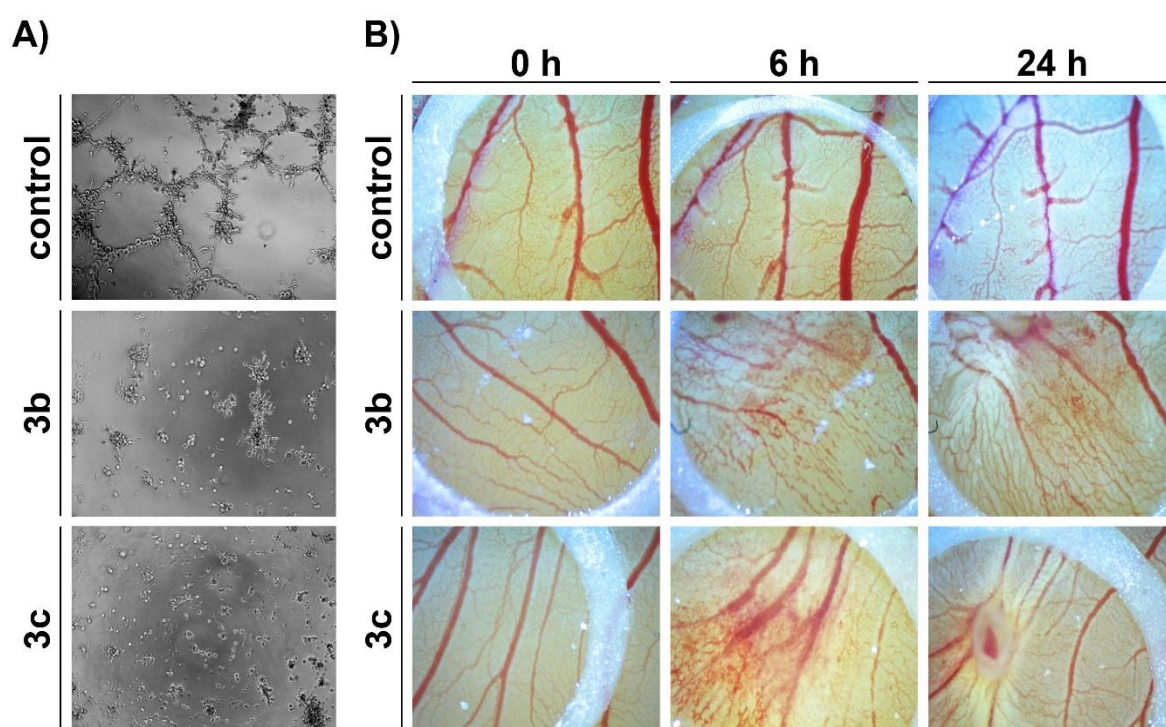


Abbildung 22. Antivaskuläre Effekte der Ruthenium-Komplexe 3b und 3c. Inhibition der Ausbildung röhrenförmiger Strukturen von U-87 Glioblastomazellen über sogenanntes Vasculäres Mimikry (A), sowie vaskular-disruptive Effekte im Chorioallantoismembran Assay im Hühnerei (B). [Reprinted with permission from F. Schmitt *et al.* J. Inorg. Biochem 184, 69-78, doi. 10.1016/j.inorgbio.2018.03.013. Copyright 2018, Elsevier Ltd.]

Weitere Details: F. Schmitt, J. Kasparikova, V. Brabec, G. Begemann, R. Schobert, B. Biersack.

New (arene)ruthenium(II) complexes of 4-aryl-4H-naphthopyrans with anticancer and anti-vascular activities

J. Inorg. Biochem. **2018** 184, 69-78.

[**Publikation III**]

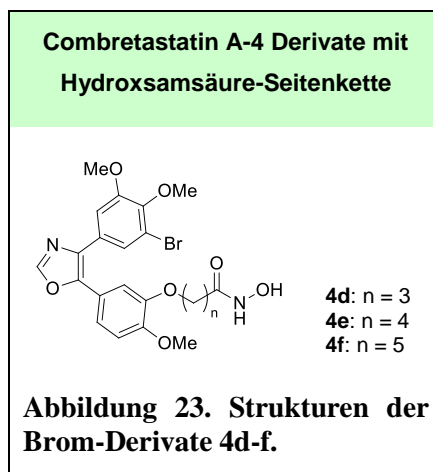
3.4 Oxazol-verbrückte Combretastatin A-4 Derivate mit Alkyl-Hydroxamsäure Seitenkette: Struktur-Aktivitätsbeziehungen neuer dualer Inhibitoren der HDAC- und Tubulinfunktion

Das Konzept hinter der Konjugation von Oxazol-Derivaten von Combretastatin A-4 mit Hydroxamsäureresten ist die Schaffung bimodaler Wirkstoffe, die neben der Destabilisierung der Mikrotubuli auch durch HDAC Inhibition anti-tumorale Effekte erzielen können (vgl. Abb. 23). Neben der Variation des für Tubulinbinder charakteristischen Trimethoxyphenyl-Motivs wurde in dieser Studie auch die Länge der Alkylseitenkette (Linker), die das CA-4 Derivat mit der Hydroxamsäurefunktion verbindet, variiert. Bei Zytotoxizitätsstudien wurde gezeigt, dass die Hydroxamsäurefunktion essentiell für die Wirkung der Verbindungen ist und Länge des Linkers starken Einfluss auf die Aktivität der Verbindungen hat. Generell lässt sich sagen, dass die

anti-proliferative Aktivität steigt, je kleiner diese Linkerfunktion gewählt wird. Während sich auch die Mikrotubuli-destabilisierende Wirkung verstärkt, je kürzer der Linker der Derivate ist, wurde genau der gegenteilige Trend bei der Inhibition von HDAC1 und HDAC6 beobachtet. Hier wiederum wirkten die Derivate mit längeren Linkern deutlich effektiver. Der beste HDACi **4f** inhibierte die rekombinanten Isoenzyme HDAC1 und HDAC6 ähnlich stark wie die bekannten HDACi Vorinostat und Tubacin. Western-Blot Analysen und Immunofluoreszenzfärbungen des Acetyl-Tubulin-Level in mit **4f** behandelten Zellen belegen die deutliche Erhöhung der Mikrotubuli-Acetylierung und bestätigten so die Inhibition der HDAC6 durch **4f**.

Bei Studien zum Einfluss der Linkerlänge auf die durch die Testverbindungen ausgelösten Veränderungen des Aktin-Zytoskeletts konnte indes kein Unterschied zwischen den Derivaten ausgemacht werden. So konnte bei allen der getesteten Verbindungen eine erhöhte Ausbildung von *Aktin-Stress Fibres* detektiert werden. Die daraus resultierende verringerte Migrierfähigkeit der behandelten Zellen konnte für alle Derivate gleichermaßen belegt werden. Der Effekt der Linkerlänge auf den Zellzyklus ist wiederum sehr unterschiedlich zwischen den Derivaten. So führen die Derivate mit kurzem Linker, die vor allem durch ihre Tubulinbindende Aktivität bestehen und weniger effektive HDAC-Inhibitoren darstellen zu dem für MDA typischen G2/M Arrest. Im Gegensatz dazu induzierten Derivate mit längerem Linker die Arretierung des Zellzyklus in G1, welche die Ursache wohl in der starken HDAC Inhibition

Bei Studien zum Einfluss der Linkerlänge auf die durch die Testverbindungen ausgelösten Veränderungen des Aktin-Zytoskeletts konnte indes kein Unterschied zwischen den Derivaten ausgemacht werden. So konnte bei allen der getesteten Verbindungen eine erhöhte Ausbildung von *Aktin-Stress Fibres* detektiert werden. Die daraus resultierende verringerte Migrierfähigkeit der behandelten Zellen konnte für alle Derivate gleichermaßen belegt werden. Der Effekt der Linkerlänge auf den Zellzyklus ist wiederum sehr unterschiedlich zwischen den Derivaten. So führen die Derivate mit kurzem Linker, die vor allem durch ihre Tubulinbindende Aktivität bestehen und weniger effektive HDAC-Inhibitoren darstellen zu dem für MDA typischen G2/M Arrest. Im Gegensatz dazu induzierten Derivate mit längerem Linker die Arretierung des Zellzyklus in G1, welche die Ursache wohl in der starken HDAC Inhibition



sowie der fehlenden Tubulin-bindenden Aktivität hat.

Die durch die hier getesteten Verbindungen verursachten zytoskelettalen Veränderung und deren Fähigkeit HDACs zu inhibieren sind ein deutliches Indiz für das Potential der Verbindungen auch Einfluss auf Angiogenese und die Integrität bereits bestehender Tumorblutgefäße zu nehmen. Erste *in vivo* Versuche im Hühnerei und Zebrafisch deuteten bereits diese anti-vaskularen Effekte an. Weiterführende *in vivo* Studien, unter anderem auch in Mäusen, die aktuell durchgeführt werden, sollen weitere Einblicke in das Potential dieser Verbindungsklasse gewähren.

Weitere Details: F. Schmitt, L. C. Gosch, R. Schobert, B. Biersack, A. Volkamer, M. Höpfner.

Oxazole-bridged combretastatin A-4 derivatives with alkyl hydroxamate side chains: Structure activity relationship studies on their application as dual HDAC-tubulin inhibitors

To be submitted

4 Literaturverzeichnis

- (1) *Todesursachen in Deutschland 2015*; 2120400157004; Statistisches Bundesamt (Destatis), 2017.
- (2) *Krebs in Deutschland Für 2013/2014*; 11. Ausgabe; Gemeinsame Publikation des Zentrums für Krebsregisterdaten und der Gesellschaft der Epidemiologischen Krebsregisters in Deutschland e.V.: Berlin, 2017.
- (3) Barnes, B.; Bertz, J.; Buttman-Schweiger, N.; Fiebig, J.; Jordan, S.; Kraywinkel, K.; Niemann, H.; Nowossadeck, E.; Poethko-Müller, C.; Prütz, F.; et al. *Bericht Zum Krebsgeschehen in Deutschland 2016*; Robert-Koch Institut: Berlin, 2016.
- (4) Berger, N. A.; Savvides, P.; Koroukian, S. M.; Kahana, E. F.; Deimling, G. T.; Rose, J. H.; Bowman, K. F.; Miller, R. H. Cancer in the Elderly. *Trans. Am. Clin. Climatol. Assoc.* **2006**, *117*, 147.
- (5) Hanahan, D.; Weinberg, R. A. Hallmarks of Cancer: The Next Generation. *Cell* **2011**, *144* (5), 646–674.
- (6) Hanahan, D.; Weinberg, R. A. The Hallmarks of Cancer. *Cell* **2000**, *100* (1), 57–70.
- (7) Hanahan, D. Rethinking the War on Cancer. *The Lancet* **2014**, *383* (9916), 558–563.
- (8) Valastyan, S.; Weinberg, R. A. Tumor Metastasis: Molecular Insights and Evolving Paradigms. *Cell* **2011**, *147* (2), 275–292.
- (9) Siemann, D. W.; Bibby, M. C.; Dark, G. G.; Dicker, A. P.; Eskens, F. A. L. M.; Horsman, M. R.; Marmé, D.; LoRusso, P. M. Differentiation and Definition of Vascular-Targeted Therapies. *Clin. Cancer Res.* **2005**, *11*, 416–420.
- (10) Potente, M.; Gerhardt, H.; Carmeliet, P. Basic and Therapeutic Aspects of Angiogenesis. *Cell* **2011**, *146* (6), 873–887.
- (11) Swift, M. R.; Weinstein, B. M. Arterial-Venous Specification During Development. *Circ. Res.* **2009**, *104* (5), 576–588.
- (12) Adams, R. H.; Alitalo, K. Molecular Regulation of Angiogenesis and Lymphangiogenesis. *Nat. Rev. Mol. Cell Biol.* **2007**, *8* (6), 464–478.
- (13) Hoeben, A. Vascular Endothelial Growth Factor and Angiogenesis. *Pharmacol. Rev.* **2004**, *56* (4), 549–580.
- (14) Folkman, J. Role of Angiogenesis in Tumor Growth and Metastasis. *Semin. Oncol.* **2002**, *29* (6Q), 15–18.
- (15) Folkman, J. Tumor Angiogenesis: Therapeutic Implications. *N. Engl. J. Med.* **1971**, *285* (21), 1182–1186.
- (16) Gimbrone Jr, M. A.; Leapman, S. B.; Cotran, R. S.; Folkman, J. Tumor Angiogenesis: Iris Neovascularization at a Distance From Experimental Intraocular Tumors. *J. Natl. Cancer Inst.* **1973**, *50* (1), 219–228.
- (17) Gimbrone Jr, M. A.; Cotran, R. S.; Leapman, S. B.; Folkman, J. Tumor Growth and Neovascularization: An Experimental Model Using the Rabbit Cornea. *J. Natl. Cancer Inst.* **1974**, *52* (2), 413–427.
- (18) Folkman, J.; Hochberg, M. Self-Regulation of Growth in Three Dimensions. *J. Exp. Med.* **1973**, *138* (4), 745–753.
- (19) Knighton, D.; Ausprunk, D.; Tapper, D.; Folkman, J. Avascular and Vascular Phases of Tumour Growth in the Chick Embryo. *Br. J. Cancer* **1977**, *35* (3), 347–356.
- (20) Ausprunk, D. H.; Knighton, D. R.; Folkman, J. Vascularization of Normal and Neoplastic Tissues Grafted to the Chick Chorioallantois. Role of Host and Preexisting Graft Blood Vessels. *Am. J. Pathol.* **1975**, *79* (3), 597.
- (21) Folkman, J.; Watson, K.; Ingber, D.; Hanahan, D. Induction of Angiogenesis during the Transition from Hyperplasia to Neoplasia. *Nature* **1989**, *339*, 58–61.

- (22) Nishida, N.; Yano, H.; Nishida, T.; Kamura, T.; Kojiro, M. Angiogenesis in Cancer. *Vasc. Health Risk Manag.* **2006**, *2* (3), 213–219.
- (23) Denekamp, J. Angiogenesis, Neovascular Proliferation and Vascular Pathophysiology as Targets for Cancer Therapy. *Br. J. Radiol.* **1993**, *66* (783), 181–196.
- (24) Baeriswyl, V.; Christofori, G. The Angiogenic Switch in Carcinogenesis. *Semin. Cancer Biol.* **2009**, *19* (5), 329–337.
- (25) North, S.; Moenner, M.; Bikfalvi, A. Recent Developments in the Regulation of the Angiogenic Switch by Cellular Stress Factors in Tumors. *Cancer Lett.* **2005**, *218* (1), 1–14.
- (26) Zumsteg, A.; Christofori, G. Corrupt Policemen: Inflammatory Cells Promote Tumor Angiogenesis: *Curr. Opin. Oncol.* **2009**, *21* (1), 60–70.
- (27) Farooqi, A. A.; Siddik, Z. H. Platelet-Derived Growth Factor (PDGF) Signalling in Cancer: Rapidly Emerging Signalling Landscape: PDGF-Induced Signalling Cascades. *Cell Biochem. Funct.* **2015**, *33* (5), 257–265.
- (28) Kadomatsu, K. Midkine and Pleiotrophin in Neural Development and Cancer. *Cancer Lett.* **2004**, *204* (2), 127–143.
- (29) Bergers, G.; Brekken, R.; McMahon, G.; Vu, T. H.; Itoh, T.; Tamaki, K.; Tanzawa, K.; Thorpe, P.; Itohara, S.; Werb, Z. Matrix Metalloproteinase-9 Triggers the Angiogenic Switch during Carcinogenesis. *Nat. Cell Biol.* **2000**, *2* (10), 737–744.
- (30) Meirovitz, A.; Goldberg, R.; Binder, A.; Rubinstein, A. M.; Hermano, E.; Elkin, M. Heparanase in Inflammation and Inflammation-Associated Cancer. *FEBS J.* **2013**, *280* (10), 2307–2319.
- (31) Joyce, J. A.; Baruch, A.; Chehade, K.; Meyer-Morse, N.; Giraud, E.; Tsai, F.-Y.; Greenbaum, D. C.; Hager, J. H.; Bogyo, M.; Hanahan, D. Cathepsin Cysteine Proteases Are Effectors of Invasive Growth and Angiogenesis during Multistage Tumorigenesis. *Cancer Cell* **2004**, *5* (5), 443–453.
- (32) Sottile, J. Regulation of Angiogenesis by Extracellular Matrix. *Biochim. Biophys. Acta BBA - Rev. Cancer* **2004**, *1654* (1), 13–22.
- (33) Venning, F. A.; Wullkopf, L.; Erler, J. T. Targeting ECM Disrupts Cancer Progression. *Front. Oncol.* **2015**, *5*.
- (34) Porcù, E.; Bortolozzi, R.; Basso, G.; Viola, G. Recent Advances in Vascular Disrupting Agents in Cancer Therapy. *Future Med. Chem.* **2014**, *6* (13), 1485–1498.
- (35) Hinnen, P.; Eskens, F. A. L. M. Vascular Disrupting Agents in Clinical Development. *Br. J. Cancer* **2007**, *96* (8), 1159–1165.
- (36) Carmeliet, P. Angiogenesis in Life, Disease and Medicine. *Nature* **2005**, *438* (7070), 932–936.
- (37) A Spear, M.; LoRusso, P.; Mita, A.; Mita, M. Vascular Disrupting Agents (VDA) in Oncology: Advancing towards New Therapeutic Paradigms in the Clinic. *Curr. Drug Targets* **2011**, *12* (14), 2009–2015.
- (38) Mita, M. M.; Sargsyan, L.; Mita, A. C.; Spear, M. Vascular-Disrupting Agents in Oncology. *Expert Opin. Investig. Drugs* **2013**, *22* (3), 317–328.
- (39) Sund, M.; Zeisberg, M.; Kalluri, R. Endogenous Stimulators and Inhibitors of Angiogenesis in Gastrointestinal Cancers: Basic Science to Clinical Application. *Gastroenterology* **2005**, *129* (6), 2076–2091.
- (40) Cao, Y. Tumor Angiogenesis and Molecular Targets for Therapy. *Front. Biosci.* **2009**, *14*, 3962–3973.
- (41) Thorpe, P. E. Vascular Targeting Agents as Cancer Therapeutics. *Clin. Cancer Res.* **2004**, *10*, 415–427.
- (42) Gupta, G. P.; Massagué, J. Cancer Metastasis: Building a Framework. *Cell* **2006**, *127* (4), 679–695.
-

-
- (43) Steeg, P. S. Tumor Metastasis: Mechanistic Insights and Clinical Challenges. *Nat. Med.* **2006**, *12* (8), 895–904.
- (44) Alizadeh, A. M.; Shiri, S.; Farsinejad, S. Metastasis Review: From Bench to Bedside. *Tumor Biol.* **2014**, *35* (9), 8483–8523.
- (45) Lambert, A. W.; Pattabiraman, D. R.; Weinberg, R. A. Emerging Biological Principles of Metastasis. *Cell* **2017**, *168* (4), 670–691.
- (46) Guan, X. Cancer Metastases: Challenges and Opportunities. *Acta Pharm. Sin. B* **2015**, *5* (5), 402–418.
- (47) Efferth. Molecular Principles of Cancer Invasion and Metastasis (Review). *Int. J. Oncol.* **2009**, *34* (4).
- (48) Mahal, K. A Mechanistic Assessment of Novel Anticancer Drugs Targeting the Metastatic Cascade and Tumour Vascularisation, Universität Bayreuth: Bayreuth, 2015.
- (49) Nelson, W. J. Regulation of Cell–cell Adhesion by the Cadherin–catenin Complex. *Biochem. Soc. Trans.* **2008**, *36* (2), 149–155.
- (50) Kalluri, R.; Weinberg, R. A. The Basics of Epithelial-Mesenchymal Transition. *J. Clin. Invest.* **2009**, *119* (6), 1420–1428.
- (51) Tania, M.; Khan, M. A.; Fu, J. Epithelial to Mesenchymal Transition Inducing Transcription Factors and Metastatic Cancer. *Tumor Biol.* **2014**, *35* (8), 7335–7342.
- (52) Zhang, L.; Huang, G.; Li, X.; Zhang, Y.; Jiang, Y.; Shen, J.; Liu, J.; Wang, Q.; Zhu, J.; Feng, X.; et al. Hypoxia Induces Epithelial-Mesenchymal Transition via Activation of SNAI1 by Hypoxia-Inducible Factor -1 α in Hepatocellular Carcinoma. *BMC Cancer* **2013**, *13* (1).
- (53) Huber, F.; Schnauß, J.; Rönicke, S.; Rauch, P.; Müller, K.; Fütterer, C.; Käs, J. Emergent Complexity of the Cytoskeleton: From Single Filaments to Tissue. *Adv. Phys.* **2013**, *62* (1), 1–112.
- (54) Fife, C. M.; McCarroll, J. A.; Kavallaris, M. Movers and Shakers: Cell Cytoskeleton in Cancer Metastasis: Cytoskeleton and Cancer Metastasis. *Br. J. Pharmacol.* **2014**, *171* (24), 5507–5523.
- (55) Blanchoin, L.; Boujemaa-Paterski, R.; Sykes, C.; Plastino, J. Actin Dynamics, Architecture, and Mechanics in Cell Motility. *Physiol. Rev.* **2014**, *94* (1), 235–263.
- (56) Olson, M. F.; Sahai, E. The Actin Cytoskeleton in Cancer Cell Motility. *Clin. Exp. Metastasis* **2009**, *26* (4), 273–287.
- (57) Yamaguchi, H.; Condeelis, J. Regulation of the Actin Cytoskeleton in Cancer Cell Migration and Invasion. *Biochim. Biophys. Acta BBA - Mol. Cell Res.* **2007**, *1773* (5), 642–652.
- (58) Klaile, E. Identifizierung und Charakterisierung neuer intrazellulärer Bindungspartner von CEACAM1-L und deren Einfluss auf CEACAM1-L-vermittelte zelluläre Funktionen, Charité - Universitätsmedizin Berlin, Campus Benjamin Franklin, Institut für Biochemie und Molekularbiologie: Berlin, 2005.
- (59) Mattila, P. K.; Lappalainen, P. Filopodia: Molecular Architecture and Cellular Functions. *Nat. Rev. Mol. Cell Biol.* **2008**, *9* (6), 446–454.
- (60) Wozniak, M. A.; Modzelewska, K.; Kwong, L.; Keely, P. J. Focal Adhesion Regulation of Cell Behavior. *Biochim. Biophys. Acta BBA - Mol. Cell Res.* **2004**, *1692* (2–3), 103–119.
- (61) Carragher, N. O.; Frame, M. C. Focal Adhesion and Actin Dynamics: A Place Where Kinases and Proteases Meet to Promote Invasion. *Trends Cell Biol.* **2004**, *14* (5), 241–249.
- (62) Pellegrin, S.; Mellor, H. Actin Stress Fibers. *J. Cell Sci.* **2007**, *120*(20), 3491–3499.
-

- (63) Ridley, A. J. Rho GTPases and Cell Migration. *J. Cell Sci.* **2001**, *114* (15), 2713–2722.
- (64) Iden, S.; Collard, J. G. Crosstalk between Small GTPases and Polarity Proteins in Cell Polarization. *Nat. Rev. Mol. Cell Biol.* **2008**, *9* (11), 846–859.
- (65) Hall, A. Rho GTPases and the Actin Cytoskeleton. *Science* **1998**, *279* (5350), 509–514.
- (66) *Molecular Biology of the Cell*, 5th ed.; Alberts, B., Ed.; Garland Science: New York, 2008.
- (67) Gigant, B.; Cormier, A.; Dorléans, A.; Ravelli, R. B. G.; Knossow, M. Microtubule-Destabilizing Agents: Structural and Mechanistic Insights from the Interaction of Colchicine and Vinblastine with Tubulin. In *Tubulin-Binding Agents*; Carlomagno, T., Ed.; Springer Berlin Heidelberg: Berlin, Heidelberg, 2008; Vol. 286, pp 259–278.
- (68) de Forges, H.; Bouissou, A.; Perez, F. Interplay between Microtubule Dynamics and Intracellular Organization. *Int. J. Biochem. Cell Biol.* **2012**, *44* (2), 266–274.
- (69) Akhmanova, A.; Steinmetz, M. O. Control of Microtubule Organization and Dynamics: Two Ends in the Limelight. *Nat. Rev. Mol. Cell Biol.* **2015**, *16* (12), 711–726.
- (70) Walczak, C. E.; Heald, R. Mechanisms of Mitotic Spindle Assembly and Function. In *International Review of Cytology*; Elsevier, 2008; Vol. 265, pp 111–158.
- (71) Komis, G.; Illés, P.; Beck, M.; Samaj, J. Microtubules and Mitogen-Activated Protein Kinase Signalling. *Curr. Opin. Plant Biol.* **2011**, *14* (6), 650–657.
- (72) Kyriakis, J. M.; Avruch, J. Mammalian MAPK Signal Transduction Pathways Activated by Stress and Inflammation: A 10-Year Update. *Physiol. Rev.* **2012**, *92* (2), 689–737.
- (73) Small, J. V.; Geiger, B.; Kaverina, I.; Bershadsky, A. How Do Microtubules Guide Migrating Cells? *Nat. Rev. Mol. Cell Biol.* **2002**, *3* (12), 957–964.
- (74) Bates, D.; Eastman, A. Microtubule Destabilising Agents: Far More than Just Antimitotic Anticancer Drugs: MDA Mechanisms of Action. *Br. J. Clin. Pharmacol.* **2017**, *83* (2), 255–268.
- (75) Kaverina, I.; Straube, A. Regulation of Cell Migration by Dynamic Microtubules. *Semin. Cell Dev. Biol.* **2011**, *22* (9), 968–974.
- (76) Chitale, K.; Webb, R. . Microtubule Depolymerization Facilitates Contraction of Vascular Smooth Muscle via Increased Activation of RhoA/Rho-Kinase. *Med. Hypotheses* **2001**, *56* (3), 381–385.
- (77) Kaverina, I.; Rottner, K.; Small, J. V. Targeting, Capture, and Stabilization of Microtubules at Early Focal Adhesions. *J. Cell Biol.* **1998**, *142* (1), 181–190.
- (78) Wu, X.; Kodama, A.; Fuchs, E. ACF7 Regulates Cytoskeletal-Focal Adhesion Dynamics and Migration and Has ATPase Activity. *Cell* **2008**, *135* (1), 137–148.
- (79) Ezratty, E. J.; Partridge, M. A.; Gundersen, G. G. Microtubule-Induced Focal Adhesion Disassembly Is Mediated by Dynamin and Focal Adhesion Kinase. *Nat. Cell Biol.* **2005**, *7* (6), 581–590.
- (80) Ezratty, E. J.; Bertaux, C.; Marcantonio, E. E.; Gundersen, G. G. Clathrin Mediates Integrin Endocytosis for Focal Adhesion Disassembly in Migrating Cells. *J. Cell Biol.* **2009**, *187* (5), 733–747.
- (81) Historical Review of Vinca Alkaloids. *Acta Radiol.* **1969**, *8* (s291), 7–12.
- (82) Larrick, G. Excerpts from the Federal Register. *Clin. Pharmacol. Ther.* **1964**, *5* (3), 360–376.
- (83) Borisy, G. G.; Taylor, E. W. The Mechanism of Action of Colchicine: Colchicine Binding to Sea Urchin Eggs and the Mitotic Apparatus. *J. Cell Biol.* **1967**, *34* (2), 535–548.

- (84) Fanale, D.; Bronte, G.; Passiglia, F.; Calò, V.; Castiglia, M.; Di Piazza, F.; Barraco, N.; Cangemi, A.; Catarella, M. T.; Insalaco, L.; et al. Stabilizing versus Destabilizing the Microtubules: A Double-Edge Sword for an Effective Cancer Treatment Option? *Anal. Cell. Pathol.* **2015**, *2015*, 1–19.
- (85) Altmann, K.-H. Microtubule-Stabilizing Agents: A Growing Class of Important Anticancer Drugs. *Curr. Opin. Chem. Biol.* **2001**, *5* (4), 424–431.
- (86) Kerkweg, U.; Liekweg, A.; Lenssen, R.; Seidling, H.; Elixmann, M. *Intravenöse Applikation von Vincristin Sicherstellen - Einsatz von Hochrisikoarzneimitteln; Handlungsempfehlung; Aktionsbündnis Patientensicherheit e.V.*: Berlin, 2015.
- (87) Geiger, P. L. Ueber Einige Neue Giftige Organische Alkalien. *Eur. J. Org. Chem.* **1833**, *7* (3), 269–280.
- (88) Negi, A. S.; Gautam, Y.; Alam, S.; Chanda, D.; Luqman, S.; Sarkar, J.; Khan, F.; Konwar, R. Natural Antitubulin Agents: Importance of 3,4,5-Trimethoxyphenyl Fragment. *Bioorg. Med. Chem.* **2015**, *23* (3), 373–389.
- (89) Gaukroger, K.; Hadfield, J. A.; Lawrence, N. J.; Nolan, S.; McGown, A. T. Structural Requirements for the Interaction of Combretastatins with Tubulin: How Important Is the Trimethoxy Unit? *Org. Biomol. Chem.* **2003**, *1* (17), 3033–3037.
- (90) Lu, Y.; Chen, J.; Xiao, M.; Li, W.; Miller, D. D. An Overview of Tubulin Inhibitors That Interact with the Colchicine Binding Site. *Pharm. Res.* **2012**, *29* (11), 2943–2971.
- (91) Pettit, G. R.; Singh, S. B.; Hamel, E.; Lin, C. M.; Alberts, D. S.; Garcia-Kendal, D. Isolation and Structure of the Strong Cell Growth and Tubulin Inhibitor Combretastatin A-4. *Cell. Mol. Life Sci.* **1989**, *45* (2), 209–211.
- (92) Martel-Frchet, V.; Keramidis, M.; Nurisso, A.; DeBonis, S.; Rome, C.; Coll, J.-L.; Boumendjel, A.; Skoufias, D. A.; Ronot, X. IPP51, a Chalcone Acting as a Microtubule Inhibitor with in Vivo Antitumor Activity against Bladder Carcinoma. *Oncotarget* **2015**, *6* (16), 14669.
- (93) Ducki, S.; Rennison, D.; Woo, M.; Kendall, A.; Chabert, J. F. D.; McGown, A. T.; Lawrence, N. J. Combretastatin-like Chalcones as Inhibitors of Microtubule Polymerization. Part 1: Synthesis and Biological Evaluation of Antivascular Activity. *Bioorg. Med. Chem.* **2009**, *17* (22), 7698–7710.
- (94) Boumendjel, A.; McLeer-Florin, A.; Champelovier, P.; Allegro, D.; Muhammad, D.; Souard, F.; Derouazi, M.; Peyrot, V.; Toussaint, B.; Boutonnat, J. A Novel Chalcone Derivative Which Acts as a Microtubule Depolymerising Agent and an Inhibitor of P-Gp and BCRP in in-Vitro and in-Vivoglioblastoma Models. *BMC Cancer* **2009**, *9* (1).
- (95) Wood, D.; Panda, D.; Wiernicki, T. R.; Wilson, L.; Jordan, M. A.; Singh, J. P. Inhibition of Mitosis and Microtubule Function through Direct Tubulin Binding by a Novel Antiproliferative Naphthopyran LY290181. *Mol. Pharmacol.* **1997**, *52*, 437–444.
- (96) van Vuuren, R. J.; Visagie, M. H.; Theron, A. E.; Joubert, A. M. Antimitotic Drugs in the Treatment of Cancer. *Cancer Chemother. Pharmacol.* **2015**, *76* (6), 1101–1112.
- (97) Rovini, A.; Savry, A.; Braguer, D.; Carré, M. Microtubule-Targeted Agents: When Mitochondria Become Essential to Chemotherapy. *Biochim. Biophys. Acta BBA - Bioenerg.* **2011**, *1807* (6), 679–688.
- (98) Hübner, A.; Cavanagh-Kyros, J.; Rincon, M.; Flavell, R. A.; Davis, R. J. Functional Cooperation of the Proapoptotic Bcl2 Family Proteins Bmf and Bim in Vivo. *Mol. Cell. Biol.* **2010**, *30* (1), 98–105.
- (99) Chen, J.; Sun, W.-L.; Wasyluk, B.; Wang, Y.-P.; Zheng, H. C-Jun N-Terminal Kinase Mediates Microtubule-Depolymerizing Agent-Induced Microtubule Depolymerization

- and G2/M Arrest in MCF-7 Breast Cancer Cells: *Anticancer. Drugs* **2012**, 23 (1), 98–107.
- (100) Stone, A. A.; Chambers, T. C. Microtubule Inhibitors Elicit Differential Effects on MAP Kinase (JNK, ERK, and P38) Signaling Pathways in Human KB-3 Carcinoma Cells. *Exp. Cell Res.* **2000**, 254 (1), 110–119.
- (101) Wang, T.-H.; Wang, H.-S.; Ichijo, H.; Giannakakou, P.; Foster, J. S.; Fojo, T.; Wimalasena, J. Microtubule-Interfering Agents Activate c-Jun N-Terminal Kinase/Stress-Activated Protein Kinase through Both Ras and Apoptosis Signaling Pathways. *J. Biol. Chem.* **1998**, 273 (9), 4928–4936.
- (102) Bates, D. J. P.; Lewis, L. D.; Eastman, A.; Danilov, A. V. Vincristine Activates C-Jun N-Terminal Kinase in Chronic Lymphocytic Leukaemia *in Vivo*: Vincristine Activates JNK in CLL Patients. *Br. J. Clin. Pharmacol.* **2015**, 80 (3), 493–501.
- (103) Davies, C.; Tournier, C. Exploring the Function of the JNK (c-Jun N-Terminal Kinase) Signaling Pathway in Physiological and Pathological Processes to Design Novel Therapeutic Strategies. *Biochem. Soc. Trans.* **2012**, 40 (1), 85–89.
- (104) Mollinedo, F.; Gajate, C. Microtubules, Microtubule-Interfering Agents and Apoptosis. *Apoptosis* **2003**, 8, 413–450.
- (105) Pietkiewicz, S. Die Bedeutung Der JNK-Isoformen JNK1 Und JNK2 Für Die Apoptose Nach Proteasomaler Inhibition, Heinrich-Heine-Universität: Düsseldorf, 2012.
- (106) Liu, B. P.; Chrzanowska-Wodnicka, M.; Burridge, K. Microtubule Depolymerization Induces Stress Fibers, Focal Adhesions, and DNA Synthesis via the GTP-Binding Protein Rho. *Cell Adhes. Commun.* **1998**, 5 (4), 249–255.
- (107) Kolodney, M. S.; Elson, E. L. Contraction Due to Microtubule Disruption Is Associated with Increased Phosphorylation of Myosin Regulatory Light Chain. *Proc. Natl. Acad. Sci.* **1995**, 92 (22), 10252–10256.
- (108) Guo, H.; Zheng, H.; Wu, J.; Ma, H.; Yu, J.; Yiliyaer, M. The Key Role of Microtubules in Hypoxia Preconditioning-Induced Nuclear Translocation of HIF-1 α in Rat Cardiomyocytes. *PeerJ* **2017**, 5, e3662.
- (109) Carbonaro, M.; Escuin, D.; O’Brate, A.; Thadani-Mulero, M.; Giannakakou, P. Microtubules Regulate Hypoxia-Inducible Factor-1 α Protein Trafficking and Activity: Implications for Taxane Therapy. *J. Biol. Chem.* **2012**, 287 (15), 11859–11869.
- (110) Schwartz, E. L. Antivascular Actions of Microtubule-Binding Drugs. *Clin. Cancer Res.* **2009**, 15 (8), 2594–2601.
- (111) Vincent, L. Combretastatin A4 Phosphate Induces Rapid Regression of Tumor Neovessels and Growth through Interference with Vascular Endothelial-Cadherin Signaling. *J. Clin. Invest.* **2005**, 115 (11), 2992–3006.
- (112) Sherbet, G. V. Suppression of Angiogenesis and Tumour Progression by Combretastatin and Derivatives. *Cancer Lett.* **2017**, 403, 289–295.
- (113) Lin, H.-L.; Chiou, S.-H.; Wu, C.-W.; Lin, W.-B.; Chen, L.-H.; Yang, Y.-P.; Tsai, M.-L.; Uen, Y.-H.; Liou, J.-P.; Chi, C.-W. Combretastatin A4-Induced Differential Cytotoxicity and Reduced Metastatic Ability by Inhibition of AKT Function in Human Gastric Cancer Cells. *J. Pharmacol. Exp. Ther.* **2007**, 323 (1), 365–373.
- (114) Dalyot-Herman, N.; Delgado-Lopez, F.; Gewirtz, D. A.; Gupton, J. T.; Schwartz, E. L. Interference with Endothelial Cell Function by JG-03-14, an Agent That Binds to the Colchicine Site on Microtubules. *Biochem. Pharmacol.* **2009**, 78 (9), 1167–1177.
- (115) Aparicio, L. A.; Castosa, R.; Haz-Conde, M.; Rodríguez, M.; Blanco, M.; Valladares, M.; Figueroa, A. Role of the Microtubule-Targeting Drug Vinflunine on Cell-Cell Adhesions in Bladder Epithelial Tumour Cells. *BMC Cancer* **2014**, 14 (1), 507.

-
- (116) Mahal, K.; Resch, M.; Ficner, R.; Schobert, R.; Biersack, B.; Mueller, T. Effects of the Tumor-Vasculature-Disrupting Agent Verubulin and Two Heteroaryl Analogues on Cancer Cells, Endothelial Cells, and Blood Vessels. *ChemMedChem* **2014**, *9* (4), 847–854.
- (117) Greene, L. M.; Meegan, M. J.; Zisterer, D. M. Combretastatins: More Than Just Vascular Targeting Agents? *J. Pharmacol. Exp. Ther.* **2015**, *355* (2), 212–227.
- (118) Dumontet, C.; Jordan, M. A. Microtubule-Binding Agents: A Dynamic Field of Cancer Therapeutics. *Nat. Rev. Drug Discov.* **2010**, *9* (10), 790–803.
- (119) Polioudaki, H.; Kastrinaki, M.-C.; Papadaki, H. A.; Theodoropoulos, P. A. Microtubule-Interacting Drugs Induce Moderate and Reversible Damage to Human Bone Marrow Mesenchymal Stem Cells. *Cell Prolif.* **2009**, *42* (4), 434–447.
- (120) Kavallaris, M. Microtubules and Resistance to Tubulin-Binding Agents. *Nat. Rev. Cancer* **2010**, *10* (3), 194–204.
- (121) Ambudkar, S. V.; Kimchi-Sarfaty, C.; Sauna, Z. E.; Gottesman, M. M. P-Glycoprotein: From Genomics to Mechanism. *Oncogene* **2003**, *22* (47), 7468–7485.
- (122) Safa, A. R. Identification and Characterization of the Binding Sites of P-Glycoprotein for Multidrug Resistance-Related Drugs and Modulators. *Curr. Med. Chem.-Anti-Cancer Agents* **2004**, *4* (1), 1–17.
- (123) Jordan, M. A.; Wilson, L. Microtubules as a Target for Anticancer Drugs. *Nat. Rev. Cancer* **2004**, *4*, 254–265.
- (124) Jane Lunt, S.; Akerman, S.; Hill, S. A.; Fisher, M.; Wright, V. J.; Reyes-Aldasoro, C. C.; Tozer, G. M.; Kanthou, C. Vascular Effects Dominate Solid Tumor Response to Treatment with Combretastatin A-4-Phosphate. *Int. J. Cancer* **2011**, *129* (8), 1979–1989.
- (125) Rosenberg, B.; Van Camp, L.; Krigas, T. Inhibition of Cell Division in Escherichia Coli by Electrolysis Products from a Platinum Electrode. *Nature* **1965**, *205*, 698–699.
- (126) Kühn, F. E.; Schmidt, A. Metallkomplexe als Antikrebsmittel: Konzepte in der Tumorforschung und Wirkmechanismen. *Chem. Unserer Zeit* **2017**, *51* (2), 86–95.
- (127) Jordan, P.; Carmo-Fonseca, M. Molecular Mechanisms Involved in Cisplatin Cytotoxicity. *Cell. Mol. Life Sci. CMLS* **2000**, *57* (8–9), 1229–1235.
- (128) Ndagi, U.; Mhlongo, N.; Soliman, M. Metal Complexes in Cancer Therapy - an Update from Drug Design Perspective. *Drug Des. Devel. Ther.* **2017**, *11*, 599–616.
- (129) Bruijninx, P. C.; Sadler, P. J. New Trends for Metal Complexes with Anticancer Activity. *Curr. Opin. Chem. Biol.* **2008**, *12* (2), 197–206.
- (130) Gasser, G.; Ott, I.; Metzler-Nolte, N. Organometallic Anticancer Compounds. *J. Med. Chem.* **2011**, *54* (1), 3–25.
- (131) Gasser, G.; Metzler-Nolte, N. The Potential of Organometallic Complexes in Medicinal Chemistry. *Curr. Opin. Chem. Biol.* **2012**, *16* (1–2), 84–91.
- (132) Leijen, S.; Burgers, S. A.; Baas, P.; Pluim, D.; Tibben, M.; van Werkhoven, E.; Alessio, E.; Sava, G.; Beijnen, J. H.; Schellens, J. H. M. Phase I/II Study with Ruthenium Compound NAMI-A and Gemcitabine in Patients with Non-Small Cell Lung Cancer after First Line Therapy. *Invest. New Drugs* **2015**, *33* (1), 201–214.
- (133) Hartinger, C. G.; Jakupec, M. A.; Zorbas-Seifried, S.; Groessl, M.; Egger, A.; Berger, W.; Zorbas, H.; Dyson, P. J.; Keppler, B. K. KP1019, A New Redox-Active Anticancer Agent—Preclinical Development and Results of a Clinical Phase I Study in Tumor Patients. *Chem. Biodivers.* **2008**, *5* (10), 2140–2155.
- (134) Meier-Menches, S. M.; Gerner, C.; Berger, W.; Hartinger, C. G.; Keppler, B. K. Structure–activity Relationships for Ruthenium and Osmium Anticancer Agents – towards Clinical Development. *Chem. Soc. Rev.* **2018**.
-

-
- (135) Biersack, B. Anticancer Activity and Modes of Action of (Arene) Ruthenium (II) Complexes Coordinated to C-, N-, and O-Ligands. *Mini Rev. Med. Chem.* **2016**, *16* (10), 804–814.
- (136) Adhireksan, Z.; Davey, G. E.; Campomanes, P.; Groessl, M.; Clavel, C. M.; Yu, H.; Nazarov, A. A.; Yeo, C. H. F.; Ang, W. H.; Dröge, P.; et al. Ligand Substitutions Between..... *Nat. Commun.* **2014**.
- (137) Ude, Z.; Romero-Canelón, I.; Twamley, B.; Fitzgerald Hughes, D.; Sadler, P. J.; Marmion, C. J. A Novel Dual-Functioning Ruthenium(II)–arene Complex of an Anti-Microbial Ciprofloxacin Derivative — Anti-Proliferative and Anti-Microbial Activity. *J. Inorg. Biochem.* **2016**, *160*, 210–217.
- (138) Clavel, C. M.; Păunescu, E.; Nowak-Sliwinska, P.; Griffioen, A. W.; Scopelliti, R.; Dyson, P. J. Modulating the Anticancer Activity of Ruthenium(II)–Arene Complexes. *J. Med. Chem.* **2015**, *58* (8), 3356–3365.
- (139) Nowak-Sliwinska, P.; van Beijnum, J. R.; Casini, A.; Nazarov, A. A.; Wagnières, G.; van den Bergh, H.; Dyson, P. J.; Griffioen, A. W. Organometallic Ruthenium(II) Arene Compounds with Antiangiogenic Activity. *J. Med. Chem.* **2011**, *54*, 3895–3902.
- (140) Kilpin, K. J.; Dyson, P. J. Enzyme Inhibition by Metal Complexes: Concepts, Strategies and Applications. *Chem. Sci.* **2013**, *4* (4), 1410.
- (141) Drazic, A.; Myklebust, L. M.; Ree, R.; Arnesen, T. The World of Protein Acetylation. *Biochim. Biophys. Acta BBA - Proteins Proteomics* **2016**, *1864* (10), 1372–1401.
- (142) Seto, E.; Yoshida, M. Erasers of Histone Acetylation: The Histone Deacetylase Enzymes. *Cold Spring Harb. Perspect. Biol.* **2014**, *6* (4), a018713–a018713.
- (143) Yao, Y.-L.; Yang, W.-M. Beyond Histone and Deacetylase: An Overview of Cytoplasmic Histone Deacetylases and Their Nonhistone Substrates. *J. Biomed. Biotechnol.* **2011**, *2011*, 1–15.
- (144) Haberland, M.; Montgomery, R. L.; Olson, E. N. The Many Roles of Histone Deacetylases in Development and Physiology: Implications for Disease and Therapy. *Nat. Rev. Genet.* **2009**, *10* (1), 32–42.
- (145) Hrabeta, J.; Stiborova, M.; Adam, V.; Kizek, R.; Eckschlager, T. Histone Deacetylase Inhibitors in Cancer Therapy. *Aa Review. Biomed. Pap.* **2013**.
- (146) Li, Y.; Seto, E. HDACs and HDAC Inhibitors in Cancer Development and Therapy. *Cold Spring Harb. Perspect. Med.* **2016**, *6* (10), a026831.
- (147) Mottamal, M.; Zheng, S.; Huang, T.; Wang, G. Histone Deacetylase Inhibitors in Clinical Studies as Templates for New Anticancer Agents. *Molecules* **2015**, *20* (3), 3898–3941.
- (148) Ceccacci, E.; Minucci, S. Inhibition of Histone Deacetylases in Cancer Therapy: Lessons from Leukaemia. *Br. J. Cancer* **2016**, *114* (6), 605–611.
- (149) Do, D. P.; Rizvi, S. A. Epigenetic Changes in Melanoma and the Development of Epigenetic Therapy for Melanoma. In *Research on Melanoma-A Glimpse into Current Directions and Future Trends*; InTech, 2011.
- (150) Licciardi, P.; Ververis; Hiong; Karagiannis. Histone Deacetylase Inhibitors (HDACIs): Multitargeted Anticancer Agents. *Biol. Targets Ther.* **2013**, *2013* (7), 47–60.
- (151) West, A. C.; Johnstone, R. W. New and Emerging HDAC Inhibitors for Cancer Treatment. *J. Clin. Invest.* **2014**, *124* (1), 30–39.
- (152) Khan, O.; La Thangue, N. B. HDAC Inhibitors in Cancer Biology: Emerging Mechanisms and Clinical Applications. *Immunol. Cell Biol.* **2012**, *90* (1), 85–94.
- (153) Glazak, M. A.; Seto, E. Histone Deacetylases and Cancer. *Oncogene* **2007**, *26* (37), 5420–5432.
-

-
- (154) Singh, B. N.; Zhang, G.; Hwa, Y. L.; Li, J.; Dowdy, S. C.; Jiang, S.-W. Nonhistone Protein Acetylation as Cancer Therapy Targets. *Expert Rev. Anticancer Ther.* **2010**, *10* (6), 935–954.
- (155) Yang, X.; Ferguson, A. T.; Nass, S. J.; Phillips, D. L.; Butash, K. A.; Wang, S. M.; Herman, J. G.; Davidson, N. E. Transcriptional Activation of Estrogen Receptor α in Human Breast Cancer Cells by Histone Deacetylase Inhibition. *Cancer Res.* **2000**, *60* (24), 6890–6894.
- (156) Duong, V.; Licznar, A.; Margueron, R.; Boulle, N.; Busson, M.; Lacroix, M.; Katzenellenbogen, B. S.; Cavailles, V.; Lazennec, G. ER α and ER β Expression and Transcriptional Activity Are Differentially Regulated by HDAC Inhibitors. *Oncogene* **2006**, *25*, 1799–1806.
- (157) Nebbioso, A.; Carafa, V.; Conte, M.; Tambaro, F. P.; Abbondanza, C.; Martens, J.; Nees, M.; Benedetti, R.; Pallavicini, I.; Minucci, S.; et al. C-Myc Modulation and Acetylation Is a Key HDAC Inhibitor Target in Cancer. *Clin. Cancer Res.* **2017**, *23* (10), 2542–2555.
- (158) Ashburner, B. P.; Westerheide, S. D.; Baldwin, A. S. The P65 (RelA) Subunit of NF- κ B Interacts with the Histone Deacetylase (HDAC) Corepressors HDAC1 and HDAC2 To Negatively Regulate Gene Expression. *Mol. Cell. Biol.* **2001**, *21* (20), 7065–7077.
- (159) Place, R. F.; Noonan, E. J.; Giardina, C. HDAC Inhibition Prevents NF- κ B Activation by Suppressing Proteasome Activity: Down-Regulation of Proteasome Subunit Expression Stabilizes I κ B α . *Biochem. Pharmacol.* **2005**, *70* (3), 394–406.
- (160) Icardi, L.; De Bosscher, K.; Tavernier, J. The HAT/HDAC Interplay: Multilevel Control of STAT Signaling. *Cytokine Growth Factor Rev.* **2012**, *23* (6), 283–291.
- (161) Licciardi, P. V.; Karagiannis, T. C. Regulation of Immune Responses by Histone Deacetylase Inhibitors. *ISRN Hematol.* **2012**, *2012*, 1–10.
- (162) Zhuang, S. Regulation of STAT Signaling by Acetylation. *Cell. Signal.* **2013**, *25* (9), 1924–1931.
- (163) Kumar, P.; Gogulamudi, V. R.; Periasamy, R.; Raghavaraju, G.; Subramanian, U.; Pandey, K. N. Inhibition of HDAC Enhances STAT Acetylation, Blocks NF- κ B, and Suppresses the Renal Inflammation and Fibrosis in *Npr1* Haplotype Male Mice. *Am. J. Physiol.-Ren. Physiol.* **2017**, *313* (3), F781–F795.
- (164) Miyake, K.; Yoshizumi, T.; Imura, S.; Sugimoto, K.; Batmunkh, E.; Kanemura, H.; Morine, Y.; Shimada, M. Expression of Hypoxia-Inducible Factor-1 α , Histone Deacetylase 1, and Metastasis-Associated Protein 1 in Pancreatic Carcinoma: Correlation with Poor Prognosis with Possible Regulation. *Pancreas* **2008**, *36* (3), e1–e9.
- (165) Kim, S.-H.; Jeong, J.-W.; Park, J.; Lee, J.-W.; Seo, J. H.; Jung, B.-K.; Bae, M.-K.; Kim, K.-W. Regulation of the HIF-1 α Stability by Histone Deacetylases. *Oncol. Rep.* **2007**, *17* (3), 647–651.
- (166) Misra, S.; Fu, A. A.; Rajan, D. K.; Juncos, L. A.; McKusick, M. A.; Bjarnason, H.; Mukhopadhyay, D. Expression of Hypoxia Inducible Factor-1 α , Macrophage Migration Inhibition Factor, Matrix Metalloproteinase-2 and -9, and Their Inhibitors in Hemodialysis Grafts and Arteriovenous Fistulas. *J. Vasc. Interv. Radiol.* **2008**, *19* (2), 252–259.
- (167) Fujiwara, S.; Nakagawa, K. O. U.; Harada, H.; Nagato, S.; Furukawa, K.; Teraoka, M.; Seno, T.; Oka, K.; Iwata, S.; Ohnishi, T. Silencing Hypoxia-Inducible Factor-1 α Inhibits Cell Migration and Invasion under Hypoxic Environment in Malignant Gliomas. *Int. J. Oncol.* **2007**, *30* (4), 793–802.
- (168) Ahn, J. K.; Koh, E.-M.; Cha, H.-S.; Lee, Y. S.; Kim, J.; Bae, E.-K.; Ahn, K.-S. Role of Hypoxia-Inducible Factor-1 in Hypoxia-Induced Expressions of IL-8, MMP-1 and
-

- MMP-3 in Rheumatoid Fibroblast-like Synoviocytes. *Rheumatology* **2008**, *47* (6), 834–839.
- (169) Aldana-Masangkay, G. I.; Sakamoto, K. M. The Role of HDAC6 in Cancer. *J. Biomed. Biotechnol.* **2011**, *2011*, ID 875824.
- (170) Mahal, K.; Kahlen, P.; Biersack, B.; Schobert, R. 4-(1-Ethyl-4-Anisyl-Imidazol-5-Yl)-N-Hydroxycinnamide – A New Pleiotropic HDAC Inhibitor Targeting Cancer Cell Signalling and Cytoskeletal Organisation. *Exp. Cell Res.* **2015**, *336* (2), 263–275.
- (171) Hancock, W. W.; Akimova, T.; Beier, U. H.; Liu, Y.; Wang, L. HDAC Inhibitor Therapy in Autoimmunity and Transplantation. *Ann. Rheum. Dis.* **2012**, *71* (Suppl 2), i46–i54.
- (172) Mann, B. S.; Johnson, J. R.; Cohen, M. H.; Justice, R.; Pazdur, R. FDA Approval Summary: Vorinostat for Treatment of Advanced Primary Cutaneous T-Cell Lymphoma. *The Oncologist* **2007**, *12* (10), 1247–1252.
- (173) Poole, R. M. Belinostat: First Global Approval. *Drugs* **2014**, *74* (13), 1543–1554.
- (174) Garnock-Jones, K. P. Panobinostat: First Global Approval. *Drugs* **2015**, *75* (6), 695–704.
- (175) Lu, X.; Ning, Z.; Li, Z.; Cao, H.; Wang, X. Development of Chidamide for Peripheral T-Cell Lymphoma, the First Orphan Drug Approved in China. *Intractable Rare Dis. Res.* **2016**, *5* (3), 185–191.
- (176) de Hematología, I. S. C. Highlights of ASH®. **2012**.
- (177) Sharma, S.; Symanowski, J.; Wong, B.; Dino, P.; Manno, P.; Vogelzang, N. A Phase II Clinical Trial of Oral Valproic Acid in Patients with Castration-Resistant Prostate Cancers Using an Intensive Biomarker Sampling Strategy. *Transl. Oncol.* **2008**, *1* (3), 141–147.
- (178) Bitzer, M.; Horger, M.; Giannini, E. G.; Ganten, T. M.; Wörns, M. A.; Siveke, J. T.; Dollinger, M. M.; Gerken, G.; Scheulen, M. E.; Wege, H.; et al. Resminostat plus Sorafenib as Second-Line Therapy of Advanced Hepatocellular Carcinoma – The SHELTER Study. *J. Hepatol.* **2016**, *65* (2), 280–288.
- (179) Wagner, J. M.; Hackanson, B.; Lübbert, M.; Jung, M. Histone Deacetylase (HDAC) Inhibitors in Recent Clinical Trials for Cancer Therapy. *Clin. Epigenetics* **2010**, *1* (3–4), 117–136.
- (180) Child, F.; Ortiz-Romero, P. L.; Alvarez, R.; Bagot, M.; Stadler, R.; Weichenthal, M.; Alves, R.; Quaglino, P.; Beylot-Barry, M.; Cowan, R. Phase II Multicentre Trial of Oral Quisinostat, a Histone Deacetylase Inhibitor, in Patients with Previously Treated Stage IB–IVA Mycosis Fungoides/Sézary Syndrome. *Br. J. Dermatol.* **2016**, *175* (1), 80–88.
- (181) Roche, J.; Bertrand, P. Inside HDACs with More Selective HDAC Inhibitors. *Eur. J. Med. Chem.* **2016**, *121*, 451–483.
- (182) Hsu, K.-C.; Liu, C.-Y.; Lin, T. E.; Hsieh, J.-H.; Sung, T.-Y.; Tseng, H.-J.; Yang, J.-M.; Huang, W.-J. Novel Class Iia-Selective Histone Deacetylase Inhibitors Discovered Using an in Silico Virtual Screening Approach. *Sci. Rep.* **2017**, *7* (1).
- (183) Breslow, R.; Marks, P. A.; Abhilash, K. G.; Wang, J. Selective HDAC Inhibitors. 20140031368, July 2013.
- (184) McKinsey, T. A. Isoform-Selective HDAC Inhibitors: Closing in on Translational Medicine for the Heart. *J. Mol. Cell. Cardiol.* **2011**, *51* (4), 491–496.
- (185) KrennHrubec, K.; Marshall, B. L.; Hedglin, M.; Verdin, E.; Ulrich, S. M. Design and Evaluation of ‘Linkerless’ Hydroxamic Acids as Selective HDAC8 Inhibitors. *Bioorg. Med. Chem. Lett.* **2007**, *17* (10), 2874–2878.

- (186) Subramanian, S.; Bates, S. E.; Wright, J. J.; Espinoza-Delgado, I.; Piekarz, R. L. Clinical Toxicities of Histone Deacetylase Inhibitors. *Pharmaceuticals* **2010**, 3 (9), 2751–2767.
- (187) Ethiraj, K. R.; Aranjani, J. M.; Khan, F.-R. N. Synthesis of Methoxy-Substituted Chalcones and *in Vitro* Evaluation of Their Anticancer Potential. *Chem. Biol. Drug Des.* **2013**, 82 (6), 732–742.
- (188) Wiernicki, T. R.; Bean, J. S.; Dell, C.; Williams, A.; Wood, D.; Kauffman, R. F.; Singh, J. P. Inhibition of Vascular Smooth Muscle Cell Proliferation and Arterial Intimal Thickening by a Novel Antiproliferative Naphthopyran. *J. Pharmacol. Exp. Ther.* **1996**, 278 (3), 1452–1459.

5 Publikationen

5.1 Darstellung des Eigenanteils

Die Manuskripte und Publikationen, die in dieser Dissertation gezeigt werden, wurden zu einem großen Teil in Kooperation mit anderen Arbeitsgruppen angefertigt. Dazu zählen das Institut für Innere Medizin IV, Onkologie/Hämatologie der Martin Luther-Universität Halle-Wittenberg, der Lehrstuhl für Entwicklungsbiologie der Universität Bayreuth, das Institut Biophysik der *Academy of Science of the Czech Republic* in Brünn (Tschechien), der Lehrstuhl für Biophysik der Wissenschaftlichen Fakultät der Palacky Universität Olmütz (Tschechien), das Institut für Physiologie der Charité-Universitätsmedizin Berlin sowie das *Research Center for Integrated Analysis and Territorial Management* der Universität Bukarest (Rumänien).

Es folgt eine detaillierte Darstellung der Beiträge der Ko-Autoren zu den jeweiligen Publikationen und Manuskripten.

5.1.1 Eigenanteil: Publikation I

Die Ergebnisse zu diesem Thema wurden im Journal *Bioorganic & Medicinal Chemistry Letters* veröffentlicht mit dem folgenden Titel:

„Halogenated naphthochalcones and structurally related naphthopyrazolines with antitumor activity”

von den Autoren

Florian Schmitt, Heidrun Draut, Bernhard Biersack, und Rainer Schobert.

- Eigenanteil: Konzeption, Durchführung und Auswertung der biologischen Assays:
MTT-Assay, BCRP-Inhibitionsassay, P-gp-Inhibitionsassay, Zellzyklusanalysen, TUNEL Assay, DNA-Ladder-Assay, Western Blot-Analysen, Zytoskelettfärbungen, Tubulinpolymerisierungsassay.
Verfassen des Manuskripts inklusive der Diskussion und Interpretation der Ergebnisse, graphische Repräsentation und Bearbeitung der Abbildungen, Bearbeitung und Korrektur der Revision.
- H. Draut: Durchführung von TUNEL Assay, Western Blot-Analysen und der DNA-Ladder Assays im Rahmen eines Forschungsmodulpraktikums (betreut von F. Schmitt und R. Schobert)
- B. Biersack: Synthese, Aufreinigung, und Charakterisierung der getesteten Verbindungen; Manuskriptkonzeption.
- R. Schobert: Manuskriptkonzeption, Diskussion, und Korrektur des Manuskripts.

Geschätzter Eigenanteil: circa 80%

5.1.2 Eigenanteil: Publikation II

Die Ergebnisse zu diesem Thema wurden im Journal *European Journal of Medicinal Chemistry* veröffentlicht mit dem folgenden Titel:

„*New Naphthopyran Analogues of LY290181 as Potential Tumor Vascular-disrupting Agents*”

von den Autoren

Florian Schmitt, Madeleine Gold, Matthias Rothmund, Ion C. Andronache, Bernhard Biersack, Rainer Schobert, Thomas Müller.

Die Arbeit wurde in Kooperation mit dem Forschungszentrum für Integrierte Analyse und Territorial Management, Fakultät für Geographie der Universität Bukarest (Rumänien) sowie dem Institut für Innere Medizin IV, Onkologie/Hämatologie der Martin Luther-Universität Halle-Wittenberg durchgeführt.

Eigenanteil: Konzeption, Durchführung, und Auswertung der biologischen Assays:

MTT-Assay, Tube Formation Assay, Zellzyklusanalysestudien, TUNEL Assay, Zytoskelettfärbungen, CAM Assay, Wound Healing Assay, Tubulinpolymerisierungsassay.

Verfassen des Manuskripts inklusive der Diskussion und Interpretation der Ergebnisse; graphische Repräsentation und Bearbeitung der Abbildungen.

M. Gold: Hilfe bei der Durchführung der MTT-Assays, der Tube Formation Assays, der Wound Healing Assays sowie der Caspase-9 Aktivitäts-Assays im Rahmen eines Mitarbeiterpraktikums (betreut von F. Schmitt und R. Schobert)

M. Rothmund:

Durchführung und Auswertung der Tubulinpolymerisierungsassays zur Bestimmung des ITP₅₀ Werte

I.C. Andronache:

Fraktalanalysen der Blutgefäßveränderung im CAM Assay

B. Biersack: Synthese, Aufreinigung und Charakterisierung aller Testsubstanzen; Überarbeitung und Korrektur des Manuskripts

R. Schobert: Diskussion, Überarbeitung und Korrektur des Manuskripts

T. Müller: Durchführung und Dokumentation der Xenograft Studien in Mäusen und der histologischen Untersuchung der Paraffinschnitte.

Geschätzter Eigenanteil: circa 70%

5.1.3 Eigenanteil: Publikation III

Die Ergebnisse zu diesem Thema wurden im *Journal of Inorganic Biochemistry* veröffentlicht unter folgendem Titel

„New (arene)ruthenium(II) complexes of 4-aryl-4H-naphthopyrans with anticancer and anti-vascular activities”

Von den Autoren

Florian Schmitt, Jana Kasparikova, Viktor Brabec, Gerrit Begemann, Rainer Schobert, und Bernhard Biersack.

Die Arbeit zu diesem Projekt wurde in Kooperation mit dem Lehrstuhl für Entwicklungsbiologie der Universität Bayreuth, dem Institut Biophysik der Academy of Science of the Czech Republic in Brünn (Tschechien), sowie dem Lehrstuhl für Biophysik der Wissenschaftlichen Fakultät der Palacky Universität Olmütz (Tschechien) durchgeführt.

Eigenanteil: Konzeption, Durchführung, und Auswertung der biologischen Assay:

MTT-Assay, EMSA, Ethidiumbromid-Assay, Zellzyklusanalyse, Zytoskelettfärbungen, Tube Formation-Assay, CAM-Assay, Zebrafischembryo-Assay, Tubulinpolymerisierungs-Assay, Mitotic Index Bestimmung;

Verfassen des Manuskripts inklusive der Diskussion und Interpretation der Ergebnisse; graphische Repräsentation und Bearbeitung der Abbildungen; Korrektur und Bearbeitung der Revision.

J. Kasparikova: Aufnahmestudien, DNA-Bindungsstudien

V. Brabec: Aufnahme- und DNA-Bindungsstudien, Diskussion des Manuskripts.

G. Begemann: Diskussion des Manuskripts.

R. Schobert: Diskussion, Überarbeitung, und Korrektur des Manuskripts.

B. Biersack: Synthese, Aufreinigung, und Charakterisierung aller Testsubstanzen; Stabilitätsstudien; Überarbeitung und Korrektur des Manuskripts.

Geschätzter Eigenanteil: circa 70%

5.1.4 Eigenanteil: Manuskript IV

Zu den Ergebnissen zu diesem Thema wurde ein Manuskript vorbereitet unter folgendem Titel
„Oxazole-bridged combretastatin A-4 derivatives with tethered hydroxamic acids: Structure activity relations of new dual inhibitors of HDAC and tubulin function”

Von den Autoren

Florian Schmitt, Lisa Chiara Gosch, Rainer Schobert, Bernhard Biersack, Andrea Volkamer, und Michael Höpfner.

Die Arbeit zu diesem Projekt wurde in Kooperation mit dem Institut für Physiologie der Charité – Universitätsmedizin Berlin durchgeführt.

Eigenanteil: Konzeption, Durchführung und Auswertung der biologischen Assays:

Zytotoxizitätsstudien (MTT-Assay), Zytoskelettfärbungen, Tubulinpolymerisationsassay, HDAC-Inhibitor-Screening, Western Blot-Analysen, Zellzyklusstudien, Wound Healing Assay.

Verfassen des Manuskripts inklusive der Diskussion und Interpretation der Ergebnisse; Erstellen und Bearbeitung der Abbildungen.

L.C. Gosch: Durchführung, Analyse, und graphische Darstellung der Docking-Studien, Verfassen entsprechender Manuskriptpassagen, Diskussion, Überarbeitung und Korrektur des Manuskripts.

R. Schobert: Diskussion, Überarbeitung und Korrektur des Manuskripts.

B. Biersack: Synthese, Aufreinigung, und Charakterisierung aller Testsubstanzen; Verfassen entsprechender Manuskriptpassagen; Diskussion, Überarbeitung und Korrektur des Manuskripts.

A. Volkamer: Durchführung, Analyse, und graphische Darstellung der Docking-Studien, Verfassen entsprechender Manuskriptpassagen, Diskussion, Überarbeitung und Korrektur des Manuskripts.

M. Höpfner: Diskussion des Manuskripts, Planung der Docking-Studien.

Geschätzter Eigenanteil: circa 65%

5.2 Publikation I

Halogenated naphthochalcones and structurally related naphthopyrazolines with antitumor activity

Florian Schmitt, Heidrun Draut, Bernhard Biersack, Rainer Schobert*

Organic Chemistry Laboratory, University Bayreuth, Universitaetsstrasse 30, 95440 Bayreuth, Germany

* Corresponding author. E-mail address: Rainer.Schobert@uni-bayreuth.de

Bioorg. Med. Chem. Lett. **2016**, 26, 5168-5171.

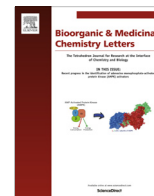
Reprinted with permission from *Halogenated naphthochalcones and structurally related naphthopyrazolines with antitumor activity*. F. Schmitt, H. Draut, B. Biersack, R. Schobert. Bioorg. Med. Chem. Lett. 2016, 26, 5168-5171. doi: 10.1016/j.bmcl.2016.09.076.

Copyright © 2016, Elsevier Ltd.



Contents lists available at ScienceDirect

Bioorganic & Medicinal Chemistry Letters

journal homepage: www.elsevier.com/locate/bmcl

Halogenated naphthochalcones and structurally related naphthopyrazolines with antitumor activity



Florian Schmitt, Heidrun Draut, Bernhard Biersack, Rainer Schobert*

Organic Chemistry Laboratory, University Bayreuth, Universitaetsstrasse 30, 95440 Bayreuth, Germany

ARTICLE INFO

Article history:

Received 28 July 2016

Revised 28 September 2016

Accepted 29 September 2016

Available online 30 September 2016

Keywords:

Chalcones

Pyrazolines

BCRP

P-gp

TUNEL

ABSTRACT

Three 3-(3-halo-4,5-dimethoxyphenyl)-1-(2-naphthyl)prop-2-en-1-ones **1** and three structurally related 2-pyrazolines **2** were prepared and assessed in vitro for anticancer activity. The chalcones **1** were antiproliferative with low double-digit micromolar IC₅₀ values against six tumor cell lines whereas the pyrazolines **2** showed low single-digit micromolar IC₅₀ values against this panel. The pyrazolines inhibited ATP-binding cassette efflux transporters of types P-gp and BCRP while the chalcones inhibited selectively BCRP. All test compounds induced an accumulation of HT-29 colon carcinoma cells in the G2/M phase of the cell cycle and they interfered with the microtubule and F-actin dynamics, but only the chalcones induced apoptosis in 518A2 melanoma cells after 24 h.

© 2016 Elsevier Ltd. All rights reserved.

A critical hurdle to a successful chemotherapy is multidrug resistance (MDR) of cancer cells which may be inherent or acquired during previous lines of therapy. The energy-dependent efflux of xenobiotics, mediated by adenosine triphosphate-binding cassette (ABC) transporters, plays a major role in the process of cellular resistance to chemotherapeutics.¹ An overexpression of these transporters in tumor cells decreases the efficacy of drugs by reducing their intracellular concentration. The multidrug resistance-associated protein 1 (MRP1), P-glycoprotein (P-gp), and the breast cancer resistance protein (BCRP) are the most important ABC-transporters involved in MDR.² Effective and selective ABC-transporter inhibitors can help to restore the impact of anticancer drugs in MDR tumors. A good deal of 1,3-diphenyl-prop-2-en-1-ones (a.k.a. chalcones), precursors in the biosynthesis of flavonoids,³ are known to inhibit ABC-transporters.^{1,2,4} We recently reported a combretastatin A4 derived chalcone and its platinum complex that inhibited BCRP and P-gp.⁴ Structure–activity relationship (SAR) studies by others showed that chalcones bearing basic functional groups are likely to be P-gp inhibitors,⁵ whereas non-basic chalcones displayed no P-gp inhibition but

Abbreviations: ABC, adenosine triphosphate binding cassette; BCRP, breast cancer resistance protein; FTC, fumitremorgin C; MDR, multidrug resistance; P-gp, P-glycoprotein; SD, standard deviation; TdT, Terminal deoxyribonucleotide Transferase; Topo, topotecan; TUNEL, Terminal deoxyribonucleotide Transferase dUTP Nick End Labeling; Vbl, vinblastin.

* Corresponding author.

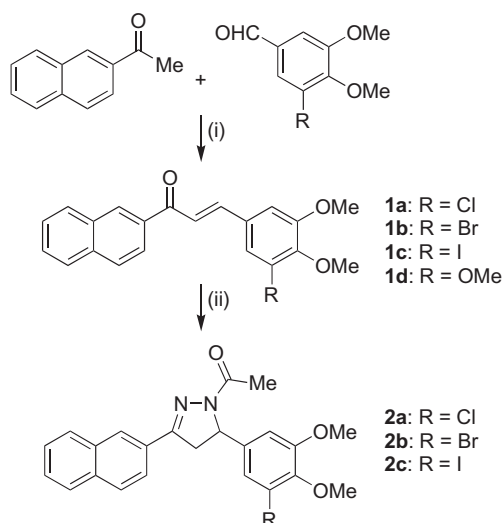
E-mail address: Rainer.Schobert@uni-bayreuth.de (R. Schobert).<http://dx.doi.org/10.1016/j.bmcl.2016.09.076>

0960-894X/© 2016 Elsevier Ltd. All rights reserved.

selectively inhibited BCRP.² A strong BCRP inhibition was noted for naphthylchalcones with a chloro substituted 3-phenyl ring. Moreover, chalcones may also exert other cancer-relevant effects, including apoptosis induction, antiproliferative effects, and an interference with the cell cycle progression.³ Herein, we report on a series of halogenated naphthylchalcones **1** and structurally related 2-pyrazolines **2**, on their potential as selective ABC-transporter inhibitors, and on further anticancer properties.

The new chalcones **1a** and **1c** were obtained as colorless solids from a Claisen–Schmidt condensation of 2-acetylnaphthalene and 3,4-dimethoxy-5-chloro-benzaldehyde or 3,4-dimethoxy-5-iodo-benzaldehyde, respectively (Scheme 1).⁶ The synthesis of the chalcones **1b** and **1d** was reported previously.^{7–9} The new acetylpyrazolines **2a–c** were prepared by reaction of **1a–c** with hydrazine hydrate in acetic acid and obtained as colorless solids (Scheme 1).⁶

The effect of the chalcones **1a–d** and of the 2-pyrazolines **2a–c** on the growth of cancer cells of five different entities was assessed using the MTT assay.¹⁰ All compounds showed dose-dependent cell growth inhibition against the entire panel of cell lines (Table 1). The chalcones featured low double-digit micromolar IC₅₀ concentrations with the 3-halophenyl chalcones **1a–c** being on average slightly more active than the trimethoxyphenyl derivative **1d**. It is known that 3,4-dimethoxy substituted chalcones inhibit ABC efflux transporters of the BCRP type.² Hence, it is not surprising that the multidrug-resistant cancer cell line MCF-7/Topo, which overexpresses these particular efflux pumps,¹¹ was approximately 10-times more sensitive to the chalcones than the other cell lines,



Scheme 1. Synthesis of chalcones **1a–d** and of acetylpyrazolines **2a–c**. Reagents and conditions: (i) NaOH, MeOH/H₂O, rt, 16 h, 80–85%; (ii) N₂H₄ × H₂O, AcOH, reflux, 3 h, 32–71%.

with IC₅₀ values in the low single-digit micromolar range. The 3-halophenyl substituted naphthylpyrazolines **2** were more active compared with their chalcone congeners. They showed low single-digit micromolar IC₅₀ values against all tested cancer cell lines including the multidrug-resistant HT-29 colon, MCF-7/Topo breast, and KB-V1/Vbl cervix carcinoma cells.

The chalcones **1a–d** and the pyrazolines **2a–c** were then screened for inhibition of the ABC-transporters P-gp/ABCB1 and BCRP/ABCG2 by means of the calcein-AM accumulation assay in KB-V1/Vbl cells and the mitoxantrone accumulation assay in MCF-7/Topo cells, respectively (Table 2).^{12,13} MCF-7/Topo breast cancer cells, which overexpress BCRP, were treated with the test compounds (**1a–d**, **2a–c**; 0–100 μM) or the known BCRP inhibitor fumitremorgin C (0.1–100 μM) for 30 min in the presence of the fluorescent BCRP substrate mitoxantrone. The mitoxantrone fluorescence intensity was taken as a measure of the degree of BCRP inhibition and used to obtain dose–response curves which allow the determination of IC₅₀ values. The halophenyl chalcones **1a–c** and their pyrazoline analogues **2a–c** proved to be equally effective inhibitors of BCRP on average with IC₅₀ values in the range of 5–9 μM, while the trimethoxy-substituted chalcone **1d** was two to three times more active. These findings are in line with the results of the MTT assay and the lower IC₅₀ values of the chalcones against MCF-7/Topo breast cancer cells compared with the other tested cell lines. P-gp overexpressing KB-V1/Vbl cervix carcinoma cells were also treated with the test compounds (**1a–d**, **2a–c**; 0–500 μM) or the P-gp inhibitor verapamil (0.1–500 μM) for 15 min in the presence of the non-fluorescent P-gp substrate calcein ace-

Table 2

Concentrations IC₅₀ [μM]^a for the inhibition of BCRP and P-gp transporters by the test compounds **1a–d** and **2a–c**, the specific BCRP inhibitor fumitremorgin C, and the specific P-gp inhibitor verapamil

	BCRP	P-gp
Fumitremorgin C	0.96 ± 0.24 ^b	–
Verapamil	–	65.6 ± 10.1
1a	8.7 ± 1.3	>500
1b	4.9 ± 0.3	>500
1c	7.8 ± 1.6	>500
1d	2.4 ± 0.5	13.0 ± 1.6
2a	7.4 ± 0.3	12.1 ± 0.1
2b	8.9 ± 1.9	12.6 ± 1.6
2c	7.1 ± 1.8	16.3 ± 1.4

^a Determined in MCF-7/Topo breast cancer cells after 30 min or in KB-V1-V1/Vbl cervix carcinoma cells after 15 min exposure to the compounds. The results are the mean ± SD of three independent experiments and derived from dose–response curves.

^b Results of two independent experiments.

toxymethyl ester (calcein-AM). Inhibition of P-gp impedes the efflux of calcein-AM and allows esterases to hydrolyze calcein-AM to give the intensely fluorescent calcein which is not a P-gp substrate anymore and thus accumulates in the cytosol.¹⁴ The calcein fluorescence intensity as a measure of P-gp inhibition was used to calculate the IC₅₀ values of the test compounds. In line with the weaker antiproliferative activities of the halophenyl chalcones **1a–c** against KB-V1/Vbl cancer cells in the MTT assays, compared with those of their 2-pyrazoline analogues, no P-gp inhibition was observed for the former, whereas the inhibitory activities of the latter even exceeded that of the established P-gp inhibitor verapamil, clinically used to re-sensitize resistant tumors.¹⁵ Interestingly, the selectivity for BCRP was lost when the substituent in the *meta* position of the phenyl ring was changed from halide (**1a–c**) to methoxy (**1d**). In terms of IC₅₀ values, **1d** and the 2-pyrazolines **2a–c** were on average four to five times better inhibitors of P-gp when compared to verapamil.

The interference of the test compounds **1a–d** and **2a–c** with the cell cycle progression of HT-29 colon carcinoma cells was determined by flow cytometry using propidium iodide staining. Treatment of the cells with 15 μM of the chalcones or pyrazolines led to a significant accumulation of cells in G2/M phase of the cell cycle whereas the population of cells in G1-phase was drastically reduced (Fig. 1). This effect was more pronounced for the pyrazolines.

The extent of apoptosis in 518A2 melanoma cells treated with **1a**, **1d**, or **2a** for 24 h, was analyzed by flow cytometry using the TUNEL (Terminal deoxynucleotide Transferase dUTP Nick End Labeling) technique (Fig. 2) to visualize DNA fragmentation typical of apoptosis. Interestingly, apoptosis was only induced by the chalcones **1a** and **1d**, whereas cells treated with the pyrazoline **2a** did not differ from untreated control cells. These findings were confirmed by DNA ladder assays using agarose gel electrophoresis to

Table 1

Inhibitory concentrations IC₅₀ (μM, 72 h) of compounds **1a–d** and **2a–c** when applied to human cancer cell lines^a

Cell line/compound	HT-29	HCT-116	518A2	MCF-7/Topo	Panc-1	KB-V1/Vbl
1a	23.9 ± 2.5	12.9 ± 0.7	16.4 ± 1.6	1.5 ± 0.4	10.3 ± 0.2	13.1 ± 1.7
1b	22.8 ± 4.8	11.2 ± 1.3	20.2 ± 2.5	2.3 ± 0.3	9.3 ± 0.2	10.5 ± 0.7
1c	13.3 ± 1.3	14.4 ± 1.3	18.1 ± 1.3	1.3 ± 0.4	10.4 ± 0.1	16.5 ± 1.0
1d ⁷	28.1 ± 7.4	13.7 ± 2.7	22.9 ± 5.6	5.6 ± 1.0	13.3 ± 0.4	13.9 ± 2.4
2a	3.5 ± 0.1	3.8 ± 0.2	4.6 ± 0.6	2.1 ± 0.1	3.1 ± 0.1	4.7 ± 0.2
2b	2.5 ± 0.1	2.7 ± 0.2	3.8 ± 0.9	2.6 ± 0.4	1.5 ± 0.1	2.2 ± 0.1
2c	2.3 ± 0.6	1.6 ± 0.1	3.8 ± 0.5	2.5 ± 0.4	1.1 ± 0.1	1.9 ± 0.1

^a Human cancer cell lines: HT-29 and HCT-116 colon carcinomas, 518A2 melanoma, MCF-7/Topo breast cancer adenocarcinoma, Panc-1 pancreatic ductular adenocarcinoma and KB-V1/Vbl cervix carcinoma. Values are the means ± SD determined in four independent experiments and derived from dose–response curves (percentage of viable cells relative to untreated controls) after 72 h incubation using the MTT assay.

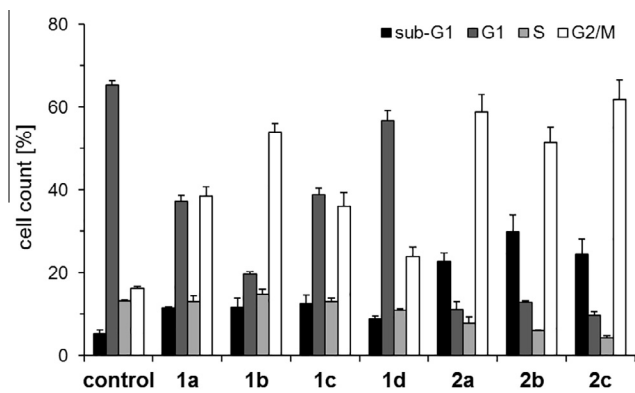


Figure 1. Percentage of HT-29 colon carcinoma cells in G1, S and G2/M cell cycle phases and the proportion of dead cells (sub-G1) as determined by flow cytometry. Cells were treated with 15 μ M of **1a–d**, or **2a–c**, or DMSO (control cells) for 24 h. Values are the means \pm SD of three independent experiments.

visualize the DNA ladder pattern typical of apoptosis (cf. [Supplementary Data](#)).

Since the G2/M arrest might be induced by the test compounds' interference with the tubulin dynamics causing a retarded cell division and mitotic progression, we investigated the effects of the test compounds on the cytoskeletal organization of the microtubules and of the microfilaments (F-actin) in 518A2 melanoma cells. The distribution of microtubules in 518A2 cells treated with **1a**, **1d** or **2a** for 24 h did not differ much from untreated controls when visualized by immunofluorescence (cf. [Supplementary Data](#)). In contrast, a moderate inhibitory effect of the test compounds **1a**, **1c**, **2a** and **2c** was observed in a cell-free polymerization assay with purified pig brain tubulin (cf. [Supplementary Data](#)). This was further confirmed by quantifying the fractions of intact microtubules in treated 518A2 melanoma cells ([Fig. 3](#)). Any interference of the test compounds with the tubulin dynamics increases the proportion of detergent-soluble tubulin heterodimers which are part of the supernatant, in contrast to the intact tubulin polymers which can be separated from the former fraction by centrifugation. In line with these results, the quantification of the intact microtubule fraction by Western blot analyses confirmed a significant reduction of this fraction with increasing concentrations of **1c** and **2c**.

In addition, we investigated potential morphological changes of the F-actin cytoskeleton of 518A2 melanoma cells upon treatment with compounds **1a**, **1d** or **2a** for 24 h. We observed the formation of stress fibers traversing the whole cell body, which is a typical stress response of cells to exposure to tubulin-binding agents ([Fig. 4](#)). Untreated control cells showed the normal cortical actin

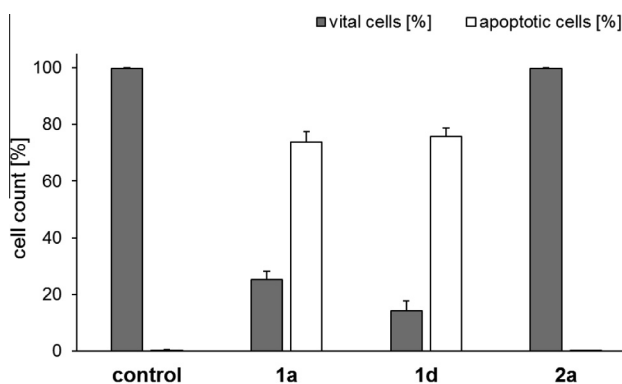


Figure 2. Flow cytometric analyses of apoptosis in 518A2 melanoma cells visualized by TUNEL technique. Cells were treated with vehicle (DMSO), 25 μ M of **1a** or **1d**, or 7.5 μ M of **2a** for 24 h and stained by transferase-mediated fluorescein-dUTP Nick End Labeling of 3'-OH ends of fragmented DNA.

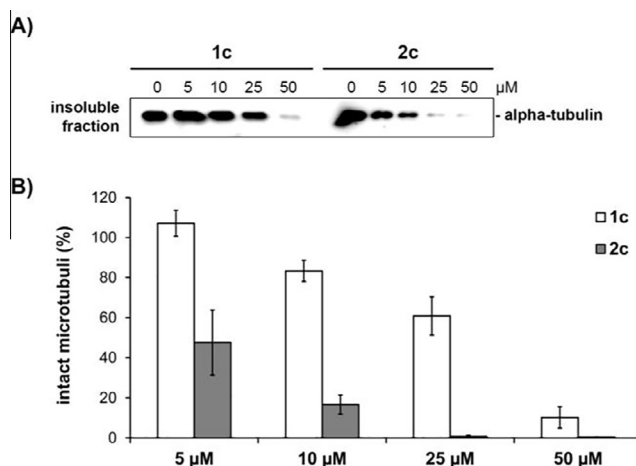


Figure 3. Decrease of intact tubulin polymers in 518A2 melanoma cells upon treatment with **1c** or **2c**. (A) Fractions of detergent-insoluble 518A2 cell lysates, treated for 4 h with various concentrations of **1c** or **2c**, were subjected to SDS-PAGE and the tubulin content was visualized by immunoblotting for alpha-tubulin (55 kDa). (B) Densitometric analyses of Western blots from at least two independent experiments (mean \pm SD) were used to quantify the concentration-dependent levels of tubulin polymers in detergent-insoluble lysate fractions.

fiber network with tenuous filaments across the cells and a greater number of intercellular connections.

Previous studies had shown that the magnitude and selectivity of the inhibition of the BCRP efflux pump by chalcones depends decisively on their substitution pattern. Wiese et al. investigated the inhibitory effects of naphthochalcones with substituents in position 2, 3 and/or 4 of the phenyl ring at C-3.^{2a} We now complemented their successful search for valid structure–activity relationships by including naphthylchalcones bearing a methoxy or halide substituent in 3-position of this ring in addition to the 4,5-dimethoxy motif. While all naphthylchalcones were strong inhibitors of the BCRP transporter, only the halogenated ones, **1a–c**, were selective for this particular type of ABC-transporter. The trimethoxy derivative **1d** inhibited both BCRP and P-gp transporters. Replacement of the enone motif in these chalcones by a 2-pyrazoline ring led to compounds **2** which inhibited both BCRP and P-gp transporters indiscriminately. However, in terms of in vitro cytotoxicity, the 2-pyrazoline analogues surpassed the chalcones considerably. Apoptosis was only induced by the chalcones, likely via the intrinsic pathway as it was already shown for other chalcones.^{16,17} The electrophilic Michael system of the chalcones seems to be crucial for eliciting cytochrome c release¹⁸ and apoptosis induction.^{19,20} The interference of the

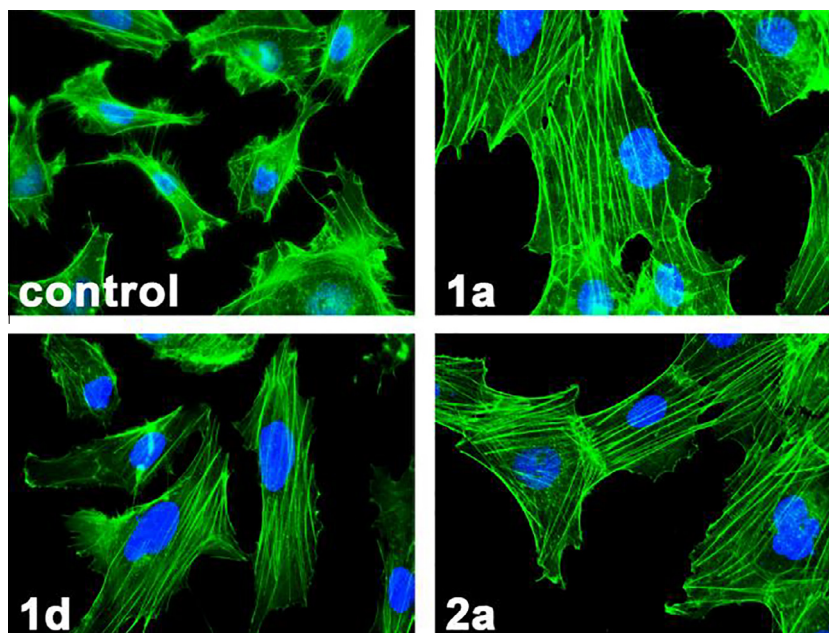


Figure 4. Effect of **1a** (10 μ M), **1d** (10 μ M) and **2a** (5 μ M) on the cytoskeletal organization of 518A2 melanoma cells. Filamentous actin (F-actin, green) stained with a fluorescent phalloidin conjugate and nuclei counterstained with DAPI (blue) (400-fold magnification).

new compounds with the microtubule dynamics impedes the cell division so that the cancer cells accumulate in G2/M phase of the cell cycle. The initiation of stress fiber formation should lead to an immobilization of cancer cells and thus a reduced migration and metastasis.

Supplementary data

Details of the syntheses and physical data of compounds **1a**, **1c**, **2a-c**, on cell culture conditions, biological assays (MTT, mitoxantrone, calcein-AM, TUNEL, fluorescence labeling of F-actin, cell cycle analysis, DNA fragmentation, fluorescence labeling of microtubules, in vitro tubulin polymerization, quantification of polymeric tubulin fractions).

Supplementary data associated with this article can be found, in the online version, at <http://dx.doi.org/10.1016/j.bmcl.2016.09.076>.

References and notes

- Rangel, L. P.; Winter, E.; Gauthier, C.; Chiaradia-Delatorre, L. D.; Mascarello, A.; Nunes, R. J.; Yunes, R. A.; Creczynski-Pasa, T. B.; Macalou, S.; Lorendeau, D.; Baubichon-Cortay, H.; Ferreira-Pereira, A.; Di Pietro, A. *Drug Des. Devel. Ther.* **2013**, 1043.
- (a) Juvale, K.; Pape, V. F. S.; Wiese, M. *Bioorg. Med. Chem.* **2012**, 20, 346; (b) Kraege, S.; Stefan, K.; Juvale, K.; Ross, T.; Willmes, T.; Wiese, M. *Eur. J. Med. Chem.* **2016**, 117, 212.
- (a) Zhang, E. H.; Wang, R. F.; Guo, S. Z.; Liu, B. *Evid. Based Complement Alternat. Med.* **2013**, 1; (b) Canela, M.-D.; Noppen, S.; Bueno, O.; Prota, A. E.; Bargsten, K.; Saez-Calvo, G.; Jimeno, M.-L.; Benkheil, M.; Ribatti, D.; Velazquez, S.; Camarasa, M.-J.; Diaz, J. F.; Steinmetz, M. O.; Priego, E.-M.; Perez-Perez, M.-J.; Liekens, S. *Oncotarget* **2016**. <http://dx.doi.org/10.18632/oncotarget.9527>; (c) Barmaoglu, S.; Algul, O.; Anil, D. A.; Gobek, A.; Duran, G.; Ersan, R. H.; Duran, N. *Bioorg. Med. Chem. Lett.* **2016**, 26, 3172.
- Zoldakova, M.; Kornyei, Z.; Brown, A.; Biersack, B.; Madarász, E.; Schobert, R. *Biochem. Pharmacol.* **2010**, 80, 1487.
- Liu, X. L.; Tee, H. W.; Go, M. L. *Bioorg. Med. Chem.* **2008**, 16, 171.
- Nepali, K.; Kadian, K.; Ojha, R.; Dhiman, R.; Garg, A.; Singh, G.; Buddhiraja, A.; Bedi, P. M. S.; Dhar, K. L. *Med. Chem. Res.* **2012**, 21, 2990.
- Ethiraj, K. R.; Aranjani, J. M.; Khan, F. R. N. *Chem. Biol. Drug Des.* **2013**, 82, 732.
- Dhar, D. N.; Misra, S. S. *J. Indian Chem. Soc.* **1972**, 49, 629.
- Misra, S. S. *J. Indian Chem. Soc.* **1975**, 52, 1095.
- Mosmann, T. *J. Immunol. Methods* **1983**, 65, 55.
- Doyle, L. A.; Yang, W.; Abruzzo, L. V.; Krogmann, T.; Gao, Y.; Rishi, A. K.; Ross, D. D. *PNAS* **1998**, 95, 15665.
- Kühnle, M.; Egger, M.; Müller, C.; Mahringer, A.; Bernhardt, G.; Fricker, G.; König, B.; Buschauer, A. *J. Med. Chem.* **2009**, 52, 1190.
- Spoerlein-Guettler, C.; Mahal, K.; Schobert, R.; Biersack, B. *J. Inorg. Biochem.* **2014**, 138, 64.
- Liminga, G.; Nygren, P.; Larsson, R. *Exp. Cell Res.* **1994**, 212, 291.
- Ozols, R. F.; Cunnion, R. E.; Klecker, R. W.; Hamilton, T. C.; Ostchega, Y.; Parrillo, J. E.; Young, R. C. *J. Clin. Oncol.* **1987**, 5, 641.
- Hseu, Y. C.; Lee, M.-S.; Wu, C.-R.; Cho, H.-J.; Lin, K.-Y.; Lai, G.-H.; Wang, S.-Y.; Kuo, Y.-H.; Kumar, K. J. S.; Yang, H.-L. *J. Agric. Food Chem.* **2012**, 60, 2385.
- Shen, K.-H.; Chang, J.-K.; Hsu, Y.-L.; Kuo, P.-L. *Clin. Pharmacol. Toxicol.* **2007**, 101, 254.
- Zenger, K.; Dutta, S.; Wolff, H.; Genton, M. G.; Kraus, B. *Toxicology* **2015**, 336, 26.
- Garrido, C.; Galluzzi, L.; Brunet, M.; Puig, P. E.; Didelot, C.; Kroemer, G. *Cell Death Differ.* **2006**, 13, 1423.
- Hsu, Y. L.; Tzeng, W. S.; Lin, C. C. *Food Chem. Toxicol.* **2006**, 44, 704.

New halogenated naphthochalcones and structurally related naphthopyrazolines with antitumor activity

Florian Schmitt^a, Heidrun Draut^a, Bernhard Biersack^a, and Rainer Schobert^{a, *}

^aOrganic Chemistry Laboratory, University Bayreuth, Universitaetsstrasse 30, 95440 Bayreuth, Germany

Table of Contents

Materials and Methods.....	2
General remarks	2
Chemistry	2
Synthesis of chalcones 1a , 1c and of acetylpyrazolines 2a-c	2
Biological studies.....	3
Cell culture conditions.....	3
Growth inhibition assay.....	3
Mitoxantrone assay for BCRP activity in MCF-7/Topo cells.....	3
Calcein-AM assay for P-gp activity of KB-V1/Vbl cells.....	3
TUNEL-based detection of apoptotic cells.....	3
Fluorescence labeling of actin filament.....	4
Cell cycle analysis. ^{5,6}	4
DNA fragmentation assay.....	4
Fluorescence labeling of microtubules.....	4
Tubulin polymerization assay. ⁸	4
Quantification of polymeric tubulin fractions. ^{8,9}	4
Results.....	6
Determination of apoptosis induction by DNA fragmentation assays.....	6
Effects on the microtubule dynamics.....	7

Materials and Methods

General remarks

Melting points (uncorrected): GALLENKAMP; IR spectra: PERKIN-ELMER Spectrum One FT-IR spectrophotometer with ATR sampling unit; Nuclear magnetic resonance (NMR) spectra: BRUKER Avance 300 spectrometer, chemical shifts are given in parts per million (δ) downfield from tetramethylsilane as internal standard for ^1H and ^{13}C ; Mass spectra: THERMO FINNIGAN MAT 8500 (EI). Microanalyses: Vario EL III elemental analyzer; all tested compounds were > 95% pure by elemental analysis. All starting compounds were purchased from ALDRICH and used without further purification.

Chemistry

Synthesis of chalcones 1a, 1c and of acetylpyrazolines 2a-c.

3-(3-Chloro-4,5-dimethoxyphenyl)-1-(naphth-2-yl)-prop-2-en-1-one (1a)

2-Acetylnaphthalene (455 mg, 2.67 mmol) was dissolved in MeOH (10 mL) and 3-chloro-4,5-dimethoxybenzaldehyde (536 mg, 2.67 mmol) was added. 5% NaOH (2.67 mL) was added and the reaction mixture was stirred at room temperature for 16 h. The formed precipitate was collected, washed with MeOH and dried in vacuum. Yield: 750 mg (2.13 mmol, 80%); colorless solid of m.p. 110-111 °C; $\nu_{\text{max}}(\text{ATR})/\text{cm}^{-1}$ 3055, 3030, 2951, 2837, 1655, 1627, 1597, 1560, 1494, 1455, 1430, 1405, 1352, 1309, 1277, 1270, 1237, 1216, 1190, 1138, 1123, 1047, 1012, 994, 972, 949, 864, 837, 820, 754, 772, 736, 655, 622, 689, 565; ^1H NMR (300 MHz, CDCl_3) δ 3.90 (3 H, s), 3.92 (3 H, s), 7.05 (1 H, d, $J = 2.0$ Hz), 7.33 (1 H, d, $J = 2.0$ Hz), 7.5-7.6 (3 H, m), 7.71 (1 H, d, $J = 16.0$ Hz), 7.9-8.1 (4 H, m), 8.50 (1 H, s); ^{13}C NMR (75.5 MHz, CDCl_3) δ 56.2, 60.9, 111.0, 122.2, 122.3, 124.4, 126.8, 127.8, 128.5, 128.6, 128.9, 129.5, 130.0, 131.4, 132.5, 135.3, 143.2, 147.3, 154.0, 190.0; m/z (EI) 354 (60) [M^+], 352 (100) [M^+], 339 (27), 337 (86), 317 (36), 155 (32), 127 (58). Anal $\text{C}_{21}\text{H}_{17}\text{ClO}_3$ (352.81) requires: C, 71.49; H, 4.86%. Found: C, 71.00; H, 5.028%

3-(3-Iodo-4,5-dimethoxyphenyl)-1-(naphth-2-yl)-prop-2-en-1-one (1c)

2-Acetylnaphthalene (511 mg, 3.0 mmol) was dissolved in MeOH (10 mL) and 3-iodo-4,5-dimethoxybenzaldehyde (876 mg, 3.0 mmol) was added. 5% NaOH (3.0 mL) was added and the reaction mixture was stirred at room temperature for 16 h. The formed precipitate was collected, washed with MeOH and dried in vacuum. Yield: 1.127 g (2.54 mmol, 85%); colorless solid of m.p. 146-147 °C; $\nu_{\text{max}}(\text{ATR})/\text{cm}^{-1}$ 3055, 3031, 2995, 2944, 2837, 1654, 1627, 1595, 1580, 1547, 1481, 1453, 1426, 1405, 1350, 1305, 1274, 1264, 1235, 1212, 1186, 1136, 1121, 1037, 1010, 991, 970, 955, 948, 868, 837, 818, 791, 753, 730; ^1H NMR (300 MHz, CDCl_3) δ 3.88 (3 H, s), 3.91 (3 H, s), 7.12 (1 H, d, $J = 1.9$ Hz), 7.5-7.7 (5 H, m), 7.9-8.1 (4 H, m), 8.51 (1 H, s); ^{13}C NMR (75.5 MHz, CDCl_3) δ 56.1, 60.6, 92.9, 112.8, 122.2, 124.4, 126.8, 127.8, 128.5, 128.6, 129.5, 130.0, 130.6, 132.5, 132.9, 135.4, 142.8, 150.9, 152.6, 189.0; m/z (EI) 444 (100) [M^+], 429 (26), 317 (12), 292 (21), 155 (18), 127 (25). Anal $\text{C}_{21}\text{H}_{17}\text{IO}_3$ (444.26) requires: C, 56.77; H, 3.86%. Found: C, 56.52; H, 4.090%

1-Acetyl-5-(3-chloro-4,5-dimethoxyphenyl)-3-(naphth-2-yl)-4,5-dihydro-(1H)-pyrazole (2a)

1a (352 mg, 1.0 mmol) was dissolved in glacial acetic acid (5 mL) and treated with hydrazine hydrate (0.3 mL). The reaction mixture was stirred under reflux for 3 h. The solution was poured on ice, the formed precipitate was collected and recrystallised from $\text{H}_2\text{O}/\text{EtOH}$. Yield: 130 mg (0.32 mmol, 32%); colorless solid of m.p. 140 °C; $\nu_{\text{max}}(\text{ATR})/\text{cm}^{-1}$ 3055, 3002, 2969, 2937, 2830, 1661, 1602, 1574, 1490, 1479, 1412, 1389, 1365, 1320, 1307, 1289, 1270, 1232, 1184, 1131, 1094, 1049, 999, 962, 908, 881, 857, 820, 770, 748, 630, 611, 592, 575, 565; ^1H NMR (300 MHz, $\text{DMSO}-d_6$) δ 2.39 (3 H, s), 3.3-3.4 (1 H, m), 3.72 (3 H, s), 3.82 (3 H, s), 3.9-4.0 (1 H, m), 5.5-5.6 (1 H, m), 6.80 (1 H, s), 6.93 (1 H, s), 7.5-7.6 (2 H, m), 7.9-8.1 (4 H, m), 8.19 (1 H, s); ^{13}C NMR (75.5 MHz, $\text{DMSO}-d_6$) δ 22.356.5, 59.5, 60.6, 109.8, 118.1, 123.6, 127.4, 127.8, 128.1, 128.2, 128.4, 128.8, 128.9, 129.0, 133.1, 134.1, 139.9, 144.1, 154.2, 154.8, 168.2; m/z (EI) 410 (25) [M^+], 409 (24) [M^+], 408 (81) [M^+], 368 (31), 367 (30), 366 (100), 365 (31), 255 (17), 195 (29). Anal $\text{C}_{23}\text{H}_{21}\text{ClN}_2\text{O}_3$ (408.87) requires: C, 67.56; H, 5.18; N, 6.85%. Found: C, 66.93; H, 4.893; N, 7.033%

1-Acetyl-5-(3-bromo-4,5-dimethoxyphenyl)-3-(naphth-2-yl)-4,5-dihydro-(1H)-pyrazole (2b)

1b (397 mg, 1.0 mmol) was dissolved in glacial acetic acid (5 mL) and treated with hydrazine hydrate (0.3 mL). The reaction mixture was stirred under reflux for 3 h. The solution was poured on ice, the formed precipitate was collected and recrystallised from $\text{H}_2\text{O}/\text{EtOH}$. Yield: 320 mg (0.71 mmol, 71%); colorless solid of m.p. 144-146 °C; $\nu_{\text{max}}(\text{ATR})/\text{cm}^{-1}$ 3050, 3005, 2939, 2830, 1662, 1591, 1566, 1539, 1487, 1478, 1428, 1410, 1388, 1364, 1341, 1321, 1285, 1265, 1252, 1229, 1177, 1156, 1132, 1044, 1017, 1000, 989, 965, 948, 906, 876, 857, 832, 819, 807, 769, 749, 668, 659; ^1H NMR (300 MHz, $\text{DMSO}-d_6$) δ 2.38 (3 H, s), 3.3-3.4 (1 H, m), 3.70 (3 H, s), 3.81 (3 H, s), 3.9-4.0 (2 H, m), 5.5-5.6 (1 H, m), 6.9-7.0 (2 H, m), 7.5-7.6 (2 H, m), 7.9-8.1 (4 H, m), 8.18 (1 H, s); ^{13}C NMR (75.5 MHz, $\text{DMSO}-d_6$) δ 21.8, 42.0, 56.1, 59.0, 60.0, 110.0, 116.7, 120.5, 123.1, 126.8, 127.3, 127.6, 127.7, 128.3, 128.4, 128.5,

132.7, 133.6, 139.9, 144.7, 153.6, 154.3, 167.7; m/z (EI) 454 (67) [M^+], 452 (69) [M^+], 412 (73), 410 (100), 301 (20), 299 (19), 215 (18), 195 (55), 169 (18), 44 (20). Anal $C_{23}H_{21}BrN_2O_3$ (453.33) requires: C, 60.94; H, 4.677; N, 6.18%. Found: C, 60.87; H, 4.25; N, 6.20%.

1-Acetyl-5-(3-iodo-4,5-dimethoxyphenyl)-3-(naphth-2-yl)-4,5-dihydro-(1H)-pyrazole (2c)

1c (444 mg, 1.0 mmol) was dissolved in glacial acetic acid (5 mL) and treated with hydrazine hydrate (0.3 mL). The reaction mixture was stirred under reflux for 3 h. The solution was poured on ice, the formed precipitate was collected and recrystallised from $H_2O/EtOH$. Yield: 220 mg (0.44 mmol, 44%); colorless solid of m.p. 99-100 °C; $\nu_{max}(ATR)/cm^{-1}$ 3050, 3000, 2966, 2933, 2821, 1655, 1591, 1562, 1479, 1443, 1411, 1389, 1365, 1320, 1296, 1265, 1232, 1182, 1133, 1093, 1042, 999, 961, 909, 858, 844, 817, 796, 748, 692, 672; 1H NMR (300 MHz, $DMSO-d_6$) δ 2.37 (3 H, s), 3.4-3.5 (1 H, m), 3.66 (3 H, s), 3.79 (3 H, s), 3.9-4.0 (1 H, m), 5.5-5.6 (1 H, m), 6.94 (1 H, s), 7.12 (1 H, s), 7.5-7.6 (2 H, m), 7.9-8.1 (4 H, m), 8.18 (1 H, s); ^{13}C NMR (75.5 MHz, $DMSO-d_6$) δ 21.8, 42.0, 55.9, 58.8, 59.7, 92.8, 110.8, 123.1, 126.1, 126.8, 127.3, 127.6, 127.7, 128.3, 128.4, 128.5, 132.7, 133.6, 140.6, 147.3, 152.5, 154.3, 167.7; m/z (EI) 500 (100) [M^+], 458 (88), 347 (22), 195 (42). Anal $C_{23}H_{21}IN_2O_3$ (500.33) requires: C, 55.21; H, 4.23; N, 5.60%. Found: C, 54.80; H, 4.19; N, 5.50%.

Biological studies

Cell culture conditions.

Cells of HT-29 (ACC-299) and HCT-116 (ACC-581) colon carcinomas, 518A2 melanoma (Department of Radiotherapy, Medical University of Vienna, Austria), MCF-7/Topo (ACC-115) breast cancer adenocarcinoma, Panc-1 (ACC-783) pancreatic ductular adenocarcinoma and KB-V1/Vbl (ACC-149) cervix carcinoma cells in DMEM (supplemented with 10% FBS and 1% antibiotic-antimycotic) at 37 °C, 5% CO_2 and 95% humidity. MCF-7/Topo and KB-V1/Vbl cells were kept resistant by adding the maximal tolerated dose of topotecan (Topo) or vinblastine (Vbl), respectively, to the cell culture medium 24 h after every cell passage. Only mycoplasma-free cell cultures were used.

Growth inhibition assay.

The cytotoxicities of the naphthylchalcones (**1a-d**) and -pyrazolines (**2a-c**) were studied in MTT assay as previously described.¹ Briefly, 100 μL /well of the cell suspension (containing 5×10^4 cells/mL) were seeded in 96-well tissue culture plates and exposed to varying concentrations of the test compounds (**1a-d**, **2a-c**) or a solvent control (DMSO) for 72 h. After incubating the cells for 2 h with MTT (0.5 mg/ml), the 96-well plates were centrifuged (300 g, 5 min, 4 °C) and the supernatant was discarded. Then, the purple formazan crystals were dissolved in 25 μL of 10% SDS in DMSO containing 0.6% acetic acid. The absorbance at 570 nm (formazan) and at 630 nm (background) wavelength was measured with a microplate reader (Tecan) after 60 min of incubation. All experiments were done in quadruplicate. The percentage of viable cells was calculated as the mean \pm SD relative to controls set to 100%.

Mitoxantrone assay for BCRP activity in MCF-7/Topo cells.

The assay was performed according to literature with slight modifications.^{2,3} MCF-7/Topo cells were adjusted to a cell number of 1.0×10^6 per mL with culture medium, transferred to a black 96-well plate (100 μL /well) and incubated with the naphthylchalcones (**1a-d**), the pyrazolines (**2a-c**) or fumitremorgin C (0.1 to 100 μM) for 10 min. After adding mitoxantrone (20 μM), cells were incubated for 30 min at 37 °C, 5% CO_2 to allow its maximal uptake into the cells. The cells were centrifuged (150 g, 5 min, 20 °C), washed twice with PBS and immediately placed in a TECAN fluorescence plate reader. Mitoxantrone fluorescence was measured at 620 nm excitation and 670 nm emission wavelengths. The cellular fluorescence was used as a measure of BCRP inhibition. The IC_{50} values were calculated from the dose-response curves as the mean \pm SD of three independent experiments.

Calcein-AM assay for P-gp activity of KB-V1/Vbl cells.

The assay was carried out according to a modified literature procedure.⁴ KB-V1/Vbl cells were trypsinized, washed with ice-cold PBS and resuspended in calcein-AM assay buffer (120 mM NaCl, 5 mM KCl, 2 mM $MgCl_2$, 1.5 mM $CaCl_2$, 10 mM glucose, 25 mM HEPES, 0.5% BSA, 0.1% Pluronic F127, pH 7.4) at a cell number of 1.0×10^6 per mL. Cells were transferred into a black 96-well plate (100 μL /well) and incubated with the test compounds **1a-d**, **2a-c** or verapamil (0.1-500 μM) for 15 min at 37 °C, 5% CO_2 . Then calcein-AM was added to a final concentration of 0.25 μM . The cells were incubated for 15 min at 37 °C to allow maximal calcein-AM uptake into the cells. After centrifugation (150 \times g, 5 min) cells were washed with PBS. The intracellular calcein fluorescence ($\lambda_{em} = 485$ nm; $\lambda_{ex} = 535$ nm) was measured in PBS (100 μL) with a microplate reader (Tecan). The cellular fluorescence equal to the P-gp inhibition was used to compile dose response curves for the tested compounds which allows the calculation of the IC_{50} values by 4 parameter Hill equation. All experiments were run in triplicate and data were depicted as mean \pm SD.

TUNEL-based detection of apoptotic cells.

DNA fragmentation in apoptotic cells was determined using the TUNEL technique (Terminal deoxynucleotidyl transferase-mediated dUTP Nick End Labelling). Labeling of 3'OH ends was performed with the commercially available *In Situ* Cell Death Detection Kit, Fluorescein (Roche) and according to manufacturer's instructions. Briefly, cells grown in 6 well plates (3 mL/well, 0.1×10^6 cells/mL) and treated with vehicle (DMSO), **1a** (25 μM), **1d** (25 μM) or **2a** (7.5 μM) for 24 h. Cells were then trypsinated and pelleted by centrifugation (300 g, 4 °C, 5 min). After washing the cells two times with PBS at room temperature, cells were fixed in 2% formaldehyde in PBS at room

temperature for 60 min followed by washing of the cell pellets in PBS. Then, the cells were permeabilized with 0.1% Triton X-100 and 0.1% sodium citrate in PBS for 2 min at 0 °C, washed twice with PBS and labeled with TdT-labelling solution containing TdT enzyme and fluorescein-coupled dUTPs at 37 °C for 60 min in the dark. Labeled cells were washed two times with PBS before analysis of the green fluorescence intensity on a Beckmann Coulter Cytomics FC500 flow cytometer. Data analyses were done with the CXP software (Beckmann Coulter). Gates defining the percentage of viable and apoptotic cells were applied with respect to control. Results are the mean \pm SD of two independent experiments.

Fluorescence labeling of actin filament.

Effects of the naphthylchalcones **1a** and **1d** and the naphthylpyrazoline **2a** on the organization of F-actin in 518A2 melanoma cells were examined by fluorescence microscopy. Labelling of actin filaments was performed with the commercially available Acti-stainTM 488 Fluorescent Phalloidin (Cytoskeleton, Inc.) and according to manufacturer's instructions. Briefly, cells (500 μ L/well; 5×10^4 cells/mL) were grown on glass coverslips to 50% confluence and treated with vehicle (DMSO), **1a** (10 μ M), **1d** (10 μ M) or **2a** (5 μ M) for 24 h. After removing the culture medium, the cells were washed with PBS (37 °C) and fixed with 3.7% formaldehyde in PBS (pH 7.0) at room temperature for 10 min. Then, the cells were washed once with PBS, permeabilized with 0.5% Triton X-100 in PBS for 5 min at room temperature followed by another washing step and the labelling with Acti-stainTM 488 phalloidin (200 μ L, 100 nM) at room temperature in the dark for 30 min. For counterstaining the nuclei the coverslips were mounted in Mowiol 4-88-based mounting medium containing 1 μ g/mL DAPI (4',6-diamidino-2-phenylindole). Fluorescence microscopic analysis of the effects on F-actin cytoskeleton was performed using an Imager A1 AX10 fluorescence microscope (Zeiss, 400 \times magnification).

Cell cycle analysis.^{5,6}

HT-29 colon carcinoma cells (3 mL/well; 1×10^5 cells/mL) grown on 6-well plates were treated with DMSO (control) or **1a-d**, **2a-c** (15 μ M, 24 h), fixed (70% EtOH, 4 °C, 1 h) and incubated with propidium iodide staining solution (50 μ g/mL PI, 0.1% sodium citrate, 50 μ g/mL RNase A in PBS) for 30 min at 37 °C, 5 % CO₂. The fluorescence intensity of 10,000 single cells was determined at $\lambda_{em} = 620$ nm ($\lambda_{ex} = 488$ nm laser source) with a Beckmann Coulter Cytomics FC 500 flow cytometer and analyzed (CXP software, Beckmann Coulter) for the proportion of single cells (%) in G1, S, or G2/M phases. The percentage of dead cells was assessed from sub-G1 peaks.

DNA fragmentation assay.

DNA-fragmentation assays were used to detect apoptosis induced by the naphthylchalcones **1a-d** and -pyrazolines **2a-c**.⁷ 518A2 melanoma cells were grown on 6-well cell culture dishes (3 mL/well; 1×10^5 cells/well), treated with test compounds **1a-d**, **2a-c** (50 μ M) or solvent control (DMSO) for 24 h. Then, cells were detached by trypsination and the cell pellets were lysed in TES lysis buffer (100 mM Tris, 20 mM EDTA, 0.8% SDS, pH 8.0) for 5 min at 60 °C. After RNA and protein digestion by RNase A (50 μ g/mL, 1 h, 37 °C) and proteinase K (200 μ g/mL, 90 min, 50 °C), the suspension was centrifuged (13,400 rpm, 10 min). The supernatant was collected and the DNA was precipitated with ice-cold isopropanol. After centrifugation (13,400 rpm, 5min) the supernatant was discarded, the DNA pellet was resuspended in TE buffer (10 mM Tris-HCl, 1 mM EDTA, pH 8.5) and then subjected to gel electrophoresis using 1% agarose gels in 0.5 \times TBE buffer (89 mM Tris, 89 mM boric acid, 25 mM EDTA, pH 8.3). Gels were stained with ethidium bromide (10 μ g/mL) and pictures of the DNA fragmentation were taken under UV excitation.

Fluorescence labeling of microtubules.

518A2 melanoma cells were seeded on glass coverslips in 24 well multiwell plates (500 μ L/well; 5×10^4 cells/well) and allowed to adhere for 24 h. After incubating the cells for 24 h with vehicle (DMSO) or with various concentrations of **1a**, **1d** or **2a**, cells were fixed with 3.7% formaldehyde in PBS for 20 min at room temperature followed by blocking and permeabilisation with 1% BSA, 0.1% Triton X-100 in PBS for 30 min at room temperature. For immunostaining of microtubules the cells were treated with a primary antibody against alpha-tubulin (anti-alpha-tubulin, mouse monoclonal antibody) followed by incubation with a secondary antibody conjugated to AlexaFluor[®]-488 (goat anti-mouse IgG-AlexaFluor[®], Cell Signaling Technology) for 1 h in the dark. The glass coverslips were mounted in 4-88-based mounting medium containing 2.5% DABCO and 1 μ g/mL DAPI for counterstaining the nuclei. Effects on the microtubule cytoskeleton were documented by fluorescence microscopy (Zeiss Imager A1 AX10, 400x magnification).

*Tubulin polymerization assay.*⁸

50 μ L of Brinkley's buffer 80 (BRB80) containing 20% glycerol and 3 mM GTP was pipetted in a 96-well half-area plate. Then, test compounds (**1a**, **1c**, **2a**, or **2c**), or control (DMSO) were added to the wells to reach a final concentration of 5 μ M. 50 μ L of tubulin in BRB80 (10 mg/mL) was added to the wells and the plate was immediately placed in the pre-heated microplate reader (Tecan). The polymerization was determined turbidimetrically at 37 °C by recording the absorption at 340 nm for 2 h in intervals of 20 sec.

Quantification of polymeric tubulin fractions.^{8,9}

518A2 melanoma cells (500 μ L/well, 5×10^4 cells/mL), grown for 24 h in 24 well plates were treated with control (DMSO) or increasing concentrations of **1c** or **2c** (5, 10, 25 and 50 μ M) for 4 h. After harvesting the cells by trypsination, they were pelleted by centrifugation (300 g, 5 min) at room temperature. Then, the cell pellet was resuspended in 100 μ L hypotonic cell lysis buffer (20 mM Tris-HCl, 1 mM MgCl₂, 2 mM EGTA, 0.5% Triton X-100,

pH 6.8) containing protease inhibitor (Inhibitor cocktail Plus, Carl Roth) for 10 min at room temperature. After pelleting the detergent-insoluble, polymeric microtubules by centrifugation (12,000 g, 10 min, room temperature), the supernatant containing the depolymerized, soluble tubulin fractions was separated from the pellet fraction. Then, 100 μ L 2x SDS-sample buffer (4% SS, 20% glycerol, 20 mM DTT, 0.0005 bromphenol blue in 125 mM Tris-HCl, pH 6.8) was added to the soluble and the pellet fractions and both boiled at 95 °C for 10 min. Equal volumes of the samples were subjected to 10% SDS-PAGE followed by a standard Western blotting procedure. After application of primary (anti-alpha tubulin mouse monoclonal antibody) and secondary antibody (goat anti-mouse IgG-HRP conjugate, Cell Signaling Technology), the alpha-tubulin content was visualized by chemoluminescent detection (LAS4000). The alpha-tubulin content was quantified densitometrically by using the ImageJ software.

Results

Determination of apoptosis induction by DNA fragmentation assays

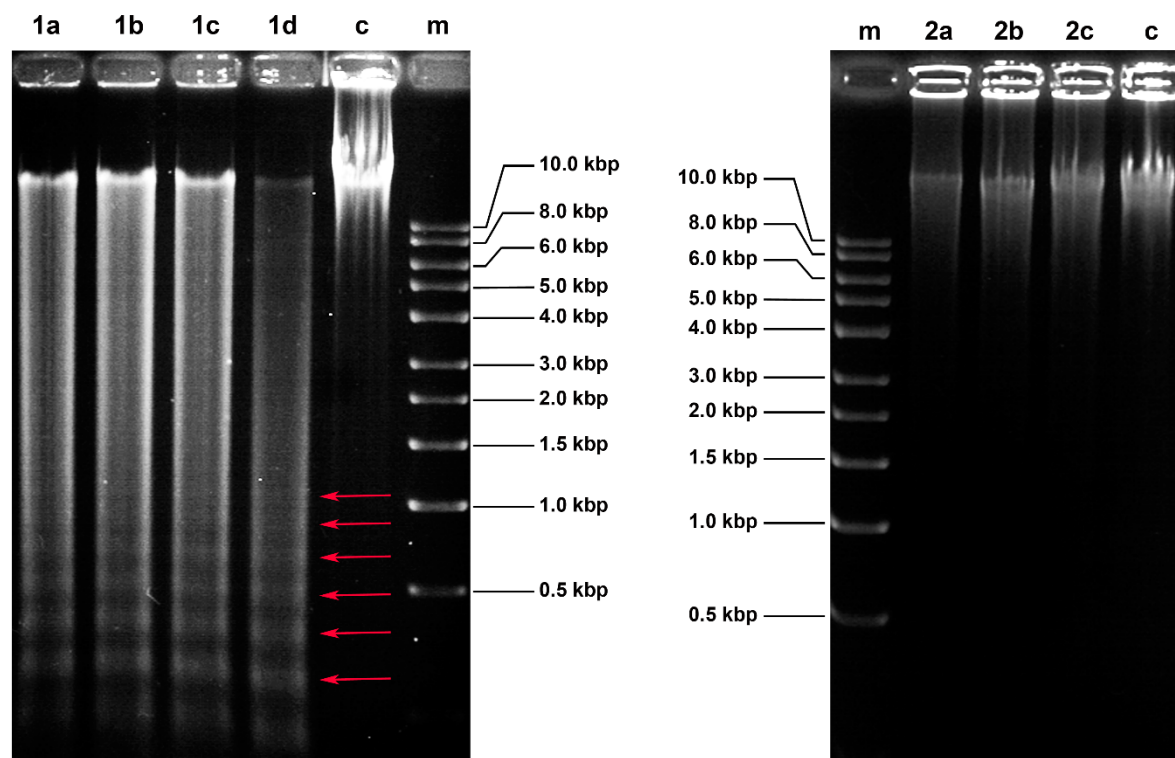


Figure S1. Analysis of apoptosis induction in 518A2 melanoma cells visualized by DNA-fragmentation assays. 518A2 melanoma cells were treated with 50 μ M of the test compounds or vehicle (DMSO) for 24 h. The extracted DNA was subjected to gel electrophoresis and stained with ethidium bromide. The fragments of DNA have interval molecular weights of \sim 180 bp, suggesting the induction of apoptosis (red arrows). m: 1 kb DNA Ladder (New England BioLabs).

Effects on the microtubule dynamics

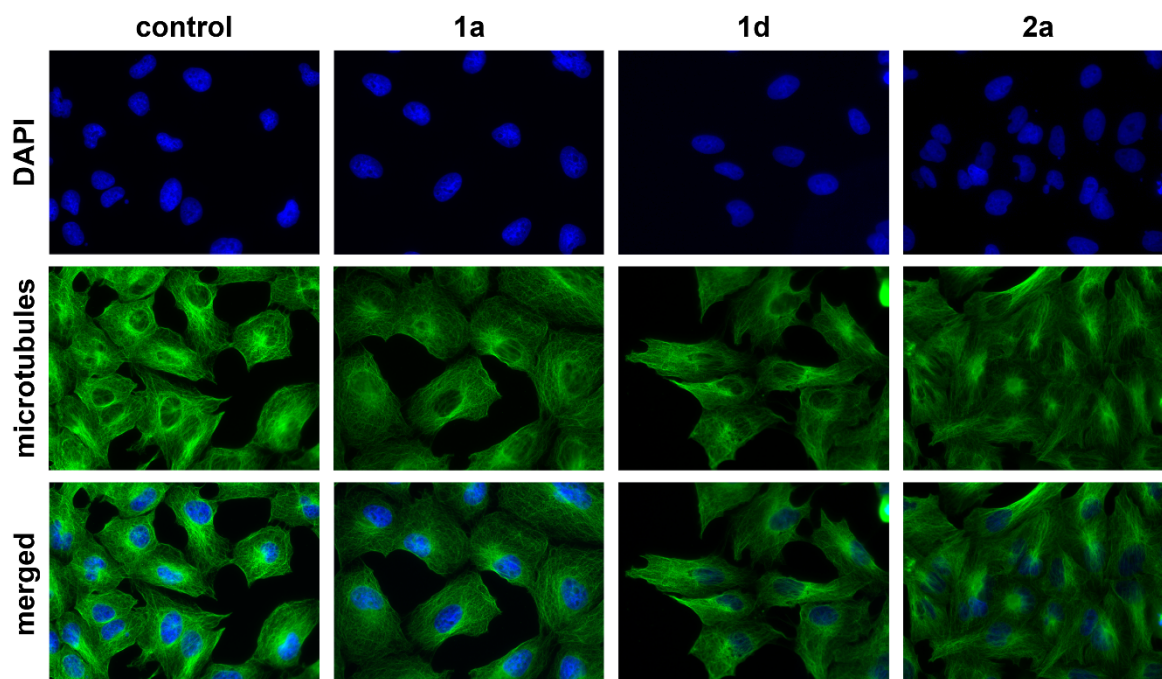


Figure S2. Effects of naphthylchalcones **1a** and **1d** (10 μ M, 24 h) and the naphthylpyrazoline **2a** (5 μ M, 24 h) on the microtubule organization in 518A2 melanoma cells. Immunofluorescent labeling of alpha-tubulin (green), nuclei (blue) were counterstained with DAPI (400-fold magnification).

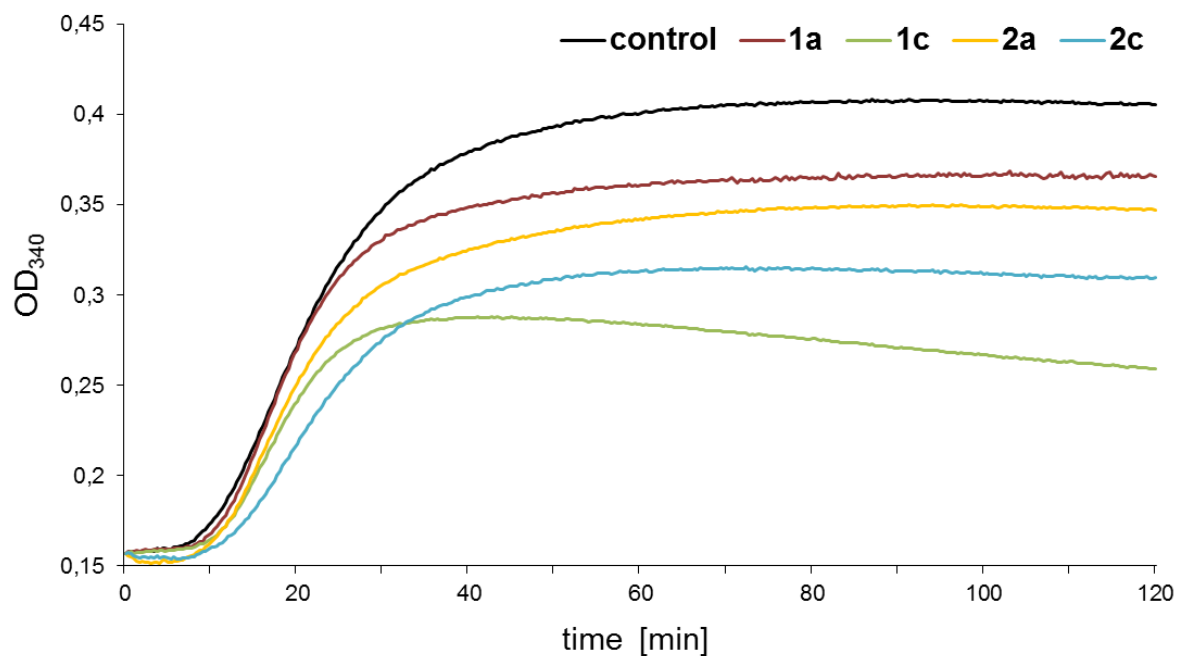


Figure S3. Effects of test compounds **1a**, **1c**, **2a**, and **2c** (5 μ M) on the polymerization of tubulin as determined by a turbidimetric-based cell-free tubulin assay. Data are representative of three independent experiments.

References

1. Mosmann, T. *J. Immunol. Methods* **1983**, *65*, 55.
2. Zoldakova, M.; Kornyei, Z.; Brown, A.; Biersack, B.; Madarász, E.; Schobert, R. *Biochem. Pharmacol.* **2010**, *80*, 1487.
3. Kühnle, M.; Egger, M.; Müller, C.; Mahringer, A.; Bernhardt, G.; Fricker, G.; König, B.; Buschauer, A. *J. Med. Chem.* **2009**, *52*, 1190.
4. Spoerlein-Guettler, C.; Mahal, K.; Schobert, R.; Biersack, B. *J. Inorg. Biochem.* **2014**, *138*, 64.
5. Muenzner, J.K.; Biersack, B.; Kalie, H.; Andronache, I.C.; Kaps, L.; Schuppan, D.; Sasse, F.; Schobert, R. *ChemMedChem.* **2014**, *9*, 1195.
6. Mahal, K.; Resch, M.; Ficner, R.; Schobert, R.; Biersack, B.; Mueller, T. *ChemMedChem* **2014**, *9*, 847.
7. Kasibhatla, S.; Amarante-Mendes, G. P.; Finucane, D.; Brunner, T.; Bossy-Wetzler, E.; Green, D. R. *Cold Spring Harb. Protoc.* **2006**, 4429.
8. Mahal, K.; Biersack, B.; Caysa, H.; Schobert, R.; Mueller, T. *Invest. New Drugs*, **2015**, *33*, 541.
9. Chang, C.-H.; Yu, F.-Y.; Wu, T.-S.; Wang, L.-T.; Liu, B.-H. *Toxicol. Sci.* **2011**, *119(1)*, 84.

5.3 Publikation II

New Naphthopyran Analogues of LY290181 as Potential Tumor Vascular-disrupting Agents

Florian Schmitt,^[a] Madeleine Gold,^[a] Matthias Rothmund,^[a] Ion C. Andronache,^[b] Bernhard Biersack,^[a] Rainer Schobert,^{*[a]} Thomas Mueller^[c]

[a] *Organic Chemistry Laboratory, University Bayreuth, Universitaetsstrasse 30, 95440 Bayreuth, Germany*

[b] *Research Centre of Integrated Analysis and Territorial Management, Faculty of Geography, University of Bucharest, Bvd. Mihail Kogalniceanu no. 36-46 Bucharest, Rumania*

[c] *Department of Internal Medicine IV, Oncology/Hematology, Martin Luther University Halle-Wittenberg, Ernst-Grube-Straße 40, 06120 Halle, Germany*

* Corresponding author; E-mail address: Rainer.Schobert@uni-bayreuth.de

Eur. J. Med. Chem. **2019**, 163, 160-168.

Reprinted with permission from *New Naphthopyran Analogues of LY290181 as Potential Tumor Vascular-disrupting Agents*. F. Schmitt, M. Gold, M. Rothmund, I.C. Andronache, B. Biersack, R. Schobert, T. Müller. Eur. J. Med. Chem. 2019, 163, 160-168. doi 10.1016/j.ejmech.2018.11.055.

Copyright © 2018, Elsevier Ltd



Contents lists available at ScienceDirect

European Journal of Medicinal Chemistry

journal homepage: <http://www.elsevier.com/locate/ejmech>

Research paper

New naphthopyran analogues of LY290181 as potential tumor vascular-disrupting agents

Florian Schmitt ^a, Madeleine Gold ^a, Matthias Rothmund ^a, Ion Andronache ^b, Bernhard Biersack ^a, Rainer Schobert ^{a,*}, Thomas Mueller ^c^a Department of Chemistry, University Bayreuth, Universitaetsstrasse 30, 95440, Bayreuth, Germany^b University of Bucharest, Research Center for Integrated Analysis and Territorial Management, 4-12, Regina Elisabeta Avenue, Bucharest, 3rd District, 030018, Romania^c Department of Internal Medicine IV, Oncology/Hematology, Martin Luther University Halle-Wittenberg, Ernst-Grube-Straße 40, 06120, Halle, Germany

ARTICLE INFO

Article history:

Received 1 March 2018

Received in revised form

4 October 2018

Accepted 22 November 2018

Available online 23 November 2018

Keywords:

Naphthopyrans

Vascular-disrupting agents (VDA)

CAM assay

Microtubule destabilizing agents (MDA)

ABSTRACT

A series of 19 analogues of the antiproliferative naphthopyran LY290181 were prepared for structure–activity relationship studies. We found the best activities for test compounds bearing small substituents at the *meta* position of the phenyl ring. The mode of action of LY290181 and eight new analogues was studied in detail. The compounds were highly anti-proliferative with IC₅₀ values in the sub-nanomolar to triple-digit nanomolar range. The new analogues led to G₂/M arrest due to interruption of the microtubule dynamics. In 518A2 melanoma cells they caused a mitotic catastrophe which eventually led to apoptosis. The naphthopyrans also induced a disruption of the vasculature in the chorioallantoic membrane (CAM) of fertilized chicken eggs as well as in xenograft tumors in mice. In a preliminary therapy trial, the difluoro derivative **2b** retarded the growth of resistant xenograft tumors in mice.

© 2018 Elsevier Masson SAS. All rights reserved.

1. Introduction

The concept of tumor vascular-disrupting agents (VDAs) is to selectively shut down tumor vasculature and consequently to destroy tumors by blocking off their supply with oxygen and nutrition [1]. The known VDAs can be subdivided in flavonoids and microtubule binding/destabilizing agents (MDA) [2]. While the mechanism of action of the former is still poorly understood [3], that of MDAs has been studied extensively. MDAs utilize the morphological differences between the highly dynamic and mostly irregular tumor vascularization and the regular blood vessels. The tumor blood vessels lack pericytes and are marked by abnormal basement membranes and increased vascular permeability [4]. Hence, one target of VDAs is the further destabilization of the vessels by destructing the cytoskeleton and cell-to-cell junctions of the endothelial cells to the effect of the collapse of the entire vessel and ultimately of tumor cell necrosis. Several small molecule MDAs such as NPI-2358 [5], dolastatin-10 [6,7], MPC6827 [8], CYT997 [9], ZD6126 [10], AVE8062 [11], Oxi4503 [12], fosbretabulin [13], or

BNC105P [14] were already investigated in clinical trials. The naphthopyran LY290181 (**2a**) [2-amino-4-(3-nitrophenyl)-4H-naphtho(1,2-b)pyran-3-carbonitrile], first synthesized by Dell et al. in 1991 [15], represents such an MDA with highly anti-proliferative activity. The microtubule destabilizing effect of LY290181 and several analogous 4H-naphthopyran derivatives is a consequence of their direct binding to tubulin which inhibits tubulin polymerization and eventually leads to a disruption of the microtubule cytoskeleton [16–18]. Early investigations of these agents focused on their application in the treatment of restenosis [15], and diabetes [19], or their use as anti-rheumatic or antimicrobial agents [20,21]. Recently, the focus shifted on their beneficial anticancer properties. For instance, it is known that they are highly anti-proliferative [15,16,18,22] and vascular-disruptive [16], that they can induce apoptosis [16,22] and arrest cells in G₂/M phase of the cell cycle [16,17]. In addition, a variety of derivatives with different substitution patterns is easily accessible by a three component one-pot synthesis making drug optimization fast and efficient. In close analogy to LY290181, we prepared several new *meta*-substituted derivatives with fluoro-, cyano- and pentafluorothio-substituents we assumed to be significantly active. We also investigated analogous *para*-substituted compounds for structure activity relationships. In addition, we have investigated the 3,5-dihalo-4-

* Corresponding author.

E-mail address: Rainer.Schobert@uni-bayreuth.de (R. Schobert).

methoxyphenyl scaffold, a structural motif known from other potent natural and synthetic tubulin binders [23–25]. After studying the structure-activity relationships of these 19 derivatives of LY290181, we chose the nine most active compounds and tested them in more detail for their anti-proliferative, antiangiogenic, and vascular-disruptive properties *in vitro* and *in vivo*. In addition, their biocompatibility and vascular-disrupting activity was assessed in xenografted mice.

2. Results and discussion

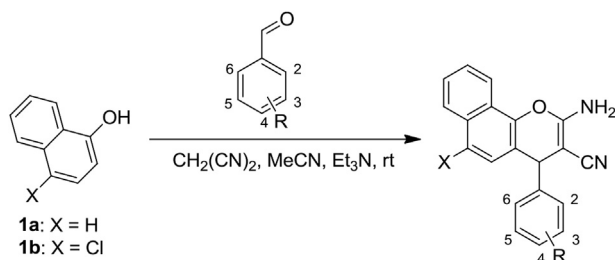
2.1. Chemistry

All naphthopyrans **2a–l** and **3a–h** were prepared via the base-catalyzed one-pot reaction of malononitrile with the corresponding substituted benzaldehyde and 1-naphthol/4-chloro-1-naphthol **1a/b** (Scheme 1). The target compounds precipitated from the reaction solution after a short time and were obtained as pure solids in moderate to high yields (Table 1). Apart from the animal studies, freshly prepared DMSO stock solutions (10 mM) were used for the biological evaluation. For the respective experiments the stock solutions were further diluted in pure water. Turbidimetric changes or precipitation were excluded spectrometrically and by microscopy. Vehicle caused effects were excluded by using controls with equal vehicle concentrations. In all experiments the DMSO concentration was less than 1%.

2.2. Antiproliferative activity

The antiproliferative activities of the test compounds were screened by MTT and SRB assays [28]. A panel of ten cancer cell lines of six entities as well as the endothelial hybrid cell line Ea.Hy926 were used to determine the IC₅₀ values after 72 h of incubation (Table 2). The whole series was tested for cytotoxicity against 518A2 melanoma and HT-29 colon carcinoma cells. In addition, all compounds were tested in the A2780/A2780cis ovarian cancer cell line model of acquired drug resistance [29]. The cell line A2780cis shows resistance to cisplatin, doxorubicin and other drugs. Furthermore, the *in vitro* resistance to doxorubicin and cisplatin is maintained *in vivo* when grown as xenograft tumors in nude mice [30,31]. Therefore, this model is well suitable to test the abilities of compounds to overcome drug resistance.

All tested compounds showed a dose dependent inhibition of 518A2 melanoma cell growth with IC₅₀ values ranging from sub-nanomolar to single-digit micromolar. Compounds with small electron withdrawing groups in *meta* position of the phenyl-ring were performing best. Increasing activities were found when going from pentafluorothio (**2h**) over nitro (**2a**), fluoro (**2b**) to cyano substitution (**2c**). Substituents in *ortho* (**3h**) and *para* (**2g**, **2i**, **2j**, **3e**, or **3f**) position of the phenyl ring were less active. In a direct comparison of test compounds bearing the same substituent either in *meta* or in *para* position (**2c** vs. **2g**, **2h** vs. **2i**, and **3c** vs. **3e**), the *meta* ones were more than 10-times more active compared to the



Scheme 1. Synthesis of the naphthopyrans **2a–l**, and **3a–h**.

Table 1

Substituents X and R of the naphthopyrans **2a–l**, and **3a–h** and the yield of the three-component-one-pot syntheses.

compound	X:	R:	yield (%)
2a	-H	3-NO ₂	[15]
2b	-H	3-F; 5-F	45
2c	-H	3-CN	62
2d	-H	3-Cl; 4-OMe; 5-Cl	50
2e	-H	3-Br; 4-OMe; 5-Br	71
2f	-H	3-I; 4-OMe; 5-I	83
2g	-H	4-CN	[26]
2h	-H	3-SF ₅	15
2i	-H	4-SF ₅	48
2j	-H	4-SMe	48
2k	-H	3-OMe; 4-OBn	60
2l	-H	3-F; 4-Cl	[21]
3a	-Cl	3-NO ₂	63
3b	-Cl	3-F; 5-F	53
3c	-Cl	3-CN	61
3d	-Cl	3-Br; 4-OMe; 5-Br	50
3e	-Cl	4-CN	73
3f	-Cl	4-SMe	49
3g	-Cl	3-Br	63
3h	-Cl	2-Cl	[27]

para ones. Bulky substituents such as pentafluorothio (**2h–i**) or benzyloxy (**2k**) led to drastically reduced cytotoxicities. **2l** which was first synthesized by Smith et al. and investigated for its anti-rheumatic activity represents a special case [21]. With the fluoro substituent in *meta* and chloro in *para* position of the phenyl ring it showed moderate activity against 518A2 cells when compared to the other test compounds but was among the most active ones when applied to HT-29 and A2780/A2780cis. On average, the introduction of a chloro substituent at the naphthyl moiety (**3a–h**) attenuated the antiproliferative activity of naphthopyrans when compared to their parent substances **2**. Independent of their absolute activities the compounds were comparably active in the A2780/A2780cis model indicating their potential to generally overcome resistance of tumors against conventional anticancer drugs.

Nine compounds were selected for further investigation, namely the mono-*meta* substituted **2a** and **2c**, the *m,m*-difluoro substituted **2b** and their chloro substituted congeners **3a–c**. We also chose the naphthopyrans **2d–f** with a *m,m*-dihalide, *p*-methoxy substitution pattern which is frequently found in good tubulin binders. All of the chosen compounds showed dose dependent inhibition curves for all cell lines of the panel with IC₅₀ values in the nanomolar and sub-nanomolar range. On average, HT-29 and HCT-116 colon carcinoma cells were least susceptible, and Panc-1 pancreatic carcinoma and the multi-drug resistant KB-V1^{Vbl} cervix and MCF-7^{Topo} mamma carcinoma cells were most sensitive to the compounds. Overall, the chloro-substituted derivatives **3a–c** were slightly less cytotoxic against the whole panel. Only **3b** (518A2 and HT-29) and **3c** (HT-29) get out of line showing more antiproliferative activity at the indicated cell lines when compared to their congeners **2b** and **2c**, respectively. Compound **2c** stands out with single-digit nanomolar IC₅₀ values against Ea.Hy926 endothelial hybrid and DLD-1 colon carcinoma cells and an even sub-nanomolar IC₅₀ value against MCF-7^{Topo} mamma carcinoma cells. For 518A2 melanoma, Panc-1 pancreatic carcinoma and KB-V1^{Vbl} cervix carcinoma cells, no IC₅₀ values could be determined in our customarily used concentration range (100 μM–0.1 nM). Only the HT-29 and HCT-116 colon carcinoma cells tolerated **2c** to an extent of double- and triple-digit nanomolar IC₅₀ values, respectively. Besides **2c**, the *m,m*-dihalide, *p*-methoxy substituted naphthopyrans **2e** and **2f** were the most active test compounds. Low double-digit nanomolar IC₅₀ values against the endothelial hybrid cell

Table 2
Inhibitory concentrations IC₅₀ (nM, 72 h) of the test compounds (**2a–l**, **3a–h**) when applied to human cancer cell lines and to Ea.Hy926 endothelial hybrid cells.^a

	Cell lines									
	518A2	HT-29	A2780 ^b	A2780cis ^b	DLD-1	Ea.Hy926	Panc-1	HCT-116	KB-V1 ^{Vbl}	MCF-7 ^{Topo}
2a	35.9 ± 0.8	46.9 ± 3.2	18.7 ± 2.9	26.0 ± 8.9	33.7 ± 1.5	35.6 ± 2.7	12.5 ± 3.2	44.3 ± 4.3	22.6 ± 3.3	11.8 ± 1.4
2b	26.4 ± 0.6	176 ± 19	17.0 ± 2.2	20.3 ± 4.8	32.3 ± 3.5	31.5 ± 1.5	19.5 ± 6.1	47.0 ± 1.9	25.8 ± 4.3	20.1 ± 0.6
2c	<0.1	110 ± 4	14.8 ± 1.3 ^c	17.9 ± 0.1 ^c	2.6 ± 0.6	4.3 ± 1.0	<0.1	30.1 ± 0.6	<0.1	0.41 ± 0.04
2d	44.6 ± 2.7	103 ± 9	16.7 ± 2.9	19.2 ± 1.9	59.0 ± 3.5	32.6 ± 3.8	27.9 ± 5.6	69.2 ± 9.4	30.2 ± 1.2	29.9 ± 1.4
2e	24.4 ± 1.9	52.1 ± 3.8	12.1 ± 3.4	15.8 ± 1.5	39.5 ± 2.4	15.9 ± 0.8	14.7 ± 0.4	19.1 ± 1.4	33.4 ± 4.2	24.8 ± 2.4
2f	37.1 ± 0.3	45.2 ± 2.3	16.4 ± 1.3	18.2 ± 1.8	15.0 ± 1.4	17.9 ± 2.3	13.1 ± 0.3	29.5 ± 4.1	16.5 ± 1.2	22.8 ± 2.8
2g	939 ± 122	1227 ± 117	759 ± 163	774 ± 210	–	–	–	–	–	–
2h	505 ± 38	570 ± 41	188 ± 17	265 ± 79	–	–	–	–	–	–
2i	7130 ± 900	9970 ± 410	5164 ± 895	5578 ± 498	–	–	–	–	–	–
2j	1980 ± 180	1102 ± 72	363 ± 96 ^c	430 ± 48 ^c	–	–	–	–	–	–
2k	1660 ± 430	5820 ± 570	2150 ± 175	2337 ± 03	–	–	–	–	–	–
2l	425 ± 62	172 ± 18	48.5 ± 11.7	57.3 ± 10.9	–	–	–	–	–	–
3a	225 ± 24	209 ± 16	61.1 ± 11.6	46.0 ± 26.6	22.3 ± 1.9	90.8 ± 4.5	65.9 ± 5.4	112 ± 16	73.3 ± 4.8	88.5 ± 7.7
3b	24.1 ± 1.6	102 ± 7	104 ± 43	155 ± 11	98.4 ± 2.2	67.8 ± 3.4	92.7 ± 3.0	91.0 ± 18.3	92.0 ± 7.0	79.8 ± 3.4
3c	60.5 ± 5.1	67.3 ± 6.6	49.9 ± 2.1	56.7 ± 3.5	69.4 ± 7.1	78.6 ± 7.3	54.9 ± 2.6	73.5 ± 0.8	55.9 ± 3.2	58.1 ± 9.1
3d	144 ± 9	188 ± 9	160 ± 19	168 ± 12	–	–	–	–	–	–
3e	753 ± 55	1590 ± 80	1439 ± 298	1412 ± 223	–	–	–	–	–	–
3f	1350 ± 50	1540 ± 110	1066 ± 186	1294 ± 190	–	–	–	–	–	–
3g	229 ± 20	245 ± 8	155 ± 1	166 ± 9	–	–	–	–	–	–
3h	9910 ± 1680	2030 ± 200	912 ± 300	973 ± 347	–	–	–	–	–	–

^a Human cancer cell lines: HT-29, HCT-116 and DLD-1 colon carcinoma, 518A2 melanoma, Panc-1 pancreatic ductular adenocarcinoma, KB-V1^{Vbl} cervix carcinoma, MCF-7^{Topo} breast adenocarcinoma, A2780, A2780cis ovarian cancer cells. Values are the means ± SD determined in four independent experiments and derived from dose-response (percentage of viable cells relative to untreated controls) after 72 h of incubation using the MTT assay.

^b Values are the means ± SD determined in three independent experiments and derived from dose-response curves after 72 h of incubation using the SRB-assay.

^c Values are the means ± SD determined in two independent experiments.

line Ea.Hy926 suggested that these naphthopyrans might act as vascular-disrupting agents.

2.3. Antiangiogenic activity

The antiangiogenic effects of the test compounds were assessed *in vitro* by using tube formation assays, which are based on the ability of endothelial cells to form tubular and cord-like networks on matrigel [32,33]. In contrast to the complex tube-like networks of the control, the cells co-incubated with the test compounds did not organize in such a manner (Fig. 1). Cells treated with LY290181 (**2a**) and **2b** formed rudimentary cords but did not fuse together as tubes, whereas the cells incubated with **2c** and **2e** were only spread in small stray colonies all over the wells in a way similar to the ones treated with the known MDA and anti-angiogenic agent

combretastatin A-4 (C-A4). To exclude that the effects were due to the test compounds' cytotoxicity, we determined the vitality by MTT assays to be higher than 68% compared to untreated controls.

2.4. Effects on the cell cycle and apoptosis induction

The influence of the test compounds on the cell cycle progression was first determined in 518A2 melanoma cells by flow cytometry (*data not shown*). Since the test compounds only caused a drastic increase of apoptotic cells (sub-G1) without affecting the cell cycle, their effect on the cell cycle was additionally determined in HT-29 colon carcinoma cells, which are known to be less sensitive to VDAs [34,35]. In these cells, the test compounds **2a–b**, **2e**, **3a–c** caused a dose-dependent (100, 250, and 350 nM) increase of the cells in G2/M (*cf. Supporting Information*). Again, **2c** is an exception

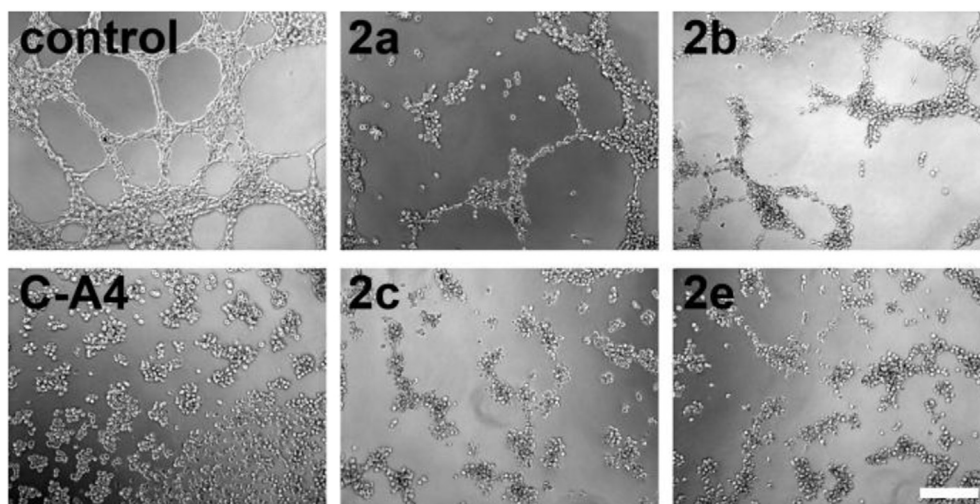


Fig. 1. Inhibitory effect of the known C-A4, naphthopyran derivatives **2a–c** or **2e** on the spontaneous tube formation of Ea.Hy926 endothelial cells. Ea.Hy926 cells were grown on thin matrigel layers for 24 h in the presence of vehicle (DMSO) or 100 nM of the test compounds. Scale bar: 100 μm; images shown are representative of two independent experiments. The vitality of treated cells was determined to be >68% with respect to untreated control cells (MTT assay).

for showing no significant accumulation of HT-29 cells in G2/M phase which might be the cause of its general toxicity. At 350 nM (Fig. 2) the proportion of cells in G2/M was distinctly higher in cells treated with the chloro substituted naphthopyrans **3a-c** (**3a**: $73.5\% \pm 5.2$, **3b**: $90.3\% \pm 2.4$, **3c**: $51.6\% \pm 11.2$) compared to that incubated with their unchlorinated congeners **2a-c** (**2a**: $23.9\% \pm 1.8$, **2b**: $43.5\% \pm 4.3$, **2c**: $13.3\% \pm 1.5$). In vehicle treated cells just about 11.4% were in G2/M. While the incubation with **2e** arrested about 65% of the cells in G2/M without a distinct increase of cells in the sub-G1 region, **2l** led to a less pronounced G2/M arrest ($34.0\% \pm 3.7$) but a higher proportion of events in the sub-G1 region ($27.0\% \pm 5.0$). A slight to moderate increase of apoptotic HT-29 cells in the sub-G1 region was also observed for the other test compounds.

By using the TUNEL technique, we confirmed that the drastic increase of 518A2 cells in the sub-G1 region was indeed due to apoptosis induction which in part is initiated by caspase-9 activation (cf. Supporting Information). Compared with **2a** ($61.4\% \pm 12.7$), **2b** ($67.5\% \pm 2.5$), and **2c** ($69.4\% \pm 2.5$), the apoptosis induction caused by **2e** ($46.5\% \pm 2.1$) was less pronounced.

2.5. Effects on the cytoskeletal organization in 518A2 melanoma cells

The increasing proportions of cells in G2/M are indicative of their inability to divide. Since naphthopyrans are known for their tubulin affinity, the microtubule cytoskeleton might be disrupted so that the microtubule spindle apparatus, which is essential for cell division, could not be formed [36]. Hence, the test compounds' influence on the microtubule and on the actin cytoskeleton was studied by immunofluorescence staining of 518A2 melanoma cells (Fig. 3, and Fig. 4). The exposure for 3 h to 100 nM of the naphthopyrans caused a complete disruption of the highly organized microtubule filaments and the even distribution of the stained tubulin throughout the whole cell body. On average, the size of the treated cells was increased and the cell membrane had begun to bleb. This blebbing is likely an indication for an early stage apoptosis [37]. Since it is known that **2a** interrupts the tubulin dynamics by directly binding to it [17], we studied the molecular interactions of compounds **2a-b**, **2e**, and **2l** with purified tubulin in a tubulin polymerization assay. For comparison, we also tested the known MDA C-A4. **2l** was tested in a brief assay using 10 μM , which revealed that it inhibited the polymerization to $44.1\% \pm 10.2$ when compared with vehicle treated controls. For the known

microtubule-disrupting agent C-A4 as well as for **2a-b** and **2e** the ITP₅₀, the concentration causing 50% tubulin inhibition, was determined. Like C-A4 whose ITP₅₀ value was $4.1 \pm 0.1 \mu\text{M}$, **2a** and **2b** also had single-digit micromolar ITP₅₀ values (**2a**: $7.1 \pm 1.5 \mu\text{M}$, **2b**: $9.6 \pm 0.2 \mu\text{M}$). **2e** was slightly weaker with an ITP₅₀ value of $13.0 \pm 1.0 \mu\text{M}$.

In addition to the drastic changes of the tubulin dynamics, the treatment of 518A2 cells with naphthopyrans **2a-c** and **2e** modified the filamentous actin (F-actin; Fig. 4). Untreated control cells showed the characteristic cortical microfilaments and only few thin fibers traversing the cells. In contrast to the controls, treated cells formed thick stress fibers. Stress fiber formation as cause of MDA treatment is indicative of the immobilization of cancer cells and a consequently reduced migration and metastasis [38]. Therefore, we also determined the motility of cancer cells treated with the test compounds by wound healing assays. We found, that the migration of treated 518A2 melanoma cells in the artificial wound was significantly reduced when compared to that of untreated control cells (cf. Supporting Information).

2.6. Vascular-disruptive activity

The vascular-disruptive effects of the naphthopyrans **2a-c**, **2e** and **3a-c** as well as that of the known VDA C-A4 were assessed *in ovo* by using the chorioallantoic membrane (CAM) assay (**2a-c**, **2e**; Fig. 5; C-A4, **3a-c**; cf. Supporting Information) [39]. The test compounds were applied topically into a small ring of silicon foil atop the CAM, and the changes of the membrane and its extraembryonal blood vessels were monitored for 24 h. The naphthopyrans **2a-c**, and **3a-c** induced very similar effects, causing disruption especially of the smaller blood vessels 6 h past application (hpa). Moreover, hemorrhages were observed. However, the main blood vessels seemed to remain intact. Interestingly, 24 hpa the CAM had regenerated and no hemorrhages were observed anymore. Nevertheless, the diameter of the main blood vessels was significantly reduced. In contrast, C-A4 disrupted also bigger blood vessels 6 hpa and the hemorrhages and corrosion 24 hpa were even more severe. **2e** stands in marked contrast causing no hemorrhages 6 hpa whereas the membrane as a whole appeared irritated and the size of the main blood vessels was reduced. 6 hpa the treated region of the CAM began to contract. After 24 h the contraction and the irritation were even more pronounced, probably due to the general toxicity of **2e**. Fractal analyses of the area covered by blood vessels allowed the quantification of the vascular disruptive effects of the

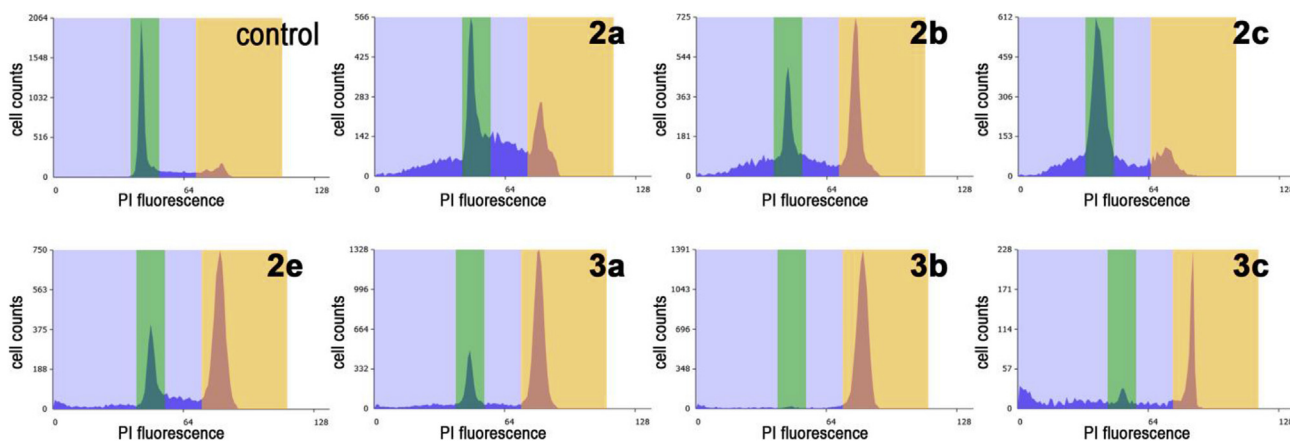


Fig. 2. Effects of 350 nM of the test compounds **2a-c**, **2e**, and **3a-c** on the cell cycle of HT-29 colon carcinoma cells after 24 h exposure. Typical cell cycle profiles and percentage of treated cells in G1 (green bar), S (right blue bar) and G2/M (orange bar) phase of the cell cycle progression as well as proportion of apoptotic cells (sub-G1; left blue bar) as obtained by flow cytometry after DNA staining with propidium iodide (PI). Control: DMSO. (For interpretation of the references to color in this figure legend, the reader is referred to the Web version of this article.)

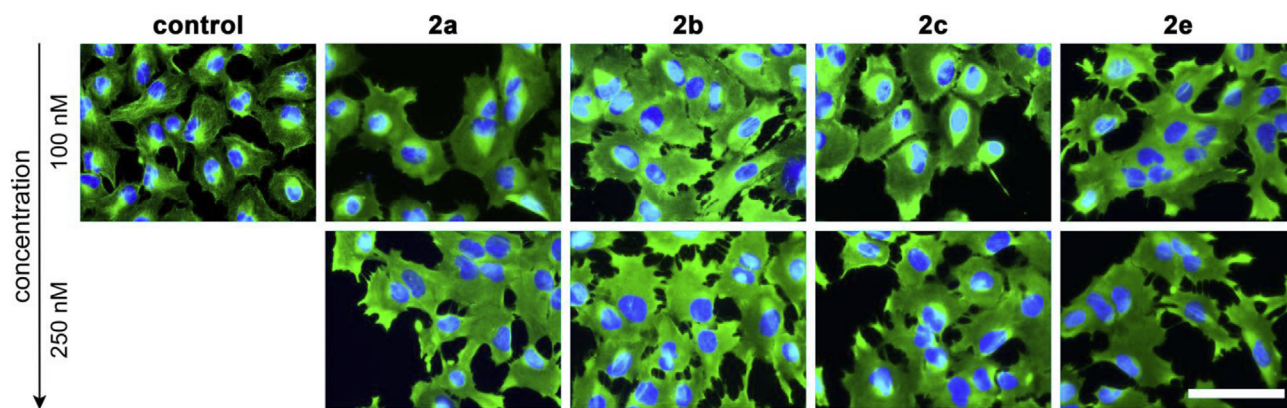


Fig. 3. Effect of **2a-c** and **2e** on the organization of microtubules (green) in 518A2 melanoma cells after 3 h of incubation. Nuclei (blue) were counterstained with DAPI. Scale bar: 50 μ m; the pictures are representative of two independent experiments. (For interpretation of the references to color in this figure legend, the reader is referred to the Web version of this article.)

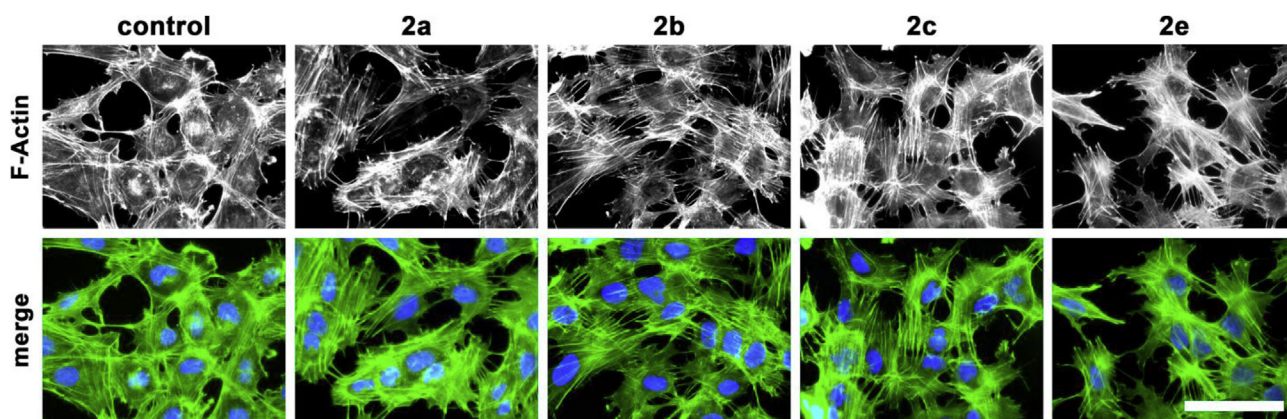


Fig. 4. Effects of **2a-c** and **2e** (100 nM, 3 h) on the organization of the actin cytoskeleton in 518A2 melanoma cells. Fluorescence labeling of filamentous actin (F-actin, green). Nuclei counterstained with DAPI (blue). Scale bar: 50 μ m; pictures are representative of two independent experiments. (For interpretation of the references to color in this figure legend, the reader is referred to the Web version of this article.)

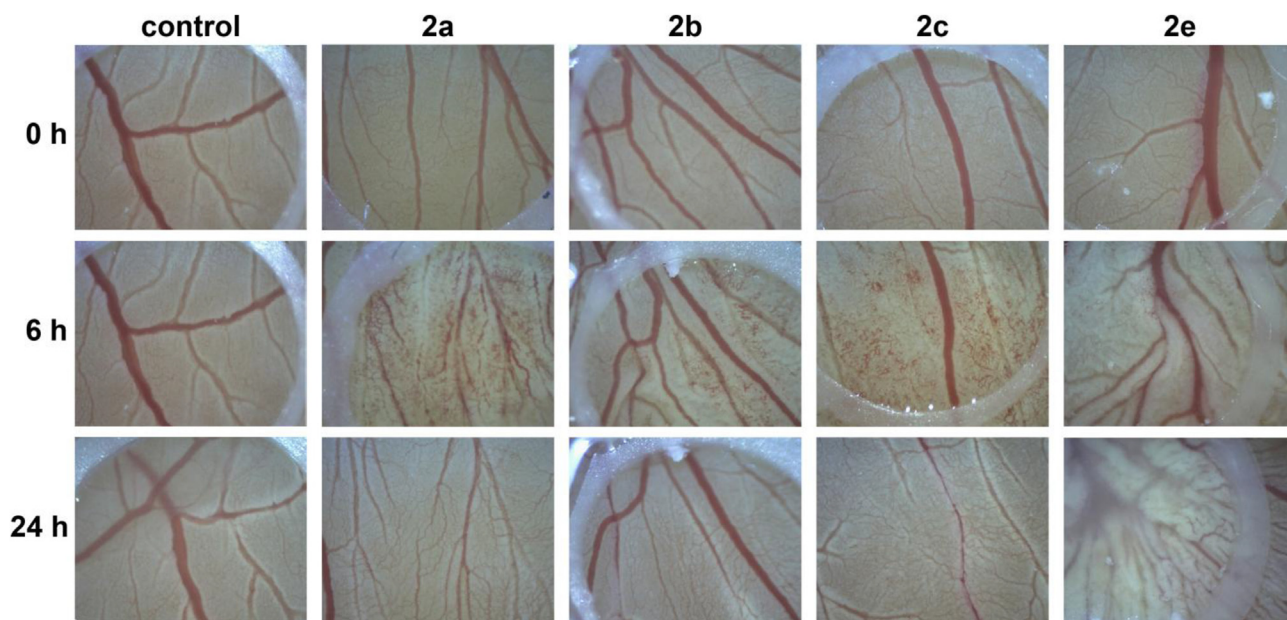


Fig. 5. Effects of the compounds **2a** (10 nmol), **2b-c** (5 nmol), or **2e** (5 nmol) on the blood vessels of the chorioallantoic membrane in fertilized eggs inside a ring of silicon foil (5 mm diameter) after 0, 6 and 24 h; control: DMSO. Images are representative of at least three independent assays (60-fold magnification). (For interpretation of the references to color in this figure legend, the reader is referred to the Web version of this article.)

test compounds *in ovo* after 6 hpa (C-A4, **2a-c**, **2e**: Fig. 6; **3a-c**: cf. Supporting Information) [40,41]. Even though the effect of **2a-c** and **3a-c** seemed to be quite similar at first glance, the detailed analyses revealed that the effects on the blood vessels differed considerably between the derivatives. The greatest blood vessel area reduction after 6 h was caused by **2a** with 32% area covered by blood vessels remaining which is quite similar to that effected by C-A4. The effects of the further unchlorinated naphthopyrans **2b-c** and **2e** were slightly weaker compared to **2a** as the treatment reduced the blood vessel area just to 59%, 56%, and 45%, respectively. The chloro-substituted naphthopyrans **3a-c** were even less vascular-disruptive lowering the area covered by blood vessels only to 74% (**3a**) or leaving the area rather unaltered (**3b-c**) compared to that at 0 hpa (cf. Supporting Information). Quite similar gradations were observed in vessel length analyses where C-A4 and **2a** performed best followed by **2b-c** and **2e** whereas **3a-c** had the least impact on the vessel length (cf. Supporting Information). However, concerning reductions of the diameter of the vessels, C-A4, **2a-c** and **2e** were similarly efficient whereas **3a-c** had hardly any effect (cf. Supporting Information).

2.7. Mouse xenograft model

Finally, the biocompatibility and the vascular-disruptive effects of the test compounds were investigated in nude mice bearing A2780 human ovarian carcinoma xenografts. **2d** and **2f** were excluded due to their poor solubility in tween80/ethanol (1:1). **2a** and **2c** were injected as single doses up to a concentration of 200 mg/kg without showing significant effects on vascularization, i.e. no signs of tumor discoloration were observed. A dose of 30 mg/kg of **2e** was sufficient to induce tumor discoloration indicating vascular disrupting activity. However, this was associated with noticeable toxicity. Compound **2b** induced tumor discoloration at a dose of 100 mg/kg, and was also better tolerated than **2e**. As shown in Fig. 7 A, **2b** caused a strong discoloration of the xenografted tumor due to substantial hemorrhage. This finding was confirmed by a histological examination of the treated tumor, which revealed hemorrhages and extensive necrosis at the tumor core surrounded by a rim of surviving tumor cells, features that are typical of treatment with VDAs (Fig. 7 B). Due to its favorable characteristics, **2b** was chosen to finally prove anticancer activity in a therapy trial with mice bearing cisplatin-resistant A2780cis xenograft tumors. Overall, the tumor growth of A2780cis xenografts was significantly reduced compared to controls (Fig. 8).

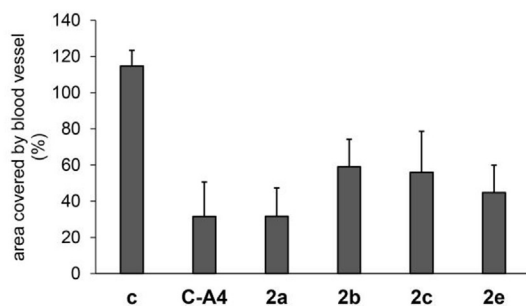


Fig. 6. Vessel area analysis (derived from fractal analysis) after 6 h incubation with C-A4 (2.5 nmol), **2a** (10 nmol), **2b-c** (5 nmol), **2e** (5 nmol) or vehicle (DMSO; c). The area in the image sections covered by blood vessels before treatment with the test compounds (0 h) was set to 100%. Values are the means \pm SD of three vessel area analysis calculations except for C-A4 which was only analyzed from two experiments.

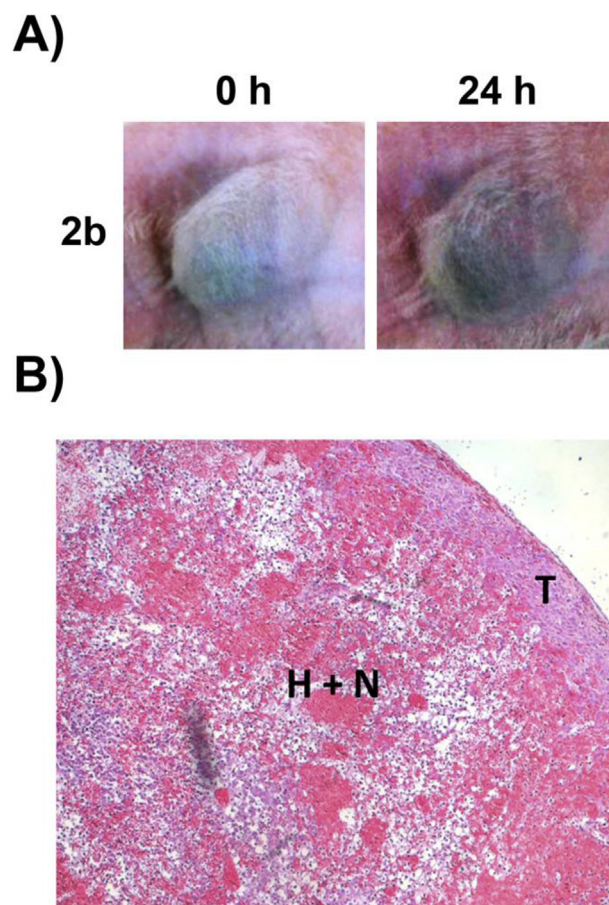


Fig. 7. A) Discoloration of A2780 xenograft tumors due to intratumoral hemorrhage caused by the treatment with **2b**. B) Lateral section of an A2780 tumor xenograft after HE staining, featuring a large necrotic area (N) and hemorrhages (H) surrounded by a cortical layer of vital tumor cells (T).

3. Conclusions

In summary, SAR studies revealed that 2-amino-4-phenyl-4H-naphtho(1,2-b)pyran-3-carbonitrile derivatives with small substituents in *meta* position of the phenyl ring were most cytotoxic. Sterically more demanding substituents such as benzyl or SF₅

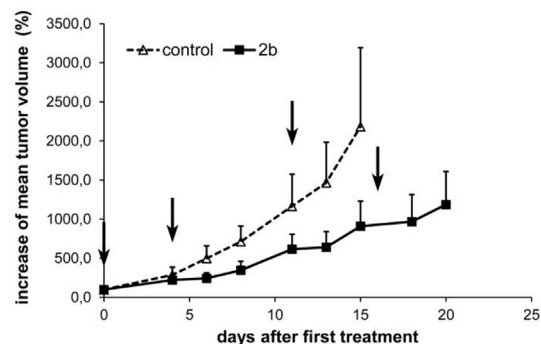


Fig. 8. Antitumor activity of **2b** in A2780cis xenograft tumors. Shown is the increase of mean tumor volume (%) of each group ($n = 5$) \pm standard deviation normalized to day 0 (start of treatment). Mice were treated with 60 mg/kg body weight of **2b** by i.p. injections on days 0, 4, 11, and 16, indicated by arrows. Control group received vehicle. The treatment and monitoring of the control group was discontinued on day 15 when four mice had tumors exceeding 2500 mm³ volume. On day 20, two tumors of the treatment group had exceeded 2500 mm³.

probably obstruct the naphthopyran–tubulin approaching. Moreover, *ortho* and *para* substituents as well as a chloro substituent at the naphthyl fragment proved detrimental.

The cytoskeletal reorganization, if not causative, at least contributes to the high antiproliferative activity of the naphthopyrans. By binding to tubulin they inhibit its polymerization and so lead to a disruption of the microtubule cytoskeleton. The observed effects by the test compounds on a cellular level as well as *in vivo* can be attributed to this tubulin binding. Besides the reorganization of the microtubule cytoskeleton, the naphthopyrans also induced drastic alterations of the filamentous actin. Stress fiber formation and inhibition of the cell migration are hallmarks of their significant antimetastatic potential.

The cytoskeletal reorganization weakened the vasculature *in vivo* and caused the disruption of blood vessels and hemorrhages. Interestingly, we observed that upon treatment with **2a-c** the vasculature of the CAM regenerated within 24 h. This rare effect might be exploited to “normalize” the blood vessels in a tumor by first abrogating the irregular ones. Then, the antiangiogenic activity might be used to allow normal or at least less leaky blood vessels to sprout [42–44]. A normalized tumor vasculature would facilitate drug delivery into the tumor enabling a more efficient chemotherapy.

4. Experimental

4.1. Chemistry

All starting compounds were purchased from Aldrich. Compounds **2a**, **2g**, **2l** and **3h** were prepared as previously described [15,21,26,27]. The following instruments were used: melting points (uncorrected), Gallenkamp; IR spectra, Perkin-Elmer Spectrum One FT-IR spectrophotometer with ATR sampling unit; nuclear magnetic resonance spectra, BRUKER Avance 300 spectrometer; chemical shifts are given in parts per million (δ) downfield from tetramethylsilane as internal standard; mass spectra, Varian MAT 311A (EI), UPLC/Orbitrap (ESI); microanalyses, Perkin-Elmer 2400 CHN elemental analyzer. All tested compounds are >95% pure by elemental analysis.

4.1.1. 2-Amino-4-(3,5-difluorophenyl)-4H-benzo[h]chromene-3-carbonitrile (**2b**) – Typical procedure

3,5-Difluorobenzaldehyde (142 mg, 1.0 mmol) and malononitrile (70 mg, 1.0 mmol) were dissolved in MeCN (3 mL) and three drops of Et₃N were added. The reaction mixture was stirred at room temperature for 30 min. 1-Naphthol (144 mg, 1.0 mmol) was added and the reaction mixture was stirred at room temperature for 16 h. The formed precipitate was collected, washed with MeCN/H₂O (1:1) and *n*-hexane and dried in vacuum. Yield: 149 mg (0.45 mmol, 45%); colorless solid of m.p. 201 °C; $\nu_{\max}(\text{ATR})/\text{cm}^{-1}$ 3456, 3406, 3335, 3281, 3256, 3204, 3058, 2190, 1664, 1621, 1597, 1573, 1505, 1458, 1407, 1374, 1349, 1309, 1286, 1263, 1223, 1190, 1150, 1115, 1104, 1042, 1023, 989, 945, 890, 865, 842, 812, 785, 767, 755, 696, 688; ¹H NMR (300 MHz, CDCl₃) δ 4.84 (3 H, s), 6.68 (1 H, t, J_{H-F} = 8.8 Hz, 2.3 Hz), 6.7–6.8 (2 H, m), 6.98 (1 H, d, J = 8.6 Hz), 7.5–7.6 (3 H, m), 7.7–7.8 (1 H, m), 8.1–8.2 (1 H, m); ¹³C NMR (75.5 MHz, CDCl₃) δ 41.3, 60.3, 103.0 (t, J_{C-F} = 25.4 Hz), 111.0 (d, J_{C-F} = 25.4 Hz), 115.9, 119.2, 120.8, 123.2, 125.0, 125.6, 126.9, 127.1, 127.8, 133.5, 143.3, 148.3 (t, J_{C-F} = 7.9 Hz), 159.3, 163.2 (dd, J_{C-F} = 250 Hz, 12.5 Hz); *m/z* (%) (EI) 334 (52) [M⁺], 221 (100); *m/z* (%) (HRMS, ESI) 335.09802 [M⁺ + H] (100).

4.2. Biological evaluation

4.2.1. Tube formation assay

Ea.Hy926 cells (5 × 10⁵ cells/mL, 100 μ L/well) were seeded on thin layers of matrigel (Corning) in 96 well plates in Endothelial Cell Growth Medium 2 (PromoCell GmbH) and immediately treated with vehicle (DMSO), with 100 nM of C-A4, **2a-c**, and **2e**. The ability or inability to form tubular networks was documented after 24 h by light microscopy (Zeiss Axiovert 135, 100 × magnification). Experiments were done in duplicate. The cell vitality was determined by MTT-assay to be higher than 68% compared with the controls set to 100%.

4.2.2. Chorioallantoic membrane (CAM) assay in fertilized chicken eggs [37].

Fertilized white leghorn chicken eggs (SPF eggs, VALO Bio-media) were incubated (37 °C, 50–60% humidity) until day 5 past fertilization. Then, windows of 2–3 cm diameter were cut in the more rounded pole of the eggshell and then sealed with tape followed by 24 h incubation. Rings of silicon foil (5 mm diameter) were placed onto the CAM and C-A4 (2.5 nmol, 10 μ L of a 0.25 mM dilution), **2b-c**, **2e** (all 5 nmol, 10 μ L of a 0.5 mM dilution), **2a**, **3a-c** (all 10 nmol, 10 μ L of a 1.0 mM dilution), or vehicle (DMSO) were pipetted inside the silicon ring. The alterations in the blood vessel organization were documented 0, 6, and 24 h post application using a light microscope (60-fold magnification, Traveller). The test compounds were applied onto the CAM of at least three eggs. The quantitative evaluation was performed on image sections taken from the light microscope pictures and the area covered by blood vessels was determined by fractal analysis using the following software: ImageJ 1.51a (FracLac_2015Jul plugin) and Fractal Analysis System 3.4.7 [37,45–51]. The blood vessel area before treatment was set to 100% and the increase/decrease in this area after 6 h of treatment with the test compounds **2a-c**, **2e** or control (DMSO) was determined.

4.2.3. Cell cycle analyses

HT-29 cells (3 mL/well, 1 × 10⁵ cells/mL) were seeded in 6-well plates and allowed to attach for 24 h. The cells were treated with 100, 250, and 350 nM of the test compounds (**2a-c**, **2e**, **2l** or **3a-c**) for another 24 h. Then, the cells were detached by trypsinization, pelleted by centrifugation (300 × g, 5 min, 4 °C) and fixed in 1 mL 70% EtOH for at least 24 h. After removing the EtOH, the cells were washed with 1 mL PBS and stained with 300 μ L PI-staining solution (50 μ g/mL propidium iodide, 50 μ g/mL RNase A, 1% sodium citrate in PBS) for 30 min at 37 °C. Then, the cell solution was filtered and the fluorescence intensity of 10,000 single cells was analyzed at $\lambda_{\text{em}} = 570$ nm ($\lambda_{\text{ex}} = 488$ nm laser source) by using a flow cytometer (BioRad). The percentages of cells in the different phases of the cell cycle progression (G1, S, and G2/M) was determined using the ProSort software (Bio-Rad Laboratories). The proportion of apoptotic cells was calculated from sub-G1 peaks. Results are the mean \pm SD of at least three independent experiments.

4.2.4. Immunofluorescence staining of microtubules

518A2 melanoma cells (0.5 mL/well, 1 × 10⁵ cells/well) were grown on glass cover slips in 24-well plates. Then, the cells were treated with 100, or 250 nM of the test compounds (**2a-c**, or **2e**), or vehicle (DMSO) for 3 h. After removal of the cell medium, the cells were washed with 1 mL PBS and fixed with 1 mL of a 3.7% formaldehyde solution in PBS for 20 min. Then, the cells were washed three times with 1 mL PBS and followed by the permeabilization and blocking with a 1% BSA, 0.1% triton-X 100 solution in PBS for 30 min. The tubulin cytoskeleton was treated with a primary antibody against α -tubulin (anti- α -tubulin, mouse monoclonal

antibody) for 2 h at 37 °C. After washing the cells three times with 1 mL PBS, the secondary antibody conjugated to AlexaFluor®-488 (goat anti-mouse IgG-AlexaFluor®-488, Cell Signaling Technology) was applied for 1 h at room temperature in the dark. After mounting the glass coverslips in 4-88-based mounting medium containing 2.5% DABCO and 1 µg/mL DAPI for counterstaining the nuclei, the effects on the microtubule cytoskeleton were documented by fluorescence microscopy (Zeiss Imager A1 AX10, 400 × magnification).

4.2.5. Immunofluorescence staining of F-actin

Staining of F-actin was performed with the commercially available Acti-stain™ 488 Fluorescent Phalloidin (Cytoskeleton) and according to manufacturer's instructions. Briefly, 518A2 melanoma cells (0.5 mL/well, 1×10^5 cells/well) were seeded on glass cover slips in 24-well plates and incubated for 24 h at 37 °C. Then, the cells were treated with 100 nM of the test compounds (**2a-c**, or **2e**) for 3 h at 37 °C followed by the removal of the medium. After washing the cells with pre-warmed PBS at 37 °C, the cells were fixed with 3.7% formaldehyde solution in PBS (pH 7.0) for 10 min at room temperature. Then, the cells were washed again with PBS and permeabilized with 0.5% triton X-100 in PBS for 5 min at room temperature. After another washing step with PBS, the cells were stained with Acti-stain™ 488 phalloidin (100 nM in PBS) for 20 min at room temperature in the dark. Then, the cells were washed three times with PBS and the coverslips were mounted in 4-88-based mounting medium containing 2.5% DABCO and 1 µg/mL DAPI for counterstaining the nuclei. Effects on the actin filaments were documented by fluorescence microscopy (Zeiss Imager A1 AX10, 400 × magnification).

4.2.6. TUNEL assay

DNA fragmentation of apoptotic cells was studied by using the TUNEL technique (Terminal deoxyribonucleotide transferase-mediated dUTP nick end labelling). The assay was performed with the commercially available *In Situ* Cell Death Detection Kit, Fluorescein (Roche) and according to manufacturer's instructions. Briefly, 518A2 melanoma cells (3 mL/well, 1.0×10^5 cells/mL) were grown in 6-well plates and treated with 100 nM of **2a-c**, or **2e** for 24 h. The cell medium and the treated cells, which were detached by trypsination, were collected and pelleted by centrifugation (300 × g, 5 min, 4 °C). Then, the supernatant was withdrawn, the cells washed twice with 1 mL PBS and fixed in 2% formaldehyde in PBS at room temperature for 60 min. After washing the cells once with PBS, they were permeabilized with 0.1% triton X-100 and 0.1% sodium citrate in PBS for 2 min at 0 °C. Then, the cells were washed again twice with PBS and labelled with TdT-labelling solution containing the TdT enzyme and the fluorescein-coupled dUTPs at 37 °C for 1 h. After two more washing steps, the fluorescence intensity of the labelled cells was determined by using a Beckmann Coulter Cytomics FC500 flow cytometer. Data were analyzed with the CXP software (Beckmann Coulter). Gates defining the percentage of vital and apoptotic cells were applied with respect to controls. Results are the mean ± SD of two independent experiments.

4.2.7. Animal studies

The investigations of this study were approved by the Laboratory Animal Care Committee of Sachsen-Anhalt, Germany. Xenograft tumors were generated in athymic nude mice (Charles River, Germany) using the ovarian carcinoma cell lines A2780 and A2780cis. 8.0×10^6 cells of either cell line were resuspended in PBS and injected subcutaneously into the flank of mice. Both cell lines form highly vascularized xenograft tumors in nude mice and the A2780cis is resistant to various anticancer drugs.

For preparation of solutions for injection, compounds were dissolved in tween80/ethanol (1:1) to further dilute it 1:5 in normal saline. To test the *in vivo* applicability of selected compounds, mice bearing A2780 xenograft tumors (n = 2) were injected with increasing doses (10, 20, 30, 50, 100, 150 and 200 mg/kg body weight) on every other day and body weight and behavior as well as tumor discoloration were controlled daily to analyze toxicity and vascular disrupting effects. The resulting tumor discoloration was documented after 24 h with a Canon IXUS 50. For histological examinations, the tumors were explanted, fixed in 5% formalin, and embedded in paraffin. Hematoxylin/eosin (HE) staining of the tissue slices was performed according to standard protocols. HE images were analyzed by microscopy (Axio Lab, Zeiss).

The antitumor activity of **2b** was analyzed in nude mice bearing xenograft tumors grown from resistant A2780cis cells. After establishment of tumors the mice were divided in two groups (n = 5) with similar mean tumor volumes at the start of treatment. The mice received i.p. applications of 60 mg/kg body weight on days 0, 4, 11, and 16. The control group received vehicle. The tumor volumes were calculated by caliper measurement using the formula $a^2 \times b \times 0.5$ with *a* being the short and *b* the long dimension.

Abbreviations

C-A4	combretastatin A-4
CAM	chorioallantoic membrane
DAPI	4',6-diamidino-2-phenylindole
DMSO	dimethyl sulfoxide
HE	hematoxylin and eosin
Hpa	hours past application
MDA	microtubule destabilizing agent
MTT	3-(4,5-dimethylthiazol-2-yl)-2,5-diphenyltetrazolium bromide
SAR	structure-activity relationship
TUNEL	Terminal deoxyribonucleotide transferase-mediated dUTP nick end labelling
VDA	vascular-disrupting agents

Appendix A. Supplementary data

Chemical syntheses, cell culture conditions, MTT assay, SRB assay, wound healing assay, tubulin polymerization assay, caspase-9 activity assay, additional results from wound healing assays, cell cycle analyses, caspase-9 activity assay, tubulin polymerization assay, CAM assay and CAM vessel analyses, ¹H and ¹³C NMR spectra of the test compounds doi:xxxx.

Supplementary data to this article can be found online at <https://doi.org/10.1016/j.ejmech.2018.11.055>.

References

- [1] P.E. Thorpe, Vascular targeting agents as cancer therapeutics, *Clin. Cancer Res.* 10 (2002) 415–427.
- [2] X.Y. Wu, W. Ma, K. Gurung, C.H. Guo, Mechanisms of tumor resistance to small-molecule vascular disrupting agents: treatment and rationale of combination therapy, *J. Formos. Med. Assoc.* 112 (2013) 115–124.
- [3] D.W. Siemann, M.C. Bibby, G.G. Dark, A.P. Dicker, F.A.L.M. Eskens, M.R. Horsman, D. Marmé, P.M. LoRusso, Differentiation and definition of vascular-targeted therapies, *Clin. Cancer Res.* 11 (2005) 416–420.
- [4] P. Hinnen, F.A.L.M. Eskens, Vascular disrupting agents in clinical development, *Br. J. Cancer* 96 (2007) 1159–1165.
- [5] M. Millward, P. Mainwaring, A. Mita, K. Federico, G.K. Lloyd, N. Reddinger, S. Nawrocki, M. Mita, M.A. Spear, Phase 1 study of the novel vascular disrupting agent plinabulin (NPI-2358) and docetaxel, *Invest. New Drug* 30 (2012) 1065–1073.
- [6] H.C. Pitot, E.A.J. McElroy, J.M. Reid, A.J. Windebank, J.A. Sloan, C. Erlichman, P.G. Bagniewski, D.L. Walker, J. Rubin, R.M. Goldberg, A.A. Adjei, M.M. Ames, Phase I trial of dolastatin-10 (NSC 376128) in patients with advanced solid tumors, *Clin. Cancer Res.* 5 (1999) 525–531.

- [7] E.A. Perez, D.W. Hillman, P.A. Fishkin, J.E. Krook, W.W. Tan, P.A. Kuriakose, S.R. Alberts, S.R. Dakhil, T. Warren, G.G. Mather, B.A. Evans, D.P. Woodland, E.A. Swabb, R. Kurzrock, Phase II trial of dolastatin-10 in patients with advanced breast cancer, *Invest. New Drug* 23 (2005) 257–261.
- [8] A.M.M. Tsimberidou, W. Akerley, M.C. Schabel, D.S. Hong, C. Uehara, A. Chhabra, et al., Phase I clinical trial of MPC-6827 (azixa), a microtubule destabilizing agent, in patients with advanced cancer, *Mol. Cancer Ther.* 9 (12) (2010) 3410–3419.
- [9] J. Lickliter, A. Francesconi, G. Smith, M. Burge, A. Coulthard, S. Rose, M. Griffin, R. Milne, J. McCarron, T. Yeardon, A. Wilks, A. Cubitt, D.K. Wyld, P.A. Vasey, Phase I trial of CYT997, a novel cytotoxic and vascular-disrupting agent, *Br. J. Cancer* 103 (2010) 597–606.
- [10] L.V. Beerepoot, S.A. Radema, E.O. Witteveen, T. Thomas, C. Wheeler, S. Kempin, E.E. Voest, Phase I clinical evaluation of weekly administration of the novel vascular-targeting agent, ZD6126, in patients with solid tumors, *J. Clin. Oncol.* 24 (10) (2006) 1491–1498.
- [11] F.A.L.M. Eskens, P. Tresca, D. Tosi, L. Van Doorn, H. Fontaine, A. Van der Gaast, C. Veyrat-Follet, C. Opera, M. Hospelit, V. Dieras, A phase I pharmacokinetic study of the vascular disrupting agent ombrabulin (AVE8062) and docetaxel in advanced solid tumours, *Br. J. Cancer* 110 (2014) 2170–2177.
- [12] D.M. Patterson, M. Zweifel, M.R. Middleton, P.M. Price, L.K. Folkes, M.R.L. Stratford, P. Ross, S. Halford, J. Peters, J. Balkisson, D.J. Chaplin, A.R. Padhani, G.J.S. Rustin, Phase I clinical and pharmacokinetic evaluation of the vascular-disrupting agent OXi4503 in patients with advanced solid tumors, *Clin. Cancer Res.* 18 (5) (2012) 1415–1425.
- [13] C.J. Mooney, G. Nagaiah, P. Fu, J.K. Wasman, M.M. Cooney, P.S. Savvides, J.A. Bokar, A. Dowlati, D. Wang, S.S. Agarwala, S.M. Flick, P.H. Hartman, J.D. Ortiz, P.N. Lavertu, S.C. Remick, A phase II trial of fosbretabulin in advanced anaplastic thyroid carcinoma and correlation of baseline serum-soluble intracellular adhesion molecule-1 with outcome, *Thyroid* 19 (3) (2009) 233–240.
- [14] S. Pal, A. Azad, S. Bhatia, H. Drabkin, B. Costello, J. Sarantopoulos, R. Kanesvaran, R. Lauer, A. Starodub, R. Hauke, C.J. Sweeney, N.M. Hahn, G. Sonpavde, S. Richey, T. Breen, G. Kremmidiotis, A. Leke, E. Doolin, D.C. Bibby, J. Simpson, J. Iglesias, A phase I/II trial of BNC105P with everolimus in metastatic renal cell carcinomas (mRCC), *Clin. Canc. Res.* 21 (15) (2015) 3420–3427.
- [15] a) C.P. Dell, J.P. Singh, C.W. Smith, *Pharmaceutical Compounds*, Pat. No. US005284868A (1994). b) T.R. Wiernicki, J.S. Bean, C. Dell, A. Williams, D. Wood, R.F. Kauffman, J.P. Singh, Inhibition of vascular smooth muscle cell proliferation and arterial intimal thickening by a novel antiproliferative naphthopyran, *J. Pharmacol. Exp. Ther.* 278 (3) (1996) 1452–1459.
- [16] S. Kasibhatla, H. Gourdeau, K. Meerovitch, J. Drewe, S. Reddy, L. Qiu, H. Zhang, F. Bergeron, D. Bouffard, Q. Yang, J. Herich, S. Lamothe, S.X. Cai, B. Tseng, Discovery and mechanism of action of a novel series of apoptosis inducers with potential vascular targeting activity, *Mol. Cancer Ther.* 3 (11) (2004) 1365–1374.
- [17] D. Wood, D. Panda, T.R. Wiernicki, L. Wilson, M.A. Jordan, J.P. Singh, Inhibition of mitosis and microtubule function through direct tubulin binding by a novel antiproliferative naphthopyran LY290181, *Mol. Pharmacol.* 52 (1997) 437–444.
- [18] S.A. Patil, J. Wang, X.S. Li, J. Chen, T.S. Jones, A. Hosni-Ahmed, R. Patil, W.L. Seibel, W. Li, D.D. Miller, New substituted 4H-chromenes as anticancer agents, *Bioorg. Med. Chem. Lett* 22 (13) (2012) 4458–4461.
- [19] K.A. Birch, W.F. Heath, R.N. Hermeling, C.M. Johnston, L. Stramm, C. Dell, C. Smith, J.R. Williamson, A. Reifel-Miller, LY290181, an inhibitor of diabetes-induced vascular dysfunction, blocks protein kinase C-stimulated transcriptional activation through inhibition of transcription factor binding to a phorbol response element, *Diabetes* 45 (5) (1996) 642–650.
- [20] N.J. Thumar, M.P. Patel, Synthesis and in vitro antimicrobial evaluation of 4H-pyrazolopyran-, benzopyran and naphthopyran derivatives of 1H-pyrazole, *Arkivoc* 13 (2009) 363–380.
- [21] W. Smith, J.M. Bailey, M.E.J. Billingham, S. Chandrasekhar, C.P. Dell, A.K. Harvey, C.A. Hicks, A.E. Kingston, G.N. Wishart, The anti-rheumatic potential of a series of 2,4-di-substituted-4H-naphtho[1,2-b]pyran-3-carbonitriles, *Bioorg. Med. Chem. Lett* 5 (1995) 2783–2788.
- [22] W. Kemnitzer, J. Drewe, S. Jiang, H. Zhang, J. Zhao, C. Crogan-Grundy, L. Xu, S. Lamothe, H. Gourdeau, R. Denis, B. Tseng, S. Kasibhatla, S.X. Cai, Discovery of 4-aryl-4 H -chromenes as a new series of apoptosis inducers using a cell- and caspase-based high-throughput screening assay. 3. Structure–Activity relationships of fused rings at the 7,8-positions, *J. Med. Chem.* 50 (12) (2007) 2858–2864.
- [23] B. Biersack, Y. Muthukumar, R. Schobert, F. Sasse, Cytotoxic and antivascular 1-methyl-4-(3-fluoro-4-methoxyphenyl)-5-(halophenyl)-imidazoles, *Bioorg. Med. Chem. Lett* 21 (2011) 6270–6273.
- [24] T.M. Beale, R.M. Myers, J.W. Shearman, D.S. Charnock-Jones, J.D. Brenton, F.V. Gergely, S.V. Ley, Antivascular and anticancer activity of dihalogenated A-ring analogs of combretastatin A-4, *Med. Chem. Commun.* 1 (2010) 202–208.
- [25] G. Karjala, Q. Chan, E. Manzo, R.J. Andersen, M. Roberge, Ceratamines, structurally simple microtubule-stabilizing antimotocytic agents with unusual cellular effects, *Cancer Res.* 65 (2005) 3040–3043.
- [26] R. Naimi-Jamal, S. Mashkouri, A. Sharifi, An efficient, multicomponent approach for solvent-free synthesis of 2-amino-4H-chromene scaffold, *Mol. Divers.* 14 (2010) 473–477.
- [27] A.M. El-Agrody, A.M. Fouda, E. Shawky, A.E.H. Khattab, Halogenated 2-amino-4H-benzo[h]chromene derivatives as antitumor agents and the relationship between lipophilicity and antitumor activity, *Med. Chem. Res.* 26 (2017) 691–700.
- [28] T. Mosmann, Rapid colorimetric assay for cellular growth and survival: application to proliferation and cytotoxicity assays, *J. Immunol. Methods* 65 (1983) 55–63.
- [29] B.C. Behrens, T.C. Hamilton, H. Masuda, K.R. Grotzinger, J. Whang-Peng, K.G. Louie, t. Knutsen, W.M. McKoy, R.C. Young, R.F. Ozols, Characterization of cis-diamminedichloroplatinum(II)-resistant human ovarian cancer cell line and its use in evaluation of platinum analogues, *Cancer Res.* 47 (2) (1987) 414–418.
- [30] A.K. Heinrich, H. Lucas, L. Schindler, P. Chytil, T. Etrych, K. Mäder, T. Mueller, Improved tumor-specific drug accumulation by polymer therapeutics with pH-sensitive drug release overcomes chemotherapy resistance, *Mol. Cancer Ther.* 15 (5) (2016) 998–1007.
- [31] T. Mueller, D.B. Pfankuchen, K.W. von Rekowski, M. Schlesinger, F. Reipsch, G. Bendas, The impact of the low molecular weight heparin tinzaparin on the sensitization of cisplatin-resistant ovarian cancers – preclinical in vivo evaluation in xenograft tumor models, *Molecules* 22 (2017) 728. <https://doi.org/10.3390/molecules22050728>.
- [32] J. Bauer, M. Margolis, C. Schreiner, C.J. Edgell, J. Azizkhan, E. Lazarowski, R.L. Juliano, In vitro model of angiogenesis using a human endothelium-derived permanent cell line: contributions of induced gene expression, G-proteins, and integrins, *J. Cell. Physiol.* 153 (3) (1992) 437–449.
- [33] E. Aranda, G.I. Owen, A semi-quantitative assay to screen for angiogenic compounds and compounds with angiogenic potential using the EA. hy926 endothelial cell line, *Biol. Res.* 42 (2009) 377–389.
- [34] K. Mahal, B. Biersack, H. Caysa, R. Schobert, T. Müller, Combretastatin A-4 derived imidazoles show cytotoxic, antivascular, and antimetastatic effects based on cytoskeletal reorganization, *Invest. New Drug* 33 (2015) 541–554.
- [35] K. Mahal, B. Biersack, S. Schrufer, M. Resch, R. Ficner, R. Schobert, T. Mueller, Combretastatin A-4 derived 5-(1-methyl-4-phenyl-imidazol-5-yl)indoles with superior cytotoxic and anti-vascular effects on chemoresistant cancer cells and tumors, *Eur. J. Med. Chem.* 118 (2016) 9–20.
- [36] H.Y. Yamada, G.J. Gorbosky, Spindle checkpoint function and cellular sensitivity to antimitotic drugs, *Mol. Cancer Ther.* 5 (2006) 2963–2969.
- [37] R.C. Taylor, S.P. Cullen, S.J. Martin, Apoptosis: controlled demolition at the cellular level, *Nat. Rev. Mol. Cell Biol.* 9 (2008) 231–241.
- [38] S. Pellegrini, H. Mellor, Actin stress fibers, *J. Cell Sci.* 120 (20) (2007) 3491–3499.
- [39] B. Nitzsche, C. Goesenkamp, M. Schrader, M. Ocker, R. Preissner, M. Lein, A. Zakrzewicz, B. Hoffmann, M. Höpfer, Novel compounds with anti-angiogenic and antiproliferative potency for growth control of testicular germ cell tumours, *Br. J. Cancer* 103 (1) (2010) 18–28.
- [40] J.K. Muenzner, B. Biersack, H. Kalie, I.C. Andronache, L. Kaps, D. Schuppan, F. Sasse, R. Schobert, Gold(I) bis-carbene complexes derived from vascular-disrupting combretastatin A-4 address different targets and show anti-metastatic potential, *ChemMedChem* 9 (2014) 1–11.
- [41] L.M. Kirchner, S.P. Schmidt, B.S. Gruber, Quantitation of angiogenesis in the chick chorioallantoic membrane model using fractal analysis, *Microvasc. Res.* 51 (1996) 2–14.
- [42] M.M. Cooney, W. van Heeckeren, S. Bhakta, J. Ortiz, S.C. Remick, Drug insights: vascular disrupting agents and angiogenesis—novel approaches for drug delivery, *Nat. Clin. Pract. Oncol.* 3 (2006) 682–692.
- [43] D.W. Siemann, The unique characteristics of tumor vasculature and preclinical evidence for its selective disruption by tumor-vascular disrupting agents, *Cancer Treat Rev.* 37 (1) (2011) 63–74.
- [44] S. Goel, A.H.-K. Wong, R.K. Jain, Vascular normalization as a therapeutic strategy for malignant and nonmalignant disease, *Cold Spring Harb. Perspect. Med.* 2 (3) (2012). <https://doi.org/10.1101/cshperspect.a006486>.
- [45] H. Sasaki, S. Shibata, T. Hatanaka, An evaluation method of ecotypes of Japanese lawn grass (*Zoysia japonica* STEUD.) for three different ecological functions, *Bull. Natl. Grassl. Res. Inst.* 49 (1994) 17–24.
- [46] A.P. Condurache, A.A. Mertins, Segmentation of retinal vessels with a hysteresis binary-classification paradigm, *Comput. Med. Imaging Graph.* 36 (4) (2012) 325–335.
- [47] A. Karperien, H. Ahammer, H.F. Jelinek, Quantitating the subtleties of microglial morphology with fractal analysis, *Front. Cell. Neurosci.* 7 (2013). <https://doi.org/10.3389/fncel.2013.00003>.
- [48] D. Russel, J. Hanson, E. Ott, Dimension of strange attractors, *Phys. Rev. Lett.* 45 (14) (1980) 1175–1178.
- [49] A. Di Ieva, F. Grizzi, G. Ceva-Grimaldi, C. Russo, P. Gaetani, E. Aimar, D. Levi, P. Pisano, F. Tancioni, G. Nicola, M. Tschabitscher, N. Dioguardi, R. Rodriguez y Baena, Fractal dimension as a quantifier of the microvasculature of normal and adenomatous pituitary tissue, *J. Anat.* 211 (5) (2007) 673–680.
- [50] I.C. Andronache, H. Ahammer, H.F. Jelinek, D. Peptenatu, A.M. Ciobotaru, C.C. Draghici, R.D. Pintilii, A.G. Simion, C.F. Teodorescu, Fractal analysis for studying the evolution of forests, *Chaos, Solitons Fractals* 91 (2016) 310–318.
- [51] P. Kainz, M. Mayrhofer-Reinhartshuber, H. Ahammer, IQM: an extensible and portable open source application for image and signal analysis in java, *PLoS ONE* 10 (1) (2015). <https://doi.org/10.1371/journal.pone.0116329>.

-Supplementary Information-

New Naphthopyran Analogues of LY290181 as Potential Vascular-disrupting Agents

Florian Schmitt,^[a] Madeleine Gold,^[a] Matthias Rothemund,^[a] Ion C.
Andronache,^[b] Bernhard Biersack,^[a] Rainer Schobert,^{*[a]} Thomas
Mueller^[c]

*[a] Organic Chemistry Laboratory, University of Bayreuth, Universitätsstraße
30, 95440 Bayreuth (Germany); e-mail: Rainer.Schobert@uni-bayreuth.de*

*[b] Research Centre for Integrated Analysis and Territorial Management,
Faculty of Geography, University of Bucharest, Bvd. Mihail Kogalniceanu no.
36-46 Bucharest (Romania)*

*[c] Department of Internal Medicine IV, Oncology/Hematology, Martin Luther
University Halle-Wittenberg, Ernst-Grube-Straße 40, 06120 Halle (Germany)*

Table of Content

Material and Methods.....	3
Chemistry	3
Cell culture conditions.	8
MTT assay.....	9
SRP assay.	9
Wound healing assay.....	9
Caspase-9 Activity Assay.....	9
Tubulin Polymerization Assay	9
Results	10
Effect of the test compounds on migration	10
Effects on the cell cycle progression.....	10
Vascular-disruptive activity	11
NMR spectra	12
¹ H NMR spectrum of 2b	12
¹³ C NMR spectrum of 2b	13
¹ H NMR spectrum of 2c	14
¹³ C NMR spectrum of 2c	15
¹ H NMR spectrum of 2d	16
¹³ C NMR spectrum of 2d	17
¹ H NMR spectrum of 2e	18
¹³ C NMR spectrum of 2e	19
¹ H NMR spectrum of 2f	20
¹³ C NMR spectrum of 2f	21
¹ H NMR spectrum of 2h	22
¹³ C NMR spectrum of 2h	23
¹ H NMR spectrum of 2i	24
¹³ C NMR spectrum of 2i	25
¹ H NMR spectrum of 2j	26
¹³ C NMR spectrum of 2j	27
¹ H NMR spectrum of 2k	28
¹³ C NMR spectrum of 2k	29
¹ H NMR spectrum of 3a	30
¹³ C NMR spectrum of 3a	31
¹ H NMR spectrum of 3b	32
¹³ C NMR spectrum of 3b	33
¹ H NMR spectrum of 3c	34
¹³ C NMR spectrum of 3c	35
¹ H NMR spectrum of 3d	36
¹³ C NMR spectrum of 3d	37
¹ H NMR spectrum of 3e	38
¹³ C NMR spectrum of 3e	39
¹ H NMR spectrum of 3f	40
¹³ C NMR spectrum of 3f	41
¹ H NMR spectrum of 3g	42
¹³ C NMR spectrum of 3g	43
References	44

Material and Methods

Chemistry

2-Amino-4-(3-cyanophenyl)-4H-benzo[h]chromene-3-carbonitrile (2c)

3-Cyanobenzaldehyde (131 mg, 1.0 mmol) and malononitrile (70 mg, 1.0 mmol) were dissolved in MeCN (3 mL) and three drops of Et₃N were added. The reaction mixture was stirred at room temperature for 30 min. 1-Naphthol (144 mg, 1.0 mmol) was added and the reaction mixture was stirred at room temperature for 1 h. The formed precipitate was collected, washed with MeCN and *n*-hexane and dried in vacuum. Yield: 200 mg (0.62 mmol, 62%); colorless solid of m.p. 250-251 °C; $\nu_{\max}(\text{ATR})/\text{cm}^{-1}$ 3417, 3324, 3201, 3058, 2235, 2194, 1655, 1636, 1601, 1572, 1508, 1474, 1434, 1415, 1401, 1369, 1316, 1286, 1261, 1186, 1147, 1098, 1020, 963, 897, 806, 795, 783, 766, 751, 735, 725, 694, 663; ¹H NMR (300 MHz, DMSO-d₆) δ 5.06 (1 H, s), 7.11 (1 H, d, *J* = 8.6 Hz), 7.28 (2 H, s), 7.5-7.7 (5 H, m), 7.7-7.8 (1 H, m), 7.78 (1 H, s), 7.8-7.9 (1 H, m), 8.2-8.3 (1 H, m); ¹³C NMR (75.5 MHz, DMSO-d₆) δ 40.4, 55.3, 111.6, 116.7, 118.7, 120.2, 120.8, 122.8, 124.2, 125.9, 126.8, 127.0, 127.7, 130.2, 131.0, 131.2, 132.8, 142.9, 147.1, 160.3; *m/z* (%) (EI) 323 (32) [M⁺], 222 (25), 221 (100); *m/z* (%) (HRMS, ESI) 324.11314 [M⁺ + 1] (100).

2-Amino-4-(3,5-dichloro-4-methoxyphenyl)-4H-benzo[h]chromene-3-carbonitrile (2d)

3,5-Dichloro-4-methoxybenzaldehyde (205 mg, 1.0 mmol) and malononitrile (70 mg, 1.0 mmol) were dissolved in MeCN (5 mL) and three drops of Et₃N were added. The reaction mixture was stirred at room temperature for 30 min. 1-Naphthol (144 mg, 1.0 mmol) was added and the reaction mixture was stirred at room temperature for 1 h. The formed precipitate was collected, washed with MeCN and *n*-hexane and dried in vacuum. Yield: 197 mg (0.50 mmol, 50%); colorless solid of m.p. 243 °C; $\nu_{\max}(\text{ATR})/\text{cm}^{-1}$ 3434, 3327, 3199, 3067, 2936, 2825, 2188, 1656, 1634, 1600, 1576, 1558, 1506, 1478, 1451, 1424, 1409, 1374, 1296, 1263, 1219, 1189, 1148, 1105, 1082, 1047, 1023, 999, 961, 889, 868, 823, 806, 786, 779, 767, 752, 734, 683, 667; ¹H NMR (300 MHz, CDCl₃) δ 3.91 (3 H, s), 4.82 (1 H, s), 4.92 (2 H, s), 7.01 (1 H, d, *J* = 7.0 Hz), 7.20 (2 H, s), 7.5-7.7 (3 H, m), 7.8-7.9 (1 H, m), 8.2-8.3 (1 H, m); ¹³C NMR (75.5 MHz, CDCl₃/DMSO-d₆) δ 40.8, 60.0, 60.8, 115.9, 119.5, 120.8, 123.2, 125.1, 125.7, 127.0, 127.2, 127.9, 128.5, 129.8, 133.5, 142.0, 143.2, 151.5, 159.3; *m/z* (%) (EI) 398 (16) [M⁺], 396 (23) [M⁺], 221 (100); Anal (C₂₁H₁₄Cl₂N₂O₂) calcd C 63.49, H 3.55, N 7.05, found C 63.41, H 3.52, N. 7.02%.

2-Amino-4-(3,5-dibromo-4-methoxyphenyl)-4H-benzo[h]chromene-3-carbonitrile (2e)

3,5-Dibromo-4-methoxybenzaldehyde (293 mg, 1.0 mmol) and malononitrile (70 mg, 1.0 mmol) were dissolved in MeCN (5 mL) and three drops of Et₃N were added. The reaction mixture was stirred at room temperature for 30 min. 1-Naphthol (144 mg, 1.0 mmol) was added and the reaction mixture was

stirred at room temperature for 2 h. The formed precipitate was collected, washed with MeCN and *n*-hexane and dried in vacuum. Yield: 346 mg (0.71 mmol, 71%); colorless solid of m.p. 241 °C; $\nu_{\max}(\text{ATR})/\text{cm}^{-1}$ 3437, 3334, 3215, 3010, 2926, 2188, 1659, 1635, 1607, 1573, 1550, 1505, 1468, 1413, 1402, 1374, 1296, 1260, 1207, 1187, 1154, 1101, 1035, 1018, 993, 884, 872, 823, 811, 790, 769, 755, 745, 726; $^1\text{H NMR}$ (300 MHz, DMSO- d_6) δ 3.76 (3 H, s), 5.00 (1 H, s), 7.15 (1 H, d, $J = 8.6$ Hz), 7.31 (2 H, s), 7.53 (2 H, s), 7.6-7.7 (3 H, m), 7.8-7.9 (1 H, m), 8.2-8.3 (1 H, m); $^{13}\text{C NMR}$ (75.5 MHz, DMSO- d_6) δ 39.5, 55.2, 60.4, 116.7, 117.8, 120.2, 120.8, 122.7, 124.3, 125.9, 126.8, 127.0, 127.8, 131.8, 132.9, 142.8, 144.9, 152.3, 160.4; m/z (%) (EI) 488 (7) [M^+], 486 (15) [M^+], 484 (7) [M^+], 222 (22), 221 (100); m/z (%) (HRMS, ESI) 486.94580 [$\text{M}^+(\text{}^{79}\text{Br}, \text{}^{81}\text{Br}) + 1$] (100).

2-Amino-4-(3,5-diiodo-4-methoxyphenyl)-4H-benzo[h]chromene-3-carbonitrile (2f)

3,5-Diiodo-4-methoxybenzaldehyde (388 mg, 1.0 mmol) and malononitrile (70 mg, 1.0 mmol) were dissolved in MeCN (5 mL) and three drops of Et₃N were added. The reaction mixture was stirred at room temperature for 30 min. 1-Naphthol (144 mg, 1.0 mmol) was added and the reaction mixture was stirred at room temperature for 1 h. The formed precipitate was collected, washed with MeCN and *n*-hexane and dried in vacuum. Yield: 482 mg (0.83 mmol, 83%); colorless solid of m.p. 230 °C; $\nu_{\max}(\text{ATR})/\text{cm}^{-1}$ 3478, 3394, 3325, 3194, 3062, 2930, 2190, 1658, 1636, 1600, 1575, 1538, 1506, 1458, 1412, 1376, 1286, 1264, 1189, 1151, 1102, 1055, 1024, 994, 887, 864, 821, 789, 777, 767, 747, 700, 667; $^1\text{H NMR}$ (300 MHz, CDCl₃/DMSO- d_6) δ 3.60 (3 H, s), 4.54 (1 H, s), 5.76 (2 H, s), 6.77 (1 H, d, $J = 8.7$ Hz), 7.3-7.4 (3 H, m), 7.40 (2 H, s), 7.5-7.6 (1 H, m), 8.0-8.1 (1 H, m); $^{13}\text{C NMR}$ (75.5 MHz, CDCl₃/DMSO- d_6) δ 39.1, 57.6, 60.1, 90.5, 115.6, 119.7, 120.6, 122.8, 124.1, 125.3, 126.2, 127.2, 132.8, 138.7, 142.8, 144.3, 157.3, 159.6; m/z (%) (EI) 580 (49) [M^+], 221 (100); Anal (C₂₁H₁₄I₂N₂O₂) calcd C 43.48, H 2.43, N 4.83, found C 43.43, H 2.39, N. 4.78%.

2-Amino-4-(3-pentafluorothiophenyl)-4H-benzo[h]chromene-3-carbonitrile (2h)

3-Pentafluorothiobenzaldehyde (232 mg, 1.0 mmol) and malononitrile (70 mg, 1.0 mmol) were dissolved in MeCN (3 mL) and three drops of Et₃N were added. The reaction mixture was stirred at room temperature for 30 min. 1-Naphthol (144 mg, 1.0 mmol) was added and the reaction mixture was stirred at room temperature for 16 h. The formed precipitate was collected, washed with MeCN and *n*-hexane and dried in vacuum. Yield: 64 mg (0.015 mmol, 15%); colorless solid of m.p. 205-206 °C; $\nu_{\max}(\text{ATR})/\text{cm}^{-1}$ 3482, 3444, 3333, 3201, 3062, 2194, 1667, 1637, 1610, 1573, 1484, 1435, 1409, 1396, 1376, 1331, 1283, 1264, 1191, 1150, 1104, 1039, 1022, 959, 895, 873, 858, 839, 824, 800, 795, 780, 763, 752, 735, 694, 662; $^1\text{H NMR}$ (300 MHz, DMSO- d_6) δ 5.17 (1 H, s), 7.13 (1 H, d, $J = 8.6$ Hz), 7.29 (2 H, s), 7.5-7.7 (5 H, m), 7.8-8.0 (3 H, m), 8.2-8.3 (1 H, m); $^{13}\text{C NMR}$ (75.5 MHz, DMSO- d_6) δ 40.4, 55.4, 116.8, 120.1, 120.7, 122.7, 124.2, 124.5, 125.8, 126.8, 127.0, 127.7, 130.2, 131.9, 132.8, 142.9, 147.3, 153.1, 160.4; m/z (%) (EI) 424 (23) [M^+], 221 (100); Anal (C₂₀H₁₃F₅N₂OS) calcd C 56.60, H 3.09, N 6.60, found C 56.51, H 3.03, N. 6.54%.

2-Amino-4-(4-pentafluorothiophenyl)-4H-benzo[h]chromene-3-carbonitrile (2i)

4-Pentafluorothiobenzaldehyde (232 mg, 1.0 mmol) and malononitrile (70 mg, 1.0 mmol) were dissolved in MeCN (5 mL) and three drops of Et₃N were added. The reaction mixture was stirred at room temperature for 30 min. 1-Naphthol (144 mg, 1.0 mmol) was added and the reaction mixture was stirred at room temperature for 16 h. The formed precipitate was collected, washed with MeCN and *n*-hexane and dried in vacuum. Yield: 205 mg (0.48 mmol, 48%); colorless solid of m.p. 263-264 °C; $\nu_{\max}(\text{ATR})/\text{cm}^{-1}$ 3489, 3332, 3201, 3035, 2198, 1667, 1638, 1607, 1573, 1499, 1411, 1399, 1377, 1287, 1265, 1227, 1193, 1149, 1103, 1096, 1040, 1022, 889, 866, 832, 819, 810, 793, 783, 766, 750, 686, 675, 660; ¹H NMR (300 MHz, CDCl₃/DMSO-d₆) δ 4.69 (1 H, s), 5.83 (2 H, s), 6.73 (1 H, d, *J* = 8.6 Hz), 7.10 (2 H, d, *J* = 8.6 Hz), 7.2-7.5 (5 H, m), 7.5-7.6 (1 H, m), 8.00 (1 H, dd, *J* = 9.0 Hz, 1.6 Hz); ¹³C NMR (75.5 MHz, CDCl₃/DMSO-d₆) δ 40.7, 57.2, 115.5, 119.6, 120.5, 122.7, 124.0, 125.2, 125.7, 125.8, 126.1, 126.4, 127.1, 127.8, 132.8, 142.8, 148.3, 159.6; *m/z* (%) (EI) 424 (23) [M⁺], 221 (100); Anal (C₂₀H₁₃F₅N₂OS) calcd C 56.60, H 3.09, N 6.60, found C 56.53, H 3.04, N. 6.53%.

2-Amino-4-(4-methylsulfanylphenyl)-4H-benzo[h]chromene-3-carbonitrile (2j)

4-Methylsulfanylbenzaldehyde (152 mg, 1.0 mmol) and malononitrile (70 mg, 1.0 mmol) were dissolved in MeCN (5 mL) and three drops of Et₃N were added. The reaction mixture was stirred at room temperature for 30 min. The formed precipitate was redissolved by heating and 1-naphthol (144 mg, 1.0 mmol) was added. The reaction mixture was stirred at room temperature for 16 h. The formed precipitate was collected, washed with MeCN and *n*-hexane and dried in vacuum. Yield: 165 mg (0.48 mmol, 48%); colorless solid of m.p. 236-237 °C; $\nu_{\max}(\text{ATR})/\text{cm}^{-1}$ 3461, 3342, 3195, 3056, 2916, 2201, 2182, 1662, 1635, 1598, 11572, 1506, 1491, 1469, 1435, 1404, 1371, 1282, 1260, 1226, 1205, 1147, 1102, 1038, 1021, 966, 952, 886, 864, 849, 831, 816, 800, 780, 764, 750, 689, 658; ¹H NMR (300 MHz, DMSO-d₆) δ 2.43 (3 H, s), 4.87 (1 H, s), 7.09 (1 H, d, *J* = 8.6 Hz), 7.1-7.2 (6 H, m), 7.5-7.7 (3 H, m), 7.8-7.9 (1 H, m), 8.2-8.3 (1 H, m); ¹³C NMR (75.5 MHz, DMSO-d₆) δ 14.6, 40.4, 56.2, 117.8, 120.5, 120.7, 122.7, 123.9, 126.2, 126.3, 126.7, 126.8, 127.7, 128.3, 132.7, 136.6, 142.4, 142.7, 160.1; *m/z* (%) (EI) 344 (86) [M⁺], 221 (100); Anal (C₂₁H₁₆N₂OS) calcd C 73.23, H 4.68, N 8.13, found C 73.15, H 4.65, N. 8.09%.

2-Amino-4-(3-methoxy-4-benzyloxyphenyl)-4H-benzo[h]chromene-3-carbonitrile (2k)

3-Methoxy-4-benzyloxybenzaldehyde (242 mg, 1.0 mmol) and malononitrile (70 mg, 1.0 mmol) were dissolved in MeCN (3 mL) and three drops of Et₃N were added. The reaction mixture was stirred at room temperature for 30 min. 1-Naphthol (144 mg, 1.0 mmol) was added and the reaction mixture was stirred at room temperature for 16 h. The formed precipitate was collected, washed with MeCN and *n*-hexane and dried in vacuum. Yield: 260 mg (0.60 mmol, 60%); colorless solid of m.p. 230 °C; $\nu_{\max}(\text{ATR})/\text{cm}^{-1}$ 3461, 3326, 3284, 3253, 3229, 3197, 3034, 2999, 2933, 2905, 2870, 2832, 2197, 1667, 1606, 1573, 1516, 1466, 1453, 1421, 1398, 1372, 1274, 1260, 1252, 1228, 1217, 1186, 1157, 1135, 1103, 1035, 1021, 928, 862, 827, 810, 766, 745, 735, 695, 666; ¹H NMR (300 MHz, DMSO-d₆)

δ 3.72 (3 H, s), 4.84 (1 H, s), 5.02 (2 H, s), 6.7-6.8 (1 H, dd, $J = 8.3$ Hz, 2.0 Hz), 6.92 (1 H, d, $J = 2.0$ Hz), 6.98 (1 H, d, $J = 8.3$ Hz), 7.11 (2 H, s), 7.15 (1 H, d, $J = 8.6$ Hz), 7.3-7.5 (5 H, m), 7.5-7.7 (3 H, m), 7.8-7.9 (1 H, m), 8.2-8.3 (1 H, m); ^{13}C NMR (75.5 MHz, DMSO- d_6) δ 40.5, 55.6, 56.4, 70.0, 111.8, 113.8, 118.1, 119.8, 120.6, 120.7, 122.8, 123.8, 126.3, 126.6, 126.7, 127.7, 127.8, 128.4, 132.7, 137.2, 138.6, 142.5, 146.9, 149.1, 160.1; m/z (%) (EI) 435 (85) [M^+], 343 (100), 315 (27), 221 (47), 91 (88); Anal ($\text{C}_{28}\text{H}_{22}\text{N}_2\text{O}_3$) calcd C 77.40, H 5.10, N 6.45, found C 77.29, H 5.03, N. 6.41%.

2-Amino-6-chloro-4-(3-nitrophenyl)-4H-benzo[h]chromene-3-carbonitrile (3a)

3-Nitrobenzaldehyde (151 mg, 1.0 mmol) and malononitrile (70 mg, 1.0 mmol) were dissolved in MeCN (3 mL) and three drops of Et_3N were added. The reaction mixture was stirred at room temperature for 30 min. 4-Chloro-1-naphthol (178 mg, 1.0 mmol) was added and the reaction mixture was stirred at room temperature for 16 h. The formed precipitate was collected, washed with MeCN and *n*-hexane and dried in vacuum. Yield: 236 mg (0.63 mmol, 63%); colorless solid of m.p. 242-243 °C; $\nu_{\text{max}}(\text{ATR})/\text{cm}^{-1}$ 3446, 3326, 3211, 3093, 2867, 2191, 1655, 1634, 1609, 1596, 1567, 1527, 1477, 1404, 1372, 1347, 1329, 1300, 1264, 1204, 1174, 1112, 1091, 1047, 1028, 958, 940, 913, 814, 768, 751, 735, 699, 679, 671, 663; ^1H NMR (300 MHz, $\text{CDCl}_3/\text{DMSO-}d_6$) δ 4.74 (1 H, s), 5.98 (2 H, s), 6.83 (1 H, s), 7.3-7.5 (4 H, m), 7.8-8.0 (3 H, m), 8.0-8.1 (1 H, m); ^{13}C NMR (75.5 MHz, $\text{CDCl}_3/\text{DMSO-}d_6$) δ 40.8, 57.0, 115.8, 119.3, 121.2, 122.0, 122.3, 123.9, 124.8, 127.1, 127.6, 129.5, 129.9, 133.9, 142.0, 146.1, 148.1, 159.5; m/z (%) (EI) 379 (12) [M^+], 377 (35) [M^+], 257 (63), 255 (100); m/z (%) (HRMS, ESI) 378.06400 [$\text{M}^+(\text{^{35}Cl}) + 1$] (100).

2-Amino-6-chloro-4-(3,5-difluorophenyl)-4H-benzo[h]chromene-3-carbonitrile (3b)

3,5-Difluorobenzaldehyde (52 mg, 0.37 mmol) and malononitrile (25 mg, 0.38 mmol) were dissolved in MeCN (3 mL) and five drops of Et_3N were added. The reaction mixture was stirred at room temperature for 30 min. 4-Chloro-1-naphthol (65 mg, 0.36 mmol) was added and the reaction mixture was stirred at room temperature for 30 min. The formed precipitate was collected, washed with MeCN and dried in vacuum. Yield: 70 mg (0.19 mmol, 53%); colorless solid of m.p. 273-274 °C; $\nu_{\text{max}}(\text{ATR})/\text{cm}^{-1}$ 3468, 3344, 3269, 3205, 3089, 3059, 2191, 1663, 1621, 1595, 1568, 1459, 1416, 1401, 1365, 1315, 1289, 1257, 1223, 1206, 1170, 1159, 1118, 1109, 1049, 1030, 991, 936, 873, 845, 766, 712, 692, 672, 633; ^1H NMR (300 MHz, $\text{CDCl}_3/\text{DMSO-}d_6$) δ 4.74 (1 H, s), 6.12 (2 H, s), 6.64 (1 H, t, $J_{\text{H-F}} = 8.9$ Hz, 2.3 Hz), 6.7-6.8 (2 H, m), 7.03 (1 H, s), 7.5-7.6 (2 H, m), 8.0-8.1 (1 H, m), 8.2-8.3 (1 H, m); ^{13}C NMR (75.5 MHz, $\text{CDCl}_3/\text{DMSO-}d_6$) δ 40.7, 57.0, 102.3 (t, $J_{\text{C-F}} = 25.5$ Hz), 110.4 (d, $J_{\text{C-F}} = 25.5$ Hz), 115.9, 119.2, 121.1, 123.8, 124.8, 126.9, 127.5, 129.8, 141.9, 148.0 (t, $J_{\text{C-F}} = 8.0$ Hz), 159.4, 162.5 (dd, $J = 249$ Hz, 12.8 Hz); m/z (%) (EI) 370 (9) [M^+], 368 (33) [M^+], 257 (51), 255 (100); m/z (%) (HRMS, ESI) 369.06007 [$\text{M}^+(\text{^{35}Cl}) + 1$] (100).

2-Amino-6-chloro-4-(3-cyanophenyl)-4H-benzo[h]chromene-3-carbonitrile (3c)

3-Cyanobenzaldehyde (131 mg, 1.0 mmol) and malononitrile (70 mg, 1.0 mmol) were dissolved in MeCN (3 mL) and three drops of Et_3N were added. The reaction mixture was stirred at room temperature

for 30 min. 4-Chloro-1-naphthol (178 mg, 1.0 mmol) was added and the reaction mixture was stirred at room temperature for 1 h. The formed precipitate was collected, washed with MeCN and *n*-hexane and dried in vacuum. Yield: 217 mg (0.61 mmol, 61%); colorless solid of m.p. 248-249 °C; $\nu_{\max}(\text{ATR})/\text{cm}^{-1}$ 3406, 3329, 3205, 3065, 2843, 2228, 2202, 1664, 1613, 1599, 1571, 1477, 1422, 1411, 1370, 1357, 1283, 1259, 1205, 1172, 1154, 1113, 1050, 1028, 973, 944, 904, 877, 852, 806, 786, 766, 755, 725, 699, 677, 667; $^1\text{H NMR}$ (300 MHz, DMSO- d_6) δ 5.05 (1 H, s), 7.32 (1 H, s), 7.36 (2 H, s), 7.5-7.6 (2 H, m), 7.7-7.8 (4 H, m), 8.0-8.1 (1 H, m), 8.3-8.4 (1 H, m); $^{13}\text{C NMR}$ (75.5 MHz, DMSO- d_6) δ 40.4, 55.2, 111.7, 117.4, 118.6, 120.0, 121.6, 123.9, 124.0, 125.7, 125.8, 127.8, 128.5, 129.5, 130.3, 131.2, 131.3, 132.8, 142.3, 146.6, 160.1; m/z (%) (EI) 359 (8) [M^+], 357 (23) [M^+], 257 (40), 255 (100); Anal ($\text{C}_{21}\text{H}_{12}\text{ClN}_3\text{O}$) calcd C 70.49, H 3.38, N 11.74, found C 70.40, H 3.32, N 11.69%.

2-Amino-6-chloro-4-(3,5-dibromo-4-methoxyphenyl)-4H-benzo[h]chromene-3-carbonitrile (3d)

3,5-Dibromo-4-methoxybenzaldehyde (293 mg, 1.0 mmol) and malononitrile (70 mg, 1.0 mmol) were dissolved in MeCN (5 mL) and three drops of Et_3N were added. The reaction mixture was stirred at room temperature for 30 min. 4-Chloro-1-naphthol (178 mg, 1.0 mmol) was added and the reaction mixture was stirred at room temperature for 2 h. The formed precipitate was collected, washed with MeCN and *n*-hexane and dried in vacuum. Yield: 262 mg (0.50 mmol, 50%); colorless solid of m.p. 273-274 °C; $\nu_{\max}(\text{ATR})/\text{cm}^{-1}$ 3472, 3361, 3194, 3058, 2964, 2937, 2926, 2857, 2822, 2197, 1659, 1631, 1595, 1571, 1548, 1467, 1418, 1403, 1371, 1279, 1257, 1203, 1180, 1154, 1112, 1067, 1025, 987, 939, 887, 872, 777, 770, 761, 729, 689, 665; $^1\text{H NMR}$ (300 MHz, DMSO- d_6) δ 3.77 (3 H, s), 4.98 (1 H, s), 7.3-7.4 (3 H, m), 7.57 (2 H, s), 7.7-7.8 (2 H, m), 8.0-8.1 (1 H, m), 8.3-8.4 (1 H, m); $^{13}\text{C NMR}$ (75.5 MHz, DMSO- d_6) δ 40.4, 55.1, 60.4, 117.3, 117.9, 119.9, 121.6, 123.9, 124.0, 125.6, 125.9, 127.9, 128.5, 129.5, 131.9, 142.2, 144.3, 152.5, 160.2; m/z (%) (EI) 522 (17) [M^+], 520 (25) [M^+], 518 (11) [M^+], 257 (67), 255 (100); m/z (%) (HRMS, ESI) 520.90846 [$\text{M}^+(\text{^{35}Cl, ^{79}Br, ^{81}Br) + 1}$] (100).

2-Amino-6-chloro-4-(4-cyanophenyl)-4H-benzo[h]chromene-3-carbonitrile (3e)

4-Cyanobenzaldehyde (131 mg, 1.0 mmol) and malononitrile (70 mg, 1.0 mmol) were dissolved in MeCN (3 mL) and three drops of Et_3N were added. The reaction mixture was stirred at room temperature for 30 min. 4-Chloro-1-naphthol (178 mg, 1.0 mmol) was added and the reaction mixture was stirred at room temperature for 1 h. The formed precipitate was collected, washed with MeCN and *n*-hexane and dried in vacuum. Yield: 270 mg (0.76 mmol, 76%); colorless solid of m.p. 267-268 °C; $\nu_{\max}(\text{ATR})/\text{cm}^{-1}$ 3437, 3330, 3204, 3062, 2235, 2194, 1653, 1626, 1597, 1569, 1501, 1456, 1418, 1402, 1366, 1354, 1276, 1261, 1202, 1169, 1115, 1058, 1031, 966, 944, 877, 835, 779, 765, 742, 671, 661; $^1\text{H NMR}$ (300 MHz, DMSO- d_6) δ 5.07 (1 H, s), 7.31 (1 H, s), 7.37 (2 H, s), 7.48 (2 H, d, $J = 8.4$ Hz), 7.7-7.9 (4 H, m), 8.1-8.2 (1 H, m), 8.3-8.4 (1 H, m); $^{13}\text{C NMR}$ (75.5 MHz, DMSO- d_6) δ 40.5, 55.1, 110.1, 117.4, 118.6, 119.9, 121.5, 123.9, 125.7, 125.9, 127.9, 128.6, 128.8, 129.5, 132.9, 142.3, 150.4, 160.2; m/z (%) (EI) 359 (10) [M^+], 357 (31) [M^+], 257 (48), 255 (100); Anal ($\text{C}_{21}\text{H}_{12}\text{ClN}_3\text{O}$) calcd C 70.49, H 3.38, N 11.74, found C 70.41, H 3.31, N 11.70%.

2-Amino-6-chloro-4-(4-methylsulfanylphenyl)-4H-benzo[h]chromene-3-carbonitrile (3f)

4-Methylsulfanylbenzaldehyde (152 mg, 1.0 mmol) and malononitrile (70 mg, 1.0 mmol) were dissolved in MeCN (5 mL) and three drops of Et₃N were added. The reaction mixture was stirred at room temperature for 30 min. 4-Chloro-1-naphthol (178 mg, 1.0 mmol) was added and the reaction mixture was stirred at room temperature for 1 h. The formed precipitate was collected, washed with MeCN and *n*-hexane and dried in vacuum. Yield: 185 mg (0.49 mmol, 49%); colorless solid of m.p. 239 °C; $\nu_{\max}(\text{ATR})/\text{cm}^{-1}$ 3458, 3326, 3194, 3076, 2916, 2193, 1664, 1634, 1594, 1568, 1493, 1456, 1439, 1402, 1371, 1260, 1227, 1203, 1171, 1112, 1093, 1045, 1027, 1016, 972, 939, 868, 826, 818, 778, 762, 755, 725, 695, 672, 661; ¹H NMR (300 MHz, DMSO-d₆) δ 2.44 (3 H, s), 4.88 (1 H, s), 7.2-7.3 (7 H, m), 7.7-7.8 (2 H, m), 8.1-8.2 (1 H, m), 8.3-8.4 (1 H, m); ¹³C NMR (75.5 MHz, DMSO-d₆) δ 14.6, 40.0, 56.0, 118.5, 120.2, 121.5, 123.9, 124.4, 125.6, 125.9, 126.3, 127.8, 128.3, 129.3, 137.0, 141.8, 142.0, 159.9; *m/z* (%) (EI) 380 (15) [M⁺], 378 (45) [M⁺], 257 (37), 255 (100); Anal (C₂₁H₁₅ClN₂O) calcd C 66.57, H 3.99, N 7.39, found C 66.49, H 4.02, N. 7.35%.

2-Amino-6-chloro-4-(3-bromophenyl)-4H-benzo[h]chromene-3-carbonitrile (3g)

3-Bromobenzaldehyde (185 mg, 1.0 mmol) and malononitrile (70 mg, 1.0 mmol) were dissolved in MeCN (5 mL) and three drops of Et₃N were added. The reaction mixture was stirred at room temperature for 30 min. 4-Chloro-1-naphthol (178 mg, 1.0 mmol) was added and the reaction mixture was stirred at room temperature for 2 h. The formed precipitate was collected, washed with MeCN and *n*-hexane and dried in vacuum. Yield: 261 mg (0.63 mmol, 63%); colorless solid of m.p. 210 °C; $\nu_{\max}(\text{ATR})/\text{cm}^{-1}$ 3413, 3333, 3215, 2190, 1655, 1630, 1610, 1568, 1476, 1432, 1404, 1368, 1317, 1257, 1223, 1203, 1169, 1111, 1073, 1046, 1025, 999, 940, 900, 876, 791, 775, 760, 704, 690, 678; ¹H NMR (300 MHz, DMSO-d₆) δ 4.96 (1 H, s), 7.2-7.4 (5 H, m), 7.4-7.5 (2 H, m), 7.7-7.8 (2 H, m), 8.0-8.1 (1 H, m), 8.3-8.4 (1 H, m); ¹³C NMR (75.5 MHz, DMSO-d₆) δ 40.4, 55.5, 117.9, 120.0, 121.5, 122.0, 123.9, 125.8, 126.9, 127.8, 128.5, 129.4, 130.2, 130.3, 131.2, 142.1, 147.8, 160.1; *m/z* (%) (EI) 412 (32) [M⁺], 410 (25) [M⁺], 257 (73), 255 (100), 193 (16); Anal (C₂₀H₁₂BrClN₂O) calcd C 58.35, H 2.94, N 6.80, found C 58.29, H 2.98, N. 6.84%.

Cell culture conditions. 518A2 (Department of Radiotherapy, Medical University of Vienna, Austria) melanoma cells, Ea.Hy926 (ATCC[®] CRL-2922TM) endothelial hybrid cells, DLD-1 (ATCC[®] CCL-221TM), HCT-116 (ACC-581) and HT-29 (ACC-299) colon (adeno-)carcinoma cells, MCF-7^{Topo} (ACC-115) breast adenocarcinoma cells, KB-V1^{Vbl} (ACC-149) cervix carcinoma cells, Panc-1 (ACC-783) pancreatic ductular adenocarcinoma cells were grown at 37 °C, 5% CO₂, 95% humidity in Dulbecco's modified Eagle's medium (DMEM) containing 10% fetal bovine serum (FBS) and 1% antibiotic-antimycotic. For keeping the KB-V1^{Vbl} and MCF-7^{Topo} cells resistant, the maximal tolerated dose of vinblastin or topotecan, respectively, was added to the cell culture medium 24 h after every cell passage. Only mycoplasma-free cultures were used.

MTT assay. The antiproliferative activity of the test compounds was studied in MTT assay [S1]. Briefly, cells (100 μL /well) were seeded in 96-well tissue culture plates at a concentration of 5.0×10^4 cells/mL or 1.0×10^5 cells/mL for the Ea.Hy926 cell line and treated with varying concentrations of the test compounds or vehicle (DMSO) for 72 h. Then, 12.5 μL of a 0.5 mg/mL MTT solution in PBS was added to each well and the cells were incubated for 2 h at 37 °C. After centrifuging (300 g, 5 min, 4 °C) the supernatant was discarded and the formazan precipitate was dissolved in 10% SDS in DMSO containing 0.6% acetic acid. After 1 h of incubation, the absorbance at wavelength 570 nm (formazan) and 630 nm (background) was measured with a microplate reader (Tecan, Switzerland). All experiments were carried out in quadruplicate. The percentage of viable cells quoted was calculated as the mean \pm SD with respect to the controls set to 100%.

SRP assay. Cytotoxicity testing in the A2780/A2780cis model was performed using the SRB assay as previously described [S2]. The IC₅₀ values after 72 incubation were derived from dose-inhibition curves and depicted as the mean \pm SD of three independent experiments.

Wound healing assay. 518A2 melanoma cells (0.1×10^6 cells/mL, 500 μL /well) were cultured in 24-well plates for 24 h to obtain a subconfluent monolayer. Then an artificial wound was created by scratching off a small strip of cells using a 100 μL plastic tip. After changing the medium the cells were treated with 50 nM of the test compounds (**2a-c**). The wound healing process was documented by light microscopy (Zeiss Axiovert 135, 100x magnification) 0 h, 24 h and 48 h p.a.. All experiments were performed in triplicate.

Caspase-9 Activity Assay. For caspase-9 activity measurements the Caspase-Glo[®] Assay Kit (Promega Corp., Wisconsin, USA) was used. Therefore 518A2 melanoma cells (1.0×10^4 cells/well) were grown in white 96-well plates for 24 h (37 °C, 5 % CO₂ and 95 % humidity) and subsequently incubated with the test compounds (5 μM) or solvent (DMSO) for further 3.5 h under cell culture conditions. Afterwards 1 \times caspase-9 substrate solution was added to each well and the substrate transformation by potentially activated caspase-9 was performed for 60 min at rt. Finally the luminescence intensity was measured using a microplate reader (FLUOstar Omega, BMG Labtech). All experiments were carried out in quadruplicate, blank values were subtracted to reduce background signals, and the caspase-9 activity of the remaining cells was calculated as means \pm SD with solvent controls set to 100 %.

Tubulin Polymerization Assay [S3]. Porcine brain tubulin protein (5 mg/mL) in Brinkley's Buffer 80 containing 10 % glycerin and 1.5 mM guanosine 5'-triphosphate was mixed with 10 μM of **2l** or vehicle (set to 100% tubulin polymerization = 0% inhibition of the tubulin polymerization) or various concentrations of **2a-b**, **2e** and C-A4 in a black half area 96-well microtiter plate. Microtubule polymerization was monitored at 37 °C for 2 h by light scattering at 340 nm using a microplate reader (Tecan). All experiments were performed at least in duplicate. Various concentrations of C-A4, **2a-b**, and **2e** were used to determine the ITP₅₀ value (the concentration causing 50% inhibition of the tubulin polymerization when compared to vehicle treated controls after 2 h).

Results

Effect of the test compounds on migration

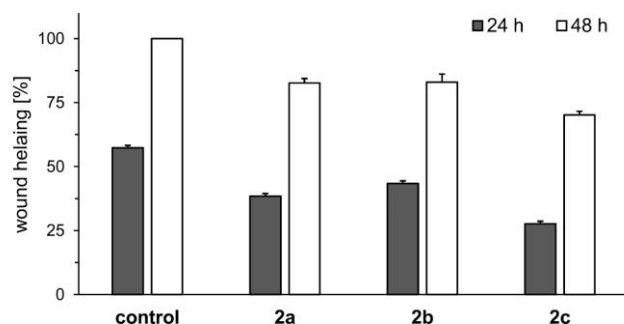


Figure S1: Inhibitory effect of **2a-c** (50 nM) on the cell migration of 518A2 melanoma cells. The values are mean \pm SD of three independent experiments. Control cells were treated with DMSO only.

Effects on the cell cycle progression

Table S1. Percentage of HT-29 colon carcinoma cells in G1, S, and G2/M phase of the cell cycle and the percentage of apoptotic cells (sub-G1) after treatment with the test compounds (**2a-c**, **2e**, **2l** and **3a-c**).

		sub-G1	G1	S	G2/M
control		1.2 \pm 0.3	75.1 \pm 1.1	12.3 \pm 0.4	11.4 \pm 1.4
2a	100 nM	6.1 \pm 0.4	49.3 \pm 0.1	26.2 \pm 0.4	18.4 \pm 0.6
	250 nM	13.0 \pm 0.6	51.7 \pm 2.7	22.4 \pm 1.7	12.9 \pm 2.3
	350 nM	12.2 \pm 0.6	39.8 \pm 2.4	24.1 \pm 2.4	23.9 \pm 1.8
2b	100 nM	7.1 \pm 1.5	40.3 \pm 3.2	20.7 \pm 0.9	31.8 \pm 1.6
	250 nM	11.3 \pm 3.2	35.9 \pm 1.6	19.2 \pm 2.0	33.6 \pm 0.9
	350 nM	13.4 \pm 1.4	30.8 \pm 2.1	12.3 \pm 2.0	43.5 \pm 4.3
2c	100 nM	4.2 \pm 0.7	51.0 \pm 3.2	25.1 \pm 1.7	19.7 \pm 2.2
	250 nM	11.8 \pm 1.8	59.6 \pm 4.8	18.5 \pm 3.3	10.1 \pm 3.7
	350 nM	10.6 \pm 0.2	60.5 \pm 2.2	15.6 \pm 1.7	13.3 \pm 1.5
2e	100 nM	2.7 \pm 0.1	51.8 \pm 1.1	19.4 \pm 0.3	26.1 \pm 1.0
	250 nM	4.4 \pm 0.4	26.8 \pm 1.5	13.9 \pm 1.1	55.0 \pm 2.4
	350 nM	5.3 \pm 1.3	19.9 \pm 2.2	10.6 \pm 0.9	64.3 \pm 4.3
2l	100 nM	9.3 \pm 2.4	56.0 \pm 8.1	14.7 \pm 1.2	20.5 \pm 5.5
	250 nM	25.0 \pm 1.1	15.4 \pm 4.8	9.4 \pm 1.5	50.4 \pm 6.9
	350 nM	30.7 \pm 3.5	21.0 \pm 1.7	14.9 \pm 2.0	34.0 \pm 3.7
3a	100 nM	2.0 \pm 0.2	55.8 \pm 1.2	23.6 \pm 0.7	18.6 \pm 0.8
	250 nM	17.6 \pm 1.7	53.5 \pm 2.2	11.3 \pm 0.2	17.7 \pm 2.8
	350 nM	6.6 \pm 1.7	14.8 \pm 3.7	5.2 \pm 1.2	73.5 \pm 5.2
3b	100 nM	3.3 \pm 0.5	52.0 \pm 1.5	19.6 \pm 0.2	25.0 \pm 1.1
	250 nM	4.5 \pm 1.6	3.0 \pm 0.8	2.3 \pm 0.1	90.3 \pm 2.4
	350 nM	3.5 \pm 0.5	1.6 \pm 0.3	2.2 \pm 0.5	92.7 \pm 1.1
3c	100 nM	19.8 \pm 1.0	51.7 \pm 1.3	16.1 \pm 1.1	12.3 \pm 2.5
	250 nM	27.8 \pm 3.5	22.2 \pm 3.9	9.1 \pm 1.0	40.9 \pm 8.2
	350 nM	27.0 \pm 5.0	13.0 \pm 4.3	8.5 \pm 1.8	51.6 \pm 11.2

Determined by flow cytometry. Cells were incubated with the test compounds at 100, 250, and 350 nM for 24 h. controls were treated with DMSO only. Values are the mean \pm SD of 3 independent experiments.

Table S2. Caspase-9 activity as determined by Caspase-Glo® Assay Kit after treating 518-A2 melanoma cells for 3.5 h with vehicle and 5 μ M of **2a** and **2b**.

	control	2a	2b
caspase-9 activity (%)	100.0 \pm 1.2	114.7 \pm 2.2	133.0 \pm 2.2

All experiments were carried out in quadruplicate, blank values were subtracted to reduce background signals, and the caspase-9 activity of the remaining cells was calculated as means \pm SD with solvent controls set to 100 %.

Vascular-disruptive activity

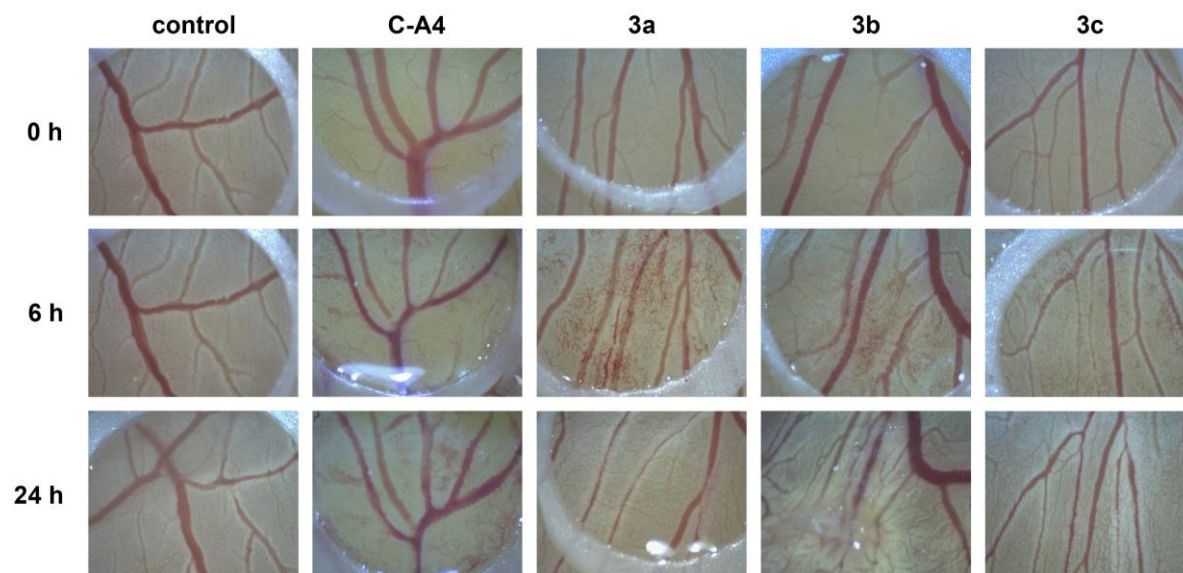


Figure S2. Effects of the compounds C-A4 (2.5 nmol) and **3a-c** (10 nmol) on the blood vessels of the chorioallantoic membrane in fertilized eggs inside a ring of silicon foil (5 mm diameter) after 0, 6 and 24 h; control: DMSO. Images are representative of at least two independent assays (60-fold magnification).

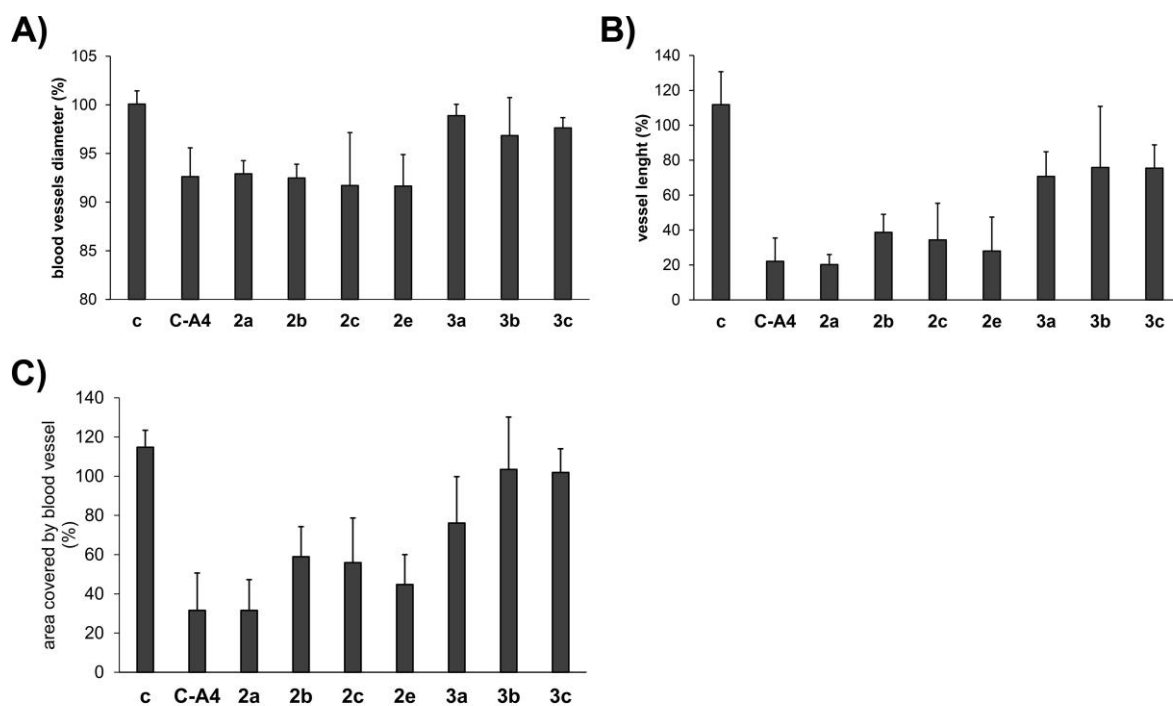
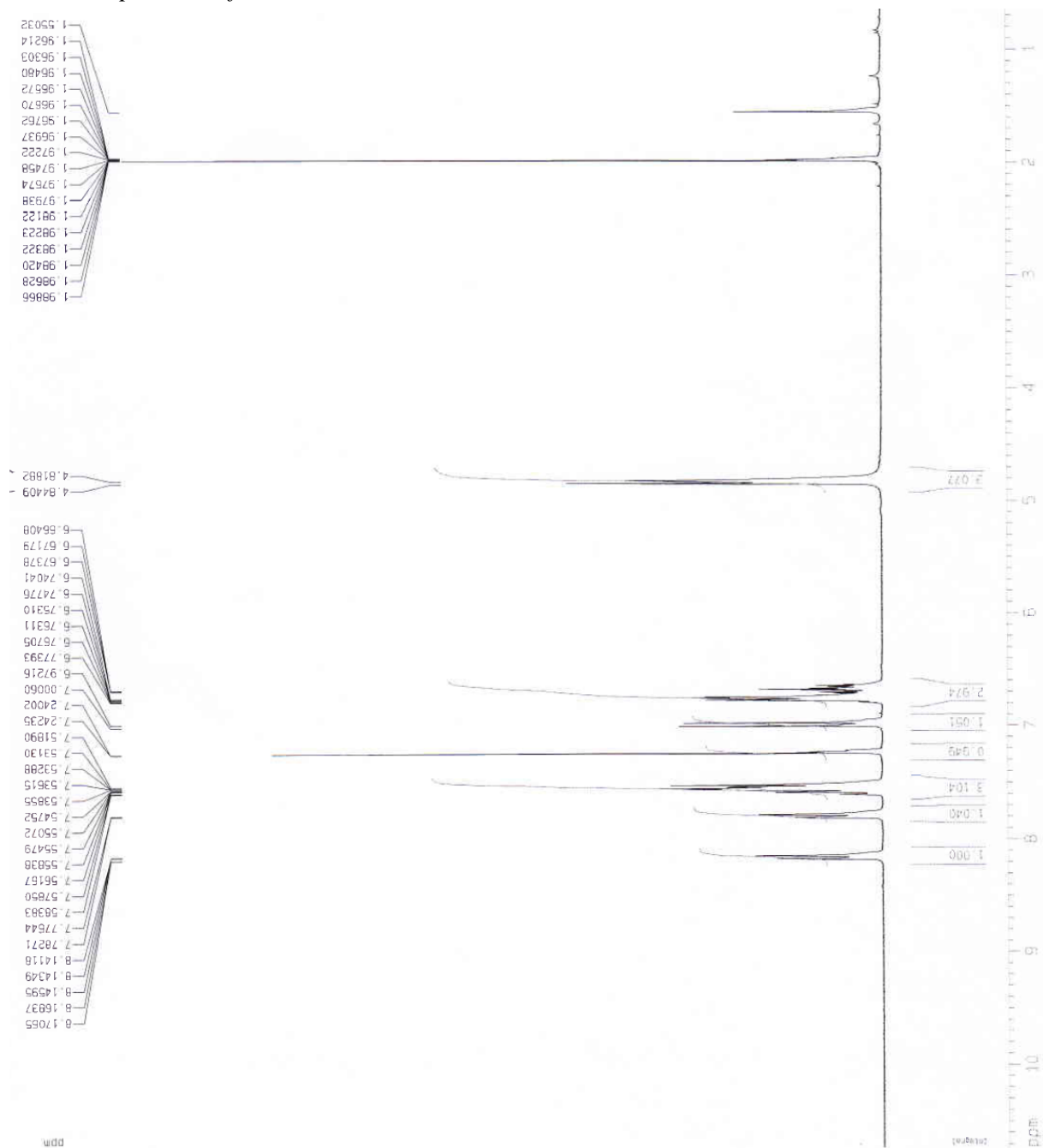


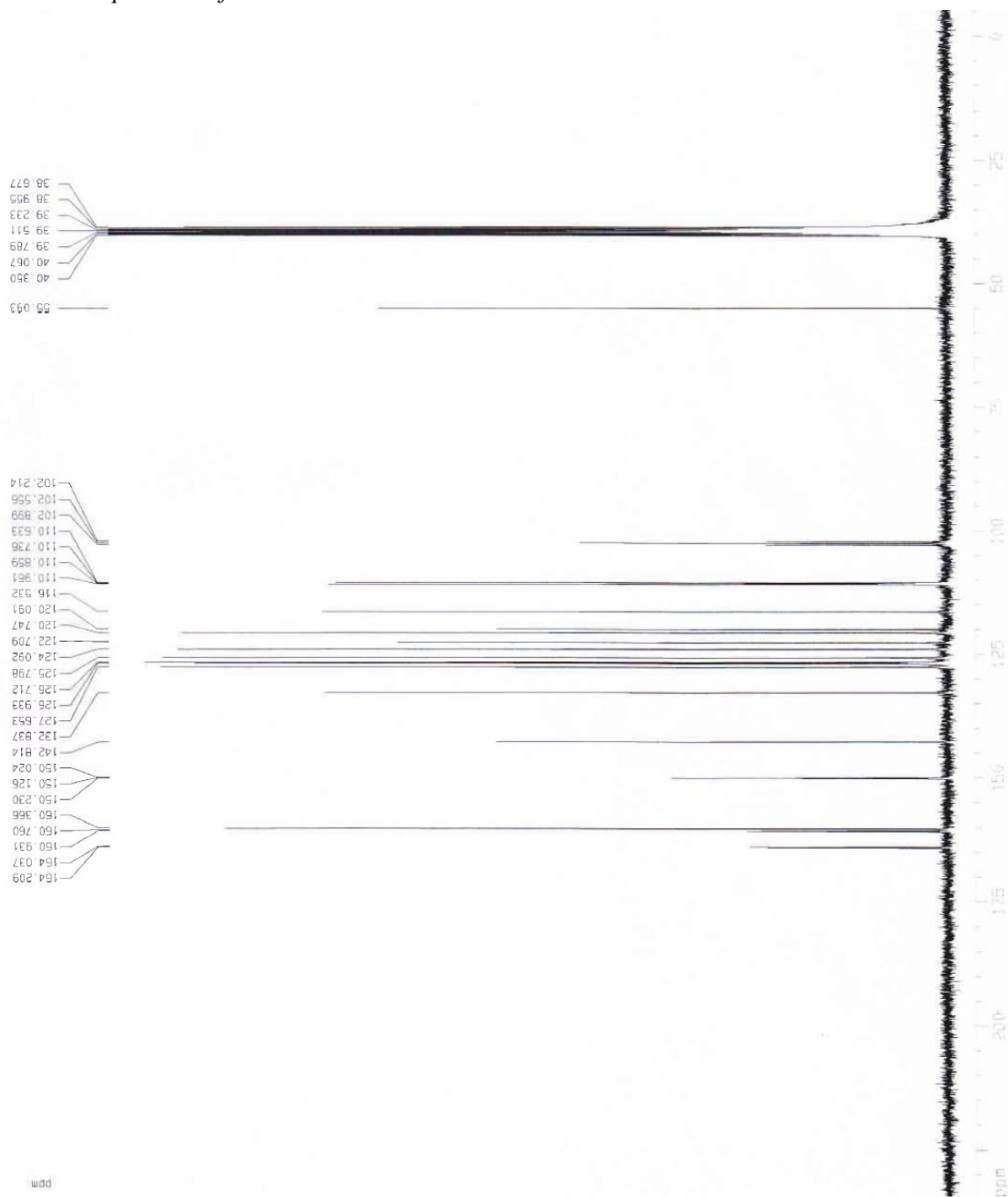
Figure S3. Vessel diameter (A), and vessel length (B) and area covered by blood vessel analyses (C; derived from fractal analysis) after 6 h incubation with vehicle (DMSO), C-A4 (2.5 nmol), **2a** (10 nmol), **2b-c** (5 nmol), **2e** (5 nmol) and **3a-c** (10 nmol). The area, length, or diameter of the blood vessels before application were set as 100%. Values are the mean \pm SD of at least two independent analyses

NMR spectra

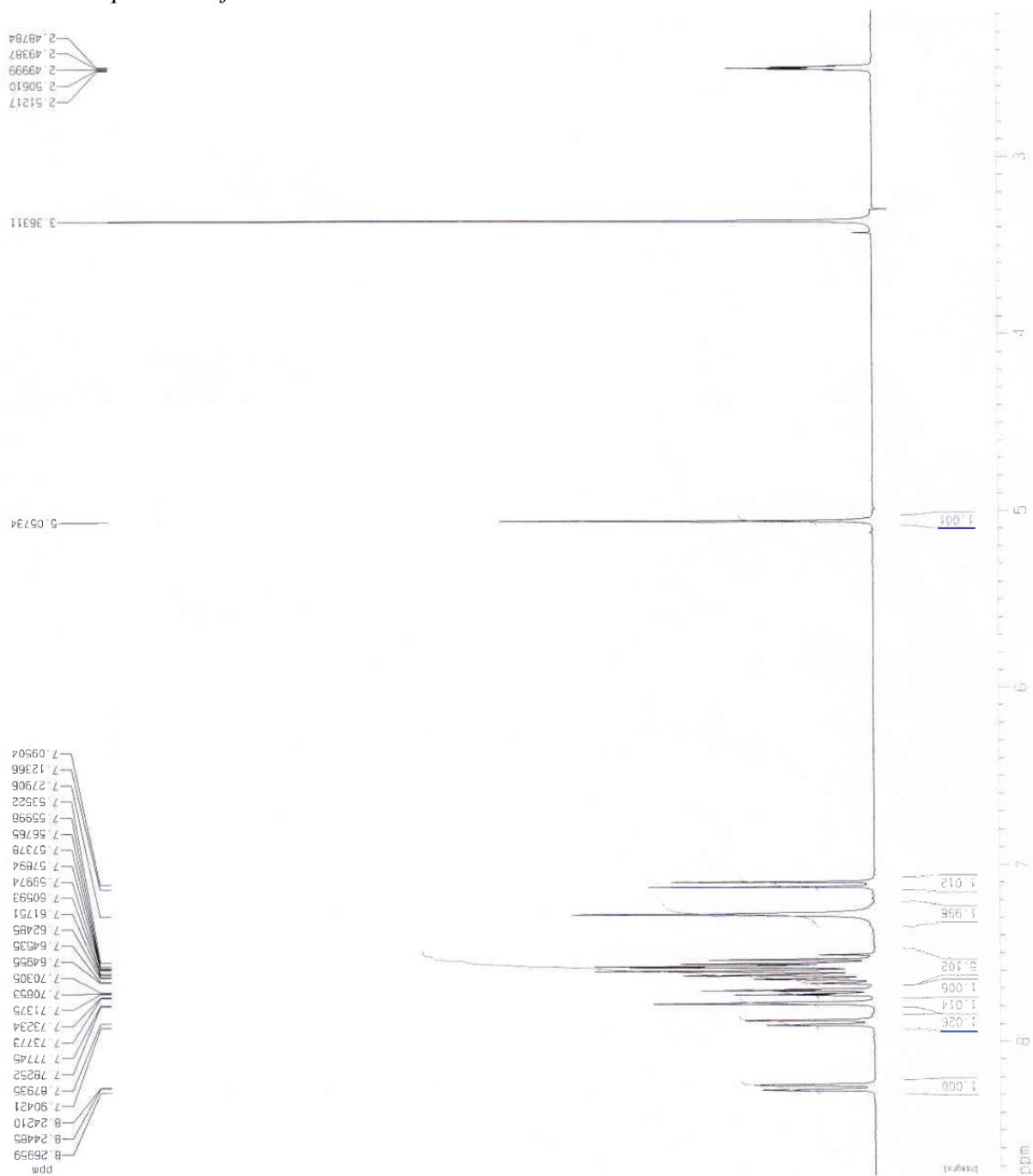
^1H NMR spectrum of **2b**



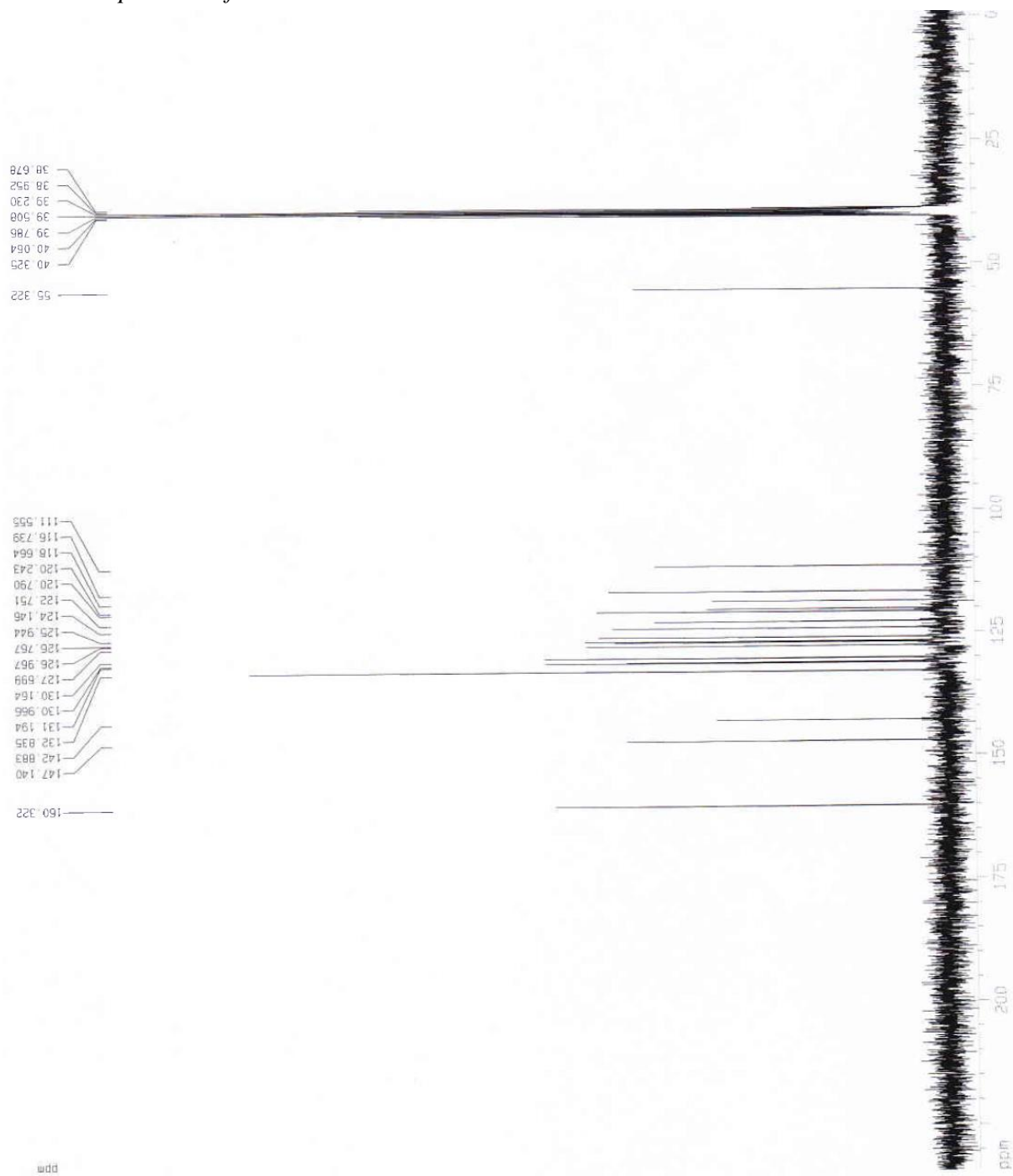
¹³C NMR spectrum of **2b**



^1H NMR spectrum of **2c**



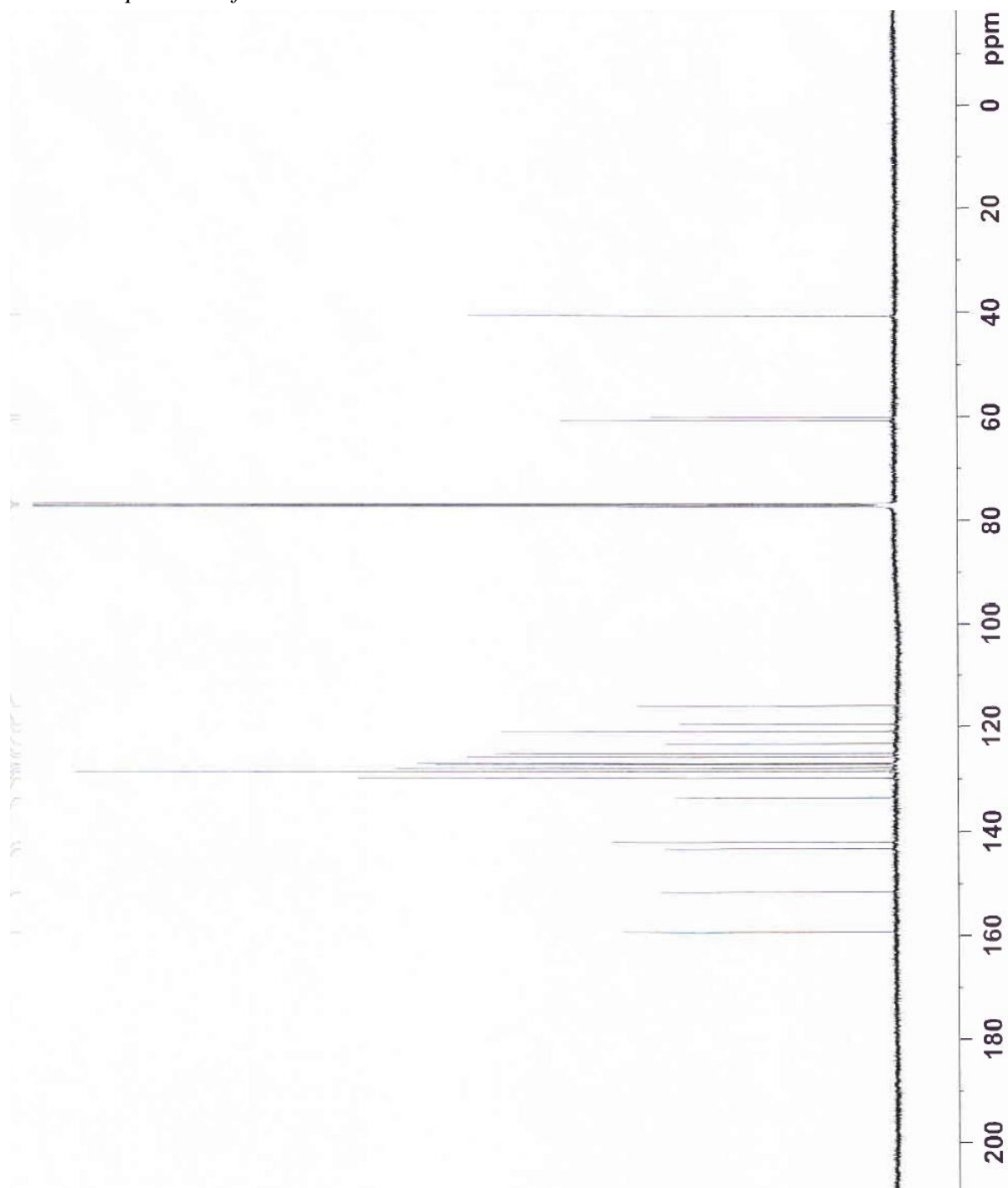
^{13}C NMR spectrum of **2c**



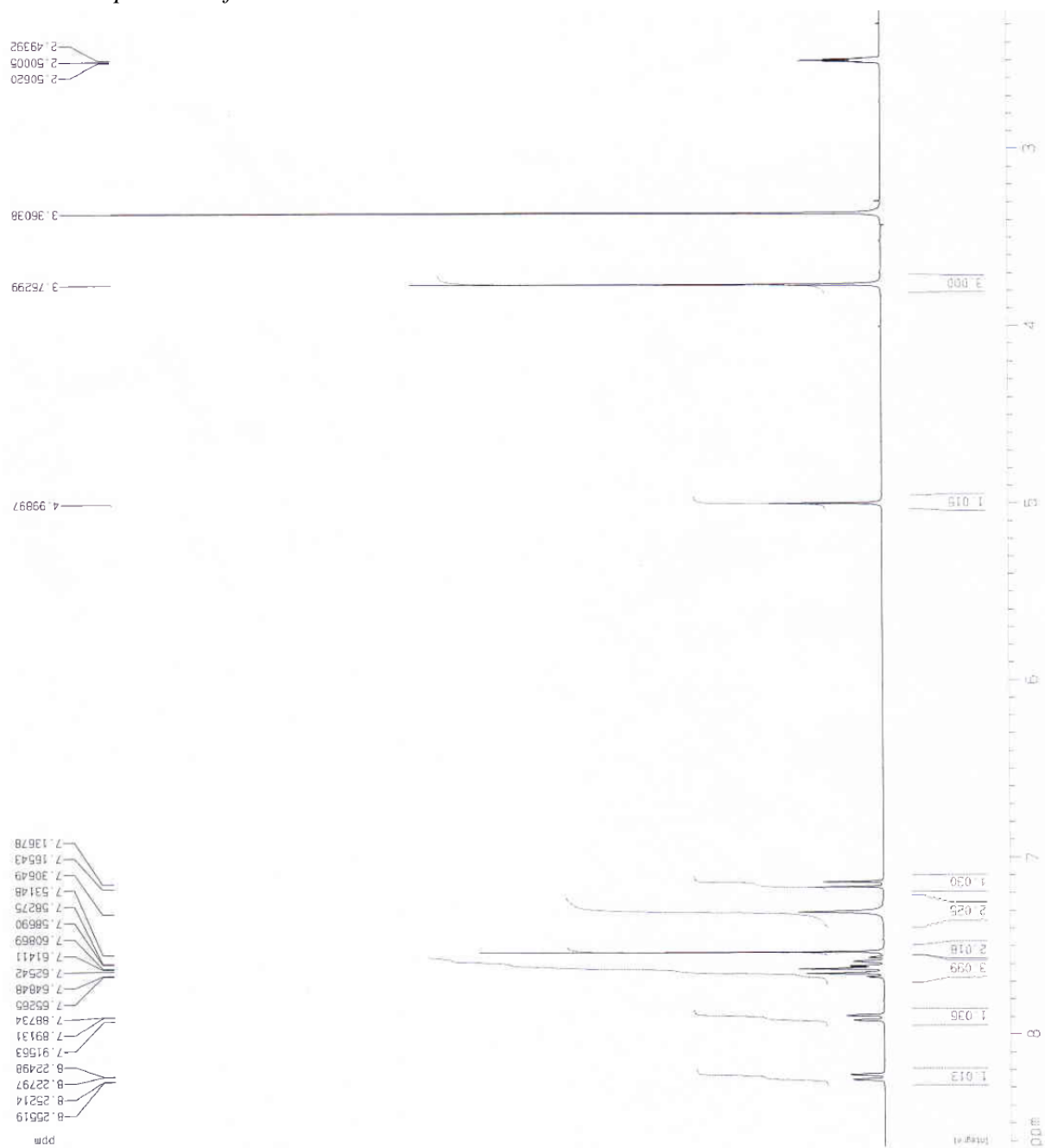
^1H NMR spectrum of **2d**



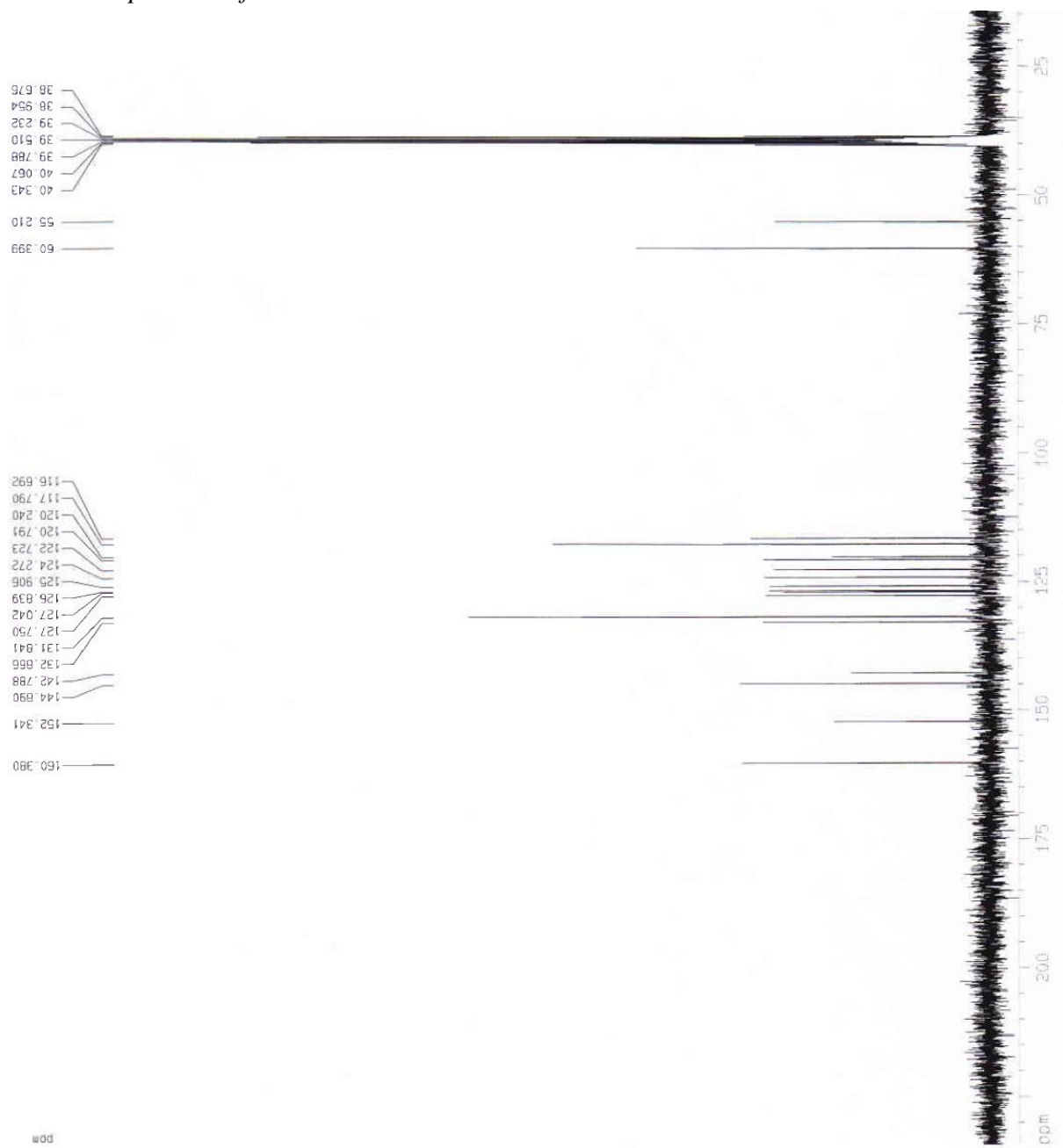
^{13}C NMR spectrum of **2d**



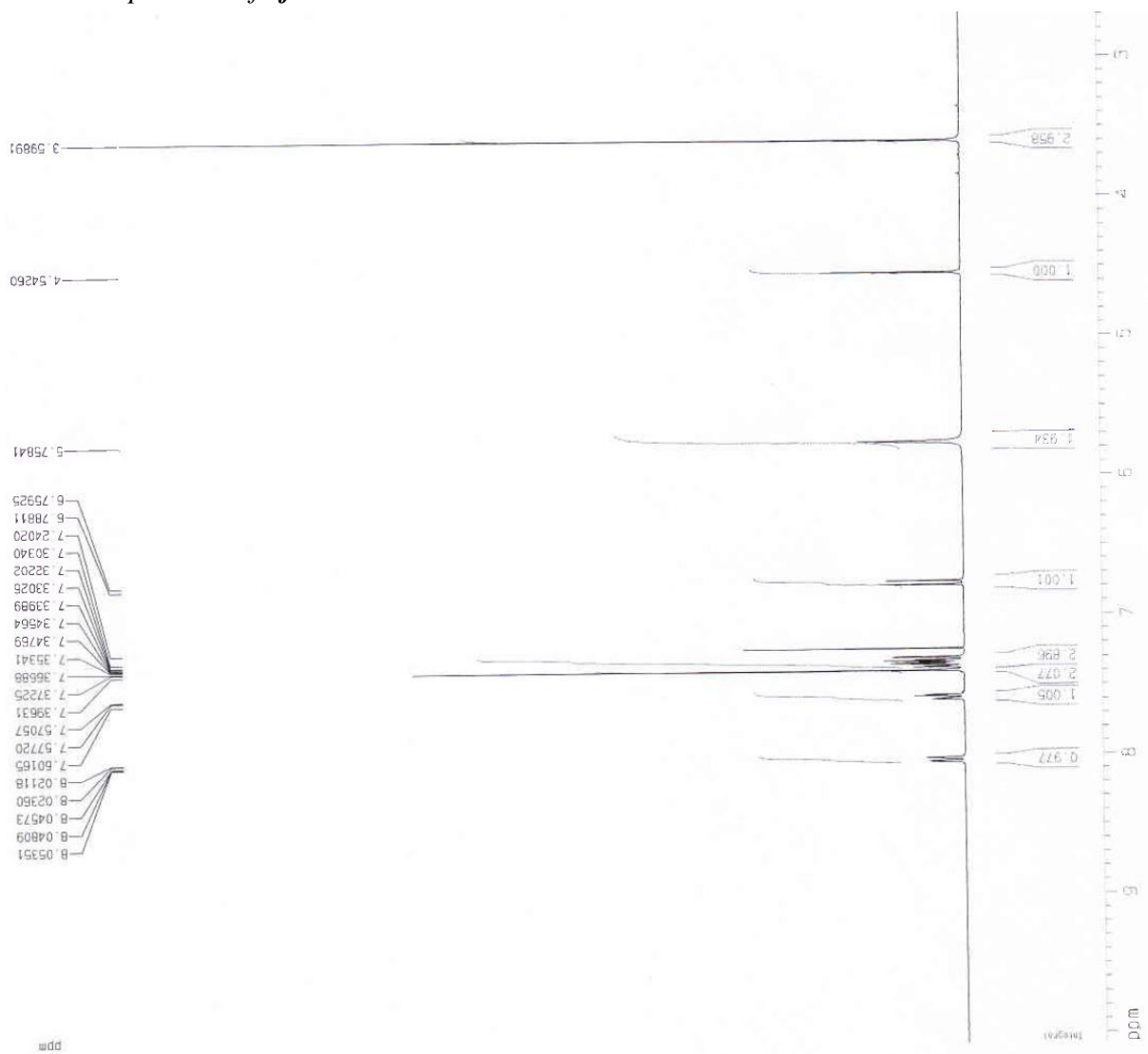
^1H NMR spectrum of **2e**



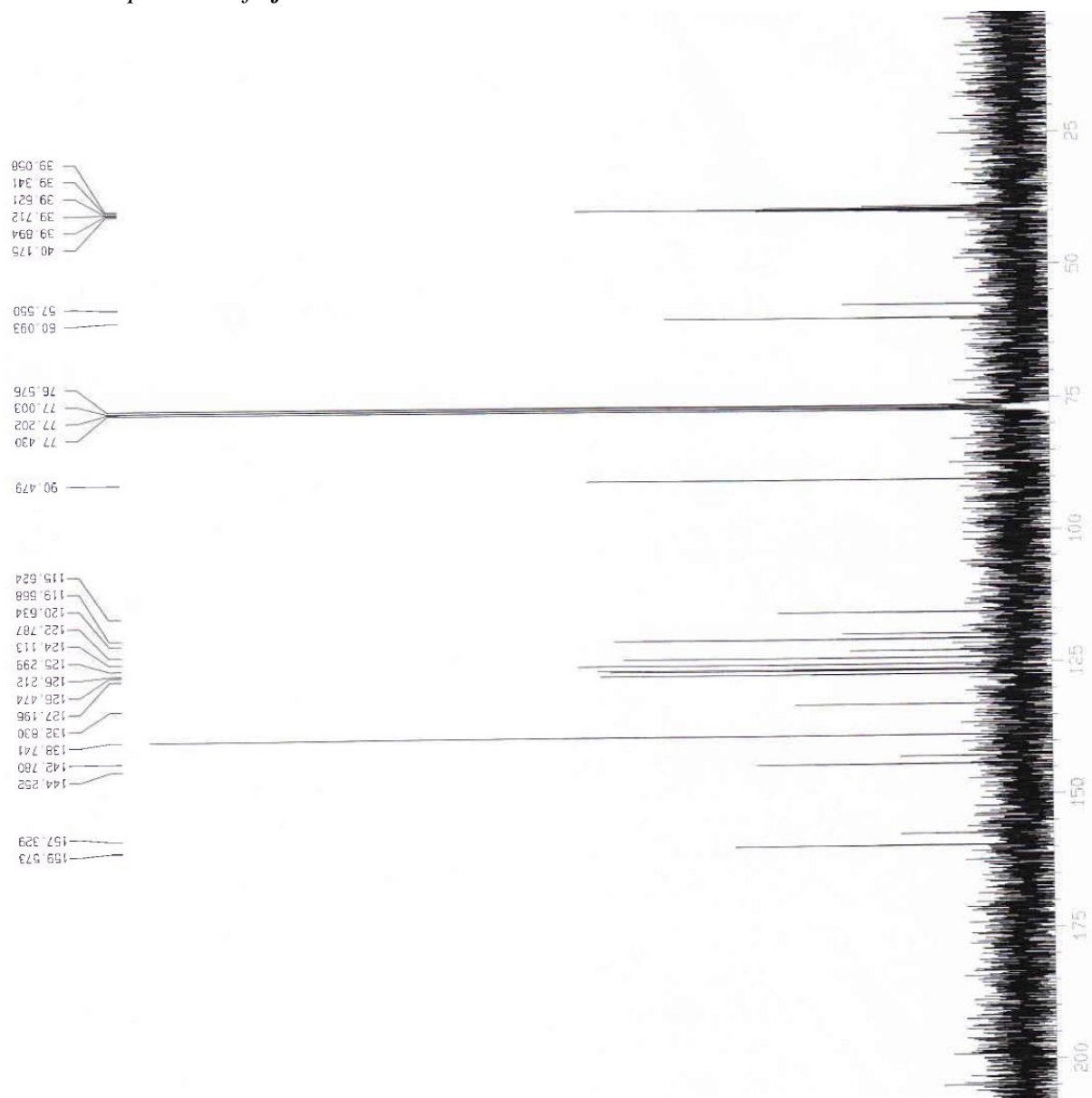
^{13}C NMR spectrum of **2e**



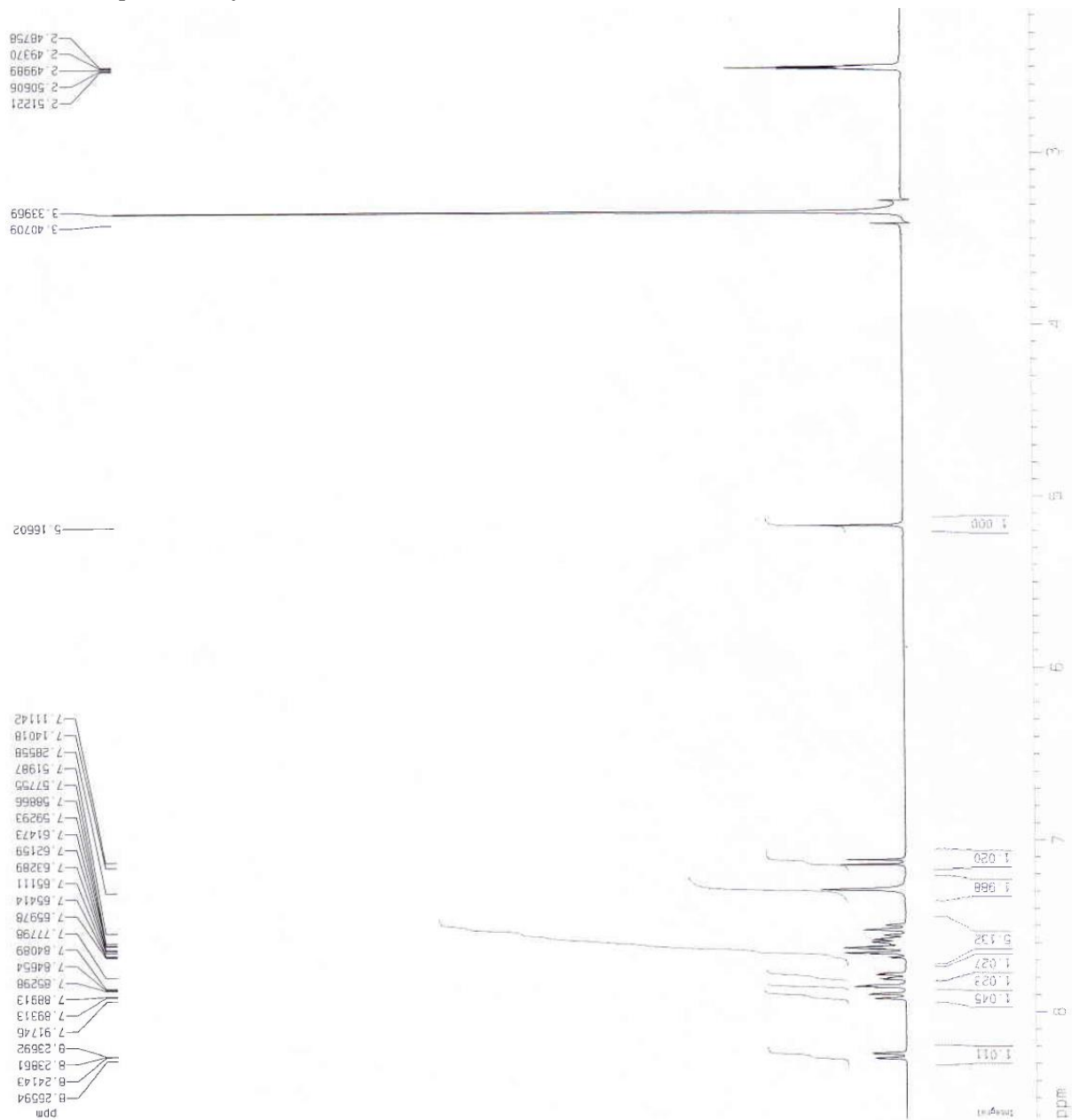
^1H NMR spectrum of **2f**



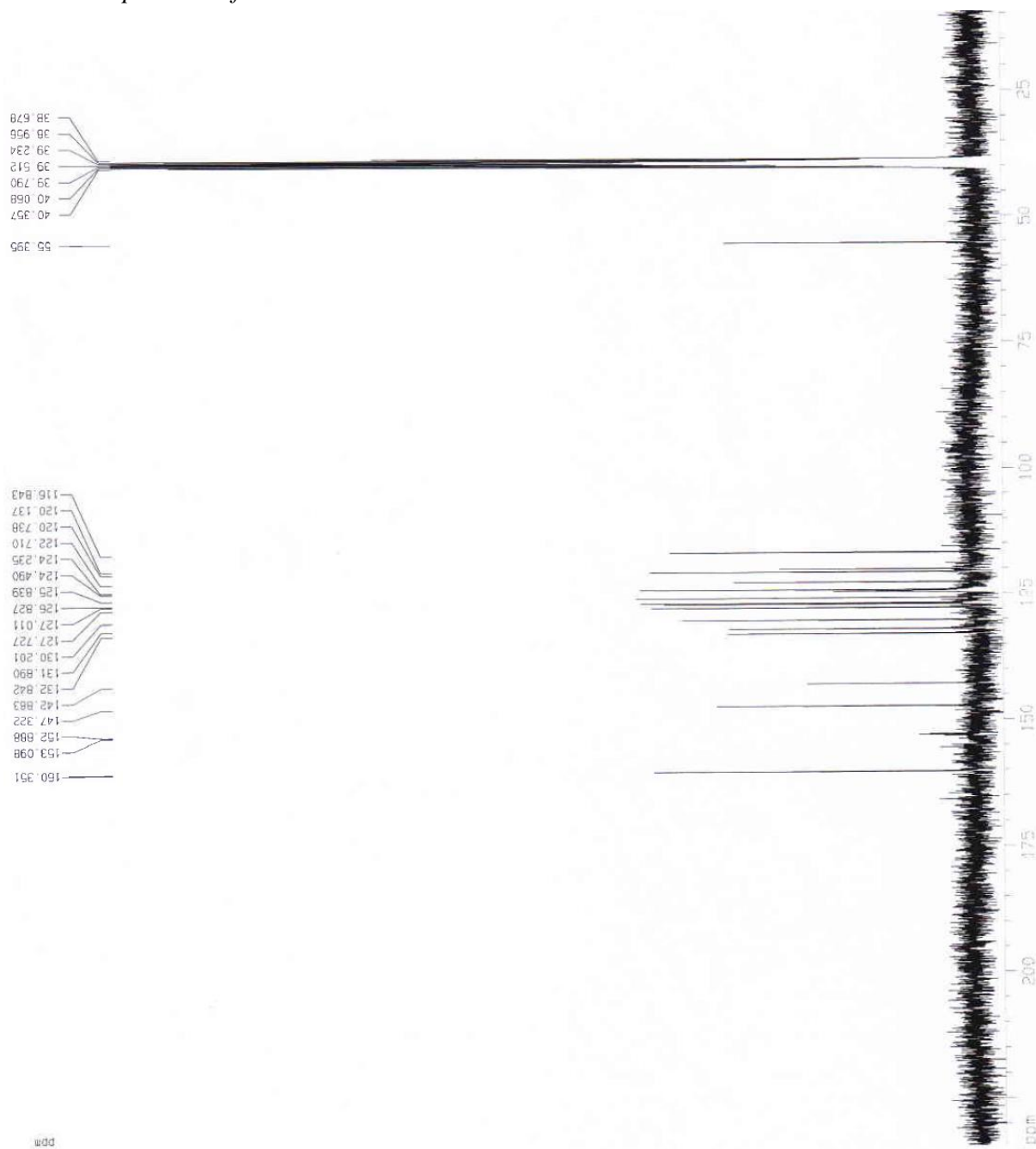
^{13}C NMR spectrum of **2f**



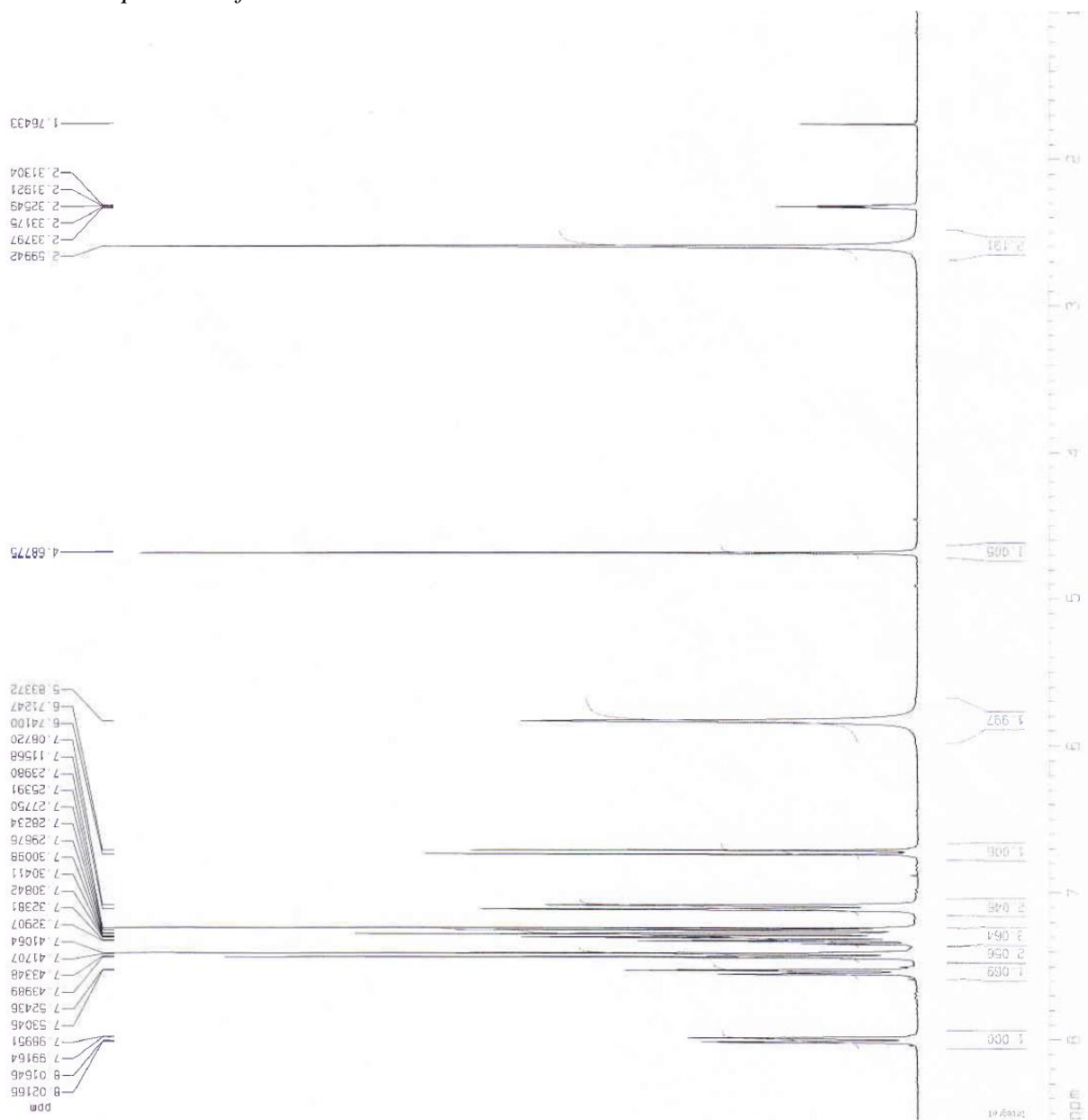
^1H NMR spectrum of **2h**



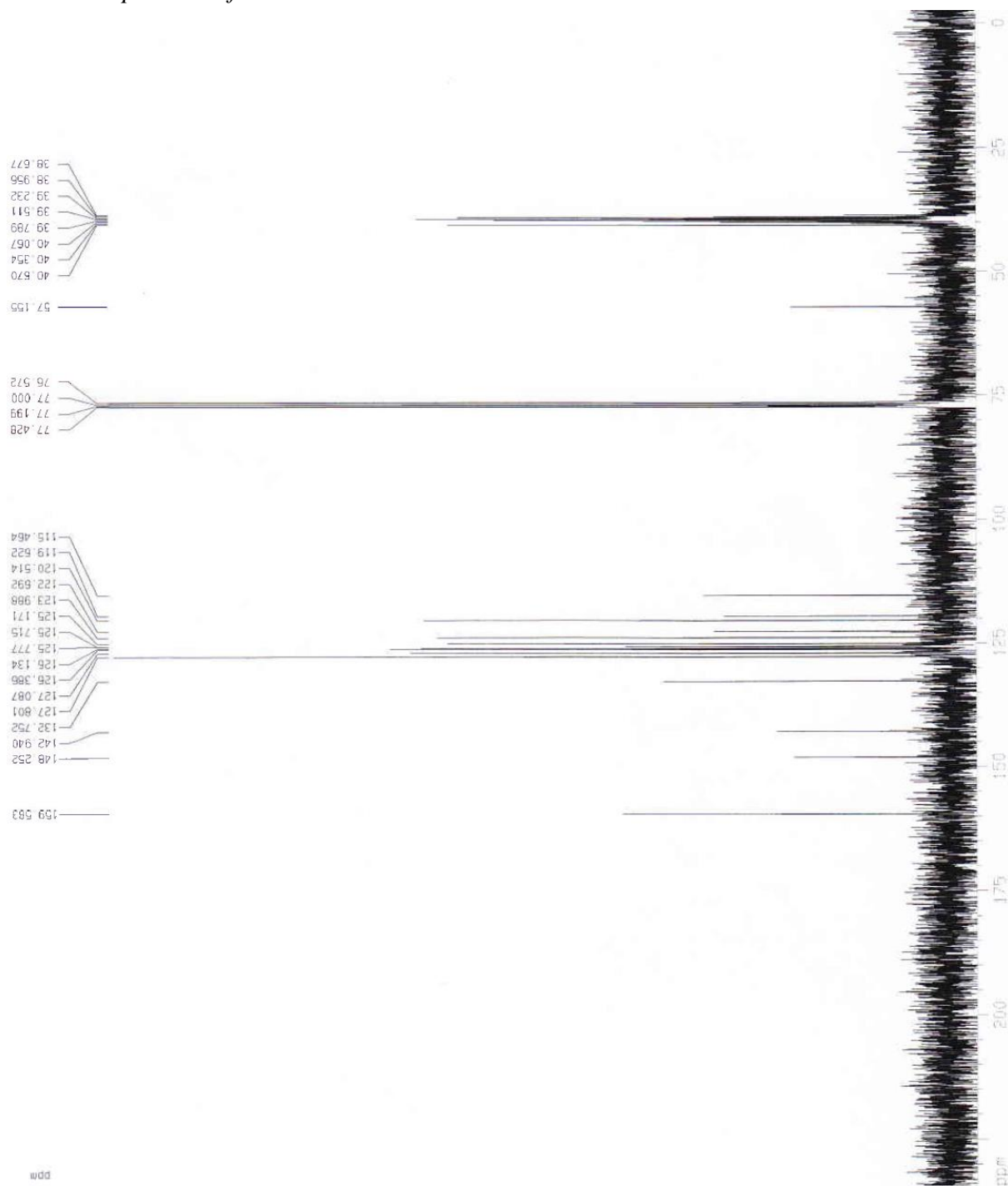
^{13}C NMR spectrum of **2h**



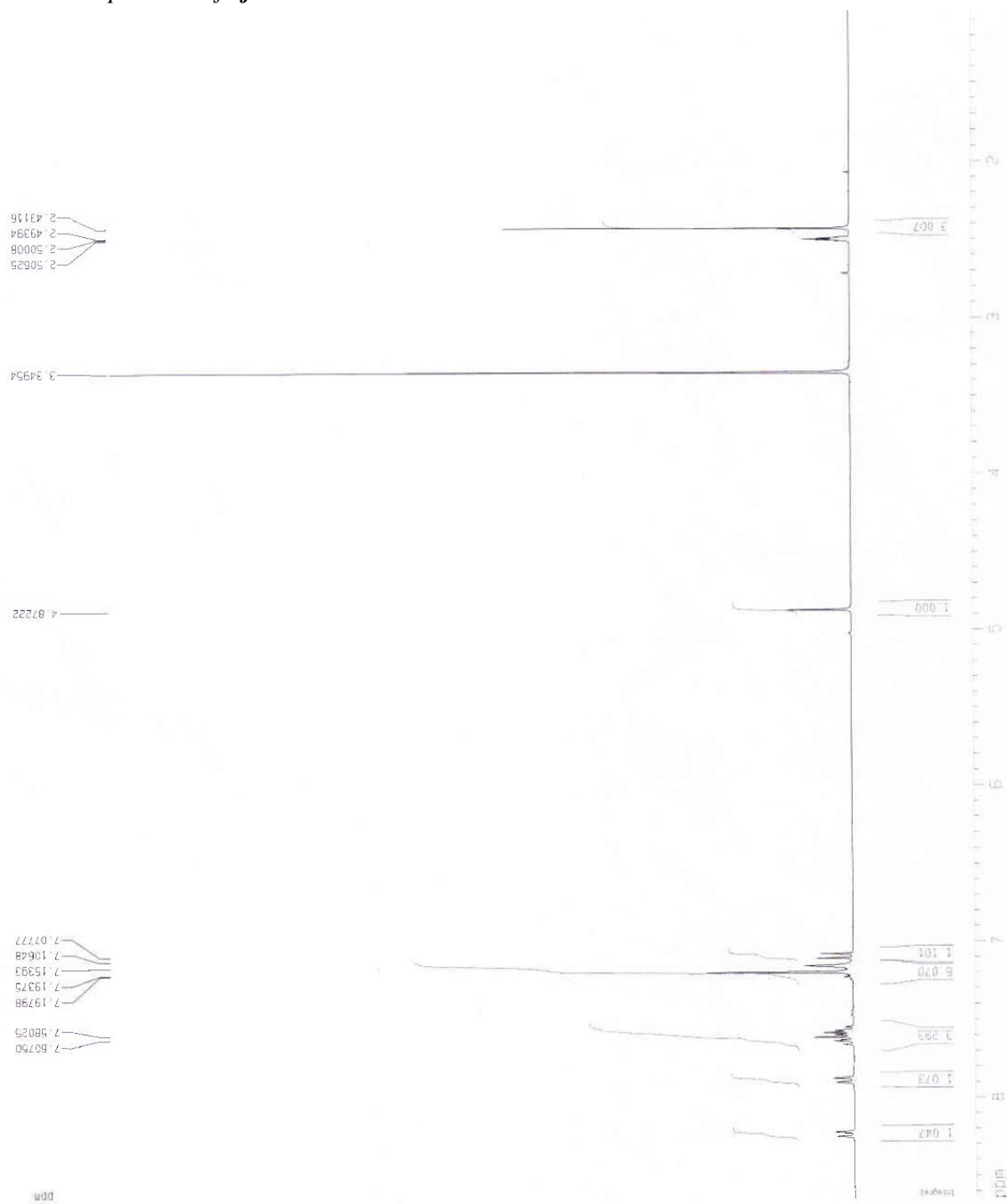
^1H NMR spectrum of **2i**



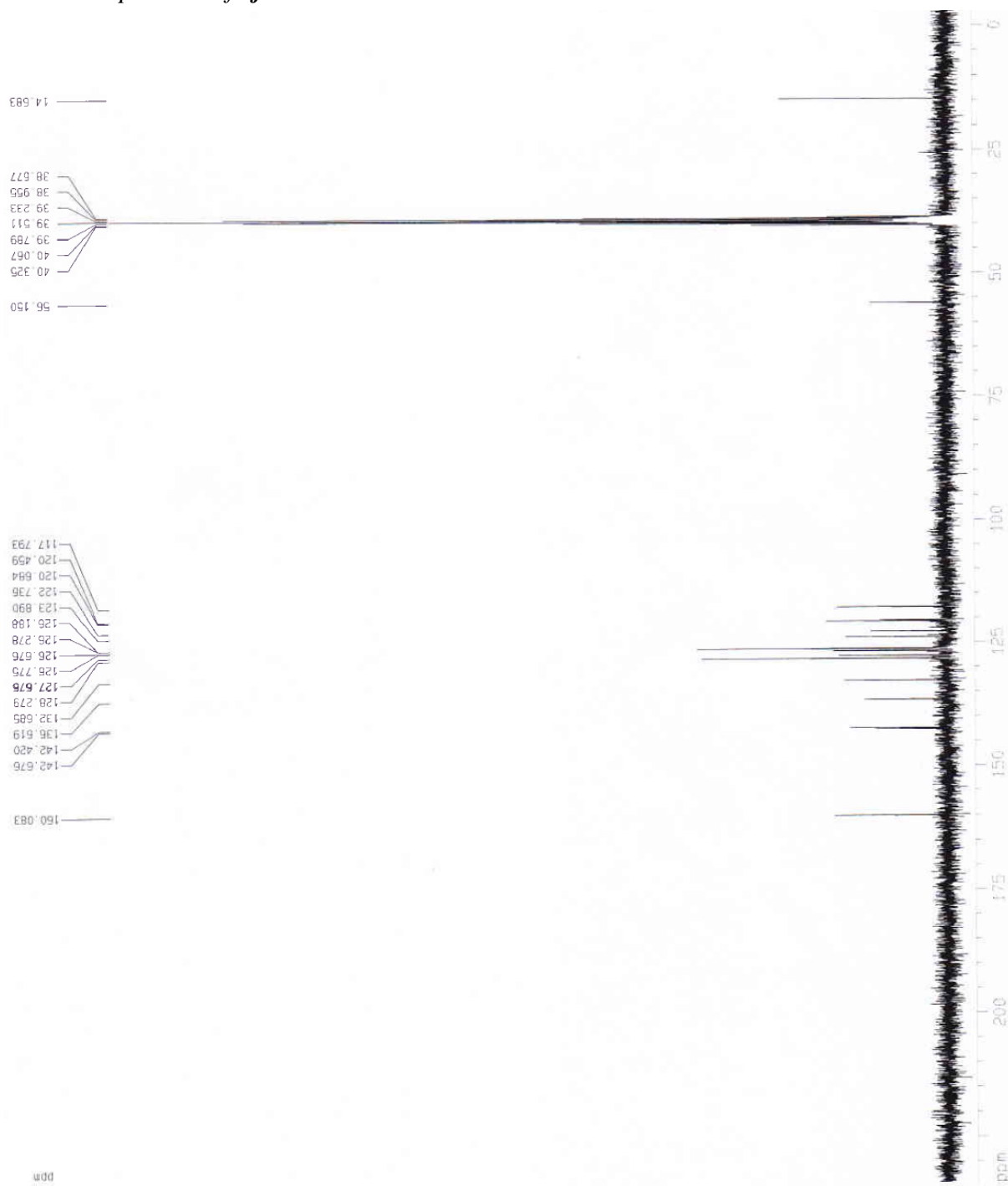
¹³C NMR spectrum of 2i



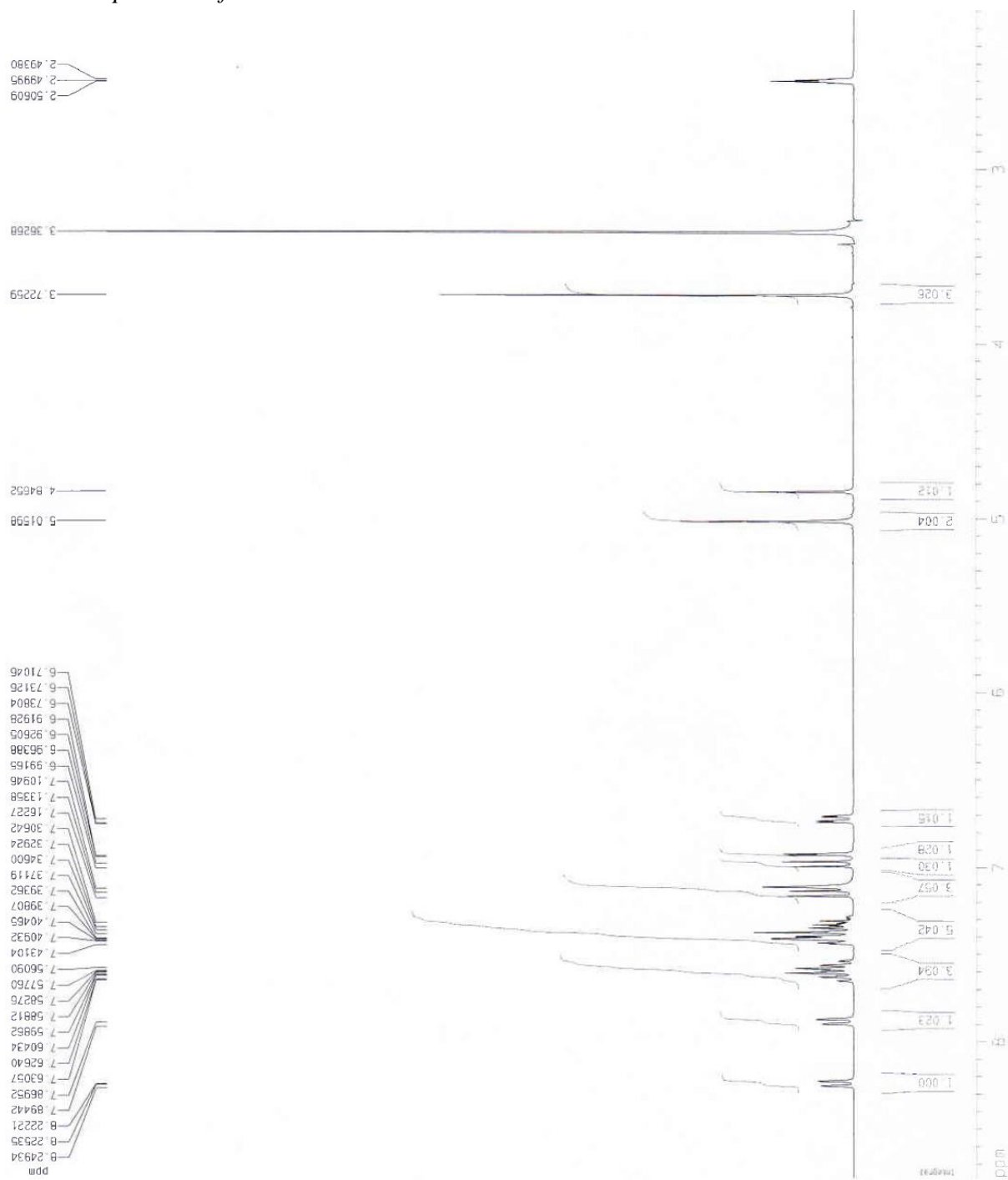
¹H NMR spectrum of 2j



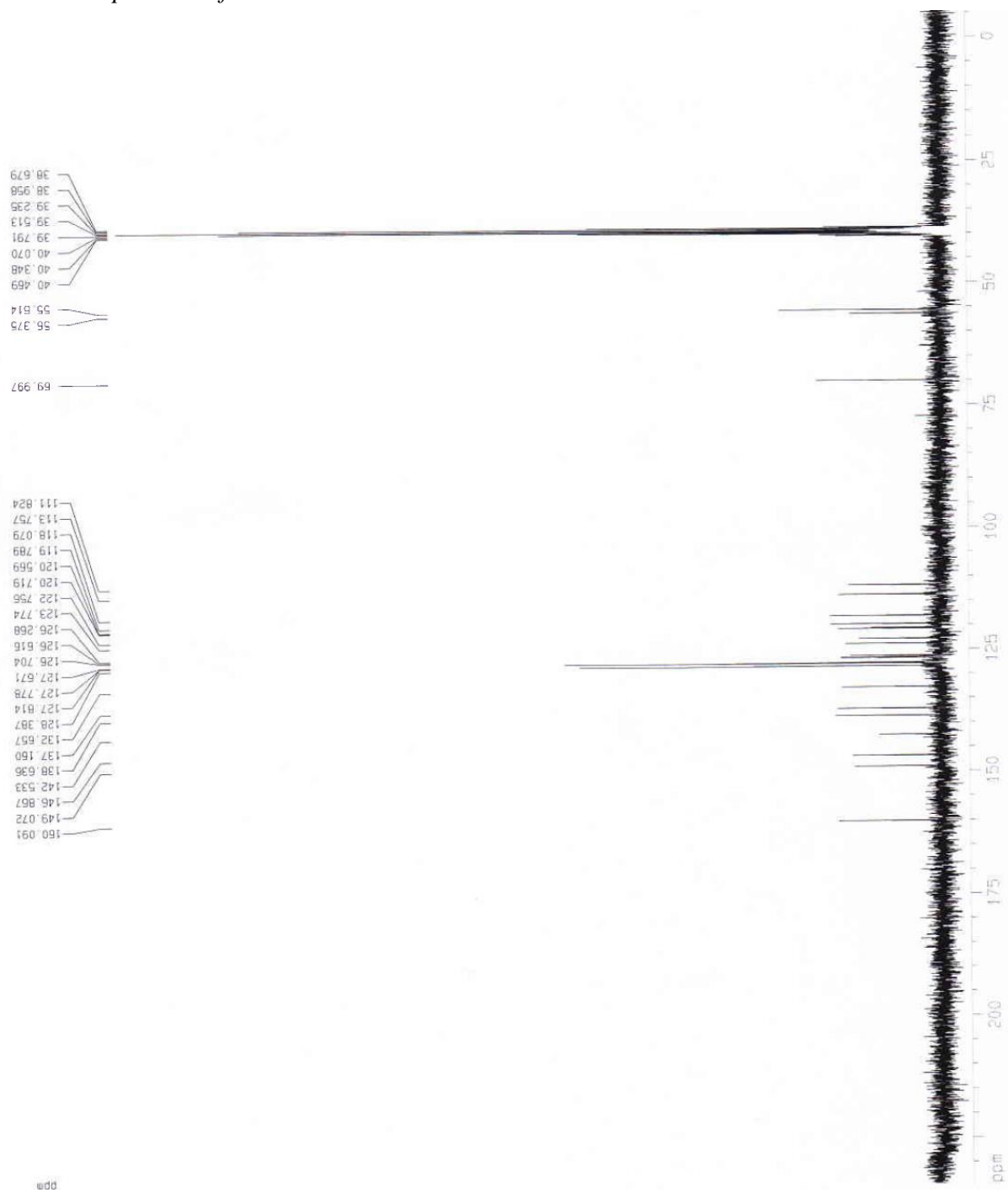
^{13}C NMR spectrum of **2j**



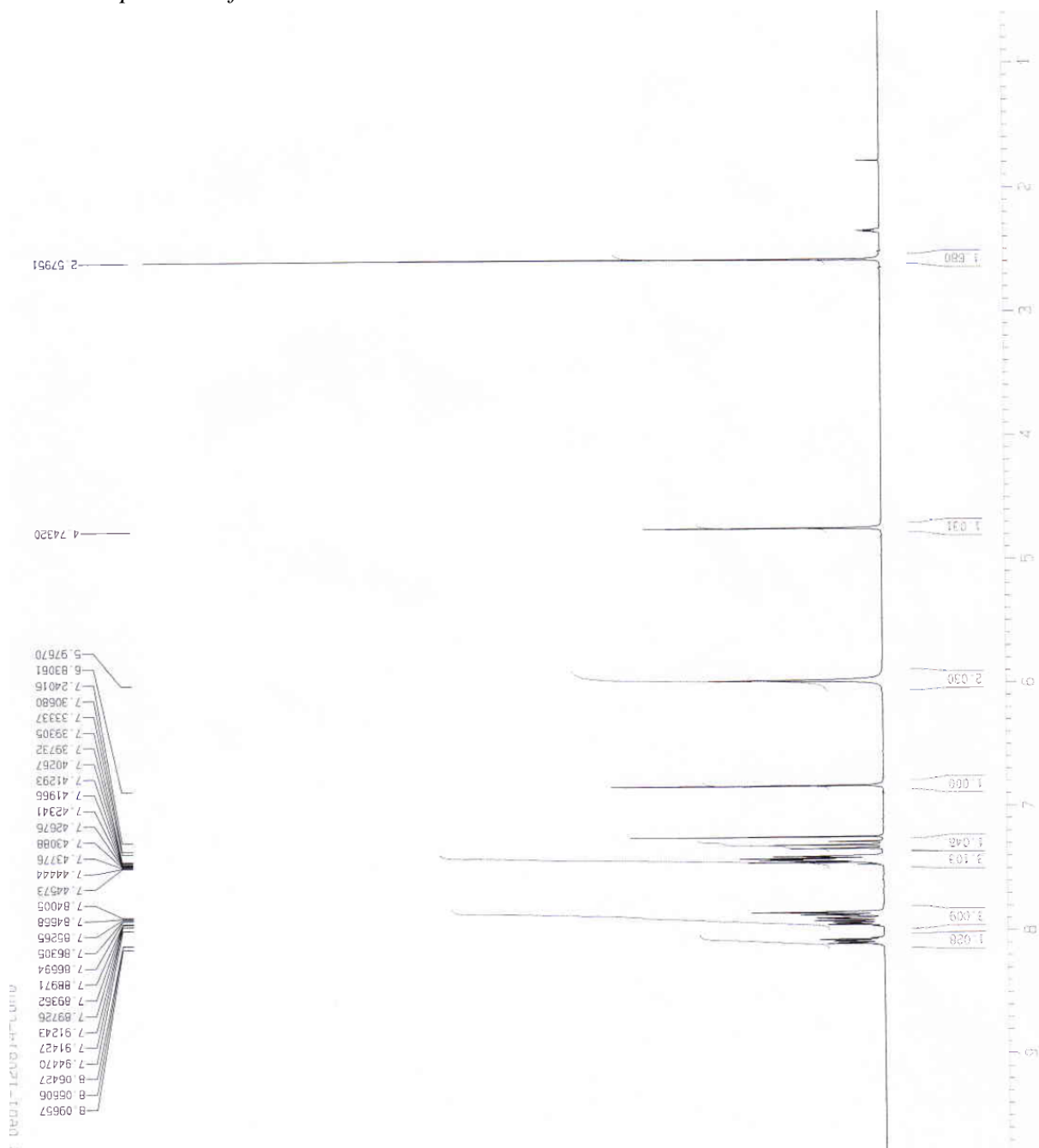
¹H NMR spectrum of 2k



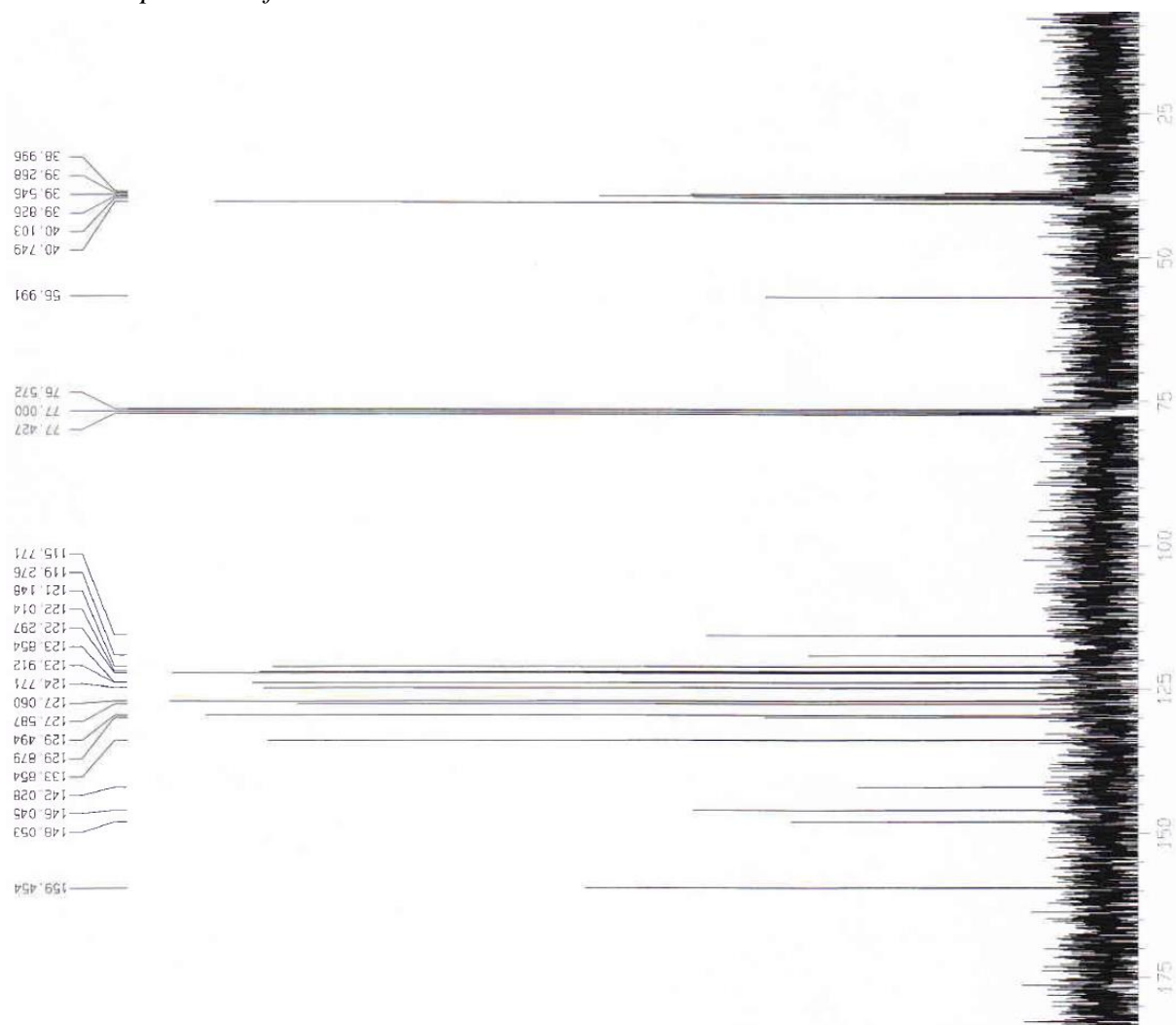
¹³C NMR spectrum of **2k**



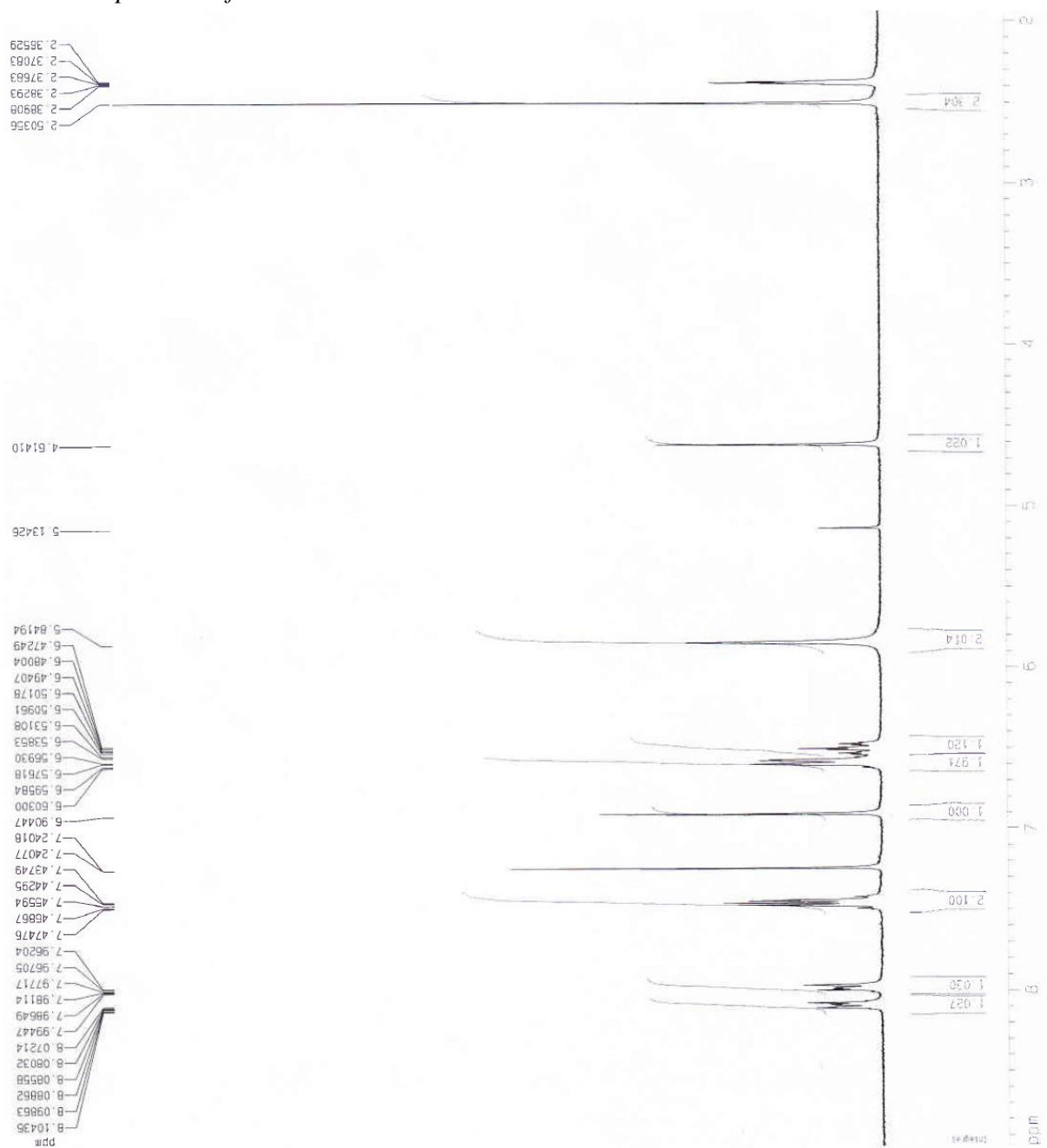
¹H NMR spectrum of 3a



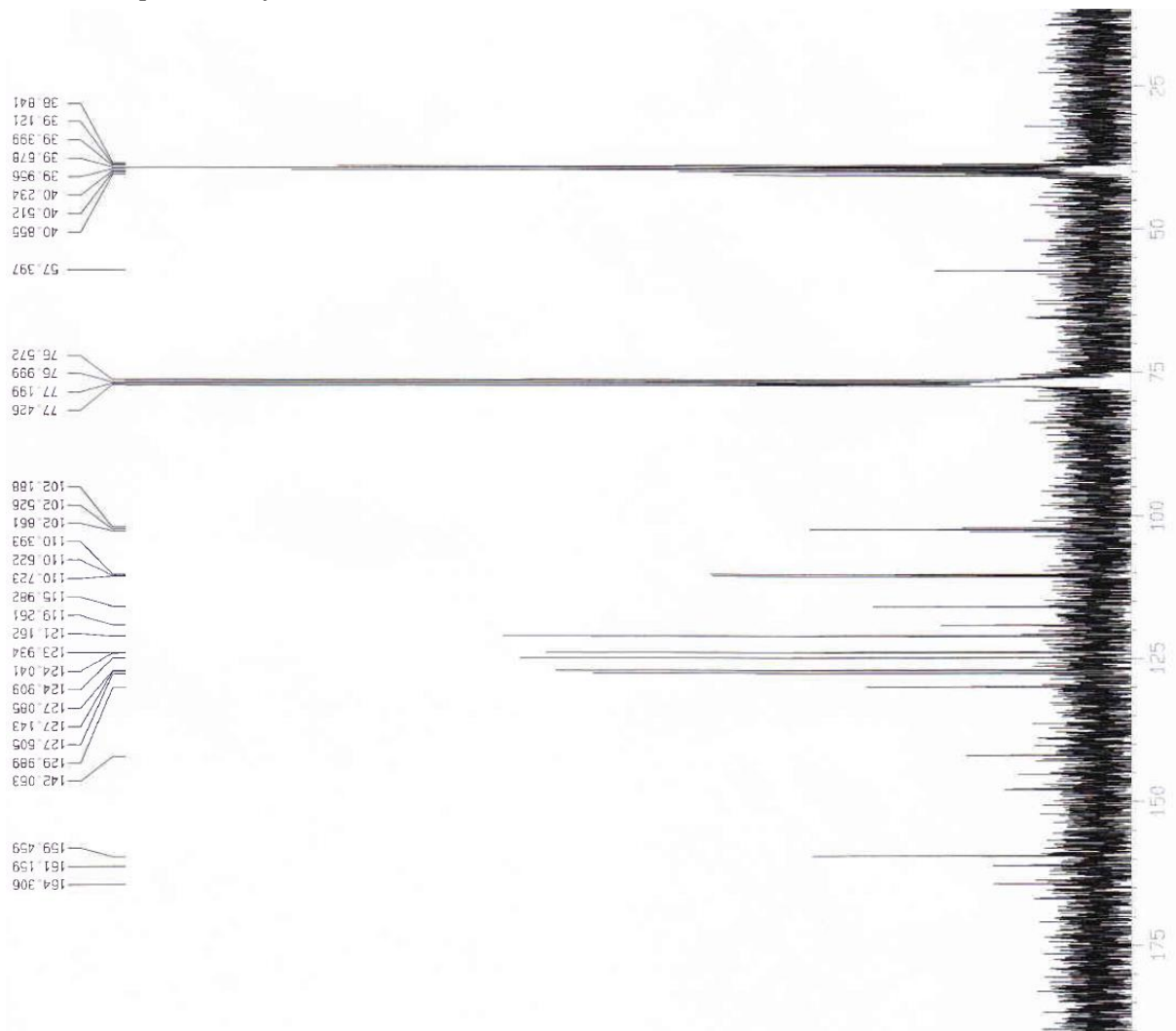
¹³C NMR spectrum of **3a**



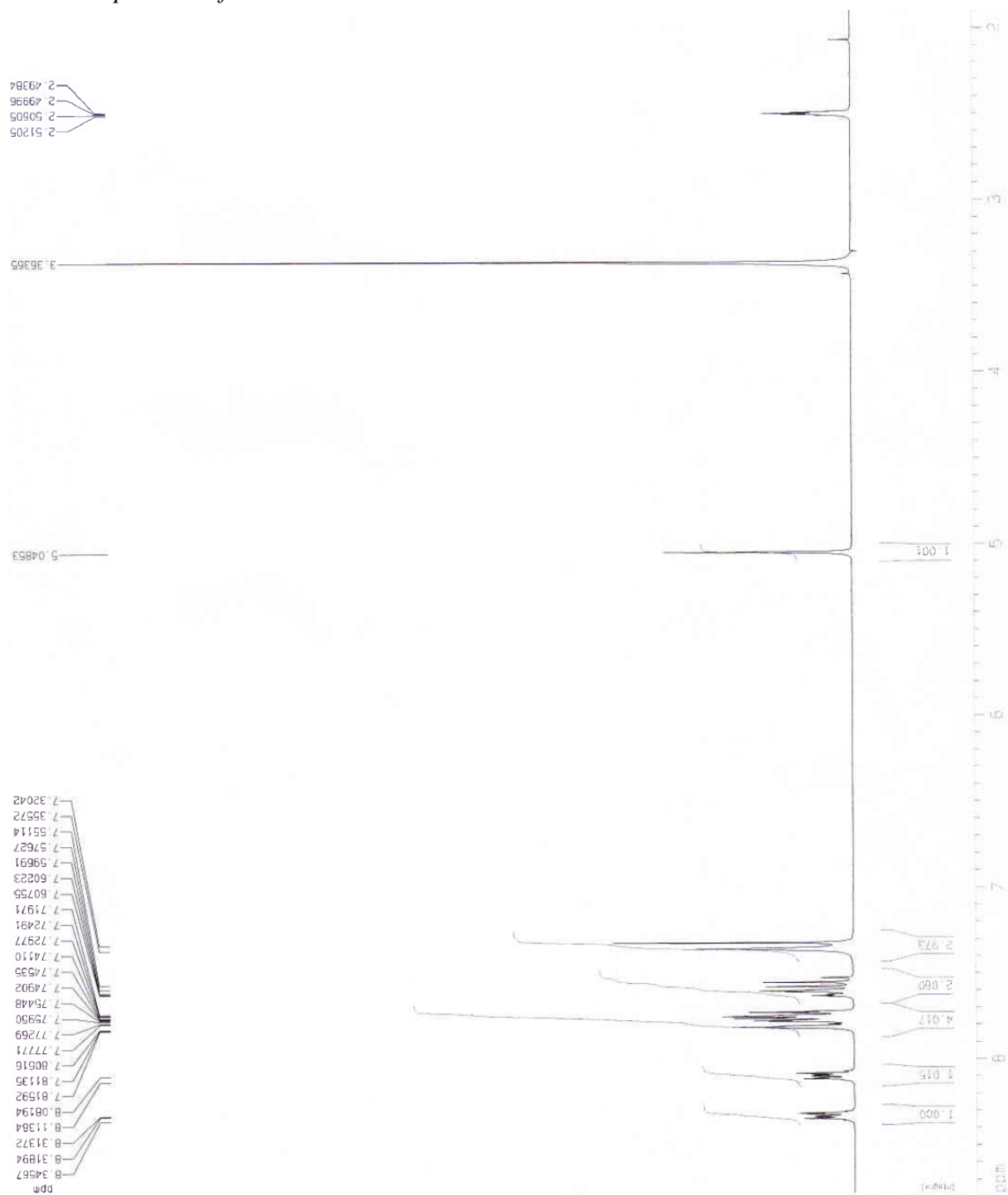
¹H NMR spectrum of 3b



¹³C NMR spectrum of **3b**



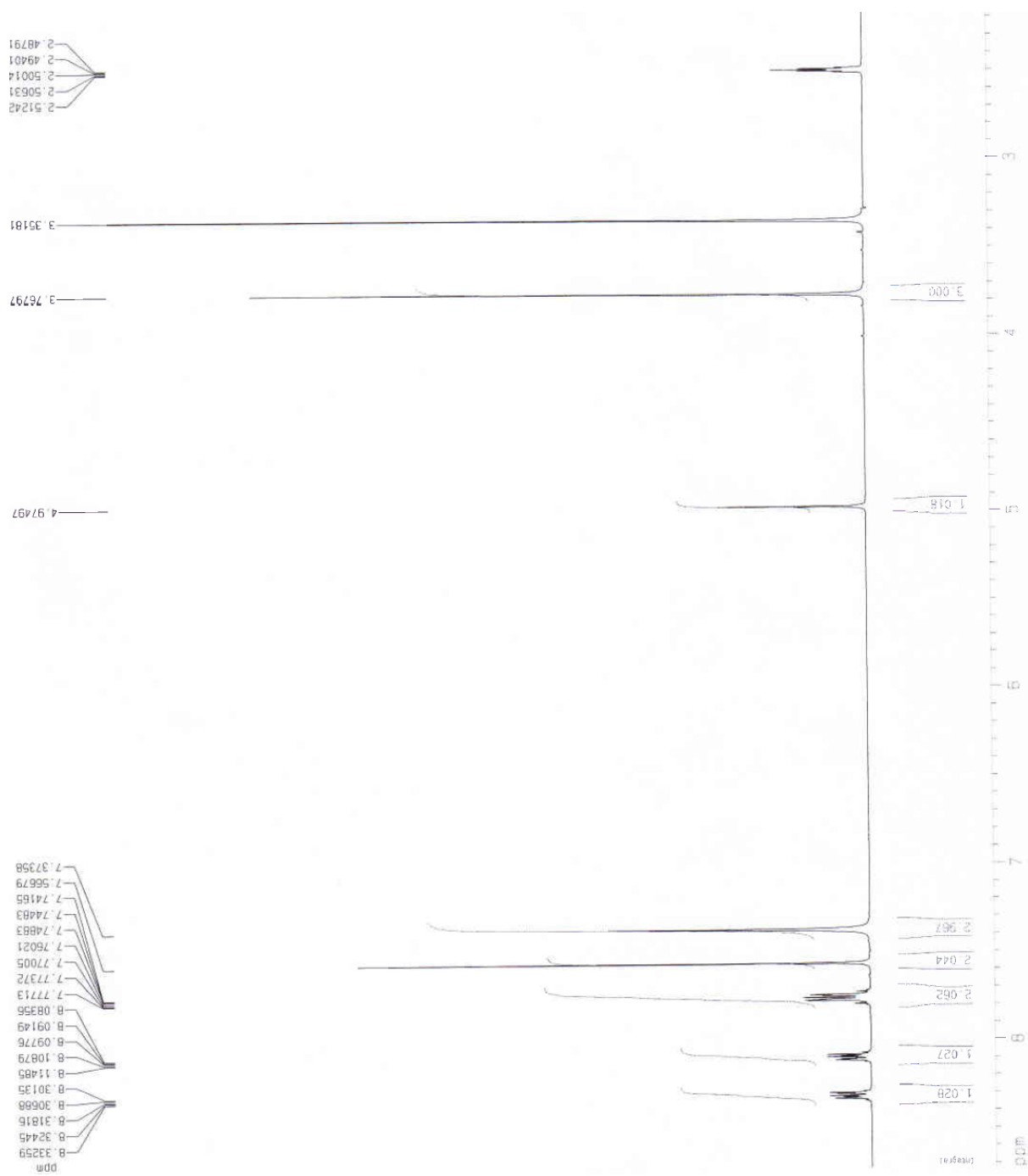
¹H NMR spectrum of 3c



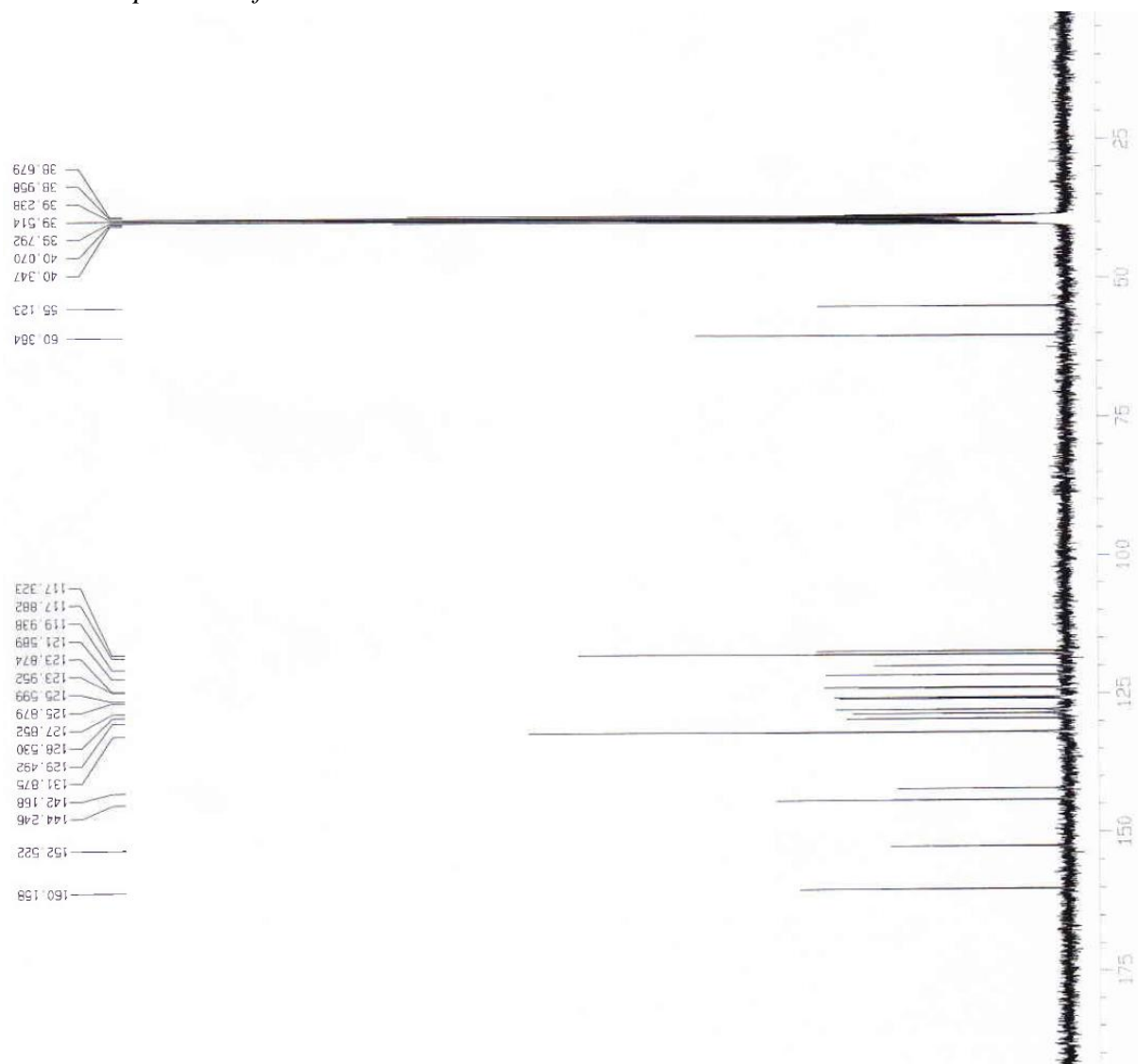
¹³C NMR spectrum of **3c**



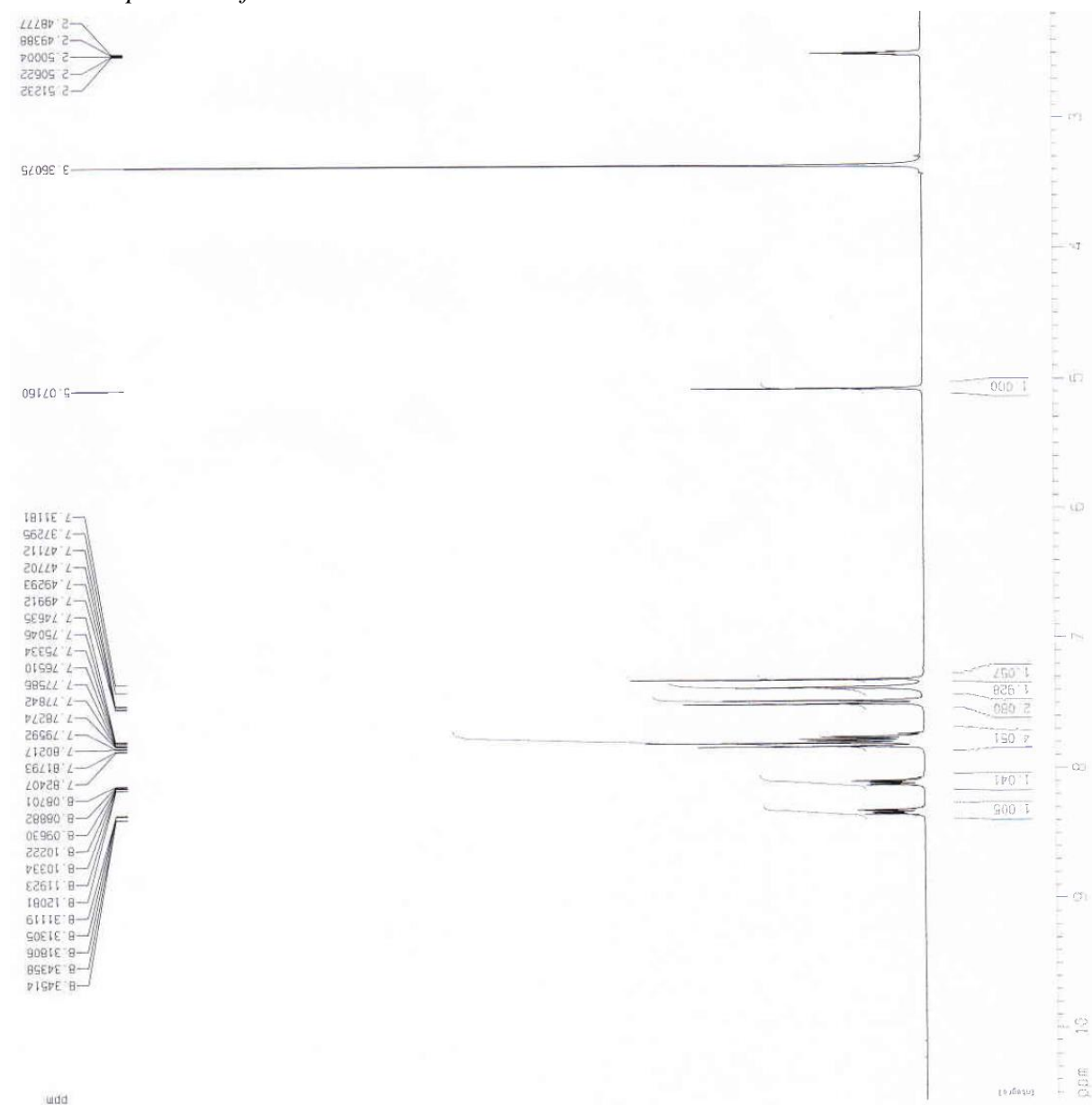
¹H NMR spectrum of 3d



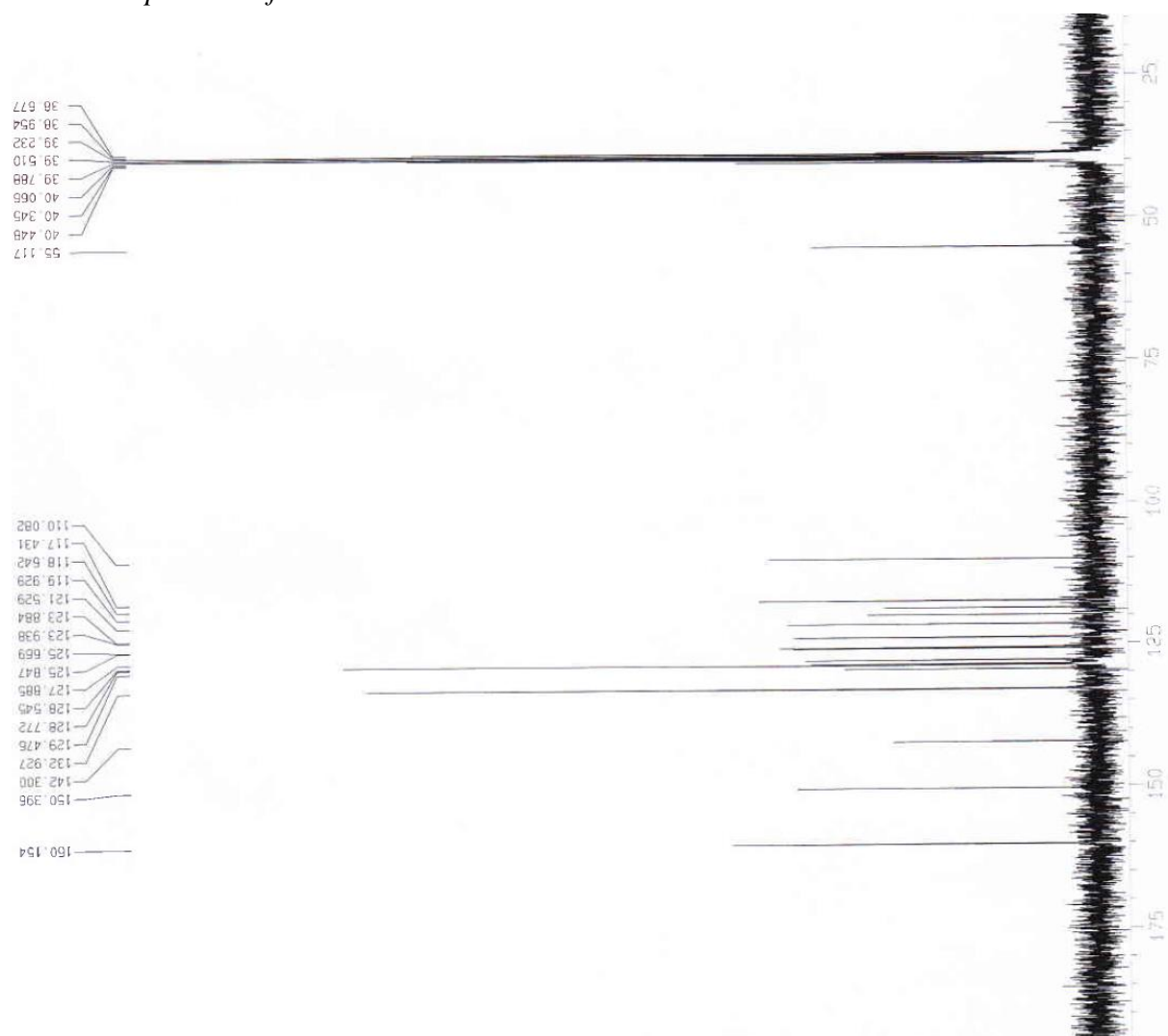
^{13}C NMR spectrum of **3d**



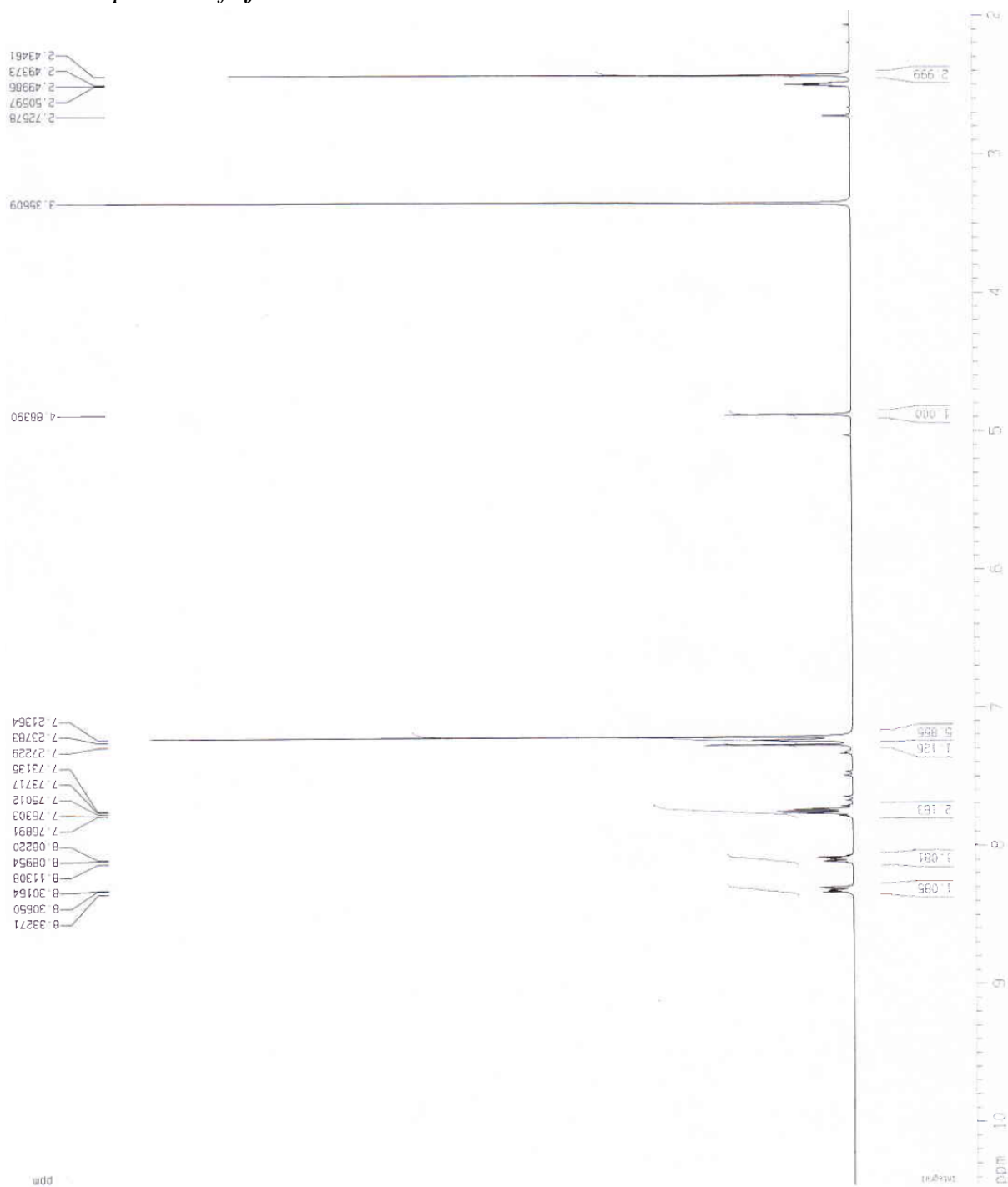
^1H NMR spectrum of **3e**



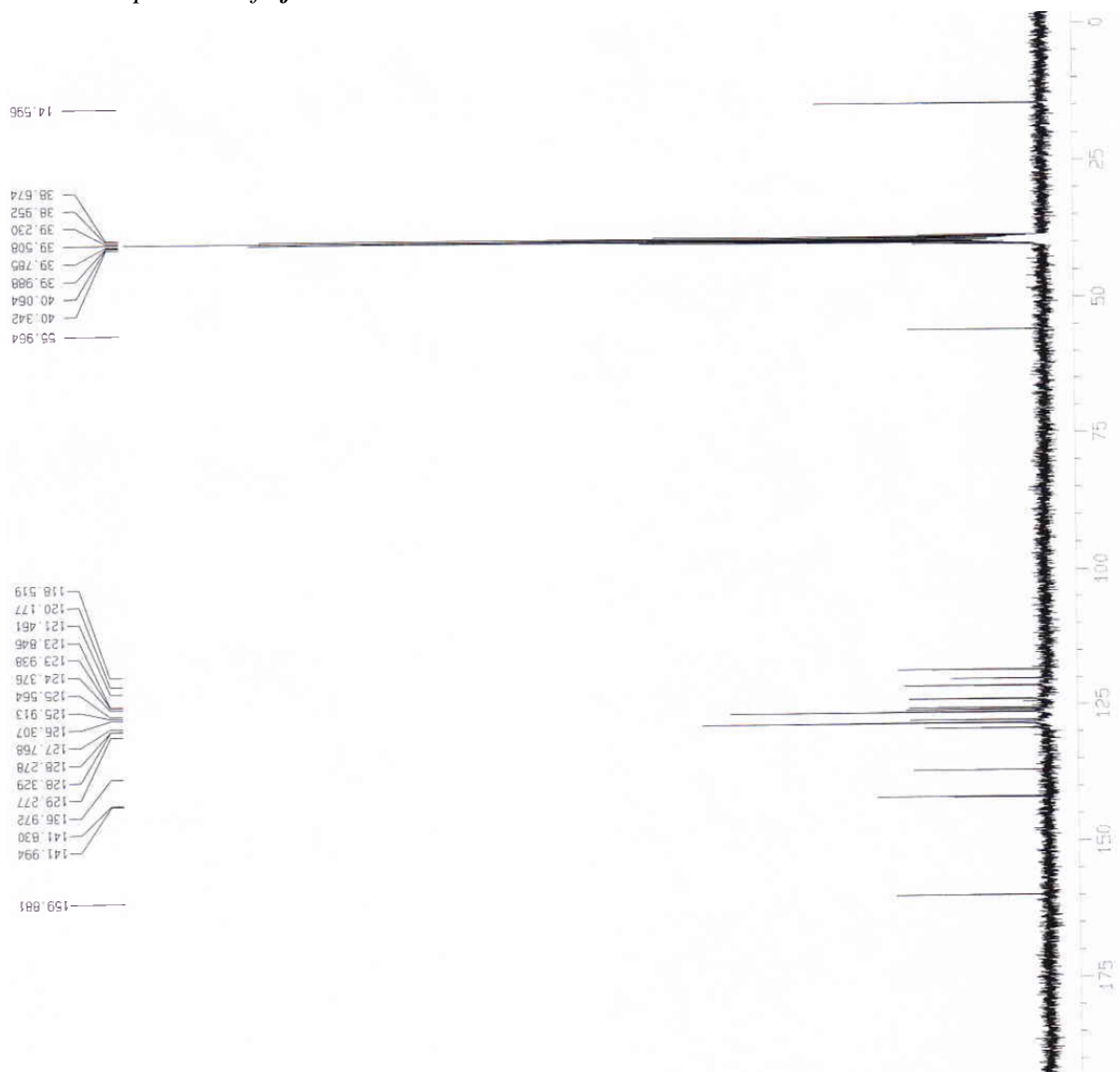
^{13}C NMR spectrum of **3e**



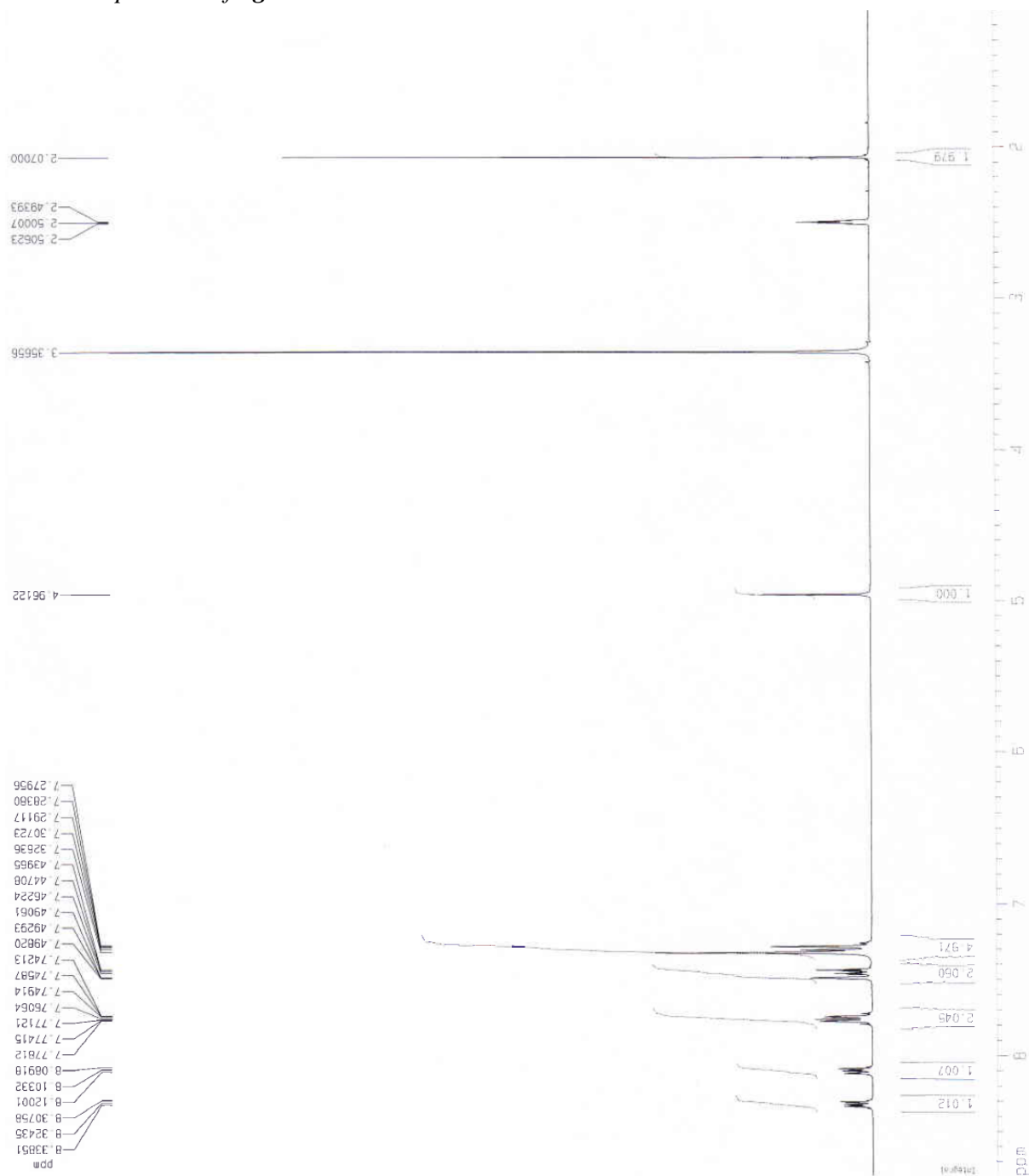
¹H NMR spectrum of 3f



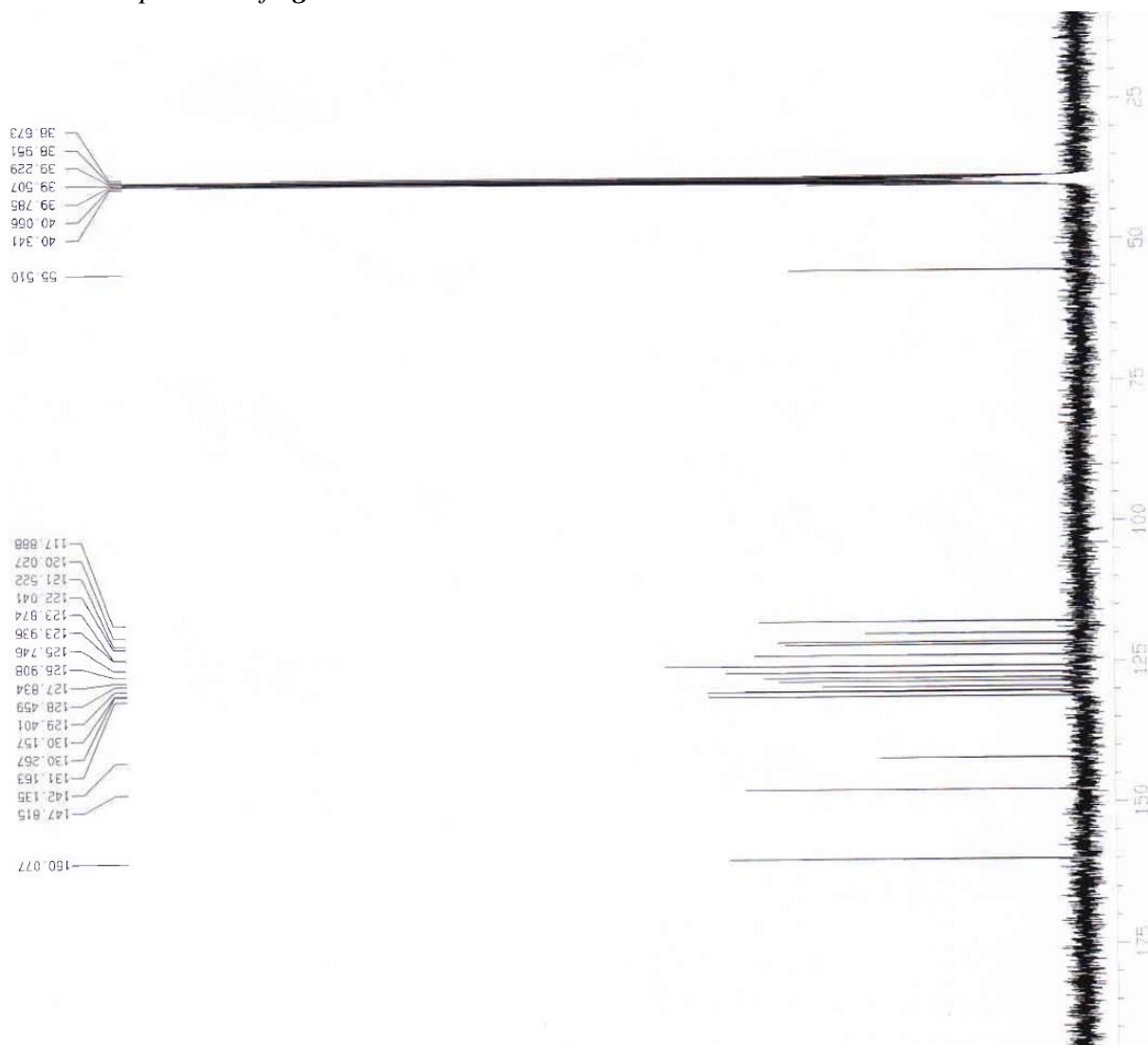
^{13}C NMR spectrum of **3f**



¹H NMR spectrum of 3g



¹³C NMR spectrum of **3g**



References

- [S1] T. Mosmann, Rapid Colorimetric Assay for Cellular Growth and Survival: Application to Proliferation and Cytotoxicity Assays, *J. Immunol. Methods* 65 (1983) 55–63.
- [S2] T. Mueller, W. Voigt, H. Simon, A. Fruehauf, A. Bulankin, A. Grothey, H.J. Schmoll, Failure of Activation of Caspase-9 Induces a Higher Threshold for Apoptosis and Cisplatin Resistance in Testicular Cancer, *Cancer Research* 63 (2003) 513-521.
- [S3] K. Mahal, B. Biersack, H. Caysa, R. Schobert, T. Mueller, *Invest. New Drugs* 33 (2015) 541-554.

5.4 Publikation III

New (arene)ruthenium(II) complexes of 4-aryl-4*H*-naphthopyrans with anticancer and anti-vascular activities

Florian Schmitt,^[a] Jana Kasparikova,^[b] Viktor Brabec,^[c] Gerrit Begemann,^[d] Rainer Schobert,*^[a] Bernhard Biersack^[a]

[a] *Department of Chemistry, University of Bayreuth, Universitaetsstrasse 30, 95440 Bayreuth, Germany*

[b] *Department of Biophysics, Faculty of Science, Palacky University, 17. Listopadu 12, CZ-77146 Olomouc, Czech Republic*

[c] *Institute of Biophysics, Academy of Sciences of the Czech Republic, CZ-61265 Brno, Czech Republic*

[d] *Developmental Biology, University of Bayreuth, Universitaetsstrasse 30, 95440 Bayreuth, Germany.*

* Corresponding author, Email address: Rainer.Schobert@uni-bayreuth.de

J. Inorg. Biochem. **2018**, 184, 69-78

Reprinted with permission from *New (arene)ruthenium(II) complexes of 4-aryl-4H-naphthopyrans with anticancer and anti-vascular activities*. F. Schmitt, J. Kasparikova, V. Brabec, G. Begemann, R. Schobert, B. Biersack. J. Inorg. Biochem. 2018, 184, 69-78. Doi: 10.1016/j.inorgbio.2018.03.013.

Copyright © 2018 Elsevier Ltd.



New (arene)ruthenium(II) complexes of 4-aryl-4*H*-naphthopyrans with anticancer and anti-vascular activities

Florian Schmitt^a, Jana Kasparkova^b, Viktor Brabec^c, Gerrit Begemann^d, Rainer Schobert^{a,*}, Bernhard Biersack^a

^a Department of Chemistry, University of Bayreuth, Universitaetsstrasse 30, 95440 Bayreuth, Germany

^b Department of Biophysics, Faculty of Science, Palacky University, 17. Listopadu 12, CZ-77146 Olomouc, Czech Republic

^c Institute of Biophysics, Academy of Sciences of the Czech Republic, CZ-61265 Brno, Czech Republic

^d Developmental Biology, University of Bayreuth, Universitaetsstrasse 30, 95440 Bayreuth, Germany

ARTICLE INFO

Keywords:

Vascular-disrupting agents (VDA)

Naphthopyran

(Arene)ruthenium(II) complexes

DNA binding

Zebrafish

ABSTRACT

A series of four 2-amino-3-cyano-4-(3/4-pyridyl)-4*H*-benzo[*h*]chromenes **2a–d** and their dichlorido(*p*-cymene) ruthenium(II) complexes **3a–d** were tested for antiproliferative, vascular-disruptive, anti-angiogenic and DNA-binding activity. The coordination of the 4-pyridyl-4*H*-naphthopyrans **2** to ruthenium led to complexes with pleiotropic effects. Unlike the free ligands **2a–d**, their ruthenium complexes **3a–d** showed a significant affinity for DNA as demonstrated by electrophoretic mobility shift assays (EMSA) and ethidium bromide assays. Binding of **3a–d** to calf thymus DNA proceeded about 10-times faster compared with cisplatin. Treatment of HT-29 colon carcinoma, 518A2 melanoma and MCF-7^{Topo} breast cancer cells with **3a** and **3b** caused an accumulation of cells in the G2/M phase and an increase of the fraction of mitotic cells in the case of HT-29, due to alterations of the microtubule cytoskeleton as shown by immunofluorescence staining. Complexes **3b–c** showed a dual effect on the vascular system. They suppressed angiogenesis in zebrafish embryos and they destroyed the vasculature of the chorioallantoic membrane (CAM) in fertilized chicken eggs. They also inhibited the vasculogenic mimicry, typical of U-87 glioblastoma cells in tube formation assays.

1. Introduction

cis-Diamminedichloroplatinum(II) (cisplatin, CDDP) has represented the gold standard of metal-based chemotherapeutics since the serendipitous discovery of its anticancer effect in the 1960s [1]. Even though the treatment of various solid tumors with cisplatin is quite successful, this comes at the price of severe side effects such as neural damage and cardio- as well as nephrotoxicity which limit its clinical applicability [2,3]. Many common types of cancer do not respond to cisplatin treatment, and acquired drug resistance is quite frequently observed. Hence, there is a need for new metal-based chemotherapeutics which overcome these limitations. Against the backdrop of metastatic tumors claiming far more lives than the primary tumor, anti-metastatic ruthenium complexes such as NAMI-A (imidazolium *trans*-imidazoletetrachlororuthenate, Fig. 1) [4] or KP1019 (*trans*-[tetrachlorobis(1*H*-indazole)ruthenate(III)] [5], which already passed clinical trials, have attracted great attention. Although their detailed mechanism of action is still not fully understood, these Ru(III) complexes are thought to get activated intracellularly by reduction to

distinctly more cytotoxic Ru(II) species [6]. In addition, the transport and the selective cellular uptake of Ru(III) complexes *via* transferrin and the transferrin receptors appear to play a decisive role [7,8]. Anti-tumoral (arene)ruthenium(II) complexes constitute another important class. The arene ligand of these so-called “piano stool” complexes is believed to stabilize the bioactive Ru(II) state [9]. They are particularly attractive to the medicinal chemist because of their ease of synthesis and their structural variability. (Arene)ruthenium(II) complexes may feature various anticancer properties. While some derivatives display an anti-metastatic mode of action similar to NAMI-A, involving their binding to proteins, others bind to DNA in a way comparable with the DNA interaction of cisplatin [9–13]. The introduction of ligands with appropriate intrinsic anticancer activities may give rise to pleiotropic complexes with synergistic or additive effects [14]. We have recently observed that the complexation of highly toxic ligands attenuates their general toxicity leading to more tumor-selective Ru(II) complexes [15]. Herein, we report on a series of new (arene)ruthenium(II) complexes bearing naphthopyran ligands. Naphthopyrans such as LY290181 [2-amino-4-(3-nitrophenyl)-4*H*-naphtho(1,2-*b*)pyran-3-carbonitrile,

* Corresponding author.

E-mail address: Rainer.Schobert@uni-bayreuth.de (R. Schobert).

Fig. 1] are microtubule destabilizing agents (MDA) which exert their effect by binding to tubulin, causing the inhibition of the tubulin polymerization which leads to alterations of the microtubule cytoskeleton [16–19]. Because of these alterations, the spindle apparatus cannot be formed correctly causing the arrest of the cell cycle in G2/M phase and the induction of apoptosis [19]. Hence, these MDA are highly anti-proliferative [16–18,20–22]. Moreover, the destruction of the microtubule cytoskeleton leads to a reduction of the mechanical stability of cells and of the irregular tumor blood vessels, which eventually causes their collapse and induces tumor cell necrosis [16,17,22]. By the synthesis of (arene)ruthenium(II) complexes bearing naphthopyran ligands we investigated if ruthenation leads to complexes featuring a combination of typical naphthopyran properties such as anti-proliferative [17,18,20–22], vascular-disruptive [17,22] and microtubule destabilizing activity [17–19], and of typical (arene)ruthenium (II) properties such as DNA binding [8,9,23,24] and anti-angiogenic activity [2,13].

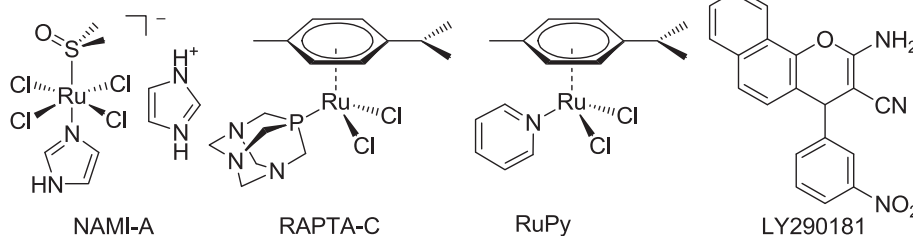


Fig. 1. Structures of the Ru(III) complex NAMI-A, the “piano stool” (arene)ruthenium(II) complexes RAPTA-C [Ru(η^6 -*p*-cymene)Cl₂(1,3,5-triaza-7-phosphaadamantane)] and RuPy [Ru(η^6 -*p*-cymene)Cl₂(pyridine)], and the microtubule destabilizing naphthopyran LY290181.

2. Experimental

2.1. General

Melting points were determined with a Gallenkamp apparatus and are uncorrected. IR spectra were recorded on a Perkin–Elmer One FT-IR spectrophotometer. Magnetic resonance (NMR) spectra were recorded under conditions as indicated on a Bruker Avance 300 spectrometer. Chemical shifts (δ) are given in parts per million downfield from TMS as internal standard. Mass spectra were recorded using a Varian MAT 311A (EI) or a UPLC/Orbitrap MS system (ESI). Elemental analyses were carried out with a Perkin–Elmer 2400 CHN elemental analyzer. Satisfactory microanalyses (C, \pm 0.2; H, \pm 0.1) were obtained for all new complexes.

2.2. Chemistry

All starting compounds were purchased from Sigma-Aldrich. Compounds **2a**, **2b**, and RuPy were prepared according to literature procedures [25–27].

2.2.1. 2-Amino-6-chloro-4-(pyridin-3-yl)-4H-benzo[h]chromene-3-carbonitrile **2c**

Pyridine-3-carboxaldehyde (107 mg, 1.0 mmol) and malononitrile (70 mg, 1.0 mmol) were dissolved in MeCN (5 mL) and three drops of Et₃N were added. The reaction mixture was stirred at room temperature for 30 min. 4-Chloro-1-naphthol (178 mg, 1.0 mmol) was added and the reaction mixture was stirred at room temperature for 1 h. The formed precipitate was collected, washed with MeCN and *n*-hexane and dried in vacuum. Yield: 196 mg (0.59 mmol, 59%); colorless solid of m.p. 255 °C; ν_{\max} (ATR)/cm⁻¹ 3441, 3037, 2187, 1651, 1629, 1609, 1579, 1569, 1481, 1428, 1405, 1372, 1289, 1277, 1260, 1203, 1172, 1155, 1112, 1058, 1043, 1030, 963, 942, 873, 862, 829, 762, 744, 716, 682; ¹H NMR (300 MHz, DMSO-*d*₆) δ 5.03 (1H, s), 7.3–7.4 (4H, m), 7.6–7.7 (1H, m), 7.7–7.8 (2H, m), 8.1–8.2 (1H, m), 8.3–8.4 (1H, m), 8.4–8.5

(1H, m), 8.6 (1H, s); ¹³C NMR (75.5 MHz, DMSO-*d*₆) δ 38.5, 55.6, 118.2, 120.6, 122.1, 124.4, 124.5, 124.8, 126.3, 128.4, 129.1, 129.9, 136.1, 141.0, 141.1, 142.8, 149.1, 149.2, 149.3, 160.6; *m/z* (EI) 335 (12) [M⁺], 333 (35) [M⁺], 257 (55), 255 (100), 193 (15). Anal. calcd. for C₁₉H₁₂ClN₃O: C, 68.37; H, 3.62. Found: C, 68.13; H, 3.55.

2.2.2. 2-Amino-6-chloro-4-(pyridin-4-yl)-4H-benzo[h]chromene-3-carbonitrile **2d**

Pyridine-4-carboxaldehyde (107 mg, 1.0 mmol) and malononitrile (70 mg, 1.0 mmol) were dissolved in MeCN (5 mL) and three drops of Et₃N were added. The reaction mixture was stirred at room temperature for 30 min. 4-Chloro-1-naphthol (178 mg, 1.0 mmol) was added and the reaction mixture was stirred at room temperature for 1 h. The formed precipitate was collected, washed with MeCN and *n*-hexane and dried in vacuum. Yield: 200 mg (0.60 mmol, 60%); colorless solid of m.p. 246 °C; ν_{\max} (ATR)/cm⁻¹ 3333, 3292, 3054, 2867, 2198, 1664, 1614, 1596, 1571, 1404, 1372, 1281, 1260, 1202, 1173, 1114, 1067, 1053,

1027, 1001, 963, 942, 875, 860, 817, 766, 747, 679; ¹H NMR (300 MHz, DMSO-*d*₆) δ 4.99 (1H, s), 7.30 (2H, dd, *J* = 6.1 Hz, 1.6 Hz), 7.34 (1 H, s), 7.39 (2H, s), 7.7–7.8 (2H, m), 8.1–8.2 (1H, m), 8.3–8.4 (1H, m), 8.53 (2H, dd, *J* = 6.1 Hz, 1.6 Hz); ¹³C NMR (75.5 MHz, DMSO-*d*₆) δ 39.9, 54.7, 117.1, 119.9, 121.5, 122.8, 123.9, 125.6, 125.9, 127.9, 128.6, 129.5, 142.4, 150.2, 153.2, 160.3; *m/z* (EI) 335 (11) [M⁺], 333 (33) [M⁺], 257 (53), 255 (100), 193 (16). Anal. calcd. for C₁₉H₁₂ClN₃O: C, 68.37; H, 3.62. Found: C, 68.16; H, 3.54.

2.2.3. Dichlorido(*p*-cymene)[2-amino-4-(pyridin-3-yl)-4H-benzo[h]chromene-3-carbonitrile]ruthenium(II) **3a**

2a (68 mg, 0.23 mmol) was dissolved in CH₂Cl₂ (5 mL) and five drops of MeOH. [Ru(*p*-cymene)Cl₂]₂ (70 mg, 0.12 mmol) was added and the reaction mixture was vigorously stirred for 30 min. Ethyl acetate/*n*-hexane (1:4, 50 mL) was added and the formed precipitate was collected, washed with *n*-hexane and dried in vacuum. Yield: 110 mg (0.18 mmol, 79%); amber solid of m.p. 173–175 °C; ν_{\max} (ATR)/cm⁻¹ 3302, 3153, 3057, 2964, 2186, 1652, 1629, 1598, 1505, 1472, 1409, 1375, 1290, 1263, 1188, 1104, 1057, 1023, 874, 815, 753, 732, 702; ¹H NMR (300 MHz, CDCl₃) δ 1.28 (6H, d, *J* = 6.9 Hz), 2.09 (3H, s), 2.9–3.0 (1H, m), 4.95 (2H, s), 4.98 (1H, s), 5.2–5.3 (2H, m), 5.43 (1H, d, *J* = 5.9 Hz), 5.49 (1H, d, *J* = 5.9 Hz), 6.88 (1H, d, *J* = 8.6 Hz), 7.1–7.2 (1H, m), 7.3–7.4 (1H, m), 7.5–7.6 (3H, m), 7.7–7.8 (1H, m), 8.15 (1H, d, *J* = 8.1 Hz), 8.9–9.0 (1H, m), 9.08 (1 H, s); ¹³C NMR (75.5 MHz, CDCl₃) δ 18.1, 22.1, 22.5, 30.7, 38.7, 59.7, 82.4, 83.3, 97.3, 103.7, 114.4, 119.6, 120.7, 123.0, 124.8, 125.5, 125.8, 127.0, 127.3, 127.9, 133.7, 137.5, 141.0, 143.7, 153.7, 154.3, 159.2; *m/z* (EI) 299 (17), 234 (3), 232 (4), 221 (100), 119 (39); *m/z* (ESI) 563.8 (13), 390.3 (13), 301.3 (80), 282.4 (100), 221.2 (70). Anal. calcd. for C₂₉H₂₇Cl₂N₃ORu: C, 57.52; H, 4.49. Found: C, 57.40; H, 4.43.

2.2.4. Dichlorido(*p*-cymene)[2-amino-4-(pyridin-4-yl)-4H-benzo[h]chromene-3-carbonitrile]ruthenium(II) **3b**

2b (68 mg, 0.23 mmol) and [Ru(*p*-cymene)Cl₂]₂ (70 mg, 0.12 mmol) were dissolved in CH₂Cl₂ (5 mL) and the reaction mixture was

vigorously stirred for 30 min. Ethyl acetate/*n*-hexane (1:4, 50 mL) was added and the formed precipitate was collected, washed with *n*-hexane and dried in vacuum. Yield: 110 mg (0.18 mmol, 79%); amber solid of m.p. 218–219 °C; $\nu_{\max}(\text{ATR})/\text{cm}^{-1}$ 3273, 3159, 3051, 2961, 2185, 1652, 1630, 1608, 1574, 1495, 1471, 1403, 1375, 1290, 1264, 1189, 1103, 1062, 1023, 963, 860, 804, 771, 756, 734, 690, 669, 649, 618; ^1H NMR (300 MHz, $\text{CDCl}_3/\text{DMF-}d_7$) δ 1.07 (6H, d, $J = 7.0$ Hz), 1.87 (3H, s), 2.7–2.8 (1H, m), 4.70 (1H, s), 5.02 (2H, d, $J = 6.2$ Hz), 5.2–5.3 (2H, m), 6.02 (2H, s), 6.70 (1H, d, $J = 8.6$ Hz), 6.98 (2H, d, $J = 6.6$ Hz), 7.3–7.4 (3H, m), 7.5–7.6 (1H, m), 7.9–8.0 (1H, m), 8.69 (2H, d, $J = 6.6$ Hz); ^{13}C NMR (125 MHz, $\text{CDCl}_3/\text{DMF-}d_7$) δ 17.6, 21.7, 30.1, 40.4, 53.1, 81.9, 96.4, 103.1, 114.3, 119.3, 120.5, 122.8, 123.3, 124.0, 125.0, 126.3, 126.6, 127.2, 133.1, 143.3, 154.5, 154.9, 160.2; m/z (ESI) 563.8 (9), 300.3 (28), 282.4 (100), 221 (31), 100.2 (29). Anal. calcd. for $\text{C}_{29}\text{H}_{27}\text{Cl}_2\text{N}_3\text{ORu}$: C, 57.52; H, 4.49. Found: C, 57.43; H, 4.45.

2.2.5. Dichlorido(*p*-cymene)[2-amino-6-chloro-4-(pyridin-3-yl)-4H-benzo[h]chromene-3-carbonitrile]ruthenium(II) 3c

2c (76 mg, 0.23 mmol) was dissolved in CH_2Cl_2 (5 mL) and five drops of MeOH. $[\text{Ru}(\text{p-cymene})\text{Cl}_2]_2$ (70 mg, 0.12 mmol) was added and the reaction mixture was vigorously stirred for 30 min. Ethyl acetate/*n*-hexane (1:4, 50 mL) was added and the formed precipitate was collected, washed with *n*-hexane and dried in vacuum. Yield: 120 mg (0.19 mmol, 84%); amber solid of m.p. 195–197 °C; $\nu_{\max}(\text{ATR})/\text{cm}^{-1}$ 3290, 3150, 3057, 2964, 2191, 1651, 1626, 1594, 1567, 1471, 1431, 1405, 1368, 1286, 1261, 1204, 1174, 1111, 1058, 1027, 964, 940, 863, 838, 804, 764, 744, 705; ^1H NMR (300 MHz, CDCl_3) δ 1.27 (6H, d, $J = 6.9$ Hz), 2.07 (3H, s), 2.9–3.0 (1H, m), 4.91 (1H, s), 5.08 (1H, s), 5.2–5.3 (2H, m), 5.42 (1H, d, $J = 5.9$ Hz), 5.47 (1H, d, $J = 5.9$ Hz), 6.99 (1H, s), 7.2–7.3 (1H, m), 7.3–7.4 (1H, m), 7.6–7.7 (2H, m), 8.1–8.2 (2H, m), 8.9–9.0 (1H, m), 9.06 (1H, s); ^{13}C NMR (75.5 MHz, CDCl_3) δ 18.1, 22.1, 22.4, 30.7, 38.6, 59.5, 82.4, 83.2, 97.3, 103.8, 114.8, 119.3, 121.4, 124.1, 124.8, 125.2, 127.9, 128.3, 128.7, 130.8, 137.4, 140.4, 142.8, 153.9, 154.4, 159.0; m/z (EI) 335 (6), 333 (20), 257 (34), 255 (100), 193 (12), 134 (17), 119 (55), 91 (12), 36 (15); m/z (ESI) 563.8 (14), 336.3 (83), 282.4 (100), 255.1 (26). Anal. calcd. for $\text{C}_{29}\text{H}_{26}\text{Cl}_3\text{N}_3\text{ORu}$: C, 54.43; H, 4.09. Found: C, 54.31; H, 4.02.

2.2.6. Dichlorido(*p*-cymene)[2-amino-6-chloro-4-(pyridin-4-yl)-4H-benzo[h]chromene-3-carbonitrile]ruthenium(II) 3d

2d (76 mg, 0.23 mmol) and $[\text{Ru}(\text{p-cymene})\text{Cl}_2]_2$ (70 mg, 0.12 mmol) were dissolved in CH_2Cl_2 (5 mL) and the reaction mixture was vigorously stirred for 30 min. Ethyl acetate/*n*-hexane (1:4, 50 mL) was added and the formed precipitate was collected, washed with *n*-hexane and dried in vacuum. Yield: 104 mg (0.16 mmol, 71%); amber solid of m.p. > 220 °C; $\nu_{\max}(\text{ATR})/\text{cm}^{-1}$ 3282, 3160, 3066, 2964, 2186, 1648, 1627, 1608, 1594, 1570, 1499, 1473, 1406, 1369, 1281, 1261, 1206, 1174, 1113, 1062, 1024, 963, 939, 867, 839, 805, 767, 732, 681, 646, 618; ^1H NMR (300 MHz, $\text{CDCl}_3/\text{DMF-}d_7$) δ 1.06 (6H, d, $J = 7.0$ Hz), 1.88 (3H, s), 2.7–2.8 (1H, m), 4.68 (1H, s), 5.03 (2H, d, $J = 6.3$ Hz), 5.2–5.3 (2H, m), 6.14 (2H, s), 6.84 (1H, s), 6.99 (2H, d, $J = 6.6$ Hz), 7.4–7.5 (2H, m), 7.9–8.0 (1H, m), 8.0–8.1 (1H, m), 8.71 (2H, d, $J = 6.6$ Hz); ^{13}C NMR (75 MHz, $\text{CDCl}_3/\text{DMF-}d_7$) δ 17.6, 21.7, 30.2, 40.3, 53.1, 81.9, 82.0, 96.5, 103.2, 114.8, 121.1, 123.3, 123.9, 124.1, 127.2, 127.5, 127.8, 130.2, 142.4, 154.4, 154.7, 160.0; m/z (ESI) 563.8 (10), 334.2 (53), 282.4 (100), 255.1 (33), 97.2 (24). Anal. calcd. for $\text{C}_{29}\text{H}_{26}\text{Cl}_3\text{N}_3\text{ORu}$: C, 54.43; H, 4.09. Found: C, 54.29; H, 4.04.

2.3. Biological evaluation

2.3.1. Cell culture

MCF-7^{Topo} (ACC-115) breast carcinoma, KB-V1^{Vbl} (ACC-149) cervix carcinoma, HT-29 (ACC-299), DLD-1 (ACC-278) and HCT-116 (ACC-581) colon carcinoma, 518A2 (Department of Radiotherapy, Medical University of Vienna, Austria) melanoma, Panc-1 (ACC-783) pancreatic ductular adenocarcinoma, and U-87 (ATCC: HTB-14) glioblastoma cells

were cultivated in Dulbecco's Modified Eagle Medium (DMEM; supplemented with 10% fetal bovine serum (FBS) and 1% Antibiotic-Antimycotic) at 37 °C, 5% CO_2 and 95% humidity. Human dermal fibroblasts HDFa (ATCC: PCS-201-012TM) were grown in DMEM supplemented with 10% FBS, 1% Antibiotic-Antimycotic, and 2 mM glutamine at 37 °C, 5% CO_2 , and 95% humidity. The maximum-tolerated dose of topotecan or vinblastine was added to the cell culture medium 24 h after every cell passage to keep the MCF-7^{Topo} or the KB-V1^{Vbl} cells resistant. Only mycoplasma-free cultures were used.

2.3.2. MTT assay

All cell lines were seeded at a concentration of 5×10^4 cells/mL in 96-well plates (100 μL /well), except for U-87 glioblastoma cells, and HDFa human dermal fibroblasts, which were seeded at a concentration of 1×10^5 cells/mL. After 24 h of incubation, the cells were treated with various concentrations (100 μM –0.5 nM) of the test compounds, cisplatin, RuPy, or vehicle (DMF; maximum concentration 1%) for 24 or 72 h at 37 °C. Then, 12.5 μL of a 0.5% MTT [3-(4,5-dimethylthiazol-2-yl)-2,5-diphenyltetrazolium bromide] solution were added per well and incubated for 2 h at 37 °C to convert water-soluble MTT into insoluble formazan crystals. After centrifugation (300g, 5 min, 4 °C) the medium was discarded and the formazan was dissolved in 25 μL of DMSO containing 10% SDS and 0.6% acetic acid for at least 2 h at 37 °C. Then, the absorbance at wavelength 570 nm (formazan) and 630 nm (background) was measured with a microplate reader (Tecan). Each experiment was carried out in quadruplicate and the IC_{50} values determined as means \pm SD (standard deviation) with respect to control cells set to 100% viable cells.

2.3.3. Electrophoretic mobility shift assay (EMSA) with pBR322 plasmid DNA

The electrophoretic mobility shift assay (EMSA) was used to study the compound-induced unwrapping of covalently closed circular (ccc) topofom of pBR322 plasmid DNA (Thermo Scientific). The circular plasmid DNA (75 $\mu\text{g}/\text{mL}$) in TE buffer (10 mM Tris-HCl, 1 mM EDTA, pH 8.5) was incubated with varying concentrations of the test compounds or positive control (cisplatin) at 37 °C for 24 h. Then, samples were subjected to gel electrophoresis using 1% agarose gels in $0.5 \times$ TBE buffer (89 mM Tris, 89 mM boric acid, 25 mM EDTA, pH 8.3). After staining the gels with ethidium bromide (10 $\mu\text{g}/\text{mL}$), pictures of the gels were taken under UV excitation.

2.3.4. Ethidium bromide saturation assay

The extent of the compounds' DNA interactions was additionally assessed by a fluorescence-based ethidium bromide staining assay [28]. 100 μL of a 10 $\mu\text{g}/\text{mL}$ solution of salmon sperm DNA in $1 \times$ TE buffer (Sigma-Aldrich) was pipetted in a black 96-well plate and incubated with concentrations of the compounds or cisplatin in the standard range (0, 25, 50, 75 and 100 μM) for 2 h at 37 °C [29]. Then, 100 μL ethidium bromide in $1 \times$ TE buffer was added to reach a final concentration of 5 $\mu\text{g}/\text{mL}$. After 5 min of incubation, the fluorescence ($\lambda_{\text{ex}} = 535$ nm, $\lambda_{\text{em}} = 595$ nm) was monitored for each well using a microplate reader (Tecan). Each fluorescence value was corrected by ethidium bromide background (samples without DNA) and the compounds' possible intrinsic fluorescence. The resulting values were expressed as percent of vehicle (100% ethidium bromide binding = 100% fluorescence). Reduced fluorescence is representative for impaired ethidium bromide-DNA adducts due to intercalation sites being blocked by the test compounds. All experiments were carried out in triplicates resulting in the mean \pm SD of relative ethidium bromide fluorescence.

2.3.5. DNA binding in cell free media

Solutions of double-helical calf thymus DNA (42% G + C) at a concentration of 64 $\mu\text{g}/\text{mL}$ were incubated with **3a–d** in NaClO_4 (10 mM) at 37 °C so that the molar ratio of ruthenium complex to nucleotide residues was 0.04. Aliquots of the reaction mixtures were

withdrawn at various time intervals, the reaction was stopped by addition of NaCl (1 M), and samples were quickly cooled in a dry ice bath. The samples were exhaustively dialyzed first against 1 M NaCl and subsequently against water to remove free unbound ruthenium complexes. The concentrations of DNA and the content of ruthenium associated with DNA were determined by absorption spectrophotometry and FAAS (Varian AA240Z), respectively.

2.3.6. Chorioallantoic membrane (CAM) assay in fertilized chicken eggs [30]

Fertilized white leg horn chicken eggs (VALO Biomedica) were incubated at 37 °C and 50–60% humidity until day six post-fertilization. Then, the eggs were opened by cutting a window of 2–3 cm diameter in the eggshell at the more rounded pole and incubated for a further 24 h. After placing a thin silicon ring ($\phi = 5$ mm) onto the chorioallantoic membrane with its developing blood vessel system, the customarily used amount of test compounds (10 μ L of a 0.5 mM solution) was pipetted inside these rings. The effect on the vasculature was documented 0, 6 and 24 h post-application (hpa) with a light microscope (Traveller, 60 \times magnification).

2.3.7. Tube formation assay

U-87 glioblastoma cells (2.5×10^6 cells/mL, 100 μ L/well) were seeded in 96-well plates on thin layers of matrigel (Corning) and subsequently treated with **3b** (500 nM), **3c** (1 μ M) or vehicle (DMF) for 24 h. The test compounds' effect on the tube formation was documented with a microscope (Zeiss, 100 \times magnification). The viability of the cells was determined by MTT assay.

2.3.8. Fluorescence labeling of microtubules

518A2 melanoma cells (1×10^5 cells/mL; 500 μ L/well) were grown for 24 h on glass coverslips at 37 °C. Then, the cells were exposed to **3a–d** (500 nM), or vehicle (DMF) for 3 h. After fixation of the cells in 3.7% formaldehyde in PBS for 20 min at room temperature, the cells were blocked and permeabilized with 1% BSA (bovine serum albumin), 0.1% Triton X-100 in PBS for 30 min at room temperature. Immunostaining of the microtubules was performed by treating the cells first with a primary antibody against alpha-tubulin (anti alpha-tubulin, mouse monoclonal antibody) followed by the incubation with a secondary antibody conjugated to AlexaFluor®-488 (goat anti-mouse IgG-AlexaFluor®-488, Cell Signaling Technology) for 1 h in the dark. Then, the glass coverslips were mounted in 4-88-based mounting medium containing 1 μ g/mL DAPI (4',6-diamidino-2-phenylindole) for counterstaining the nuclei and 2.5% DABCO (1,4-diazabicyclo[2.2.2]octane). Alterations of the microtubule cytoskeleton were documented by fluorescence microscopy using a Zeiss Imager A1 AX10 (400 \times magnification).

2.3.9. Cell cycle analyses

HT-29 colon carcinoma, MCF-7 breast cancer and 518A2 melanoma cells (5×10^4 cells/mL, 3 mL/well) grown in 6-well plates were allowed to adhere for 24 h. First, various concentrations of the test compounds or vehicle (DMF) were applied to the different cells lines for 24 h, each in a single experiment in order to estimate the range of concentrations where an effect on the cell cycle can be observed. Cell cycle analyses of concentrations within this range were then determined in three independent experiments. The cells were harvested by trypsinization and fixed in ice-cold 70% ethanol overnight. After RNA digestion and propidium iodide (PI) staining with PI staining solution (50 μ g/mL propidium iodide, 0.1% sodium citrate, 50 μ g/mL RNase A in PBS) for 30 min at 37 °C, the fluorescence intensity of 10,000 single cells was recorded with a Beckmann Coulter Cytomics FC500 flow cytometer at $\lambda_{em} = 630$ nm and $\lambda_{ex} = 488$ nm. The cell distribution of single cells (%) in G1, S and G2/M phase of the cell cycle progression as well as the proportion of sub-G1 events (apoptotic cells) were analyzed by using the CXP Analysis Software (Beckmann Coulter).

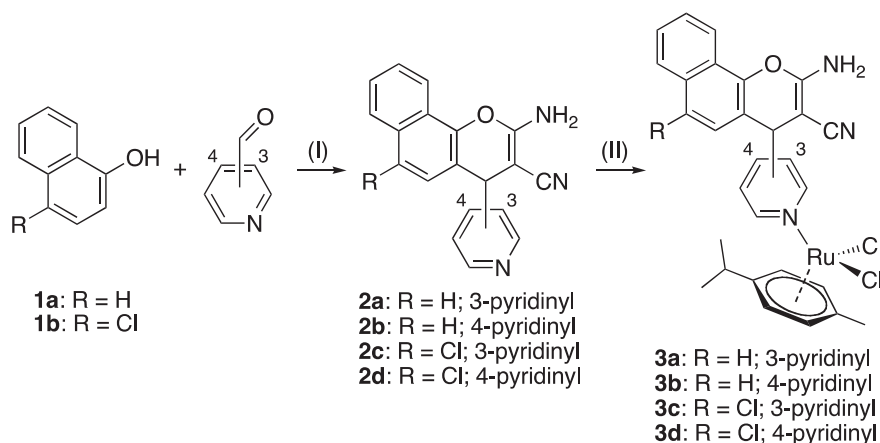
2.3.10. Zebrafish angiogenesis assay [31]

Transgenic zebrafish of the strain *Tg(fli1a:EGFP)* with a *casper* background were raised under standard conditions at 27–28 °C [32,33]. After manual dechorionation at 24–26 hpf the embryos were transferred into 6-well plates [5 embryos/well in 5 mL E3 medium (5 mM NaCl, 0.17 mM KCl, 0.33 mM CaCl₂, 0.33 mM MgSO₄, 0.01% methylene blue, pH 7.2)] and treated with **3b–c** (0.5 and 1 μ M), or vehicle (DMF) for 48 h. The development of the SIV (subintestinal veins) was documented by fluorescence microscopy ($\lambda_{ex} = 488$ nm, $\lambda_{em} = 509$ nm, Leica MZ10F with ZEISS AxioCam Mrc and Mrc-ZEN pro 2012 software). The SIV length of at least 17 identically treated fish was quantified as mean \pm SD with vehicle treated controls set to 100%. Significant deviations from the control data were determined using a *t*-test. *: $p < 0.001$.

3. Results and discussion

3.1. Chemistry

The naphthopyrans **2a–b** were synthesized by a base-catalyzed enol reaction of malononitrile with 3-pyridinaldehyde/4-pyridinaldehyde and 1-naphthol as previously described (Scheme 1) [25]. **2c–d** were prepared analogously by reaction of malononitrile with 3-pyridinaldehyde/4-pyridinaldehyde and 4-chloro-1-naphthol. The compounds precipitated from the reaction solution after a short time and were obtained as pure solids in moderate to high yields. The reaction of **2a–d** with [Ru(*p*-cymene)Cl₂]₂ afforded the corresponding Ru (II) complexes **3a–d** as brown solids in yields ranging from 71% to 84%.



Scheme 1. Reagents and conditions: (I) CH₂(CN)₂, MeCN, Et₃N, rt, 90 min, 59–60% (II) [Ru(*p*-cymene)Cl₂]₂, CH₂Cl₂/MeOH, rt, 30 min, 71–84%.

Table 1IC₅₀ values^b [nM, 72 h] derived from dose-response curves using MTT assays when applied to human cell lines^a.

	Cisplatin	RuPy	2a	2b	2c	2d	3a	3b	3c	3d
518A2	5300 ± 400 ^c	> 100,000	< 0.5	< 0.5	37.0 ± 0.3	448 ± 13	37.8 ± 2.3	33.3 ± 2.9	121 ± 8	325 ± 2
518A2 (24 h)	4800 ± 300	> 100,000	–	–	> 1000	> 1000	> 1000	> 1000	> 1000	> 1000
HT-29	> 100,000 ^c	> 100,000	< 0.5	< 0.5	38.6 ± 4.0	966 ± 20	54.3 ± 3.1	82.0 ± 6.0	158 ± 1	319 ± 33
DLD-1	32,600 ± 2400 ^c	> 100,000	< 0.5	< 0.5	45.5 ± 4.0	390 ± 21	38.8 ± 3.1	41.4 ± 2.8	139 ± 11	219 ± 24
HCT-116	5000 ± 400 ^c	> 100,000	–	–	52.4 ± 3.6	251 ± 11	61.0 ± 7.0	62.5 ± 2.5	188 ± 7	280 ± 10
MCF-7 ^{Topo}	10,600 ± 700 ^c	> 100,000	< 0.5	< 0.5	33.9 ± 1.5	139 ± 42	11.3 ± 0.5	37.4 ± 3.6	46.7 ± 1.7	195 ± 12
KB-V1 ^{Vbl}	> 100,000	> 100,000	–	–	33.0 ± 2.9	460 ± 31	12.5 ± 1.9	62.8 ± 5.9	36.5 ± 1.7	210 ± 13
Panc-1	4800 ± 700 ^c	–	–	–	14.9 ± 1.9	371 ± 13	13.1 ± 1.1	35.7 ± 3.5	105 ± 9	191 ± 10
U-87	–	> 100,000	–	–	254 ± 49	> 1000	279 ± 47	396 ± 45	73 ± 13	> 1000
HDFa	> 100,000	> 100,000	–	–	–	–	> 100,000	> 100,000	> 100,000	> 50,000

^a Human cell lines: 518A2 melanoma, MCF-7^{Topo} breast adenocarcinoma, KB-V1^{Vbl} cervix carcinoma, Panc-1 pancreatic ductular adenocarcinoma, HT-29, HCT-116 and DLD-1 colon carcinomas, U-87 glioblastoma cells, and HDFa human dermal fibroblasts.

^b IC₅₀ values are the means ± SD of four independent experiments.

^c Values determined by Muenzner et al. [28].

As is known for other ruthenium(II)-arene complexes [2], complexes **3a–d** underwent activating hydrolysis to give aqua complexes in ¹H NMR experiments in aqueous solvent mixtures. Their formation increased with the amount of water present and with time of exposure, reaching a maximum after 48 h. It could be attenuated by addition of NaCl. In contrast, the conversion of the starting dichlorido complexes was expedited by the addition of AgNO₃ (cf. Supplementary data, Figs. S1–S5).

3.2. Antiproliferative activity

The antiproliferative activity of the compounds was investigated by MTT assays [34]. They were tested against a panel of eight cancer cell lines of six different entities, as well as against the non-malignant human dermal fibroblasts HDFa (Table 1). Apart from naphthopyrans **2a–b**, all test compounds showed dose dependent inhibitory curves against the whole panel of cancer cell lines in the range of double-digit nanomolar to single-digit micromolar IC₅₀ values. In our standard concentration range no vital cells were detected for **2a–b** after 72 h. Due to this enormous toxicity, we desisted from further investigations of these two compounds. In contrast, RuPy, the known complex Ru(η⁶-*p*-cymene)Cl₂(pyridine), bearing pyridine instead of the naphthopyran ligands, had no influence on the cell viability even at concentrations as high as 100 μM. Hence, the cytotoxicity of the pertinent (arene)ruthenium(II) complexes **3a–b** with IC₅₀ values ranging from double-digit nanomolar to single-digit micromolar can presumably be attributed to the naphthopyran ligands **2a** and **2b**, the toxicity of which is obviously attenuated by their complexation to the ruthenium fragment. The analogous reduction of cytotoxicity by ruthenation was less pronounced and not observed for all cell lines in the case of the chloro-naphthopyrans **2c–d** and their complexes **3c–d**. It is also noteworthy that the complexes **3a–d** are distinctly more cytotoxic than cisplatin. Moreover, tentative structure-activity relationships and selectivities emerged for the complexes **3a–d**. On average, the 3-pyridinyl derivatives **3a** and **3c** were slightly more active than their respective 4-pyridinyl congeners **3b** and **3d**, while the unchlorinated derivatives **3a** and **3b** were more cytotoxic than their respective chloro congeners **3c** and **3d**. When we measured the uptake rates of the complexes **3a–d** by determining the ruthenium content in HT-29 and HCT-116 colon carcinoma cells after 3 h exposure, there was no significant difference between the less cytotoxic complexes **3c–d** and the more cytotoxic complexes **3a–b** (cf. Supplementary data). Hence, the difference in cytotoxicities between **3a–b** and **3c–d** must originate from different target interactions or general modes of action rather than from differences in the uptake rates. In addition, complexes **3a–d** showed a distinct selectivity for certain cell lines. On average, the multi-drug resistant (MDR) cancer cell line MCF-7^{Topo}, which overexpresses the ABC (ATP-binding cassette)-transporters BCRP (breast cancer resistance

protein), as well as the pancreatic adenocarcinoma cells Panc-1 were most sensitive to complexes **3a–d**, while the colon carcinoma cells HT-29 and HCT-116 were least sensitive. Since the IC₅₀ values of the complexes **3a–d** in the MDR cell lines KB-V1^{Vbl} and MCF-7^{Topo}, overexpressing P-gp (P-glyco protein) and BCRP, respectively, were equal to or even lower than those in the other cell lines, it can be assumed that the complexes **3a–d** are not substrates of P-gp and BCRP. Interestingly, complexes **3a–d** showed also a distinct selectivity for tumor cells over non-malignant dermal fibroblasts (HDFa), which were hardly affected even at concentrations of 100 μM.

3.3. DNA interaction

Since (arene)ruthenium(II) complexes are known to bind to DNA, we investigated the interaction of complexes **3a–d** with DNA in several cell-free assays [10,35]. Their influence on the electrophoretic mobility of the different topological forms of pBR322 plasmid DNA was monitored by EMSA (Fig. 2). To exclude that the naphthopyran ligands themselves cause any band shifts, the plasmid DNA was incubated with the ruthenium complexes **3a–d** as well as with the naphthopyrans **2a–d**.

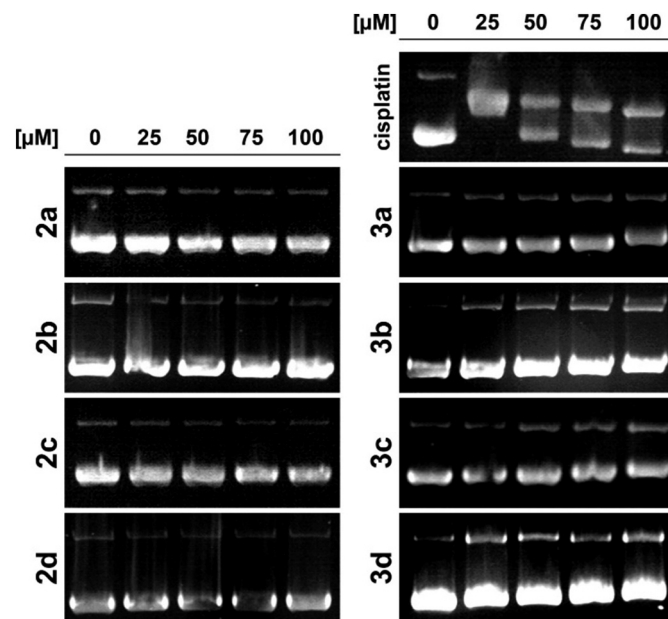


Fig. 2. Effects of cisplatin and compounds **2a–d** and **3a–d** on the electrophoretic mobility of circular pBR322 plasmid DNA as determined by electrophoretic mobility shift assays (EMSA) after 24 h of incubation. Pictures are representative of two independent experiments.

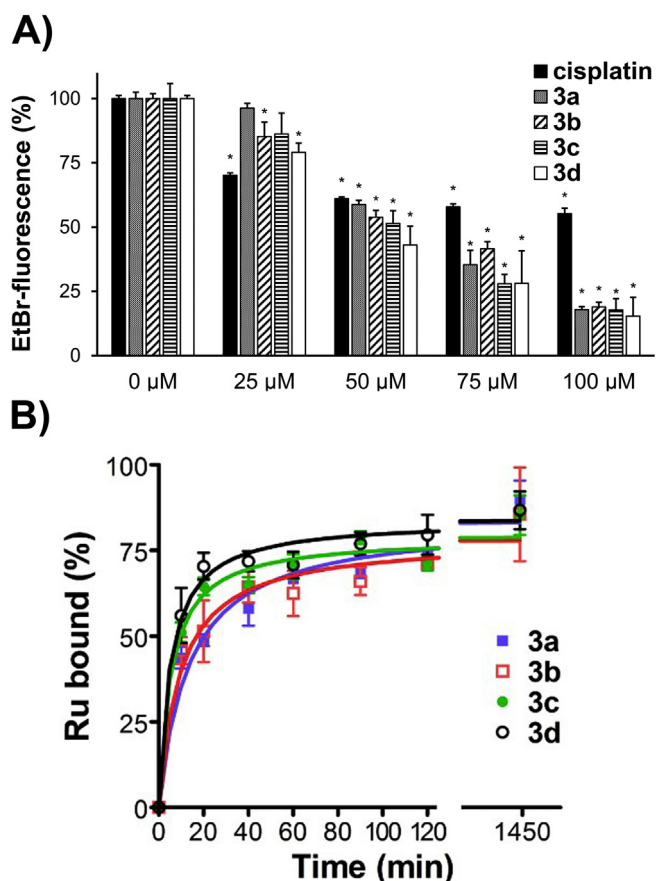


Fig. 3. A) Relative ethidium bromide fluorescence after pre-incubation with vehicle (DMF; set to 100%), cisplatin, or test compounds **3a–d** (25, 50, 75, and 100 μM) for 2 h. Decreased ethidium bromide fluorescence indicates the inhibition of ethidium bromide intercalation into DNA. Significant deviations from controls (0 μM) were determined by *t*-test. *: *p*-values < 0.05. B) Kinetics of the reaction of **3a–d** with double-helical calf thymus DNA. Solutions of DNA at a concentration of 64 $\mu\text{g}/\text{mL}$ were incubated with complexes **3a–d** (8 μM) in NaClO_4 (10 mM) at 37 $^\circ\text{C}$ in the dark. Points represent the mean value of at least three independent experiments \pm SD.

The complexes caused a slight shift whereas no interaction was observed for the ligands. The finding that the chloro-substituted complexes **3c** and **3d** led to a more distinctly decreased mobility when compared with **3a** and **3b** does not correlate with the cytotoxicities of the complexes. In addition, the shifts induced by the ruthenium complexes differed noticeably from that caused by cisplatin. The test compounds gave rise to only a slight shift of the band of the fast-moving supercoiled *ccc*-topoform whereas the mobility of the slowly moving open circular *oc*-topoform was not influenced. In contrast, cisplatin gave rise to pronounced mobility changes of both forms. At a dose of 25 μM of cisplatin only one band was observed whereas higher concentrations even induced the rewinding of the plasmid DNA which increased the electrophoretic mobility of the DNA again.

The interaction of compounds **3a–d** with DNA was confirmed in a fluorescence-based staining assay (Fig. 3A). Salmon sperm DNA (ssDNA) was first incubated with the test compounds at various concentrations and then stained with ethidium bromide (EtBr). Then, the fluorescence intensity of the EtBr-DNA adducts was measured. It is typically reduced if the test compounds inhibit the intercalation of EtBr into DNA by morphological distortions of the latter as a consequence of binding interactions. As in the EMSA, no DNA interaction was detected for the naphthopyran ligands **2a–d** in these EtBr-assays (cf. Supplementary data), while complexes **3a–d** reduced the EtBr fluorescence significantly to values < 20% compared to vehicle treated controls. By

using FAAS and absorption spectroscopy, we determined the degree of ruthenation of calf thymus DNA over time. The amount of ruthenium associated with DNA increased with time (Fig. 3B). The times at which the metal load of the DNA reached 50% were 19, 16, 9 and 8 min for **3a**, **3b**, **3c** and **3d**, respectively. These results indicate that the rates of binding of **3a–d** to natural double-helical DNA are markedly higher than those of cisplatin ($t_{50\%} \sim 120$ min) [36]. The marginal shift of pBR322 plasmid DNA in EMSA assays, on the one hand, and the much greater reduction of EtBr fluorescence in EtBr assays and the higher DNA binding rates of **3a–d** compared to cisplatin, on the other hand, suggest a DNA binding mode and bond strength for **3a–d** that are different from that of cisplatin. The ruthenium complexes **3a–d**, like RAPTA-C, are likely to form adducts with DNA mainly at the purine sites with a lower bond strength compared to cisplatin [10]. We assume that the ruthenium complexes were detached from DNA during electrophoresis which caused the smaller shift in EMSA.

3.4. Effects on the cell cycle progression

Naphthopyrans such as LY290181 are known to induce the accumulation of cells in G2/M phase of the cell cycle [19]. Therefore, we investigated the influence of **3a** and **3b** on the cell cycle progression in HT-29 colon carcinoma, 518A2 melanoma, and MCF-7^{Topo} breast cancer cells (Fig. 4). In 518A2 melanoma cells, both complexes induced a dose-dependent accumulation of cells in G2/M phase and the decrease of cells in the G1 phase whereas the percentage of cells in S phase was barely changed. At higher concentrations, we found a distinct increase of apoptotic cells in sub-G1 (cf. Supplementary data). Similar rapidly increasing proportions of apoptotic sub-G1 events had previously been observed by our group for combretastatin A-4 derivatives in 518A2 melanoma cells [37]. This sensitivity to MDA-treatment might be attributed to the high proliferation rate of this particular cell line. Interestingly, the test compounds' influence on the cell cycle progression of MCF-7^{Topo} breast cancer cells differed from that in 518A2 cells. At low concentrations of **3a** (10 nM) and **3b** (25 nM), we observed a slight accumulation of cells in G1 phase which was mainly due to the decrease of the percentage of cells in the S phase whereas the proportion of cells in G2/M was not significantly altered. However, at higher concentrations we observed the arrest of cells in G2/M phase whereas the percentages of cells in G1 and in S phase were reduced. Similar effects were observed for other microtubule targeting agents at low concentrations [38,39]. Even though these concentrations cause alterations of the microtubule dynamics, prolonged mitosis and the increase of p53 expression, they might not suffice to keep all cells from passing through mitosis but are probably sufficient to induce a post-mitotic p53-dependent G1-arrest [38,39]. Higher concentrations cause the canonical G2/M arrest. However, this phenomenon is not observed in all cell lines equally [38]. In HT-29 colon carcinoma cells, **3a** and **3b** derivatives elicited a dose-dependent increase of cells in G2/M phase whereas those in S and G1 phases were decreased. HT-29 cells were also arrested in G2/M phase when treated with **2c–d** (100 nM) or **3c–d** (250 nM) (cf. Supplementary Data). However, the arrest was more pronounced for **2c** and **3a–c** than for **2d** and **3d**. The slighter increase of apoptotic sub-G1 events in MCF-7^{Topo} and HT-29 cells is presumably due to the incubation time of only 24 h being too short for them entering into apoptosis as consequence of the mitotic arrest in contrast to the rapidly proliferating 518A2 cells for which this short space of time seems to be sufficient [37,40,41].

The increase of cells in G2/M can be attributed to the interference of naphthopyrans with the tubulin dynamics which prevents the normal microtubule formation [19,42]. Thus, cells are kept from dividing and arrested in mitosis for want of a functional spindle apparatus. Since the standard cell cycle analyses cannot distinguish between G2 and mitotic cells we additionally stained the nuclei of HT-29 cells treated with **3a–d** and counted the percentage of mitotic cells with condensed DNA. After exposing the cells to the test compounds in the highest applied

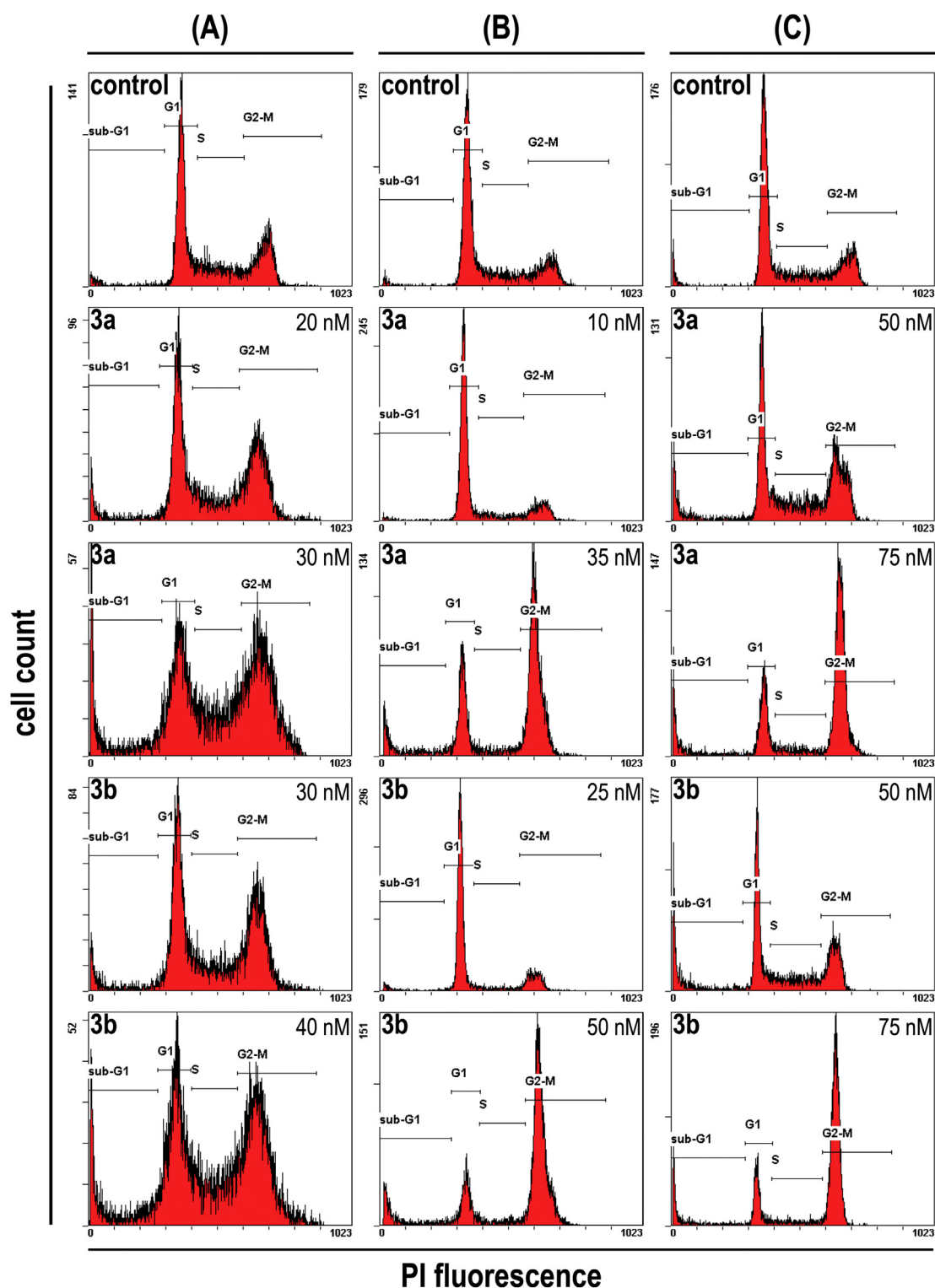


Fig. 4. Effect of **3a** and **3b** on the cell cycle progression of different cancer cell lines. Flow cytometric analyses of PI stained DNA content in 518A2 melanoma (column A), MCF-7^{T0po} breast cancer (column B), and HT-29 colon carcinoma cells (column C) after 24 h exposure to the indicated concentrations of **3a**, **3b**, and vehicle (DMF) and the distribution of cells in G1, S and G2/M phase as well as the proportion of apoptotic cells (sub-G1). The histograms are representative of at least three independent experiments.

concentrations of the cell cycle analyses (100 or 250 nM; 6 h), the proportion of mitotic cells was found to be significantly increased (*cf.* Supplementary data). While only 7% of control cells were mitotic, the mitotic indices of cells treated with **3a** (250 nM) and **3b** (250 nM) were increased markedly to 27% and 24%, respectively. The incubation with 250 nM of the chlorinated derivatives **3c** and **3d** caused a lesser

accumulation of mitotic cells (20% and 15%, respectively).

3.5. Effects on the cytoskeletal organization

Since blocking of cell division and mitotic arrest are typical consequences of the treatment with tubulin-binding agents, we additionally

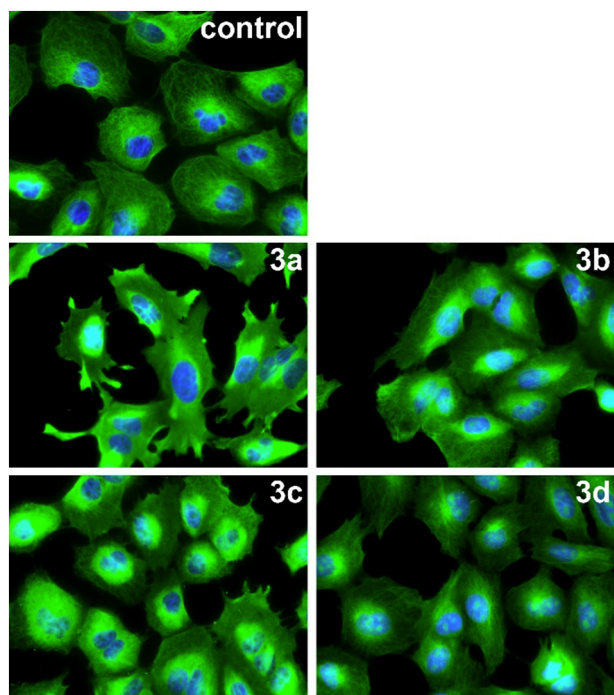


Fig. 5. Effect of compounds **3a–d** (500 nM) on the organization of the microtubule cytoskeleton (green) in 518A2 melanoma cells after 3 h incubation. Nuclei were counterstained with DAPI (blue). The pictures are representative of two independent experiments (400 × magnification).

investigated the effects of complexes **3a–d** on microtubule organization in 518A2 melanoma cells (Fig. 5) [16]. In order to visualize early effects on the microtubule cytoskeleton, we first exposed the cells to the test compounds **3a–d** for 3 h. Slight alterations in the tubulin dynamics caused by low concentrations of MDA might affect apoptosis induction, migration or angiogenesis, which are, however, hard to recognize with the naked eye. Therefore, we chose higher concentrations of the test compounds (500 nM) just to visualize the potential microtubule destabilizing effect of the complexes. While **3a** caused a complete disruption of the microtubules, **3b–c** eroded the microtubule cytoskeleton but left some clusters of intact microtubules. Complex **3d**, the test compound

with the highest IC₅₀ value against these cells, induced no distinct alteration of the microtubule organization. We additionally tested the microtubule destructing effect of **3a** and **3b** (both 60 nM, 24 h) in 518A2 cells and also found alterations of the microtubule cytoskeleton (cf. Supplementary data). Even though some filamentous microtubules were observed in cells treated with **3a** and **3b**, there were areas with destroyed microtubules where tubulin was just diffusely spread. However, there were also fragmented nuclei typical of apoptosis induction. Therefore, the inhibition of tubulin polymerization was confirmed for **3a** and **3b** *in vitro* by using a turbidimetric-based cell-free assay with purified pig brain tubulin (cf. Supplementary data).

3.6. Effect on the vasculature

Targeting tumor vasculature is still a promising approach to inhibit tumor growth [43]. While anti-angiogenic agents prevent the formation of new blood vessels, vascular-disrupting agents attack the blood supply by destruction of already established tumor blood vessels. Since the disruption of the microtubular cytoskeleton as caused by complexes **3a–d** results in the mechanical destabilization of treated cells and in alterations of cell to cell junctions which might induce the shut-down of the abnormal and fragile tumor vasculature, we surmised that complexes **3a–d** might also be vascular-disruptive [16].

The vascular-disruptive effect of complexes **3a–d** was tested on the chorioallantoic membrane (CAM) of fertilized chicken eggs. The compounds were applied topically onto the CAM in a small ring of silicon foil next to some main blood vessels. Any alterations of the blood vessels were documented 0, 6 and 24 h post-application (hpa). However, these tests were hampered by the poor solubility profile of some test compounds. Only complexes **3b** and **3c** did not precipitate under the conditions of the CAM assay. They induced the disruption of even big blood vessels and consequently caused hemorrhages at 6 hpa (Fig. 6B). 24 hpa an extensive destruction of the vasculature was observed.

Besides the conventional blood vessel formation *via* angiogenesis, which is mediated by proliferating and migrating endothelial cells, alternate mechanisms such as vascular mimicry by cancer cells play a vital role in the maintenance of the tumor vessel network, which supports tumor growth, metastasis and invasion [44–46]. Hence, the effect of the test compounds on neovascularization *via* vascular mimicry was studied by tube formation assays using U-87 glioblastoma cells [47].

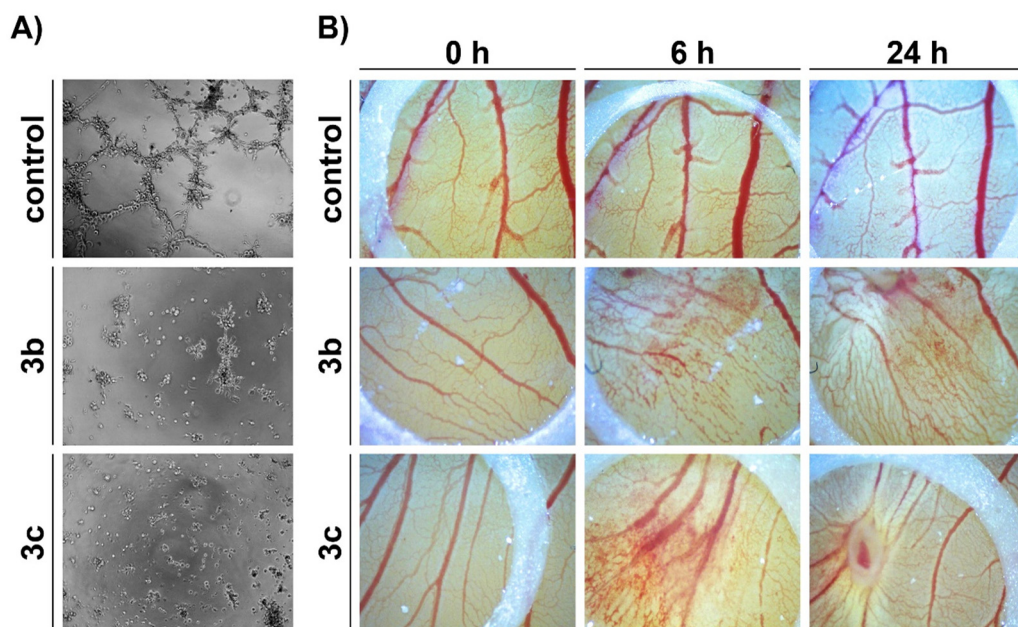


Fig. 6. A) Effects of complexes **3b** (500 nM) and **3c** (1 μM) on the formation of tubular, blood-vessel-like networks by U-87 glioblastoma cells when grown on thin layers of matrigel for 24 h. Images are representative of two independent experiments (100 × magnification). Percentage of vital cells was shown by MTT assays to be > 80% compared to DMF treated control cells. B) Effects of complexes **3b** (5 nmol) and **3c** (5 nmol) when applied topically to the vasculature in the chorioallantoic membrane of fertilized chicken eggs at 0, 6 and 24 hpa. Control: respective amount of DMF. Images are representative of at least three independent experiments (60 × magnification).

These cells form tubular blood vessel-like networks when grown on thin layers of matrigel (Fig. 6A). In contrast to the complex tubular and cord-like networks formed by untreated control cells, cells treated with complexes **3b** or **3c** were diffusely spread throughout the well showing no signs of blood vessel-like formations. As to MTT assays, the vitality of the treated cells was > 80% compared to untreated U-87 cells so that antiproliferative effects of the compounds can be excluded.

The microtubule destruction caused by compounds **3a–d** might also contribute to their anti-angiogenic effect *via* alterations of cell-cell contacts, reduced cell migration and inhibition of sprout formation [16]. In addition, it is known that (arene)ruthenium(II) complexes show anti-angiogenic activity originating from their binding to proteins or enzymes and subsequent inhibition of angiogenesis-relevant growth factor receptors such as fibroblast growth factor receptor (FGF-R1) or vascular endothelial growth factor receptor (VEGFR) [13]. Therefore, we investigated whether the new compounds affect the establishment of new blood vessels *in vivo* in *Tg(fli1a:EGFP)* zebrafish embryos with *casper* background [32,33]. Due to their transparency, the effect of test compounds on the formation of SIV, blood vessels that absorb nutrients from the yolk and develop between 48 and 72 hpf, could simply be monitored by fluorescence microscopy [48,49]. While vehicle-treated zebrafish embryos developed the typically sinoidal structure with a ladder rung-like pattern, the SIV of embryos treated with non-toxic concentrations of complexes **3b–c** were significantly underdeveloped (Fig. 7). The SIV of fish treated with **3b** were much smaller and the ladder rungs incomplete and deficient whereas in fish exposed to **3c** the SIV were only rudimentary and barely visible. The area covered by SIV was quantified using the ImageJ software and the one of untreated control fish set to 100%. The SIV area in zebrafish embryos treated with **3b** (1 μ M) was developed to 43% compared with the control fish whereas the SIV area of **3c** (1 μ M) treated fish was developed to only 10% compared to control.

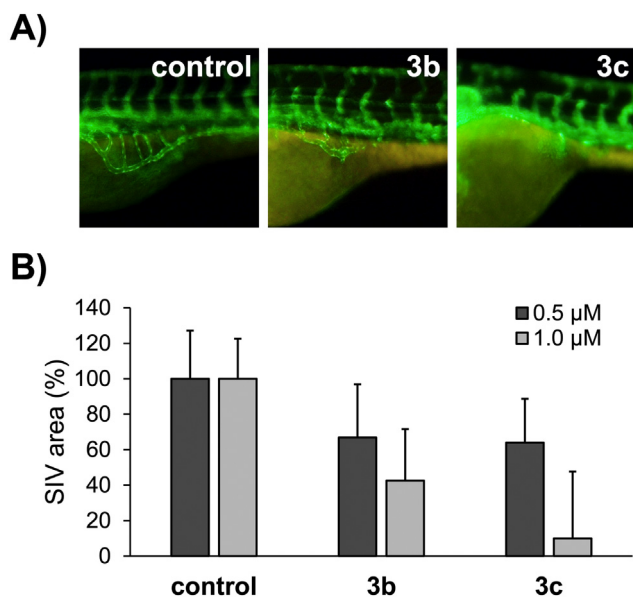


Fig. 7. Effect of test compounds **3b** and **3c** on angiogenesis in zebrafish embryos. 24 hpf old transgenic *Tg(fli1a:EGFP)* zebrafish embryos were exposed to 0.5 and 1 μ M of the test compounds for 48 h at 28 °C in embryo medium. A) Images are representative of at least 17 independent experiments (6.3-fold magnification). B) The area covered by subintestinal veins (SIV) was quantified using the ImageJ software. The SIV area of zebrafish embryos treated with vehicle (DMF) was set to 100%. Values are the means \pm SD of at least 17 independent experiments. Significant deviations from the control data were determined using a *t*-test. $p < 0.001$.

4. Conclusions

The (arene)ruthenium(II) complexes **3a–d** of 4-aryl-4*H*-naphthopyrans represent a new class of selective and potent anti-cancer agents addressing multiple targets by combining the individual effects of the naphthopyrans and the (arene)Ru(II) fragment in a beneficial manner. They retained the DNA-binding ability, typical of (arene)ruthenium(II) complexes, augmented by the anti-angiogenic, vascular-disruptive and cytotoxic activities of the naphthopyrans. By coordination to the (*p*-cymene)Ru(II) fragment even the brutal toxicity of the unchlorinated naphthopyrans **2a** and **2b** was attenuated and the resulting complexes **3a** and **3b** showed manageable cytotoxicities and a distinct selectivity for cancer over non-malignant cells. However, they were still distinctly more cytotoxic on average than their chlorinated congeners **3c** and **3d**. The preliminary DNA binding studies revealed that the new complexes **3a–d** bind about 10 times faster and in a different way to calf thymus DNA when compared to cisplatin. We assume that the complexes **3a–d**, like RAPTA-C, preferentially bind to the purine sites of DNA [10]. It cannot be excluded that these lesions might induce DNA repair mechanisms, which eventually elicit apoptosis. However, the apoptosis induction is more likely the result of the alterations of the microtubule cytoskeleton, which is another major target of the new complexes, apparent from its extensive destruction and a subsequent mitotic arrest of treated cells. As a corollary of this effect, we observed a weakening of the cell-to-cell junctions of endothelial cells resulting in the disruption of the vasculature in the chorioallantoic membrane of chicken eggs or in an impairment of the angiogenesis in zebrafish. The new pleiotropic ruthenium complexes **3a–d** are to be tested now in *in vivo* xenograft studies.

Abbreviations

ABC	ATP binding cassette
BCRP	breast cancer resistance protein
CAM	chorioallantoic membrane
ccc	covalently closed circular
DAPI	4',6-diamidino-2-phenylindole
dpf	days post-fertilization
EMSA	electrophoretic mobility shift assay
EtBr	ethidium bromide
FGF-R1	fibroblast growth factor receptor 1
hpa	hours post-application
hpf	hours post-fertilization
MDA	microtubule destabilizing agent
MDR	multi-drug resistant
MTT	3-(4,5-dimethylthiazol-2-yl)-2,5-diphenyltetrazolium bromide
oc	open circular
P-gp	P-glycoprotein
PI	propidium iodide
SD	standard deviation
SIV	subintestinal veins
ssDNA	salmon sperm DNA
VDA	vascular-disrupting agent
VEGFR	vascular endothelial growth factor receptor

Acknowledgement

RS thanks the Deutsche Forschungsgemeinschaft for a grant (Scho 402/12), JK and VB thank the Czech Science Foundation for a grant (17-05302S).

Appendix A. Supplementary data

Methods used for cellular uptake studies, determination of the mitotic index, fluorescence labeling of microtubules, tubulin

polymerization assay; additional results from stability studies, cellular uptake studies, EtBr-assays, cell cycle analyses, mitotic index determinations, and effects on microtubules at doi:<https://doi.org/10.1016/j.jinorgbio.2018.03.013>.

References

- [1] B. Rosenberg, L. Van Camp, T. Krigas, *Nature* 205 (1965) 698–699.
- [2] C.M. Clavel, E. Paunescu, P. Nowak-Sliwinska, A.W. Griffioen, R. Scopelliti, P.J. Dyson, *J. Med. Chem.* 58 (2015) 3356–3365.
- [3] S. Page, R. Wheeler, *Educ. Chem.* (2012) 26–29.
- [4] S. Leijen, S.A. Burgers, P. Baas, D. Pluim, M. Tibben, E. van Werkhoven, E. Alessio, G. Sava, J.H. Beijnen, J.H.M. Schellens, *Investig. New Drugs* 33 (2015) 201–214.
- [5] C.G. Hartinger, M.A. Jakupec, S. Zorbas-Seifried, M. Groessl, A. Egger, W. Berger, H. Zorbas, P.J. Dyson, B.K. Keppler, *Chem. Biodivers.* 5 (2008) 2140–2155.
- [6] C.S. Allardyce, P.J. Dyson, *Platin. Met. Rev.* 45 (2001) 62–69.
- [7] A. Bergamo, L. Messori, F. Piccioli, M. Cocchietto, G. Sava, *Investig. New Drugs* 21 (2003) 401–411.
- [8] C.G. Hartinger, S. Zorbas-Seifried, M.A. Jakupec, B. Kynast, H. Zorbas, B.K. Keppler, *J. Inorg. Biochem.* 100 (2006) 891–904.
- [9] B. Biersack, *Mini-Rev. Med. Chem.* 16 (2016) 804–814.
- [10] Z. Adhikarsan, G.E. Davey, P. Campomanes, M. Groessl, C.M. Clavel, H. Yu, A.A. Nazarov, C.H.F. Yeo, W.H. Ang, P. Dröge, U. Rothlisberger, P.J. Dyson, C.A. Davey, *Nat. Commun.* 5 (5) (2014) 3462, <http://dx.doi.org/10.1038/ncomms4462>.
- [11] A. Dorcier, C.G. Hartinger, R. Scopelliti, R.H. Fish, B.K. Keppler, P.J. Dyson, *J. Inorg. Biochem.* 102 (2008) 1066–1076.
- [12] R.H. Berndsen, A. Weiss, U.K. Abdul, T.J. Wong, P. Meraldi, A.W. Griffioen, P.J. Dyson, P. Nowak-Sliwinska, *Nat. Sci. Rep.* 7 (7) (2017) 43005, <http://dx.doi.org/10.1038/srep43005>.
- [13] P. Nowak-Sliwinska, J.R. van Beijnum, A. Casini, A.A. Nazarov, G. Wagnières, H. van den Bergh, P.J. Dyson, A.W. Griffioen, *J. Med. Chem.* 54 (2011) 3895–3902.
- [14] W.M. Motswainyana, P.A. Ajibade, *Adv. Chem.* 2015 (2015) 859730, <http://dx.doi.org/10.1155/2015/859730>.
- [15] a) R. Schobert, S. Seibt, K. Mahal, A. Ahmad, B. Biersack, K. Effenberger-Neidnicht, S. Padhye, F.H. Sarkar, T. Mueller, *J. Med. Chem.* 54 (2011) 6177–6182; b) B. Biersack, M. Zoldakova, K. Effenberger, R. Schobert, *Eur. J. Med. Chem.* 45 (2010) 1972–1975.
- [16] D. Bates, A. Eastman, *Br. J. Clin. Pharmacol.* 83 (2017) 225–268.
- [17] S. Kasibhatla, H. Gourdeau, K. Meerovitch, J. Drewe, S. Reddy, L. Qui, H. Zhang, F. Bergeron, D. Bouffard, Q. Yang, J. Herich, S. Lamothe, S.X. Cai, B. Tseng, *Mol. Cancer Ther.* 3 (2004) 1365–1374.
- [18] S.A. Patil, J. Wang, X.S. Li, J. Chen, T.S. Jones, A. Hosni-Ahmed, R. Patil, W.L. Seibel, W. Li, D.D. Miller, *Bioorg. Med. Chem. Lett.* 22 (2012) 4458–4461.
- [19] D.L. Wood, D. Panda, T.R. Wiernicki, L. Wilson, M.A. Jordan, J.P. Singh, *Mol. Pharmacol.* 52 (1997) 437–444.
- [20] T.R. Wiernicki, J.S. Bean, C. Dell, A. Williams, D. Wood, R.F. Kauffman, J.P. Singh, *J. Pharmacol. Exp. Ther.* 278 (1996) 1452–1459.
- [21] W. Kemnitzer, J. Drewe, S. Jiang, H. Zhang, J. Zhao, C. Crogan-Grundy, L. Xu, S. Lamothe, H. Gourdeau, R. Denis, B. Tseng, S. Kasibhatla, S.X. Cai, *J. Med. Chem.* 50 (2007) 2858–2864.
- [22] F. Schmitt, M. Gold, I. Andronache, B. Biersack, R. Schobert, T. Mueller, submitted to *Eur. J. Med. Chem.*
- [23] S.K. Singh, S. Joshi, A.R. Singh, J.K. Saxena, D.S. Pandey, *Inorg. Chem.* 46 (2007) 10869–10876.
- [24] R.E. Morris, R.E. Aird, P. del Socorro Murdoch, H. Chen, J. Cummings, N.D. Hughes, S. Parsons, A. Parkin, G. Boyd, D.I. Jodrell, P.J. Sadler, *J. Med. Chem.* 44 (2001) 3616–3621.
- [25] R. Ballini, F. Bigi, M.L. Conforti, D. De Santis, R. Maggi, G. Oppici, G. Sartori, *Catal. Today* 60 (2000) 305–309.
- [26] M. Moore, S.A. Ertem, *Treatment of ovarian cancer with 2-amino-4H-naphtho[1,2-b]pyran-3-carbonitriles*. WO/2013/070998.
- [27] C.A. Vock, C. Scolaro, A.D. Phillips, R. Scopelliti, G. Sava, P.J. Dyson, *J. Med. Chem.* 49 (2006) 5552–5561.
- [28] J.K. Muenzner, T. Rehm, B. Biersack, A. Casini, I.A.M. de Graaf, P. Worawutputtpong, A. Noor, R. Kempe, V. Brabec, J. Kasparkova, R. Schobert, *J. Med. Chem.* 58 (2015) 6283–6292.
- [29] C. Spoerlein-Guettler, K. Mahal, R. Schobert, B. Biersack, *J. Inorg. Biochem.* 138 (2014) 64–72.
- [30] B. Nitzsche, C. Gloesenkamp, M. Schrader, M. Ocker, R. Preissner, M. Lein, A. Zakrzewicz, B. Hoffmann, M. Höpfner, *Br. J. Cancer* 103 (2010) 18–28.
- [31] H. Draut, T. Rehm, G. Begemann, R. Schobert, *Chem. Biodivers.* 14 (2017) e1600302, <http://dx.doi.org/10.1002/cbdv.201600302>.
- [32] N.D. Lawson, B.M. Weinstein, *Dev. Biol.* 248 (2002) 307–318.
- [33] R.M. White, A. Sessa, C. Burke, T. Bowman, J. LeBlanc, C. Ceol, C. Bourque, M. Dovey, W. Goessling, C.E. Burns, L.I. Zon, *Cell Stem Cell* 2 (2008) 183–189.
- [34] T. Mosmann, *J. Immunol. Methods* 65 (1983) 55–63.
- [35] G. Süß-Fink, *Dalton Trans.* 39 (2010) 1673–1688.
- [36] D.P. Bancroft, C.A. Lepre, S.J. Lippard, *J. Am. Chem. Soc.* 112 (1990) 6860–6871.
- [37] K. Mahal, B. Biersack, H. Caysa, R. Schobert, T. Mueller, *Investig. New Drugs* 33 (2015) 541–554.
- [38] B. Pourroy, M. Carré, S. Honoré, V. Bourgarel-Rey, A. Kruczynski, C. Briand, D. Braguer, *Mol. Pharmacol.* 66 (3) (2004) 580–591.
- [39] Z.N. Demidenko, S. Kalurupalle, C. Hanko, C.U. Lim, E. Broude, M.V. Blagosklonny, *Oncogene* 27 (2008) 4402–4410.
- [40] C. Kanthou, G.M. Tozer, *Blood* 99 (2002) 2060–2069.
- [41] J.D. Orth, A. Loewer, G. Lahav, T.J. Mitchison, *Mol. Biol. Cell* 23 (2012) 567–576.
- [42] D. Panda, J.P. Singh, L. Wilson, *J. Biol. Chem.* 272 (12) (1997) 7681–7687.
- [43] D. Neri, R. Bicknell, *Nat. Rev. Cancer* 5 (2005) 436–446.
- [44] S. El Hallani, B. Boisselier, F. Peglion, A. Rousseau, C. Colin, A. Idbaih, Y. Marie, K. Mokhtari, J.L. Thomas, A. Eichmann, J.Y. Delattre, A.J. Maniotis, M. Sanson, *Brain* 133 (2010) 973–982.
- [45] C. Scavelli, B. Nico, T. Cirulli, R. Ria, G. Di Pietro, D. Mangieri, A. Bacigalupo, G. Mangialardi, A.M.L. Coluccia, T. Caravita, S. Molica, D. Ribatti, F. Dammacco, *A. Vacca, Oncogene* 27 (2008) 663–674.
- [46] M.J.C. Hendrix, E.A. Seftor, A.R. Hess, R.E.B. Seftor, *Nat. Rev. Cancer* 3 (2003) 411–421.
- [47] R.A. Francescone III, M. Faibish, R.A. Shao, *J. Vis. Exp.* 55 (2011) e3040, <http://dx.doi.org/10.3791/3040>.
- [48] G.N. Serbedzija, E. Flynn, C.E. Willett, *Angiogenesis* 3 (1999) 353–359.
- [49] S. Isogai, M. Horiguchi, B.M. Weinstein, *Dev. Biol.* 230 (2001) 278–301.

- Supplementary Data -

New (arene)ruthenium(II) complexes of 4-aryl-4*H*-naphthopyrans

with anticancer and anti-vascular activities

Florian Schmitt^a, Jana Kasparikova^b, Viktor Brabec^c, Gerrit Begemann^d, Rainer Schobert ^{a,*}

and Bernhard Biersack^a

^a Department of Chemistry, University of Bayreuth, Universitaetsstraße 30, 95447 Bayreuth, Germany

^b Department of Biophysics, Faculty of Science, Palacky University, 17. Listopadu 12, CZ-77146 Olomouc, Czech Republic

^c Institute of Biophysics, Academy of Sciences of the Czech Republic, CZ-61265 Brno, Czech Republic

^d Developmental Biology, University of Bayreuth, Universitaetsstrasse 30, 95440 Bayreuth, Germany.

* Corresponding author. E-mail address: Rainer.Schobert@uni-bayreuth.de, Fax: 0049 (0)921 552671

Table of content

Material and Methods	2
Cellular Uptake	2
Determination of the mitotic index.	2
Fluorescence labeling of microtubules	2
Tubulin polymerization assay.....	2
Results	3
Stability studies	3
Cellular uptake	8
EtBr assay.....	8
Cell cycle analysis.....	8
Mitotic Index	10
Effect on the microtubule cytoskeleton	10
References.....	11

Material and Methods

Cellular Uptake.

Cellular accumulation of Ru from **3a-d** was measured in human colon carcinoma cells HT-29 and HCT-116, cultured in DMEM medium supplemented with 10% FBS and gentamycin. The cells were seeded in 100 mm tissue culture dishes at a density of 5×10^6 cells/dish (ca. 6.5×10^4 cells/cm²). After overnight pre-incubation, the cells were treated with **3a-d** (5 μ M) for 3 h. After the treatment, the attached cells were washed twice with PBS, detached by trypsinization and washed twice with ice cold PBS. The cell pellets were digested by a high pressure microwave digestion system (MARS5, CEM) with HCl to give a fully homogenized solution, and the content of ruthenium taken up by the cells was determined by ICP-MS (Agilent 7500, Agilent, Japan). After 3 h of incubation, the cell viability was in all cases >90%.

Determination of the mitotic index.

The assay including the incubation time was performed as previously described.[S1] HT-29 colon carcinoma cells (0.5 mL, 1×10^5 cells/mL) seeded on glass coverslips were allowed to adhere for 24 h and then incubated with control (DMF), or the test compounds (100 nM and 250 nM) for 6 h. After fixation with 3.7% formaldehyde in PBS for 20 min at room temperature and permeabilization with 0.1% triton-X 100 in for 30 min at room temperature, the coverslips were washed three times with PBS and mounted in Mowiol 4-88-based mounting medium containing 1 μ g/mL DAPI (4',6-diamidino-2-phenylindole) over night at 4 °C. Representative pictures were recorded with a fluorescence microscope (Zeiss Imager A1 AX10, 200 \times magnification). For each concentration, at least 400 cells per coverslip were counted. The percentage of mitotic cells was calculated from the ratio of mitotic cells to the total number of counted cells determined in three independent experiments (mitotic index \pm SD).

Fluorescence labeling of microtubules.

518A2 melanoma (5×10^4 cells /mL; 500 μ L/well) and MCF-7^{Topo} breast cancer cells (1.5×10^5 cells/mL; 500 μ L/well) were seeded on glass coverslips in 24 well plates and allowed to adhere for 24 h at 37 °C. Then, the cells were exposed to vehicle (DMF), **3a**, or **3b** at the indicated concentrations for the indicated times. After fixation in 3.7% formaldehyde in PBS (20 min; rt), cells were blocked and permeabilized with 1% BSA, 0.1% Triton X-100 in PBS (30 min; rt). The immunostaining of the microtubule cytoskeleton was carried out by treating the cells first with a primary antibody against alpha-tubulin (anti alpha-tubulin, mouse monoclonal antibody) followed by the exposure to a secondary antibody conjugated to AlexaFluor[®]-488 (goat anti-mouse IgG- AlexaFluor[®]-488, Cell Signaling Technology) or a secondary antibody conjugated to AlexaFluor[™]-546 (goat anti-mouse IgG AlexaFluor[™] 546, Invitrogen) for 1 h in the dark. Then, the glass coverslips were mounted in 4-88 based mounting medium containing 1 μ g/mL DAPI and 2.5% DABCO. Alterations of the microtubules were documented using a Zeiss Imager A1 AX10 fluorescence microscope (400 \times magnification).

Tubulin polymerization assay.

50 μ L of Brinkley's buffer 80 (BRB80) containing 20% glycerol and 3 mM GTP was pipetted in a black 96-well half area plate with clear bottom. Compounds **3a-b** (final concentration: 10 μ M), colchicine (final concentration: 10 μ M) and vehicle (DMF) were added to the wells. After the addition of tubulin (50 μ L; 10 mg/mL in BRB80) the plate was immediately placed in a pre-heated microplate reader (Tecan). The polymerization was determined turbidimetrically at 37 °C by measuring the absorption at 340 nm for 90 min in intervals of 5 min.

Results

Stability studies: Figure S1 shows that the ruthenium(II) complex **3b** and its ligand **2b** are reasonably stable in acetonitrile. The shift of 2-H and 6-H protons of the pyridine scaffold of **3b** ($\delta = 8.91$ ppm) differs significantly from the 2-H and 6-H signals of the free ligand **2b** ($\delta = 8.53$ ppm). Even though the addition of 10% D₂O (Fig. S2) and of 50% D₂O (Fig. S3-5) caused variations of the chemical shifts, it is possible to distinguish between **3b** and ligand **2b** by comparing the respective signals of their 2-H and 6-H protons. By addition of 10% D₂O a small signal at $\delta = 8.53$ ppm appears between the 2-H and 6-H signals of the complex ($\delta = 8.61$ ppm) and those of the ligand ($\delta = 8.44$ ppm) which can be assigned an aqua species (Fig. S2). A small signal at $\delta = 8.44$ ppm in the spectrum of **3b** indicates some marginal loss of the ligand. By the addition of 50% D₂O (Fig. S3) the signal at $\delta = 8.51$ ppm, indicating the aqua species formation, increases over time and reaches a maximum at 48 h. Here as well, a small constant signal at $\delta = 8.42$ ppm suggests some ligand loss right from scratch. The addition of 0.9% NaCl (Fig. S4) inhibited the formation of aqua species while an excess of AgNO₃ (Fig. S5) led to an instantaneous conversion of complex **3b** to a yet unidentified species.

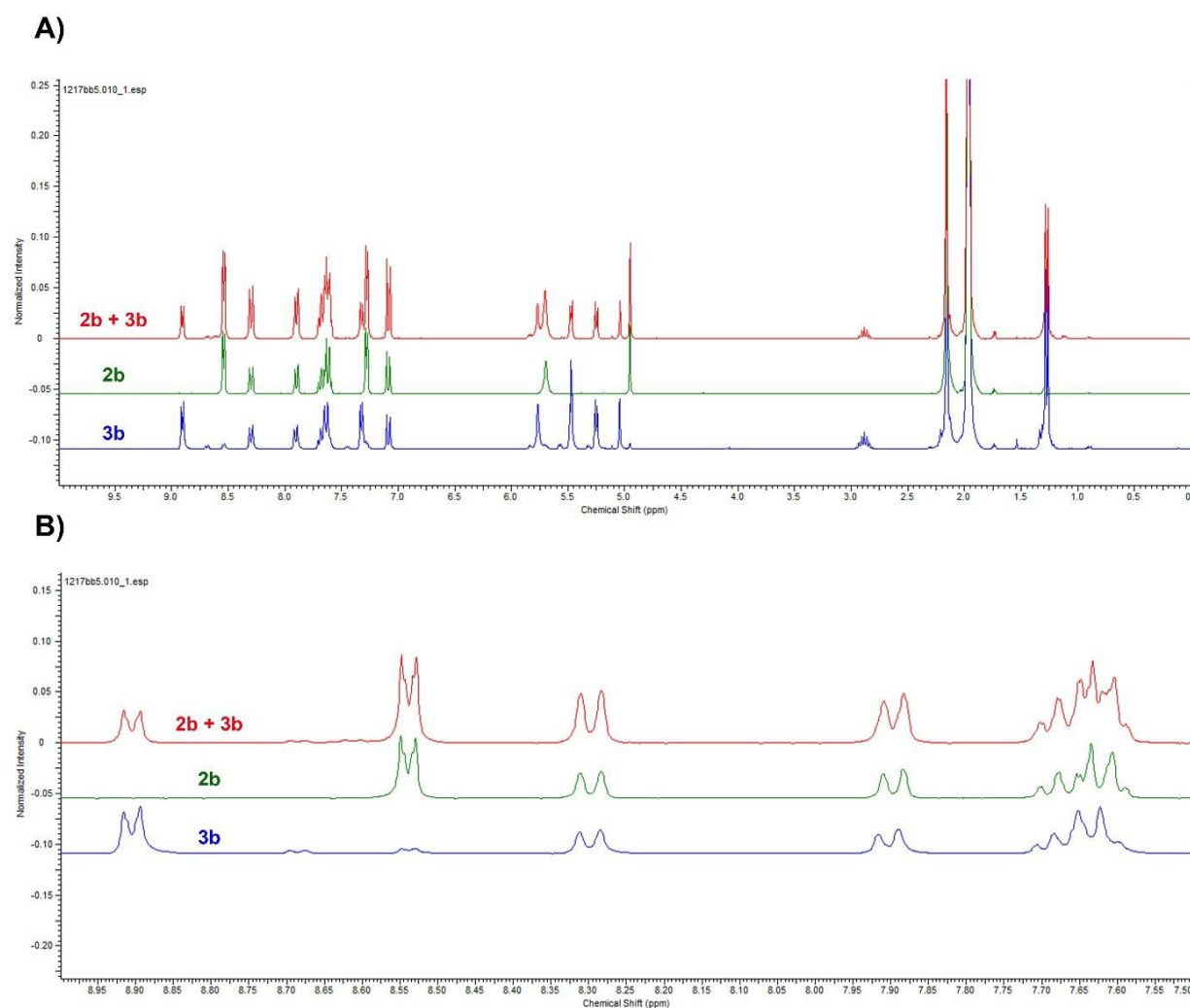


Figure S1. ¹H NMR spectrum of complex **3b** (blue), ligand **2b** (green), and complex **3b** spiked with **2b** (ca. 2-3 equiv.; red) in acetonitrile-D₃ after 3 h (complete spectrum (A); zoomed in on the relevant area 9.0-7.5 ppm (B)).

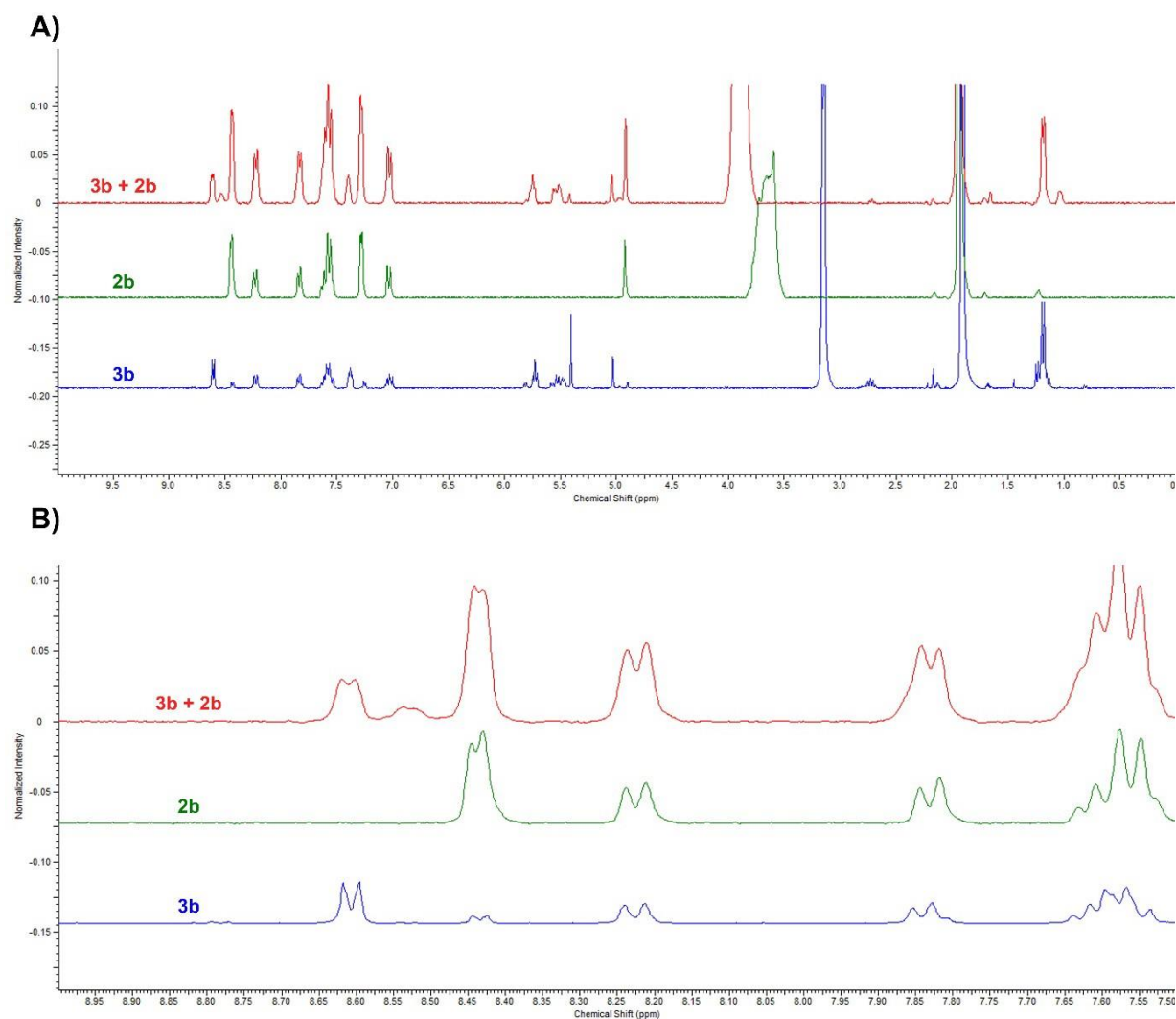


Figure S2. ^1H NMR spectrum of complex **3b** (blue), ligand **2b** (green), and complex **3b** spiked with **2b** (ca. 2-3 equiv.; red) in acetonitrile- D_3 with small amount of D_2O (ca. 10%) after 2 h (complete spectrum (A); zoomed in on the relevant area 9.0-7.5 ppm (B)).

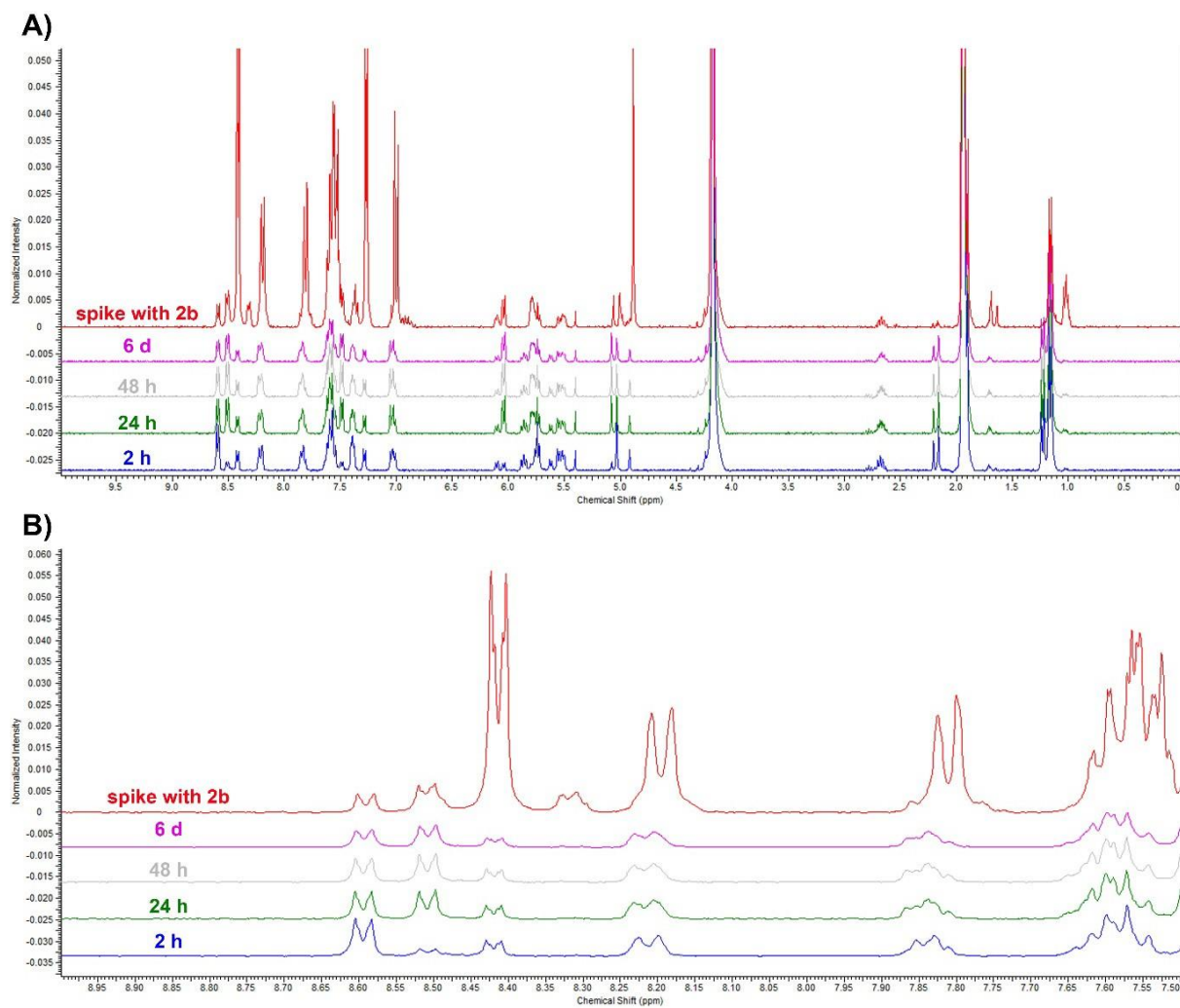


Figure S3. ^1H NMR spectra of complex **3b** in acetonitrile- D_3 with D_2O (ca. 50 %) after 2 h (blue), 24 h (green), 48 h (grey), and 6 d (pink). After 6 d the solution was spiked with an excess of **2b** (complete spectrum (A); zoomed in on the relevant area 9.0-7.5 ppm (B)).

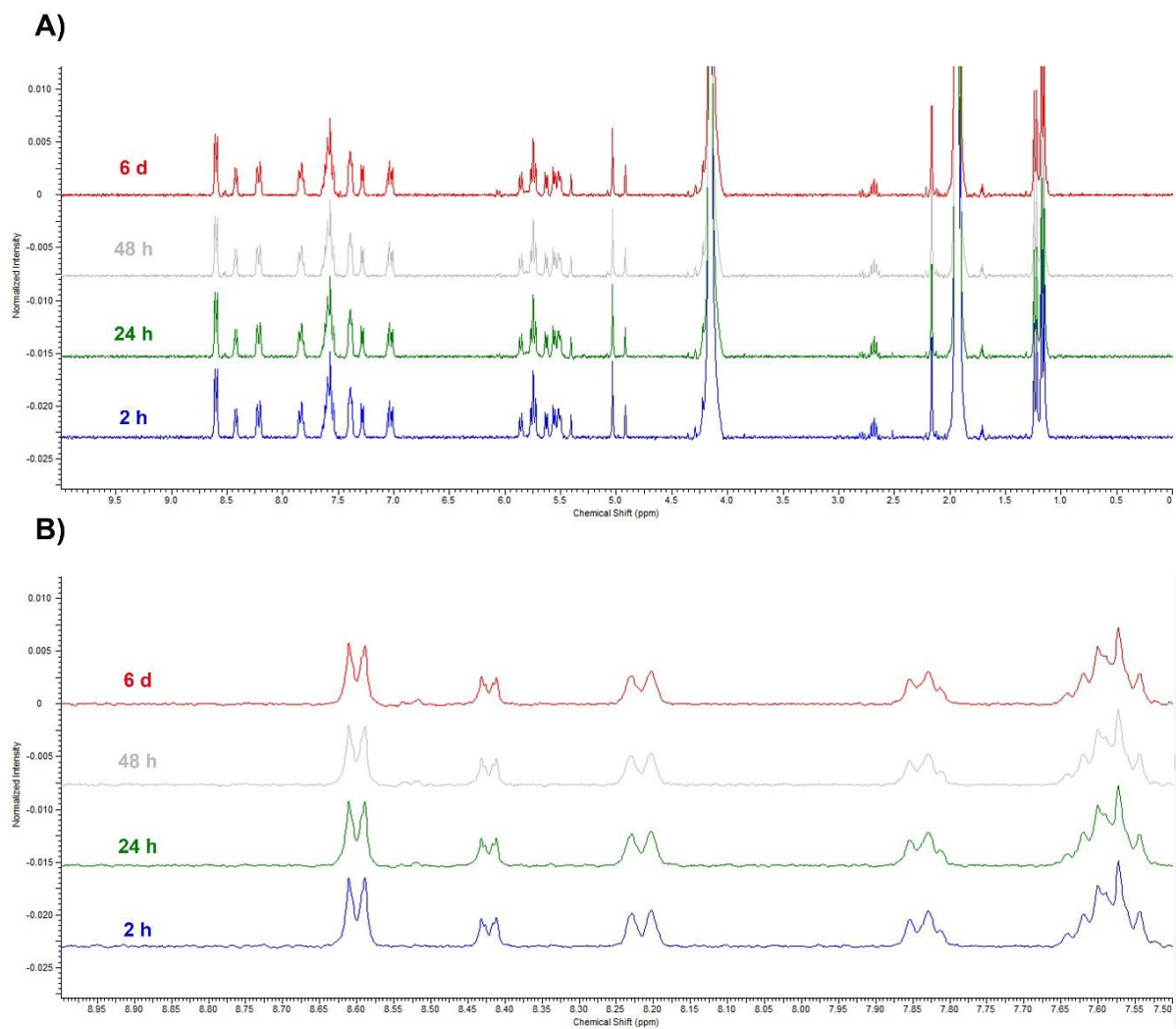


Figure S4. ^1H NMR spectra of complex **3b** in acetonitrile- D_3 with D_2O (ca. 50%) and 0.9% NaCl after 2 h (blue), 24 h (green), 48 h (grey), and 6 d (red) (complete spectrum (A); zoomed in on the relevant area 9.0 - 7.5 ppm (B)).

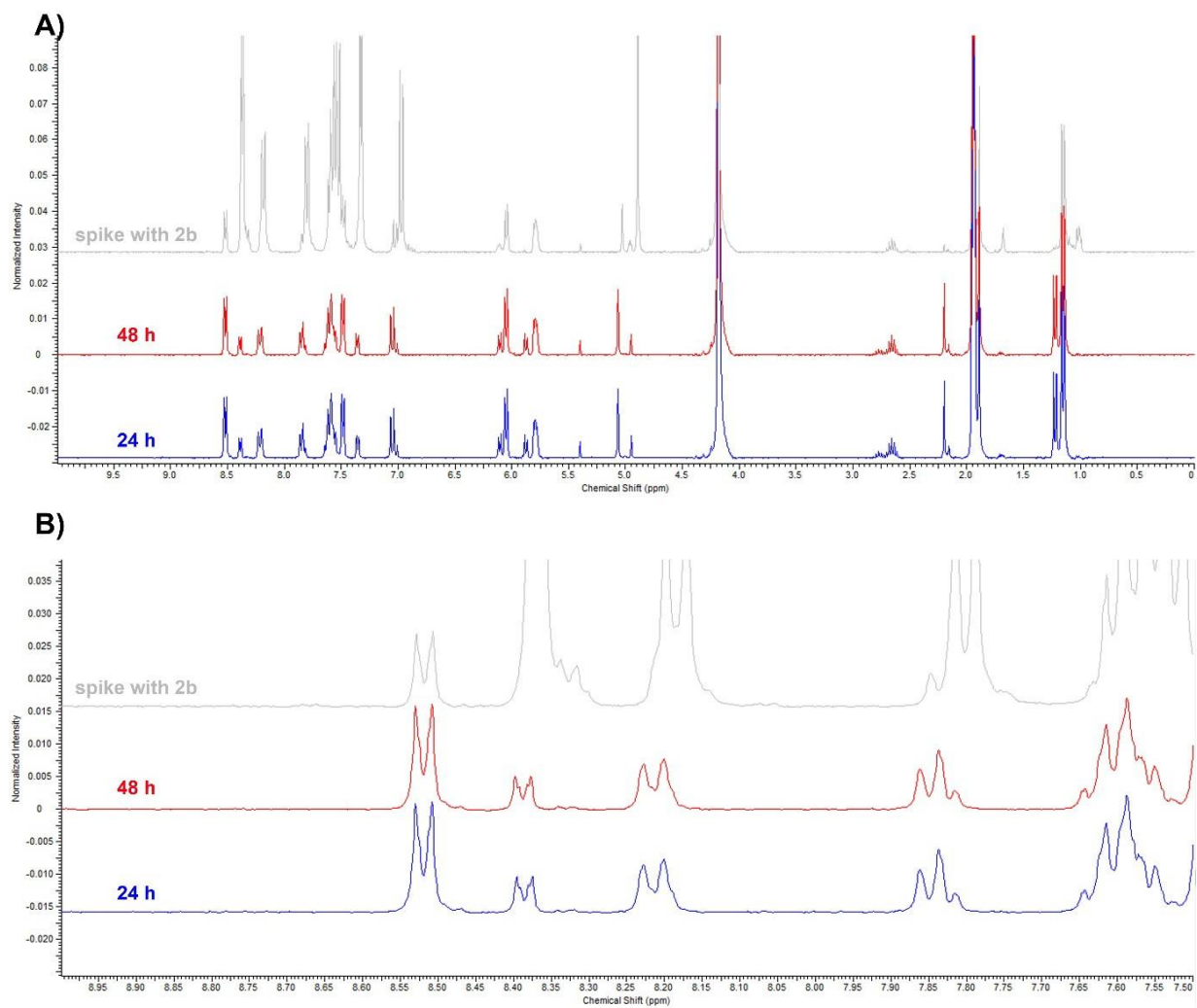


Figure S5. ^1H NMR spectra of complex **3b** in acetonitrile- D_3 with D_2O (ca. 50%) and an excess of AgNO_3 after 24 h (blue) and 48 h (red). After 48 h the solution was spiked with an excess of **2b** (grey) (complete spectrum (A); zoomed in on the relevant area 9.0 - 7.5 ppm (B)).

Cellular uptake

Table S1. Cellular ruthenium concentrations of HT-29 or HCT-116 cells exposed for 3 h to complexes **3a-d** (5 μ M) at 37 $^{\circ}$ C. Results are expressed as mean \pm SD from three independent ICP-MS experiments.

	HT-29 [pmol Ru/10 ⁶ cells]	HCT-116 [pmol Ru/10 ⁶ cells]
3a	4.91 \pm 0.43	5.51 \pm 1.71
3b	4.84 \pm 0.43	6.48 \pm 2.84
3c	7.62 \pm 1.04	8.64 \pm 3.78
3d	7.22 \pm 1.22	8.02 \pm 1.85

EtBr assay

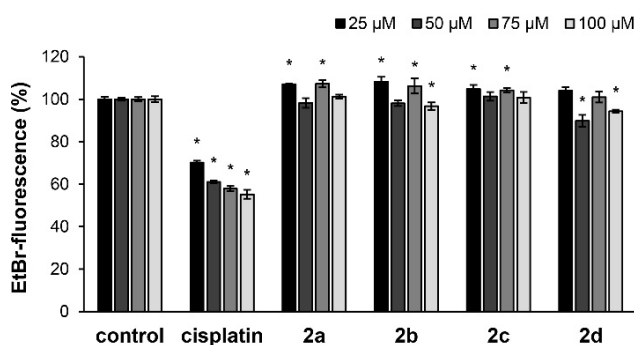


Figure S6. Relative ethidium bromide fluorescence after preincubation with vehicle (DMF; set to 100%), cisplatin, or test compounds **2a-d** (25, 50, 75, and 100 μ M) for 2 h. Decreased ethidium bromide fluorescence indicates the inhibition of ethidium bromide intercalation into DNA due to test compounds' blocking. Significant deviations from controls were determined using a t-test. *: p-value < 0.05.

Cell cycle analysis

Table S2. Effect of **3a** and **3b** on the cell cycle progression in MCF-7^{Topo} breast cancer cells. Flow cytometric analyses of the DNA content in MCF-7^{Topo} cells after treatment with vehicle (DMF), **3a** (5, 10, 20, and 35 nM), and **3b** (25, 50, and 75 nM) for 24 h and the distribution into G1, S, and G2/M phase of the cell cycle as well as the proportion of cells in sub-G1. The values are the means \pm SD of three independent experiments. Significant deviations from the particular phases and from the sub-G1 events of vehicle treated cells were determined using a t-test. *: p-value < 0.05.

	control	3a				3b		
		5 nM	10 nM	20 nM	35 nM	25 nM	50 nM	75 nM
Sub-G1	3.2 \pm 0.5	3.4 \pm 0.3	3.4 \pm 0.4	8.3 \pm 1.1*	11.5 \pm 1.2*	4.7 \pm 0.6*	12.4 \pm 0.9*	12.0 \pm 0.7*
G1	56.7 \pm 1.2	59.2 \pm 0.6*	65.7 \pm 2.6*	55.0 \pm 0.4	24.6 \pm 2.5*	66.7 \pm 1.1*	17.3 \pm 1.1*	6.1 \pm 0.6*
S	18.5 \pm 0.9	16.0 \pm 0.4*	11.2 \pm 0.4*	5.9 \pm 0.4*	6.6 \pm 0.4*	7.9 \pm 0.7*	5.8 \pm 0.5*	5.8 \pm 0.1*
G2/M	21.6 \pm 0.3	21.3 \pm 0.3	19.8 \pm 2.0	30.9 \pm 0.6*	57.2 \pm 2.2*	20.6 \pm 1.0	64.5 \pm 2.0*	76.0 \pm 0.1*

Table S3. Effect of **3a** and **3b** on the cell cycle progression in 518A2 melanoma cells. Flow cytometric analyses of the DNA content in 518A2 cells after treatment with vehicle (DMF), **3a** (15, 20, 30, and 40 nM), and **3b** (20, 30, and 40 nM) for 24 h and the distribution into G1, S, and G2/M phase of the cell cycle as well as the proportion of cells in sub-G1. The values are the means \pm SD of at least three independent experiments. Significant deviations from the particular phases and from the

	control	3a				3b			
		15 nM	20 nM	30 nM	40 nM	15 nM	20 nM	30 nM	40 nM
sub-G1	3.8 \pm 0.7	6.4 \pm 0.4*	6.9 \pm 1.1*	15.1 \pm 1.5*	26.4 \pm 1.9*	3.4 \pm 0.4	6.5 \pm 0.9*	7.2 \pm 1.1*	13.2 \pm 2.2*
G1	45.8 \pm 1.4	42.3 \pm 1.1*	39.4 \pm 0.5*	26.9 \pm 0.5*	22.1 \pm 0.9*	45.3 \pm 0.7	44.4 \pm 0.5	39.4 \pm 0.5*	29.0 \pm 0.6*
S	21.3 \pm 0.5	18.6 \pm 0.2*	18.2 \pm 0.5*	21.0 \pm 0.3	22.6 \pm 0.3*	20.8 \pm 1.2	18.5 \pm 0.9*	18.2 \pm 1.1*	20.5 \pm 0.8
G2/M	29.1 \pm 1.0	32.7 \pm 1.3*	35.4 \pm 1.1*	37.0 \pm 0.9*	28.9 \pm 1.5	30.5 \pm 1.3	30.6 \pm 0.5	35.1 \pm 1.7*	37.4 \pm 2.0*

sub-G1 events of vehicle treated cells were determined using a t-test. *: p-value < 0.05.

Table S4. Effect of **3a** and **3b** on the cell cycle progression in HT-29 colon carcinoma cells. Flow cytometric analyses of the DNA content in HT-29 cells after treatment with vehicle (DMF), **3a** (25, 50, 75, and 100 nM), and **3b** (50, 75, and 100 nM) for 24 h and the distribution into G1, S, and G2/M phase of the cell cycle as well as the proportion of cells in sub-G1. The values are the means \pm SD of three independent experiments. Significant deviations from the particular phases and from the sub-G1 events of vehicle treated cells were determined using a t-test. *: p-value < 0.05.

	control	3a				3b		
		25 nM	50 nM	75 nM	100 nM	50 nM	75 nM	100 nM
sub-G1	4.3 \pm 1.4	6.7 \pm 2.3	13.9 \pm 3.6*	13.6 \pm 1.8*	13.3 \pm 2.7*	13.5 \pm 3.7*	14.5 \pm 2.7*	10.6 \pm 3.2*
G1	53.7 \pm 0.6	48.8 \pm 1.5*	35.5 \pm 0.6*	22.9 \pm 4.3*	3.0 \pm 0.5*	36.1 \pm 2.9*	17.9 \pm 1.5*	3.9 \pm 0.4*
S	18.0 \pm 0.9	19.4 \pm 0.2*	20.5 \pm 1.7	9.9 \pm 2.5*	1.6 \pm 0.1*	19.2 \pm 0.4	8.4 \pm 1.3*	1.5 \pm 0.1*
G2/M	23.9 \pm 0.5	24.1 \pm 1.3	30.2 \pm 1.8*	53.6 \pm 7.4*	82.1 \pm 3.2*	31.2 \pm 4.4*	59.2 \pm 4.0*	84.0 \pm 3.5*

Table S5. Effect of **2c-d** and **3c-d** on the cell cycle progression in HT-29 colon carcinoma cells. Flow cytometric analyses of the DNA content in HT-29 cells after treatment with vehicle (DMF), **2c-d** (100 nM), and **3c-d** (250 nM) for 24 h and the distribution into G1, S, and G2/M phase of the cell cycle as well as the proportion of cells in sub-G1. The values are the means \pm SD of three independent experiments. Significant deviations from the particular phases and from the sub-G1 events of vehicle treated cells were determined using a t-test. *: p-value < 0.05.

	control	2c	2d	3c	3d
sub-G1	0.7 \pm 0.1	2.5 \pm 0.4*	4.5 \pm 0.6*	3.7 \pm 0.9*	3.0 \pm 0.5*
G1	59.0 \pm 0.3	34.3 \pm 4.8*	52.6 \pm 3.6*	1.9 \pm 0.3*	47.0 \pm 2.5*
S	20.8 \pm 0.8	17.2 \pm 0.7*	14.0 \pm 0.5*	2.3 \pm 0.3*	19.7 \pm 0.7
G2/M	19.5 \pm 0.5	45.9 \pm 5.3*	29.0 \pm 2.5*	92.1 \pm 0.9*	30.3 \pm 1.8*

Mitotic Index

Table S6. Effect of test compounds on mitotic arrest in HT-29 colon carcinoma cells after 6 h of incubation. Cells were fixed and stained with DAPI. Mitotic indices were determined by counting mitotic cells using a fluorescence microscope (400 \times magnification). At least 400 cells per glass coverslip were counted and depicted as mean \pm SD of three independent experiments. Significant deviations from the controls were determined using a t-test. *: p-value < 0.05.

	100 nM	250 nM
control	-	7.4 \pm 0.7
3a	21.4 \pm 0.6*	26.9 \pm 3.7*
3b	22.5 \pm 0.9*	24.1 \pm 2.1*
3c	16.4 \pm 2.5*	19.9 \pm 1.7*
3d	7.9 \pm 1.8	14.6 \pm 0.1

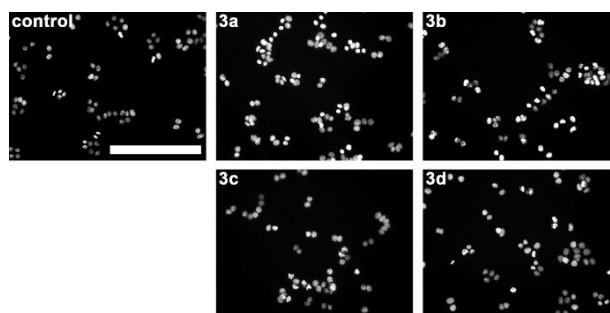


Figure S7. Accumulation of mitotic HT-29 colon carcinoma cells after exposure to **3a-d** (250 nM) for 6 h. Nuclei staining with DAPI. The images are representative of three independent experiments (200 \times magnification).

Effect on the microtubule cytoskeleton

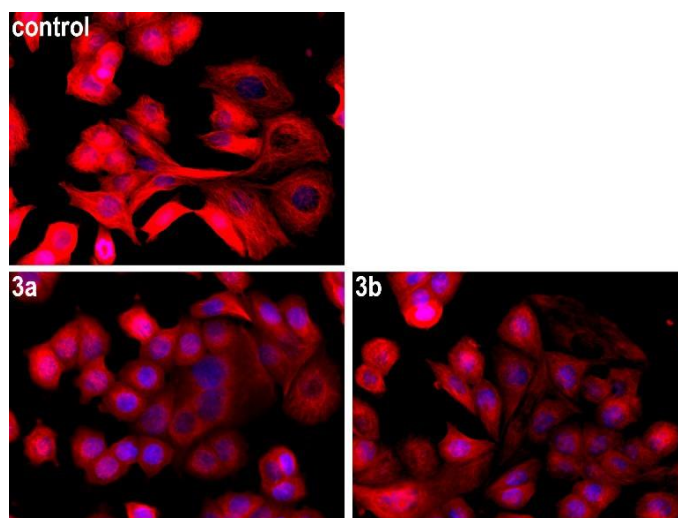


Figure S8. Effect of **3a** (200 nM) and **3b** (200 nM) on the organization of the microtubule cytoskeleton (red) in MCF-7^{Topo} breast cancer cells after 3 h incubation. Nuclei were counterstained with DAPI (blue). The pictures are representative of two independent experiments (400 \times magnification).

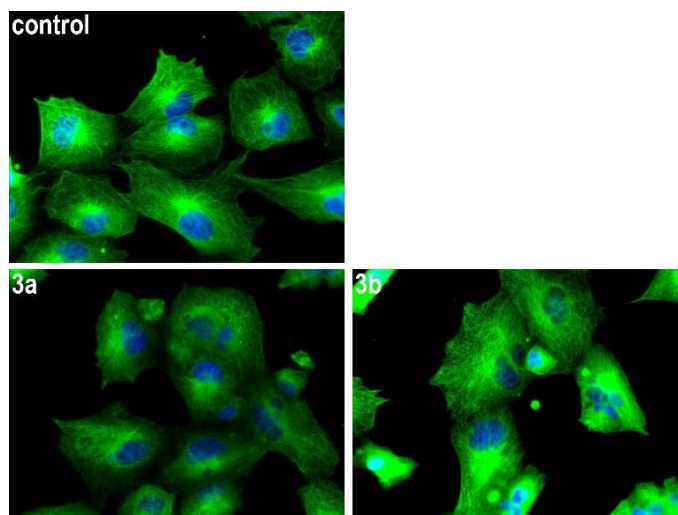


Figure S9. Effect of **3a** (60 nM) and **3b** (60 nM) on the organization of the microtubule cytoskeleton (green) in 518A2 melanoma cells after 24 h incubation. Nuclei were counterstained with DAPI (blue). The pictures are representative of two independent experiments (400 \times magnification).

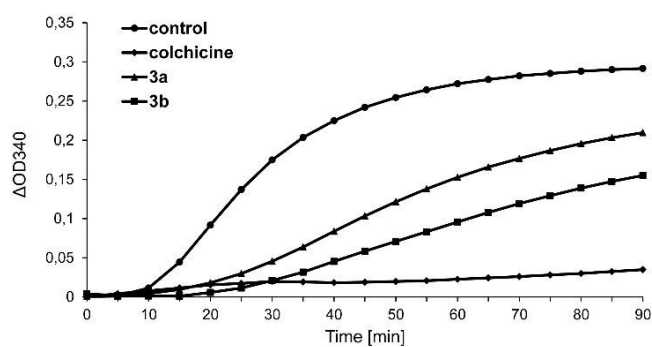


Figure S10. Effects of **3a**, **3b**, and colchicine (all 10 μ M) on the polymerization of tubulin as measured by a turbidimetric-based cell-free tubulin assay. Data of the graph are representative of two independent experiments. Δ OD₃₄₀ is the change in the absorption at 340 nm wavelength with OD₃₄₀ set as 0 at 0 min.

References

- [S1] K. Mahal, B. Biersack, H. Caysa, R. Schobert, T. Mueller, *Invest. New Drugs* 33 (2015) 541-554.

5.5 Manuskript IV

Oxazole-bridged combretastatin A-4 derivatives with tethered hydroxamic acids: Structure-activity relations of new dual inhibitors of HDAC and tubulin function

Florian Schmitt,^[a] Lisa Chiara Gosch,^{[b],[c]} Rainer Schobert,^[a] Bernhard Biersack,^{*[a]} Andrea Volkamer,^[c] and Michael Höpfner^[b]

[a] Department of Chemistry, University of Bayreuth, Universitaetsstrasse 30, 95440 Bayreuth, Germany

[b] Institute of Physiology, Charité – Universitätsmedizin Berlin, Charitéplatz 1, 10117 Berlin, Germany.

[c] In Silico Toxicology Group, Institute of Physiology, Charité – Universitätsmedizin Berlin, Charitéplatz 1, 10117 Berlin, Germany.

* Corresponding author, Email address: Bernhard.Biersack@yahoo.com

To be submitted



1 Article

2 Oxazole-bridged combretastatin A-4 derivatives with 3 tethered hydroxamic acids: Structure-activity 4 relations of new inhibitors of HDAC and/or tubulin 5 function

6 Florian Schmitt¹, Lisa Chiara Gosch^{2,3}, Alexandra Dittmer², Thomas Mueller⁴, Rainer Schobert¹,
7 Bernhard Biersack^{1,*}, Andrea Volkamer³, and Michael Höpfner^{2,*}

8 ¹ Department of Chemistry, University of Bayreuth, Universitaetsstrasse 30, 95447 Bayreuth, Germany;
9 florian1.schmitt@uni-bayreuth.de, rainer.schobert@uni-bayreuth.de

10 ² Institute of Physiology, Charité – Universitätsmedizin Berlin, Charitéplatz 1, 10117 Berlin, Germany;
11 lisa-chiara.gosch@charite.de, alexandra.dittmer@charite.de, michael.hoepfner@charite.de

12 ³ In Silico Toxicology Group, Institute of Physiology, Charité – Universitätsmedizin Berlin, Charitéplatz 1,
13 10117 Berlin, Germany; lisa-chiara.gosch@charite.de, andrea.volkamer@charite.de

14 ⁴ Internal Medicine IV, University Hospital Halle (Saale), Ernst-Grube-Str. 40, 06120 Halle, Germany;
15 thomas.mueller@medizin.uni-halle.de

16 * Correspondence: bernhard.biersack@yahoo.com; Tel.: +49-921-55-2673; michael.hoepfner@charite.de; Tel:
17 +49-030-450-528-515

18 Received: 20 September 2018; Accepted: date; Published: date

19 **Abstract:** New inhibitors of tubulin polymerization and/or histone deacetylase (HDAC) activity
20 were synthesized by attaching alkyl tethered hydroxamic acid appendages of varying length to
21 oxazole-bridged combretastatin A-4 analogous caps. While their antiproliferative and microtubule
22 disrupting effect was most pronounced for derivatives with short spacers, HDAC inhibition was
23 strongest for those with longer spacers. These findings were further supported by computational
24 methods such as structure-based docking experiments exploring the target interactions of the
25 derivatives with varying linkers. For instance, compounds **4a** and **4d** featuring short four-atom
26 spacers between cap and hydroxamic acid inhibited the growth of various cancer cell lines and
27 human endothelial hybrid cells with IC₅₀ values in the low nanomolar range. In line with their
28 ability to inhibit the microtubule assembly, **4d** and the five-atom spaced **4e** caused an
29 accumulation of 518A2 melanoma cells in G2/M phase, whereas **4f**, featuring a six-atom spacer and
30 performing best in HDAC inhibition, induced a G1 arrest in these cells. All these beneficial
31 anticancer activities together with their selectivity for cancer cells over non-malignant cells, point
32 out the great potential of these novel pleiotropic HDAC and tubulin inhibitors as drug candidates
33 for cancer therapy.

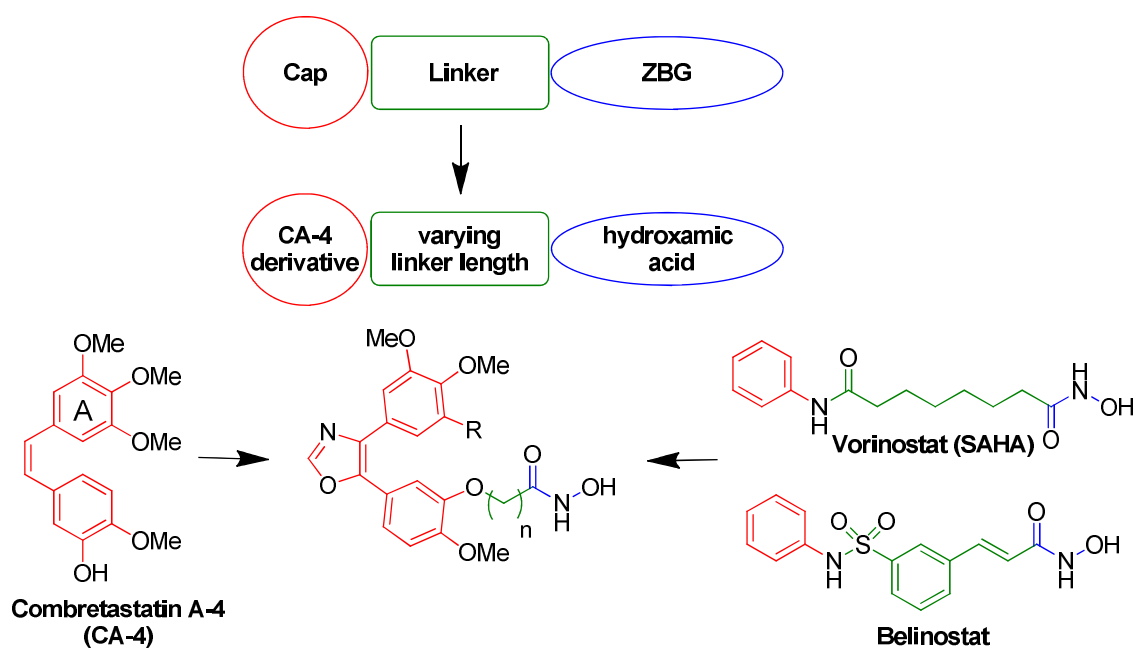
34 **Keywords:** combretastatin A-4; oxazole; histone deacetylase; tubulin; anticancer agents
35

36 1. Introduction

37 Histone deacetylases (HDAC) catalyze the *N*-deacetylation of *N*-terminal lysine residues of
38 histones thus regulating the expression of genes which are important for crucial cellular processes
39 such as chromatin condensation and decondensation (DNA replication, transcription, and repair).
40 Certain HDAC enzymes also modify non-histone proteins such as signal transduction mediators,
41 transcription factors and regulators, as well as structural proteins resulting in modulation of cell
42 growth, differentiation, migration, and angiogenesis [1]. HDACs are overexpressed in various solid

tumors, e.g. in gastric cancer, prostate cancer, breast cancer, and colorectal cancer [2–6]. HDAC of class I (HDAC1, 2, 3, and 8), class IIa (HDAC4, 5, 7, and 9), class IIb (HDAC6, and 10) and class IV (HDAC11) share a zinc(II) cation in the center of their catalytic cavity which is the target of several approved HDAC inhibitors (HDACi) [1]. By the development of quite a number of HDACi over the last two decades a robust pharmacophore model for zinc-dependent HDACi was established which typically consists of a zinc binding group (ZBG), a linker, and a capping group (Figure 1). These HDACi mimic the natural substrate acetyl-lysine and exert their effect by coordination of the zinc(II) center with ligands such as benzamides, carboxylates, or hydroxamic acids [7]. The ZBGs should be connected to the cap by a hydrophobic linker, which is slim enough to fit in the tunnel between the active site and the capping groups. The latter are used for surface recognition and can induce sub-class selectivity [8,9]. Several HDACi such as vorinostat (SAHA, Fig. 1), belinostat (PXD101, Figure 1) and panobinostat (LBH589) which were modelled on this pharmacophore template are already approved for the therapy of lymphoma and myeloma [10–13]. Several other HDACi are recently under clinical investigation, since HDACi of the first generation have shown certain shortcomings in solid tumors such as induction of epithelial-to-mesenchymal transition (EMT) in prostate cancer cells [14–16]. In order to overcome such drawbacks, HDACi with dual or multimodal activities including kinase inhibition or DNA alkylation/metalation were introduced [17].

Microtubules are vital components of the cytoskeleton and thus an important target in cancer chemotherapy [18,19]. Interestingly, HDACi have shown synergetic effects when combined with tubulin-binding anticancer drugs [20–22]. Thus, HDACi harboring tubulin-targeting structural motifs appear to be promising anticancer drug candidates [23–25]. While colchicine- and quinazoline-based dual inhibitors were already published, no dual inhibitors based on the potent microtubule disrupting agent (MDA) combretastatin A-4 (CA-4, Figure 1) are known so far. Herein, we present a new series of tubulin-targeting oxazole-bridged CA-4 derivatives with hydroxamate appendages. We chose the oxazole-bridged CA-4 scaffold because of its improved stability when compared with the *cis*-stilbene CA-4 parent compound [26,27]. We investigated how the linker length of the new hybrid compounds affects the compounds' potency to inhibit HDAC1 and HDAC6, as well as the microtubule assembly. Moreover, the anti-proliferative, anti-migratory and further anticancer activities of the new hybrid compounds were evaluated and computational methods were used to predict and to explain binding modes and affinities of the studied compounds.

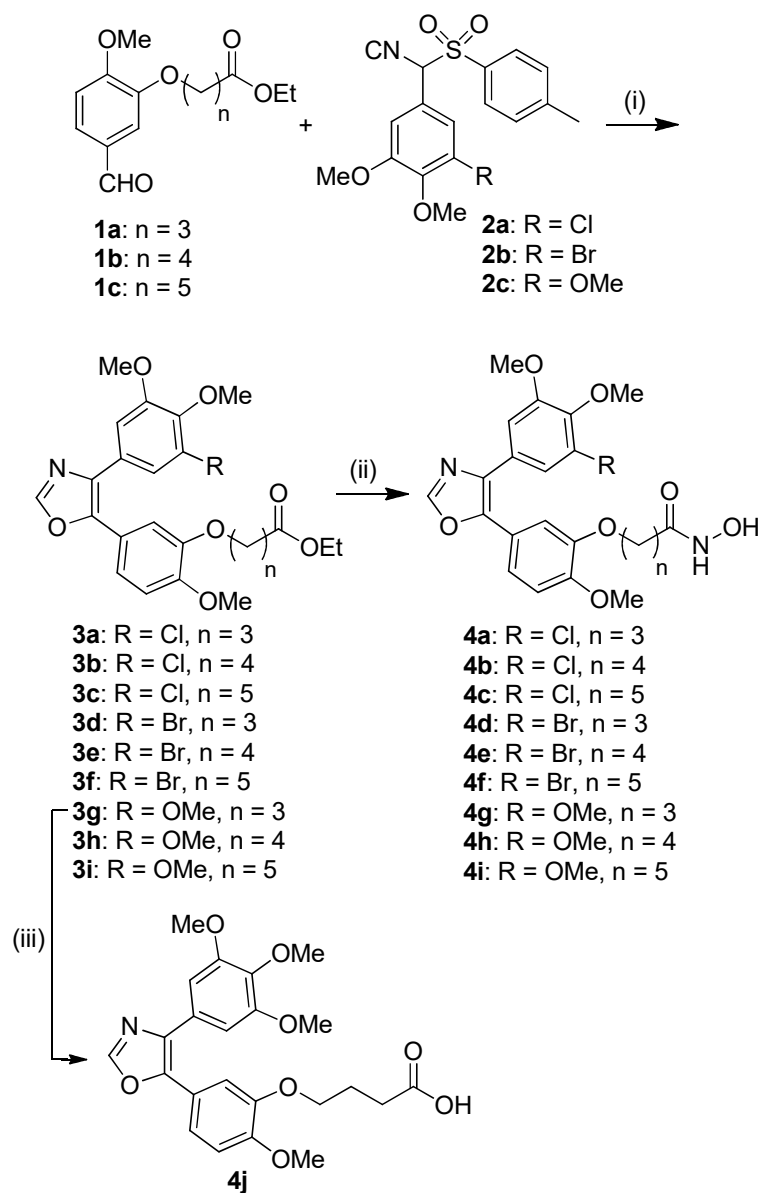


1 **Figure 1.** General pharmacophore model of HDACi, structures of the vascular-disrupting agent
 2 (VDA) combretastatin A-4 (CA-4) and of the HDACi vorinostat (SAHA) and belinostat as well as the
 3 combination of CA-4 derivatives and HDACi in our hybrid compounds.

4 2. Results

5 2.1. Chemistry

6 The 4,5-diaryloxazoles were synthesized via a Van Leusen reaction. The required starting
 7 benzaldehydes **1a-c** and TosMIC reagents **2a-c** were prepared according to literature procedures, i.e.,
 8 the former via alkylation of isovanillin with the corresponding ethyl ω -bromoalkanoates, and the
 9 latter via dehydration of their tosylmethyl formamide precursors (obtained from reaction of
 10 3-bromo/chloro-4,5-dimethoxybenzaldehyde or 3,4,5-trimethoxybenzaldehyde with toluenesulfonic
 11 acid and formamide) [25–28]. The synthesis of the target hydroxamic acids **4a-i** was carried out in
 12 two steps. Van Leusen reaction of **1a-c** and **2a-c** gave the oxazoles **3a-i** in moderate yields (Scheme 1).
 13 Conversion of the ethyl esters **3a-i** to the analogous hydroxamic acids **4a-i** was accomplished in
 14 moderate to high yields. The target compounds **4a-i** were obtained as colorless solids. In addition,
 15 carboxylic acid analog **4j** was prepared for comparison purposes and obtained from hydrolysis of **3g**
 16 under basic conditions (Scheme 1).



1 **Scheme 1.** Reagents and conditions: (i) K₂CO₃, EtOH, reflux, 2 h, 40-53%; (ii) 50% H₂N-OH in H₂O,
2 NaOH, CH₂Cl₂/MeOH (1:2), r.t., 1 h, 64-93%; (iii) 1 M aq. NaOH, MeOH, r.t., 24 h, 68%.

3 2.2. Biological Evaluation

4 First, all compounds (**4a-j**) were tested for their inhibitory potential on cancer cell growth.
5 Next, we investigated how the length of the linker of the various test compounds may influence
6 cytoskeletal components, the inhibition of HDAC1 and HDAC6, and cell cycle progression. The
7 latter analyses were performed only with the bromo substituted derivatives **4d-f** which showed
8 slightly higher anti-proliferative activity on average compared to their chloro or methoxy congeners.
9 The new derivatives **4a-i**, the new carboxylic acid analog **4j** and its ethyl-ester **3g** were screened in
10 MTT assays for anti-proliferative activity against a panel of six cancer cell lines of four entities as
11 well as against the human endothelial hybrid cell line Ea.Hy926 (Table 1). The bromo derivatives
12 **4d-f** were also tested against the non-malignant human dermal fibroblasts HDFa. IC₅₀ values of the
13 known HDACi SAHA and the VDA CA-4 were taken from earlier studies for comparison.
14 Compounds **4a-i** led to dose-dependent growth inhibition of all cancer cell lines and the endothelial
15 hybrid cells Ea.Hy926. Carboxylic acid **4j** and its ester **3g** did not affect the viability of 518A2
16 melanoma and HT-29 colon carcinoma cells even at concentrations as high as 50 μM, which suggests
17 that the hydroxamate side chain is crucial for the anti-proliferative activity. On average, the CA-4
18 resistant HT-29 colon carcinoma and the multi-drug resistant MCF-7^{Topo} mamma carcinoma cells
19 were least sensitive to **4a-I** [29,30]. In contrast, **4a-i** were most active against 518A2 melanoma,
20 HCT-116 colon carcinoma, and endothelial hybrid cells Ea.Hy926. The low IC₅₀ values of the
21 compounds **4a-i** against Ea.Hy926 cells are indicative of a potential application as a vascular
22 disruptive agent like the parent CA-4. Moreover, the bromo substituted derivatives **4d-f** showed a
23 distinct selectivity for cancer and endothelial cells over non-malignant human dermal fibroblasts
24 HDFa. The chloro substituted compounds **4a-c** and the bromo substituted compounds **4d-f** showed
25 an interesting structure-activity relationship (SAR). The anti-proliferative activity increased with
26 decreasing linker length when going from caproic acid derivatives **4c** and **4f** over valeric acid
27 derivatives **4b** and **4e** to butyric acid derivatives **4a** and **4d**. Interestingly, the trimethoxy derivatives
28 **4g-i** did not fit in this SAR since **4i** was on average more cytotoxic than **4h**. Several earlier studies
29 had shown that the substitution of an *m*-methoxy group at the A-ring of CA-4 derivatives by halide
30 increases their activity. We now observed a similar phenomenon since the chloro substituted
31 derivatives **4a-c** and the bromo substituted analogs **4d-f** were superior to the trimethoxy derivatives
32 **4g-i**. Additionally, we determined the IC₅₀ values of the test compounds when applied to 518A2
33 melanoma cells for different incubation periods (24 and 72 h). In the case of the most strongly
34 anti-proliferative compounds (**4a**, **4d**, and **4g**), the IC₅₀ values after 72 h were about eight-fold lower
35 compared with those after 24 h. Since the majority of the investigated cell lines have division periods
36 of 20-30 h, we assume that the test compounds exert their effect by blocking the cell division and by
37 triggering apoptosis [31,32].

38 **Table 1.** Inhibitory concentrations IC₅₀¹ [μM] of **3g**, **4a-j**, SAHA and CA-4 in cancer cells.

	518A2 (24 h)	518A2 (72 h)	HT-29 (24 h)	HT-29 (72 h)	DLD-1 (72 h)	HCT-116 (72 h)	KB-V1 ^{vbl} (72 h)	MCF-7 ^{Topo} (72 h)	Ea.Hy926 (72 h)	HDFa (72 h)
3g	>100	>50	>100	>50	-	-	-	-	-	-
4a	1.3 ± 0.4	0.11 ± 0.01	2.5 ± 0.4	2.9 ± 0.3	0.34 ± 0.01	0.21 ± 0.01	0.15 ± 0.02	0.66 ± 0.14	0.0012 ± 0.0006	-
4b	10.4 ± 5.1	1.0 ± 0.1	4.2 ± 0.2	3.6 ± 0.1	3.2 ± 0.1	2.4 ± 0.1	4.0 ± 0.2	2.9 ± 0.8	0.57 ± 0.07	-
4c	9.4 ± 1.4	2.2 ± 0.3	4.6 ± 0.3	4.9 ± 0.3	3.3 ± 0.5	6.5 ± 0.3	18.4 ± 3.4	6.1 ± 0.7	7.5 ± 0.5	-
4d	0.71 ± 0.05	0.11 ± 0.01	1.3 ± 0.3	1.4 ± 0.2	0.29 ± 0.02	0.13 ± 0.01	0.48 ± 0.06	2.8 ± 0.3	0.018 ± 0.004	23.9 ± 1.6
4e	2.4 ± 0.3	0.80 ± 0.07	2.1 ± 0.6	1.9 ± 0.2	2.1 ± 0.4	2.2 ± 0.3	2.0 ± 0.3	3.4 ± 0.2	0.66 ± 0.01	>100
4f	7.6 ± 0.2	6.4 ± 0.4	6.6 ± 0.6	14.2 ± 1.6	4.1 ± 0.3	6.3 ± 0.4	7.1 ± 0.2	8.3 ± 0.7	0.41 ± 0.04	>50
4g	4.4 ± 0.1	0.64 ± 0.07	5.0 ± 0.2	2.8 ± 0.2	0.92 ± 0.04	0.92 ± 0.12	2.7 ± 0.2	9.3 ± 0.8	0.41 ± 0.04	-
4h	21.6 ± 3.9	5.6 ± 0.6	53.9 ± 12.0	6.6 ± 0.6	5.8 ± 0.4	3.4 ± 0.4	11.1 ± 1.6	39.6 ± 5.9	3.4 ± 0.2	-
4i	6.9 ± 2.5	3.3 ± 0.3	47.6 ± 10.6	1.7 ± 0.1	1.3 ± 0.1	0.61 ± 0.07	9.0 ± 0.3	15.8 ± 1.4	1.7 ± 0.1	-
4j	>100	>50	>100	>100	-	-	-	-	-	-
SAHA ²	18.7 ± 0.1	1.8 ± 0.1	1.9 ± 0.3	1.8 ± 0.1	-	0.9 ± 0.1	13.1 ± 0.8	13.5 ± 0.7	1.9 ± 0.2	-
CA-4 ²	-	0.018 ±	-	3.6 ± 0.1	-	0.0026 ±	-	0.50 ± 0.20	0.011 ±	-

0.007

0.0002

0.002

¹Values are derived from dose-response curves obtained by determining the percentage of viable cells (human 518A2 melanoma, HT-29, HCT-116 and DLD-1 colon carcinomas, KB-V1^{Vbl} cervix carcinoma, and MCF-7^{Topo} breast adenocarcinoma as well as to Ea.Hy926 endothelial hybrid cells and non-malignant HDFa dermal fibroblasts) relative to vehicle treated controls after 24 h or 72 h treatment with the test compounds using MTT-assays; values are the means \pm SD of four independent experiments. ²Values taken from earlier publications, ref 27, 33, and 34. ^{c-} = not determined.

The new hybrid compounds **4d-f** were further tested for their potential inhibition of the microtubule assembly which is a typical feature of the parent compound CA-4. MTT assays already revealed some CA-4 characteristics such as selectivity for EA.Hy926 endothelial hybrid cells and a reduced efficacy against HT-29 colon carcinoma cells [33]. The effect of the test compounds on the polymerization of tubulin was determined *in vitro* using purified pig brain tubulin (Figure 2). 10 μ M of **4d** inhibited the polymerization of pig brain tubulin nearly completely, while **4e** exhibited a merely moderate inhibitory effect and **4f** virtually none. These results are in line with the anti-proliferative activity pattern of the compounds and were additionally confirmed on a cellular level by immunostaining of alpha-tubulin in 518A2 melanoma cells (Figure 3). Caproic acid derivative **4f**, showing the highest IC₅₀ values in MTT assays, did not affect the microtubule cytoskeleton even at concentrations as high as 4 μ M. In contrast, **4e** eroded the highly organized microtubule network, but left some intact clusters especially around the nuclei whereas 0.5 μ M of **4d** was enough to cause a complete disruption of the microtubule cytoskeleton. Similar alterations of the cytoskeleton of endothelial Ea.Hy926 cells were observed upon treatment with 0.2 μ M of **4d** for 24 h (Supporting Information).

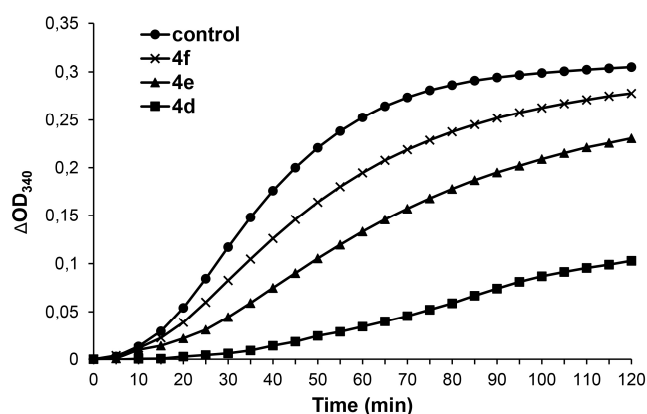


Figure 2. Effects of compounds **4d-f** (10 μ M) on the polymerization of tubulin as determined by a turbidimetric cell-free tubulin assay. Data are representative of two independent experiments. Δ OD₃₄₀ is the change in the absorption at 340 nm wavelength with OD₃₄₀ set as 0 at 0 min.

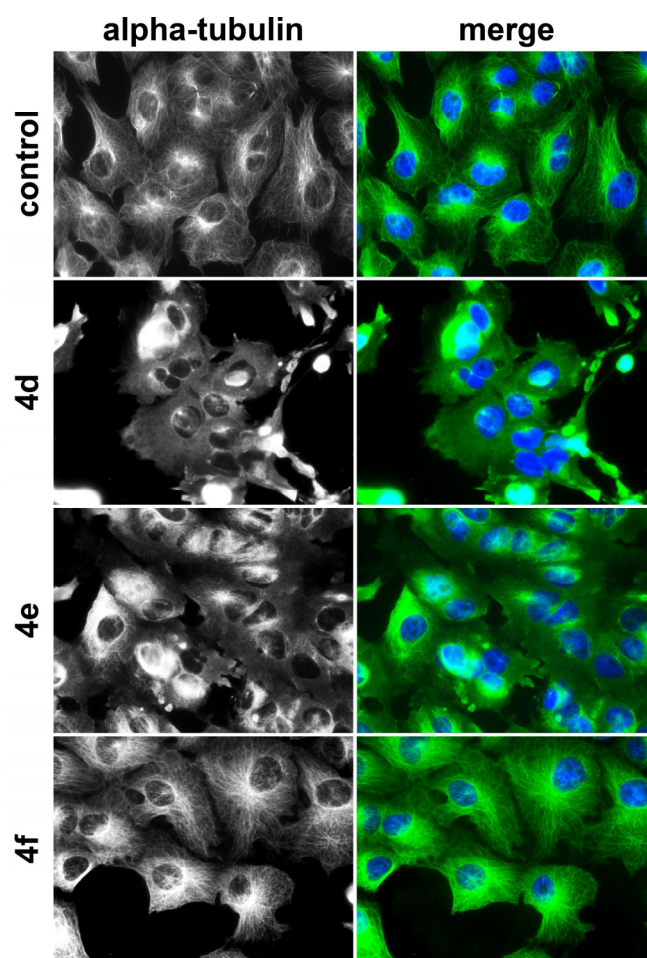


Figure 3. Effect of compounds **4d** (0.5 μM), **4e** (1.5 μM), **4f** (4 μM), and vehicle (DMSO) on the organization of microtubule cytoskeleton in 518A2 melanoma cells after 24 h incubation. Nuclei were counterstained with DAPI (merge, blue); microtubule (green). Pictures are representative of two independent experiments (400 \times magnification).

We also investigated the bromo derivatives **4d–f** with different linker lengths for their inhibitory effect on the deacetylation capacity of recombinant human HDAC1 and HDAC6 (Table 2). Contrary to the linker length-dependent decreasing potency on tubulin polymerization and cell proliferation, the HDAC inhibition increased with linker length. Compound **4d**, the most cytotoxic compound in this row featuring a four-atom spacer, showed only moderate HDAC6 inhibition (IC_{50} : $13.8 \pm 0.2 \mu\text{M}$). Compound **4e**, carrying a five-atom linker, had a distinctly lower IC_{50} value ($3.5 \pm 0.1 \mu\text{M}$) whereas **4f**, the compound with a six-atom linker, had the lowest IC_{50} value of this triad ($0.32 \pm 0.02 \mu\text{M}$) which was even slightly lower than that of the known HDAC6 selective inhibitor tubacin ($0.38 \pm 0.03 \mu\text{M}$). Concerning HDAC1 inhibition, **4d** and **4e** showed similar IC_{50} values (4.0 ± 0.1 and $3.8 \pm 0.1 \mu\text{M}$) whereas **4f** was again the most potent compound ($0.49 \pm 0.05 \mu\text{M}$). Unlike HDAC1 which is found in the nucleus of cells where it is responsible for the eponymous deacetylation of histones, HDAC6 locates predominantly in the cytoplasm and has several targets including α -tubulin, HSP90, cortactin, and β -catenin [35,36]. The inhibition of HDAC6 induces hyperacetylation of these molecules resulting in a reduction of cell motility, and proliferation, and eventually induces cell death [37]. The ability of compound **4f** to inhibit HDAC6 was confirmed by western blot analyses (Figure 4) as well as by immunofluorescence staining of acetyl- α -tubulin in 518A2 melanoma cells (Supporting Information). In both experiments, treatment of the cells with **4f** caused a distinct increase of acetyl- α -tubulin.

Table 2. HDAC inhibition [IC₅₀ (μM)]¹ by compounds 4d–f.

	4d	4e	4f	SAHA	Tubacin
HDAC1	4.0 ± 0.1	3.8 ± 0.1	0.49 ± 0.05	0.44 ± 0.04	-
HDAC6	13.8 ± 0.2	3.5 ± 0.1	0.32 ± 0.02	-	0.38 ± 0.03

¹IC₅₀ values are derived from dose-response curves obtained by measuring the percentage of deacetylated, fluorogenic substrate relative to DMSO controls. Results show inhibition of recombinant HDAC1 and HDAC6 by compounds 4d–f, pan-HDAC inhibitor SAHA and HDAC6-specific inhibitor tubacin as determined by conversion of a HDAC substrate to a fluorophore. Values are the means ± SD of two independent experiments.

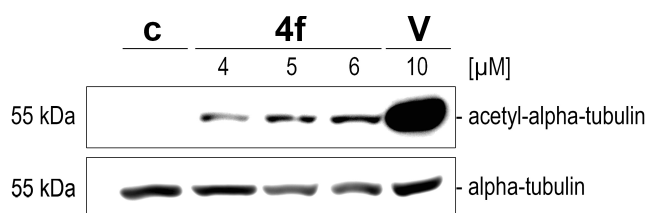


Figure 4. Compound-induced effect on the acetylation of microtubule (acetyl-alpha-tubulin) in 518A2 melanoma cells upon treatment with 4f (4, 5, and 6 μM), SAHA (10 μM), and vehicle (DMSO) for 24 h. Cells were lysed and the levels of the acetyl-alpha-tubulin was monitored by immunoblotting with the specific antibody. c: control; V: SAHA/vorinostat.

Imidazole-bridged CA-4 derivatives carrying hydroxamic acid appendages had previously been found to induce alterations of the actin cytoskeleton, such as augmented formation of stress fibers to the effect of an impaired cell motility [34,38]. Such alterations are typical reactions to microtubule destabilization and hyperacetylation of cortactin as a consequence of HDAC6 inhibition [39]. Thus, we investigated the bromo derivatives 4d–f for their effect on the actin cytoskeleton of 518A2 melanoma cells (Figure 5). Even though their effects on the microtubules of these cells differed, all of them induced the formation of actin stress fibers which traversed the whole cell body, while the control cells showed only filamentous actin in the periphery. The associated anti-migratory effects of compounds 4d–f were then tested in so-called wound healing assays. In this assay a strip of cells is scratched off a confluent grown cell monolayer of 518A2 cells, followed by monitoring the gap-closing process operating not by proliferation but by active migration (Supporting Information). The re-closure of the scratch area was significantly retarded in samples treated with compounds 4d–f for 24 h (38–45% wound closure) compared to vehicle treated control cells (63% wound closure).

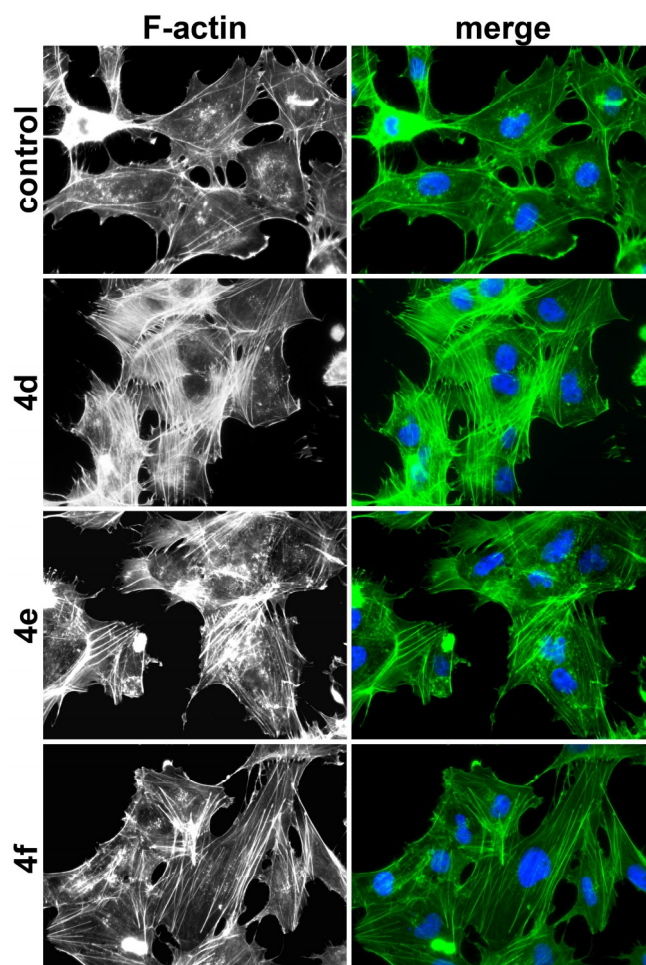
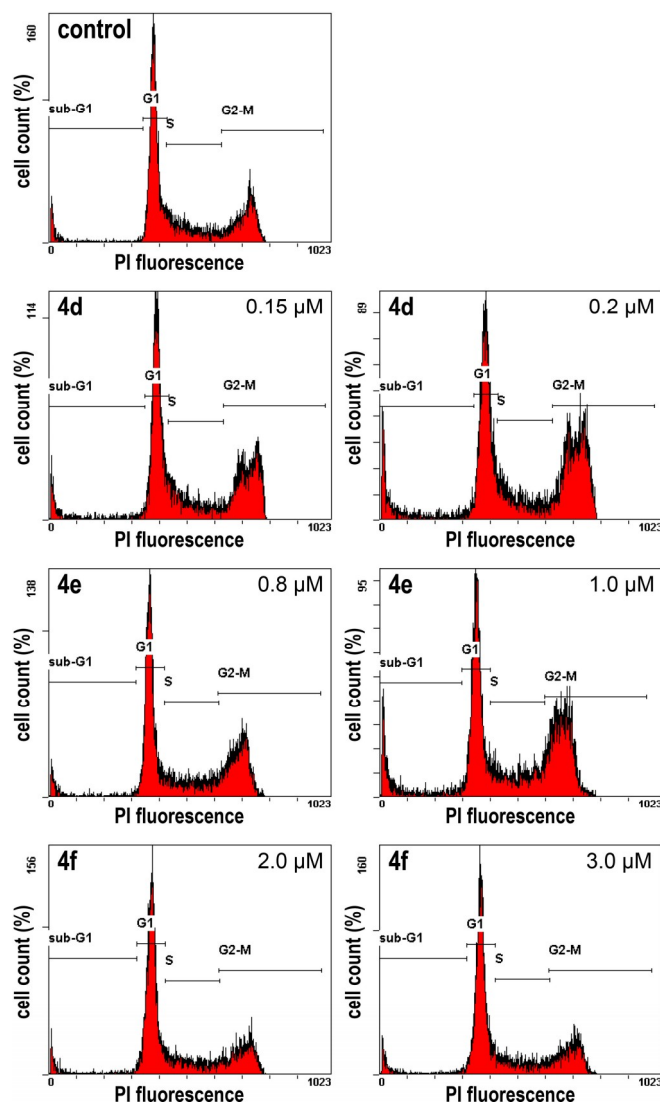


Figure 5. Effect of **4d** (0.5 μM), **4e** (1.5 μM), **4f** (4 μM), and vehicle (DMSO) on the organization of the actin cytoskeleton in 518A2 melanoma cells after 24 h exposure. Fluorescence labeling of filamentous actin (F-actin; green). Nuclei were counterstained with DAPI (merge, blue). Pictures are representative of two independent experiments (400 \times magnification).

Stress fiber formation in combination with microtubule destruction frequently leads to the arrest of cells in the G2/M phase of the cell cycle. By contrast, HDAC inhibition typically induces an arrest of cells in the G1 phase [40–45]. To investigate whether microtubule destabilization or HDAC inhibition of the test compounds **4d-f** prevails on cell cycle regulation, cell cycle arresting effects were tested in 518A2 melanoma cells by FACS analysis (Figure 6, Table 3). As expected, the strongly microtubule destabilizing compounds **4d** and **4e** led to an accumulation of 518A2 cells in G2/M phase. In contrast, the stronger HDAC inhibitor **4f**, which lacks microtubule destabilizing activity, induced a G1 phase arrest in the investigated melanoma cells.

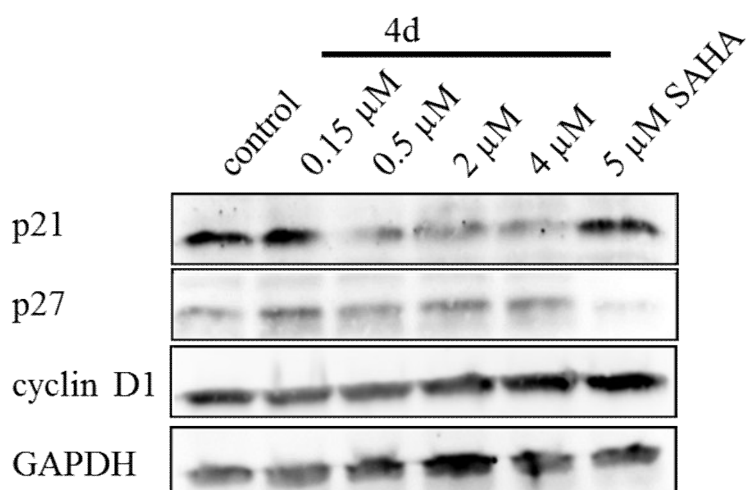
The effects of **4d** on the cell cycle regulatory proteins p21, p27, and cyclin D1 in 518A2 melanoma cells were investigated (Figure 7). At higher doses **4d** increased the level of cyclin D1 which was comparable with the effect on cyclin D1 by SAHA. It seems that the HDAC inhibitory properties of **4d** at higher concentrations caused the induction of cyclin D1. In addition, **4d** distinctly suppressed p21 expression while SAHA showed no effects on p21. It is conceivable that the observed p21 suppression is associated with the cytoskeleton targeting of **4d** which is also in line with the G2/M arrest caused by **4d** in 518A2 cells.

Finally, compound **4d** was tested concerning *in vivo* applicability and the toxicity of compound **4d** to mice was investigated. High doses of **4d** (100 mg/kg i.p., 200 mg/kg orally) were tolerated well by the treated mice and they showed no signs of toxicity (i.e., no weight loss, normal behavior). Thus, a more thorough *in vivo* investigation of **4d** in suitable tumor xenograft models is recommended due to the manageable toxicity profile of this compound.



1
2
3
4
5
6

Figure 6. Effect of **4d** (0.15 and 0.2 μM), **4e** (0.8 and 1 μM), **4f** (2 and 3 μM) or control (DMSO) on the proportions of 518A2 melanoma cells in G1, S, and G2/M phase of the cell cycle as well as the percentages of apoptotic cells in sub-G1 as determined by flow cytometry after PI staining. Cells were treated with the test compounds for 24 h. Cell cycle profiles are representatives of at least three independent experiments.



7

Figure 7. Compound-induced effects on cell cycle regulatory proteins in 518A2 melanoma cells after 24 h treatment with **4d** and SAHA. GAPDH served as a loading control. Representative data of four independent experiments are shown.

Table 3. Effect of **4d–4f** on the cell cycle of 518A2 melanoma cells¹.

	sub-G1	G1	S	G2/M
control	4.9 ± 2.0	49.7 ± 1.0	19.3 ± 0.9	26.1 ± 2.3
4d (0.15 μM)	8.9 ± 1.5	43.0 ± 0.9	19.2 ± 1.4	28.9 ± 2.7
4d (0.2 μM)	14.4 ± 2.8	33.9 ± 3.4	16.3 ± 1.1	35.4 ± 2.4
4e (0.8 μM)	5.1 ± 1.2	43.1 ± 1.3	19.2 ± 0.7	32.6 ± 1.7
4e (1 μM)	10.8 ± 4.4	35.4 ± 1.1	19.0 ± 0.3	34.9 ± 3.5
4f (2 μM)	5.6 ± 0.8	53.9 ± 0.8	18.3 ± 0.7	22.2 ± 0.5
4f (3 μM)	6.3 ± 0.9	54.2 ± 0.5	16.9 ± 0.6	22.5 ± 0.3

¹Effect of **4d** (0.15 and 0.2 μM), **4e** (0.8 and 1 μM), **4f** (2 and 3 μM), or vehicle (DMSO) on the proportions of 518A2 melanoma cells in G1, S, and G2/M phase of the cell cycle as well as the percentages of apoptotic cells in sub-G1 as determined by flow cytometry after PI staining. Cells were treated with the test compound for 24 h. Values are the means ± SD of at least three independent experiments.

2.3. In Silico Evaluation

Structure-based docking was used to explore the interactions of the different compounds with the respective target proteins on a molecular level. Molecular docking is an efficient technique for calculating the binding modes of a compound and estimating their binding affinities. Docking in general is a selection and optimization process, trying to find the best fit of a molecule in the binding site of a protein according to a scoring function [46].

To evaluate the role of the varying linker-length, the CA-4 derivative (Cap) and the hydroxamic acid group (ZBG) for the binding affinity to tubulin, docking studies were performed for the structures **4d–f**. In the tubulin structure 5LYJ, used for the docking studies, the microtubule-destabilizing agent CA-4 binds to the colchicine site of the tubulin β-chain close to the interface of the neighboring tubulin α-chain, which restrains this binding site. The CA-4 site is a buried hydrophobic pocket shaped by residues Val238, Cys241, Leu242, Leu248, Ala250, Leu255, Ala316, Ile318, Ala354, and Ile378 [47].

The docking studies for tubulin showed almost identical binding positions of the CA-4 cap of the molecules **4d–f** in the hydrophobic colchicine binding pocket similar to the original ligand CA-4 (Figure 8A). The linker extended towards the tubulin α-chain cap and the hydroxamic acid was predicted to form hydrogen bonds with Asn349 from the β-chain (**4d–f**) and potentially with Ser178 from the α-chain (**4f**). As summarized in Table 4, the estimated affinities slightly decreased with increasing linker length, a finding that is in agreement with the wet-lab results. Another observation was that the longer the linker, the more twisted it needed to be to fit into the capped cavity. Thus, the chain had to adopt torsions which are only seldom observed in crystal structures and which are considered as unfavorable, see Figure 8B [48,49].

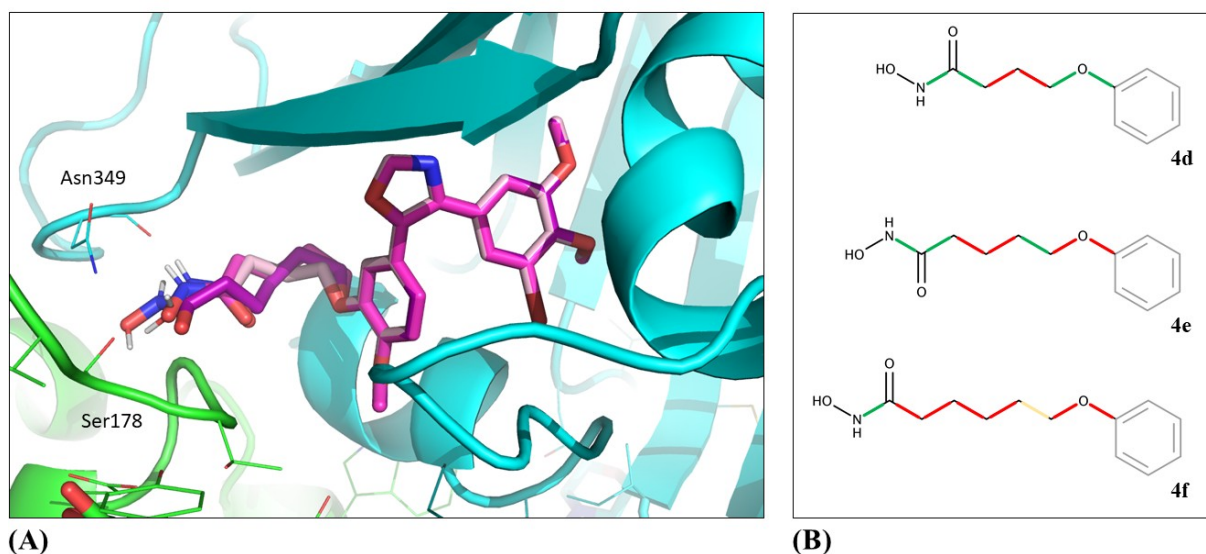


Figure 8. (a) Selected binding poses for **4d** (light), **4e** (medium) and **4f** (dark) in tubulin structure 5LYJ, exported from SeeSAR and visualized with PyMOL. (b) Illustration of frequent (green), occasional (yellow) and rare (red) torsions within the linker and hydroxamic acid group.

Table 4. SeeSAR Docking results (including estimated affinities (EA) and hydrogen bonds) for Tubulin structure 5LYJ.

	EA (SeeSAR)	Hydrogen bonds (SeeSAR)
CA-4	0.11 – 11 μ M	
4d	2.12 – 221 μ M	Asn349
4e	10 – 1019 μ M	Asn349
4f	24 – 2350 μ M	Asn349, Ser178 (Chain A)

EA Estimated Affinities according to HYDE scoring function; results ranked by best estimated affinities.

To explore reasons for the differences in the HDAC inhibitory potency of the compounds on a molecular level, computational docking studies were performed. The calculations were based on the X-ray structures 5ICN (HDAC1) and 5EDU (HDAC6) and were carried out for the compounds **4d–f** as well as for vorinostat and the respective co-crystallized ligands (see methods section). Generally, HDACs feature an active site with a relatively narrow tunnel pointing towards the buried catalytic zinc(II) cation to which the hydroxamic acid of the natural substrates and inhibitors such as vorinostat binds. The two HDAC structures used in this study exhibit very similar binding sites and can be superimposed with a low backbone RMSD of 1.9Å (superposition calculated with PyMol, see Figure 9A).

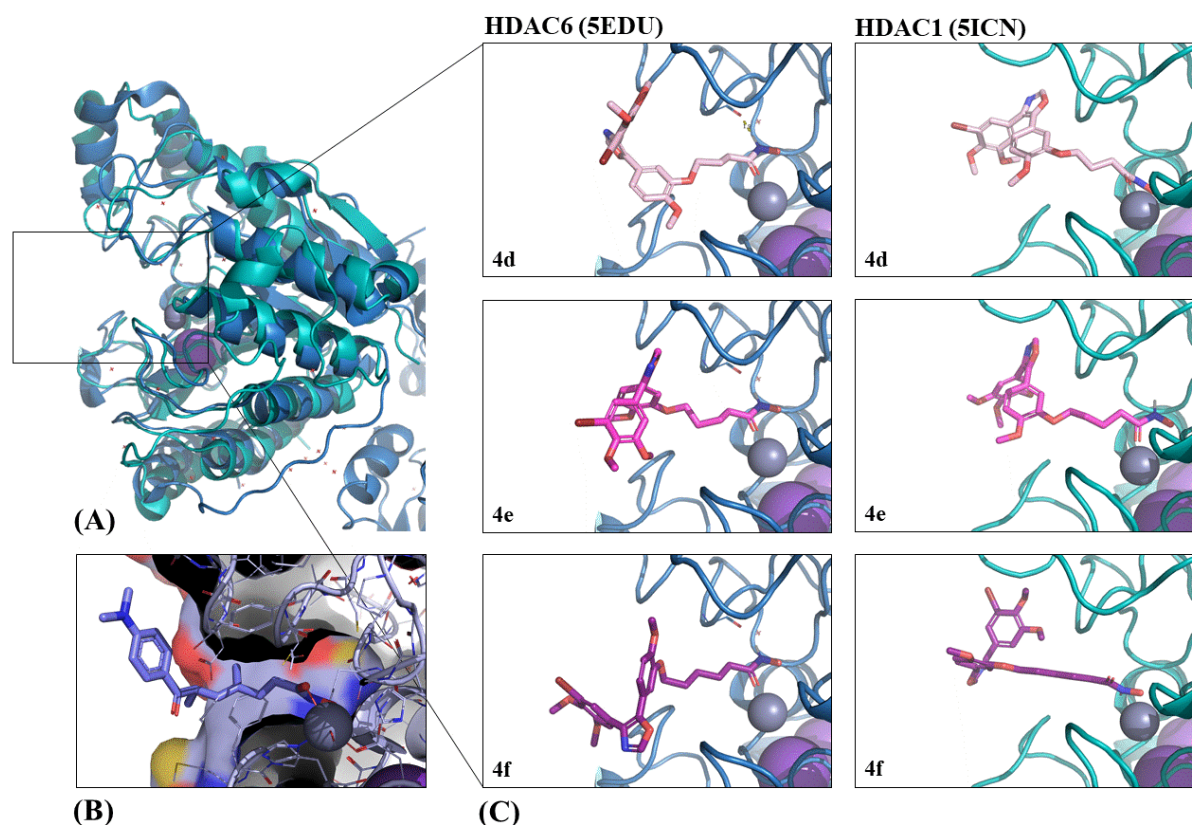


Figure 9. (a) Aligned PDB structures of HDAC1 (PDB code: 5ICN) and HDAC6 (PDB code: 5EDU). (b) Surface visualization of HDAC6 binding site with co-crystallized ligand trichostatin A (PDB code: 5EDU). (c) Selected binding pose predictions exported from SeeSAR and visualized with PyMOL.

The best poses calculated with SeeSAR for all compounds (including re-docking of the co-crystallized ligands and vorinostat) showed a similar orientation of the linker threading through the narrow tunnel and the hydroxamic acid chelating the zinc(II) cation (Figure 9B). While the estimated affinities are all in a similar range, the values suggest that a longer linker is more favorable (Table 5 and 6), which is in accordance with the experimental results (Table 2). This could be due to the better fit through the long (e.g. ~ 10 Å in HDAC6) and narrow active site tunnel, which would allow the hydroxamic acid group with longer linker length to reach the zinc ion more easily [50]. In contrast, the distance between the hydroxamic acid terminus and the first benzene attached to the linker in **4d** is only ~ 8 Å, which might make it difficult to find a good hydroxamic acid fit without causing a clash of the bulky CA-4 derived capping group with the protein.

Table 5. SeeSAR docking results (including estimated affinities (EA) and hydrogen bonds) for HDAC6 structure 5EDU.

	EA (SeeSAR)	Hydrogen bonds (SeeSAR)
Trichostatin A	< 0.02 μM	His610, Gly619, His611, Tyr782
4f	0.32 – 32 μM	His610, Gly619
4e	0.40 – 39 μM	His610, Gly619
Vorinostat	1.26 – 125 μM	His610, Gly619, His651
4d	28 – 2808 μM	His610, Gly619, His651

EA Estimated Affinities according to HYDE scoring function; results ranked by best estimated affinities. Amino acids forming hydrogen bonds with hydroxamic acid are shown in bold. Note that the estimated affinity values can be quantitatively compared within one protein structure but not necessarily across different proteins.

In all docked compounds, the hydroxamic acid group formed hydrogen bonds with the buried amino acids His610 and Gly619 of the HDAC6 structure 5EDU (co-crystallized to trichostatin A) as well as a bond to the zinc ion [50]. Generally, the hydroxamic acid and the more buried part of the linker of all three compounds **4d–f** overlap also with the respective part of the co-crystallized trichostatin A (Fig. 9C, left panel). The capping group, which is rather solvent exposed, was more variable in its position, but may form hydrogen bonds with His651 and Phe680.

The docking results for HDAC1 structure 5ICN were more diverse. This could be due to the fact that the structure is co-crystallized with a peptide inhibitor (H4K16Hx) and the loop around residue Asp99 undergoes a significant rearrangement to allow binding of the peptide [51]. Note that there are only two HDAC1 structures available to date (5ICN and 4BKX), of which 4BKX is an apo structure, so 5ICN was the only available complex structure. Reasonable poses for all compounds could be generated with LeadIT, whereas the optimization in SeeSAR was successful for all compounds but **4d** (Fig. 9C, right panel). Furthermore, the binding poses of the three compounds **4d–f** and vorinostat differed more in the hydrogen and metal bonds formed by the hydroxamic acid. While the hydroxamic acid group of **4f** was predicted to form hydrogen bonds with Tyr303 and His141, it was predicted to only form one hydrogen bond with Gly301 in **4e**. The capping group might form H-Bonds with Asn95 and Gly149.

Table 6. SeeSAR docking results (including estimated affinities (EA) and hydrogen bonds) for HDAC1 structure 5ICN.

	EA (SeeSAR)	Hydrogen bonds (SeeSAR)
H4K16Hx	< 0.81 μ M	Tyr303, His140, His141 , Asn95, Glu98, Asp99, Cys100, Gly149
4f	56 – 5,543 μ M	Tyr303, His141 , Asn95, Gly149
Vorinostat	1,049 – 104,186 μ M	His140 , Gly149
4e	3,814 – 378,935 μ M	Gly301 , Asn95
4d	Not scored	–

EA Estimated Affinities according to HYDE scoring function; results ranked by best estimated affinities. Amino acids forming hydrogen bonds with hydroxamic acid are shown in bold. Note that the estimated affinity values can be quantitatively compared within one protein structure but not necessarily across different proteins.

While the results were more distinct for HDAC6 (where a good protein-ligand complex structure was available), generally, the docking analysis showed that the molecules with longer linker length tend to have a higher affinity to HDAC1 and HDAC6.

3. Discussion

Recently, we presented conjugates of imidazoles and hydroxamic acids which combine HDAC inhibition with cytoskeletal modulation [34,38,52]. However, conjugates with imidazoles derived from CA-4 had lost crucial CA-4 typical properties such as inhibition of the polymerization of tubulin. Herein, we introduced a new series of conjugates of oxazole-bridged CA-4 and hydroxamic acids that show dual tubulin and HDAC activities which mainly depend on the length of the linker connecting these two fragments. In terms of cytotoxicity, inhibition of tubulin polymerization, and generation of reactive oxygen species (Supporting Information), the potency of these conjugates grows with decreasing linker length. The strong anti-proliferative effect especially of the derivatives with the shortest linkers **4a**, **4d**, and **4g** is probably due to their interference with formation of the spindle apparatus during mitosis. The derivatives with longer tethers increasingly lose this property resulting in a distinctly reduced anti-proliferative effect which was confirmed by *in silico* studies and was attributed to the increasingly tensed fitting of the linkers in the capped cavity.

By destabilizing the microtubules the new conjugates affect the cell division and probably the integrity of endothelial cell layers. Moreover, they showed a distinct specificity for endothelial hybrid cells Ea.Hy926 over non-malignant cells HDFa. Both properties exhibit the great potential of these derivatives as VDAs which trigger the collapse of the leaky and low-quality vasculature of

1 tumors by destabilizing their endothelial layer, initiating necrosis in the core of the tumor [19]. An
2 assessment of the vascular-disrupting activity of the new compounds is currently underway.

3 The HDAC inhibitory effect of the new conjugates showed the opposite dependency on linker
4 length. The IC₅₀ values for inhibition of both HDAC1 and HDAC6 decreased with increasing linker
5 length which reflects the fact that the active site of the zinc-dependent HDACs is accessible for
6 HDACi only by a long narrow hydrophobic channel. We rationalized this trend by *in silico*
7 experiments.

8 The observed G1-arrest of 518A2 cells by **4f** matches with similar observations for other
9 HDACi. The MDA-typical G2/M arrest by derivatives **4d** and **4e** is in line with their pronounced
10 microtubule disrupting effect which probably overrides their HDACi activity. The stress fiber
11 formation as well as the anti-migratory activity observed for **4d–f** was independent of linker length.
12 Together with the lack of toxicity in mice, compound **4d** appears to be an especially promising drug
13 candidate.

14 Within this work we were able to demonstrate the anti-proliferative, cell-cycle arresting,
15 microtubule-destabilizing and actin stress fiber-inducing effects of novel CA-4 analogues with the
16 potential to inhibit histone deacetylases. The results are indicative of the great potential of this new
17 class of compounds which probably affect the tumor vasculature either by inhibiting angiogenesis or
18 by disruption of already established tumor blood vessels. Investigations of these anti-vascular
19 effects as well as their *in vivo* activity are currently underway.

20 4. Materials and Methods

21 4.1. General Procedures

22 The following instruments were used: melting points (uncorrected), Gallenkamp; IR spectra,
23 Perkin-Elmer Spectrum One FT-IR spectrophotometer with ATR sampling unit; nuclear magnetic
24 resonance spectra, BRUKER Avance 300 spectrometer; chemical shifts are given in parts per million
25 (δ) downfield from tetramethylsilane as internal standard; mass spectra, Varian MAT 311A (EI) or
26 UPLC/Orbitrap MS system (ESI); microanalyses, Perkin-Elmer 2400 CHN elemental analyzer. All
27 tested compounds were >95% pure by elemental analysis.

28 4.2. Materials

29 The known starting compounds **1a** and **2a–c** were prepared according to literature procedures
30 [25–27]. The new compounds **1b** and **1c** were synthesized analogously to **1a** (see below). All other
31 starting compounds and reagents were purchased from Sigma-Aldrich.

32 4.3. General Procedure for the Synthesis of Intermediates **1b** and **1c**

33 Isovanillin (152 mg, 1.0 mmol) was dissolved in MeCN (5 mL) and cesium carbonate (652 mg,
34 2.0 mmol) was added. After stirring at 90 °C for 0.5 h, ethyl 5-bromovalerate (328 μ L, 2.0 mmol) or
35 ethyl 6-bromohexanoate (356 μ L, 2.0 mmol), respectively, was added and the reaction mixture was
36 stirred at 90 °C for 2 h. After filtration through celite, the solvent was removed under reduced
37 pressure and the residue was washed twice with *n*-hexane. The resulting oil was dried in vacuum
38 and used for the next step without further purification.

39 **Ethyl 5-(1-methoxy-4-formyl-2-phenoxy)valerate (1b)**. Yield: 130 mg (0.46 mmol, 46%);
40 colorless oil. ν_{\max} (ATR)/cm⁻¹ 2941, 2881, 2841, 1728, 1683, 1585, 1509, 1462, 1436, 1393, 1374, 1340,
41 1262, 1238, 1159, 1133, 1096, 1019, 935, 864, 809, 780, 749, 737, 641. ¹H NMR (300 MHz, CDCl₃): δ = 1.23
42 (t, 3H, *J* = 7.1 Hz), 1.8–2.0 (m, 4H), 2.38 (t, 2H, *J* = 7.3 Hz), 3.93 (s, 3H), 4.0–4.2 (m, 4H), 6.95 (d, 1H, *J* =
43 8.2 Hz), 7.37 (s, 1H), 7.44 (d, 2H, *J* = 8.2 Hz), 9.82 ppm (s, 1H). ¹³C NMR (75.5 MHz, CDCl₃): δ = 14.2,
44 21.6, 28.5, 33.9, 56.2, 60.3, 68.5, 110.5, 110.7, 126.7, 130.1, 149.0, 154.9, 173.3, 190.9 ppm. *m/z* (%) 280
45 (14) [M⁺], 235 (24), 151 (57), 129 (98), 101 (100), 83 (82), 55 (56), 43 (15).

46 **Ethyl 6-(1-methoxy-4-formyl-2-phenoxy)hexanoate (1c)**. Yield: 110 mg (0.37 mmol, 37%);
47 colorless oil. ν_{\max} (ATR)/cm⁻¹ 2940, 2870, 1729, 1685, 1585, 1510, 1462, 1436, 1394, 1374, 1341, 1264,
48 1239, 1161, 1134, 1068, 1021, 862, 811, 779, 749, 729, 641. ¹H NMR (300 MHz, CDCl₃): δ = 1.23 (t, 3H, *J*

1 = 7.1 Hz), 1.4-1.6 (m, 2H), 1.6-1.8 (m, 2H), 1.8-1.9 (m, 2H), 2.32 (t, 2H, $J = 7.3$ Hz), 4.01 (s, 3H), 4.0-4.2
2 (m, 4H), 6.95 (d, 1H, $J = 8.2$ Hz), 7.37 (s, 1H), 7.44 (d, 2H, $J = 8.2$ Hz), 9.82 ppm (s, 1H). ^{13}C NMR (75.5
3 MHz, CDCl_3): $\delta = 14.2, 24.7, 25.6, 28.7, 34.2, 56.2, 60.2, 68.8, 110.4, 110.6, 118.0, 126.6, 130.1, 149.1,$
4 $154.9, 173.6, 190.9$ ppm. m/z (%) 294 (48) [M^+], 249 (35), 152 (98), 143 (100), 115 (54), 97 (97), 69 (86), 55
5 (22), 41 (28).

6 4.4. General Procedure for the Synthesis of Intermediates 3a-i

7 The respective compounds **1** (0.42 mmol) and **2** (0.42 mmol) and K_2CO_3 (590 mg, 4.3 mmol)
8 were suspended in ethanol and stirred under reflux for 2 h. The solvent was removed and the
9 residue dissolved in ethyl acetate and washed with water. The organic phase was dried over Na_2SO_4 ,
10 concentrated in vacuum and the residue was purified by column chromatography (silica gel 60).

11 **Ethyl 4-[1-methoxy-4-(4'-(3''-chloro-4'')-5''-dimethoxyphenyl)oxazol-5'-yl]-2-phenoxy**
12 **butyrate (3a)**. Compound **3a** was obtained from **1a** (113 mg, 0.42 mmol), **2a** (155 mg, 0.42 mmol) and
13 K_2CO_3 (590 mg, 4.3 mmol). Yield: 103 mg (0.22 mmol, 52%); $R_f = 0.39$ (ethyl acetate / *n*-hexane, 2:3);
14 colorless oil. $\nu_{\text{max}}(\text{ATR})/\text{cm}^{-1}$ 2969, 2938, 2876, 2837, 1731, 1683, 1629, 1561, 1513, 1489, 1463, 1443,
15 1414, 1399, 1366, 1303, 1254, 1229, 1174, 1140, 1117, 1105, 1047, 1024, 1000, 960, 938, 892, 853, 810, 774,
16 758, 734, 709, 659, 629. ^1H NMR (300 MHz, CDCl_3): $\delta = 1.23$ (t, 3H, $J = 7.1$ Hz), 2.0-2.2 (m, 2H), 2.49 (t,
17 2H, $J = 7.3$ Hz), 3.81 (s, 3H), 3.87 (s, 3H), 3.88 (s, 3H), 3.98 (t, 2H, $J = 6.3$ Hz), 4.11 (q, 2H, $J = 7.2$ Hz),
18 6.87 (d, 1H, $J = 8.4$ Hz), 7.1-7.2 (m, 3H), 7.29 (s, 1H), 7.88 ppm (s, 1H). ^{13}C NMR (75.5 MHz, CDCl_3): $\delta =$
19 $14.2, 24.5, 30.7, 56.0, 56.1, 60.4, 60.8, 68.1, 110.6, 111.7, 112.0, 120.4, 120.9, 121.1, 128.3, 128.7, 132.3,$
20 $146.1, 148.4, 149.3, 150.4, 153.8, 173.0$ ppm. m/z (%) 477 (61) [M^+], 475 (100) [M^+], 432 (11), 430 (31), 361
21 (8), 265 (7), 115 (94), 87 (67), 43 (11).

22 **Ethyl 5-[1-methoxy-4-(4'-(3''-chloro-4'')-5''-dimethoxyphenyl)oxazol-5'-yl]-2-phenoxy]valerate**
23 **(3b)**. Compound **3b** was obtained from **1b** (126 mg, 0.45 mmol), **2a** (165 mg, 0.45 mmol) and K_2CO_3
24 (590 mg, 4.3 mmol). Yield: 98 mg (0.20 mmol, 44%); $R_f = 0.42$ (ethyl acetate / *n*-hexane, 2:3); colorless
25 oil. $\nu_{\text{max}}(\text{ATR})/\text{cm}^{-1}$ 2938, 2870, 2838, 1730, 1603, 1591, 1564, 1513, 1489, 1463, 1414, 1365, 1324, 1294,
26 1254, 1229, 1203, 1164, 1140, 1105, 1048, 1024, 938, 854, 811, 776, 758, 710, 659, 628. ^1H NMR (300 MHz,
27 CDCl_3): $\delta = 1.23$ (t, 3H, $J = 7.1$ Hz), 1.7-1.9 (m, 2H), 2.35 (t, 2H, $J = 7.3$ Hz), 3.81 (s, 3H), 3.87 (s, 3H),
28 3.88 (s, 3H), 3.93 (t, 2H, $J = 6.1$ Hz), 4.10 (q, 2H, $J = 7.1$ Hz), 6.87 (d, 1H, $J = 8.4$ Hz), 7.10 (s, 1H), 7.1-7.2
29 (m, 2H), 7.30 (s, 1H), 7.88 ppm (s, 1H). ^{13}C NMR (75.5 MHz, CDCl_3): $\delta = 14.2, 21.6, 28.6, 33.9, 56.0, 56.1,$
30 $60.3, 60.8, 68.7, 110.6, 111.7, 120.2, 120.9, 121.1, 128.3, 128.7, 132.3, 145.2, 146.1, 148.5, 149.3, 150.3,$
31 $153.8, 173.4$ ppm. m/z (%) 491 (43) [M^+], 489 (100) [M^+], 446 (13), 444 (41), 361 (31), 346 (17), 168 (14),
32 129 (98), 101 (98), 83 (56), 55 (39), 43 (11).

33 **Ethyl 6-[1-methoxy-4-(4'-(3''-chloro-4'')-5''-dimethoxyphenyl)oxazol-5'-yl]-2-phenoxy**
34 **hexanoate (3c)**. Compound **3c** was obtained from **1c** (91 mg, 0.31 mmol), **2a** (113 mg, 0.31 mmol) and
35 K_2CO_3 (590 mg, 4.3 mmol). Yield: 63 mg (0.13 mmol, 42%); $R_f = 0.45$ (ethyl acetate / *n*-hexane, 2:3);
36 colorless oil. $\nu_{\text{max}}(\text{ATR})/\text{cm}^{-1}$ 2939, 2871, 2837, 1730, 1605, 1591, 1563, 1513, 1489, 1463, 1414, 1366,
37 1325, 1300, 1255, 1229, 1203, 1175, 1165, 1140, 1105, 1048, 1024, 1001, 939, 854, 821, 775, 758, 710, 659,
38 629. ^1H NMR (300 MHz, CDCl_3): $\delta = 1.23$ (t, 3H, $J = 7.1$ Hz), 1.4-1.5 (m, 2H), 1.6-1.7 (m, 2H), 1.8-1.9
39 (m, 2H), 2.30 (t, 2H, $J = 7.3$ Hz), 3.80 (s, 3H), 3.87 (s, 3H), 3.88 (s, 3H), 3.92 (t, 2H, $J = 6.7$ Hz), 4.10 (q,
40 2H, $J = 7.1$ Hz), 6.88 (d, 1H, $J = 8.4$ Hz), 7.10 (s, 1H), 7.1-7.2 (m, 2H), 7.30 (s, 1H), 7.89 ppm (s, 1H). ^{13}C
41 NMR (75.5 MHz, CDCl_3): $\delta = 14.2, 24.7, 25.6, 28.8, 34.2, 56.0, 56.1, 60.2, 60.8, 68.9, 110.6, 111.6, 120.1,$
42 $120.9, 121.1, 128.3, 128.7, 132.3, 145.2, 146.1, 148.6, 149.3, 150.3, 153.8, 173.6$ ppm. m/z (%) 505 (68) [M^+],
43 503 (100) [M^+], 458 (11), 361 (37), 346 (13), 143 (51), 115 (16), 97 (28), 69 (26).

44 **Ethyl 4-[1-methoxy-4-(4'-(3''-bromo-4'')-5''-dimethoxyphenyl)oxazol-5'-yl]-2-phenoxy**
45 **butyrate (3d)**. Compound **3d** was obtained from **1a** (125 mg, 0.47 mmol), **2b** (192 mg, 0.47 mmol) and
46 K_2CO_3 (590 mg, 4.3 mmol). Yield: 100 mg (0.19 mmol, 41%); $R_f = 0.25$ (ethyl acetate / *n*-hexane, 1:2);
47 colorless oil. $\nu_{\text{max}}(\text{ATR})/\text{cm}^{-1}$ 3118, 2986, 2940, 2837, 1739, 1592, 1561, 1514, 1488, 1468, 1441, 1404,
48 1388, 1362, 1349, 1267, 1256, 1241, 1226, 1208, 1179, 1145, 1124, 1108, 1072, 1048, 1025, 997, 960, 944,
49 859, 846, 820, 807, 773, 754, 699, 654. ^1H NMR (300 MHz, CDCl_3): $\delta = 1.23$ (t, 3H, $J = 7.2$ Hz), 2.0-2.2 (m,
50 2H), 2.50 (t, 2H, $J = 7.3$ Hz), 3.80 (s, 3H), 3.86 (s, 3H), 3.88 (s, 3H), 3.98 (t, 2H, $J = 6.3$ Hz), 4.11 (q, 2H, $J =$
51 7.2 Hz), 6.88 (d, 1H, $J = 8.4$ Hz), 7.12 (s, 1H), 7.1-7.2 (m, 2H), 7.46 (s, 1H), 7.88 ppm (s, 1H). ^{13}C NMR

(75.5 MHz, CDCl₃): δ = 14.2, 24.5, 30.8, 56.0, 56.1, 60.4, 60.7, 68.2, 111.4, 111.7, 111.9, 117.6, 120.3, 120.9, 123.9, 129.3, 146.1, 148.4, 149.3, 150.4, 153.7, 173.0 ppm. *m/z* (%) 521 (38) [M⁺], 519 (37) [M⁺], 476 (6), 474 (5), 115 (100), 87 (79), 43 (14).

Ethyl 5-[1-methoxy-4-(4'-(3''-bromo-4'')-5''-dimethoxyphenyl)oxazol-5'-yl)-2-phenoxy]valerate (3e). Compound **3e** was obtained from **1b** (112 mg, 0.40 mmol) and **2b** (164 mg, 0.40 mmol) and K₂CO₃ (590 mg, 4.3 mmol). Yield: 110 mg (0.21 mmol, 53%); *R_f* = 0.33 (ethyl acetate / *n*-hexane, 2:3); colorless oil. ν_{\max} (ATR)/cm⁻¹ 3128, 2938, 2838, 1730, 1591, 1557, 1513, 1485, 1463, 1414, 1364, 1254, 1230, 1201, 1174, 1162, 1140, 1105, 1043, 1025, 1000, 939, 897, 854, 807, 776, 754, 698, 659, 628. ¹H NMR (300 MHz, CDCl₃): δ = 1.23 (t, 3H, *J* = 7.1 Hz), 1.7-1.9 (m, 4H), 2.36 (t, 2H, *J* = 7.3 Hz), 3.80 (s, 3H), 3.86 (s, 3H), 3.88 (s, 3H), 3.93 (t, 2H, *J* = 6.1 Hz), 4.10 (q, 2H, *J* = 7.1 Hz), 6.88 (d, 1H, *J* = 8.4 Hz), 7.11 (s, 1H), 7.1-7.2 (m, 2H), 7.47 (s, 1H), 7.88 ppm (s, 1H). ¹³C NMR (75.5 MHz, CDCl₃): δ = 14.2, 21.6, 28.6, 33.9, 56.0, 56.1, 60.3, 60.7, 68.7, 111.4, 111.6, 111.7, 117.6, 120.1, 120.9, 123.9, 129.4, 132.1, 146.1, 146.3, 148.6, 149.3, 150.3, 153.7, 173.3 ppm. *m/z* (%) 535 (95) [M⁺], 533 (95) [M⁺], 490 (17), 488 (16), 407 (15), 405 (15), 129 (96), 101 (100), 83 (42), 55 (40).

Ethyl 6-[1-methoxy-4-(4'-(3''-bromo-4'')-5''-dimethoxyphenyl)oxazol-5'-yl)-2-phenoxy]hexanoate (3f). Compound **3f** was obtained from **1c** (113 mg, 0.38 mmol), **2b** (158 mg, 0.38 mmol) and K₂CO₃ (590 mg, 4.3 mmol). Yield: 80 mg (0.15 mmol, 40%); *R_f* = 0.45 (ethyl acetate / *n*-hexane, 2:3); colorless oil. ν_{\max} (ATR)/cm⁻¹ 2940, 2869, 1730, 1590, 1558, 1513, 1485, 1463, 1414, 1364, 1323, 1253, 1229, 1175, 1160, 1140, 1105, 1066, 1043, 1025, 999, 938, 853, 806, 775, 753, 697, 659, 628. ¹H NMR (300 MHz, CDCl₃): δ = 1.23 (t, 3H, *J* = 7.1 Hz), 1.4-1.5 (m, 2H), 1.6-1.8 (m, 2H), 1.8-1.9 (m, 2H), 2.30 (t, 2H, *J* = 7.3 Hz), 3.80 (s, 3H), 3.86 (s, 3H), 3.88 (s, 3H), 3.9-4.0 (m, 5H), 4.10 (q, 2H, *J* = 7.1 Hz), 6.88 (d, 1H, *J* = 8.4 Hz), 7.10 (s, 1H), 7.1-7.2 (m, 2H), 7.47 (s, 1H), 7.88 ppm (s, 1H). ¹³C NMR (75.5 MHz, CDCl₃): δ = 14.2, 24.7, 25.6, 28.8, 34.2, 56.0, 56.1, 60.2, 60.7, 68.9, 111.4, 111.6, 111.7, 117.6, 120.0, 120.9, 123.9, 129.4, 132.1, 146.2, 148.6, 149.3, 150.3, 153.7, 173.6 ppm. *m/z* (%) 549 (99) [M⁺], 547 (100) [M⁺], 407 (31), 405 (32), 143 (77), 115 (20), 97 (32), 69 (27).

Ethyl 4-[1-methoxy-4-(4'-(3''-4''-5''-trimethoxyphenyl)oxazol-5'-yl)-2-phenoxy]butyrate (3g). Compound **3g** was obtained from **1a** (134 mg, 0.50 mmol), **2c** (182 mg, 0.50 mmol) and K₂CO₃ (590 mg, 4.3 mmol). Yield: 124 mg (0.26 mmol, 52%); *R_f* = 0.31 (ethyl acetate / *n*-hexane, 1:1); colorless oil. ν_{\max} (ATR)/cm⁻¹ 2939, 2840, 1730, 1583, 1515, 1463, 1415, 1372, 1306, 1255, 1236, 1173, 1122, 1022, 1004, 956, 938, 885, 837, 811, 768, 733, 659, 629. ¹H NMR (300 MHz, CDCl₃): δ = 1.27 (t, 3H, *J* = 7.1 Hz), 2.1-2.2 (m, 2H), 2.53 (t, 2H, *J* = 7.3 Hz), 3.81 (s, 6H), 3.90 (s, 3H), 3.91 (s, 3H), 4.02 (t, 2H, *J* = 6.3 Hz), 4.15 (q, 2H, *J* = 7.1 Hz), 6.90 (d, 1H, *J* = 8.4 Hz), 7.12 (s, 1H), 6.94 (s, 2H), 7.17 (s, 1H), 7.25 (d, 1H, *J* = 8.4 Hz), 7.93 ppm (s, 1H). ¹³C NMR (75.5 MHz, CDCl₃): δ = 14.2, 24.5, 30.7, 56.0, 56.1, 60.4, 60.9, 68.0, 104.9, 111.5, 112.1, 120.4, 121.3, 127.6, 133.6, 137.9, 145.6, 148.3, 149.2, 150.1, 153.3, 173.0 ppm. *m/z* (%) 471 (95) [M⁺], 456 (13), 426 (31), 195 (17), 115 (100), 87 (99), 69 (14), 43 (24). Elemental analysis calculated (%) for C₂₅H₂₉NO₈: C 63.68, H 6.20, N 2.97. Found: C 63.65, H 6.18, N 2.96.

Ethyl 5-[1-methoxy-4-(4'-(3''-4''-5''-trimethoxyphenyl)oxazol-5'-yl)-2-phenoxy]valerate (3h). Compound **3h** was obtained from **1b** (130 mg, 0.46 mmol), **2c** (168 mg, 0.46 mmol) and K₂CO₃ (590 mg, 4.3 mmol). Yield: 107 mg (0.22 mmol, 48%); *R_f* = 0.35 (ethyl acetate / *n*-hexane, 1:1); colorless oil. ν_{\max} (ATR)/cm⁻¹ 2938, 2840, 1730, 1583, 1515, 1455, 1415, 1372, 1330, 1305, 1255, 1237, 1171, 1123, 1022, 1004, 938, 894, 837, 811, 768, 734, 659, 629. ¹H NMR (300 MHz, CDCl₃): δ = 1.23 (t, 3H, *J* = 7.1 Hz), 1.7-1.9 (m, 4H), 2.34 (d, 2H, *J* = 7.2 Hz), 3.77 (s, 6H), 3.85 (s, 3H), 3.87 (s, 3H), 3.93 (t, 2H, *J* = 6.1 Hz), 4.10 (q, 2H, *J* = 7.1 Hz), 6.86 (d, 1H, *J* = 8.4 Hz), 6.90 (s, 2H), 7.11 (s, 1H), 7.20 (d, 1H, *J* = 8.4 Hz), 7.89 ppm (s, 1H). ¹³C NMR (75.5 MHz, CDCl₃): δ = 14.2, 21.6, 28.6, 33.9, 56.0, 56.1, 60.3, 60.9, 68.6, 105.0, 111.5, 111.9, 120.3, 121.3, 127.6, 133.6, 138.0, 145.7, 148.5, 149.2, 150.1, 153.3, 173.3 ppm. *m/z* (%) 485 (100) [M⁺], 440 (15), 401 (16), 153 (16), 129 (99), 101 (73), 83 (26), 55 (17).

Ethyl 6-[1-methoxy-4-(4'-(3''-4''-5''-dimethoxyphenyl)oxazol-5'-yl)-2-phenoxy]hexanoate (3i). Compound **3i** was obtained from **1c** (116 mg, 0.39 mmol), **2c** (114 mg, 0.46 mmol) and K₂CO₃ (590 mg, 4.3 mmol). Yield: 86 mg (0.17 mmol, 44%); *R_f* = 0.45 (ethyl acetate / *n*-hexane, 1:1); colorless oil. ν_{\max} (ATR)/cm⁻¹ 2938, 2870, 2839, 1730, 1583, 1515, 1462, 1415, 1372, 1327, 1305, 1255, 1236, 1173, 1123, 1022, 1005, 939, 891, 836, 811, 769, 734, 659, 630. ¹H NMR (300 MHz, CDCl₃): δ = 1.23 (t, 3H, *J* = 7.1 Hz), 1.4-1.5 (m, 2H), 1.6-1.8 (m, 2H), 1.8-1.9 (m, 2H), 2.30 (d, 2H, *J* = 7.3 Hz), 3.77 (s, 6H), 3.86 (s, 3H), 3.87

1 (s, 3H), 3.91 (t, 2H, $J = 6.6$ Hz), 4.10 (q, 2H, $J = 7.1$ Hz), 6.86 (d, 1H, $J = 8.4$ Hz), 6.90 (s, 2H), 7.11 (s, 1H),
2 7.20 (d, 1H, $J = 8.4$ Hz), 7.89 ppm (s, 1H). ^{13}C NMR (75.5 MHz, CDCl_3): $\delta = 14.2, 24.7, 25.6, 28.8, 34.2,$
3 56.0, 56.1, 60.2, 60.9, 68.8, 105.0, 111.5, 111.8, 120.2, 121.3, 127.7, 133.6, 138.0, 145.7, 148.5, 149.2, 150.1,
4 153.3, 173.6 ppm. m/z (%) 499 (100) [M^+], 484 (22), 454 (15), 357 (12), 342 (17), 249 (15), 154 (53), 143
5 (99), 115 (27), 97 (58), 69 (43).

6 4.5. General Procedure for the Synthesis of Compounds 4a–i

7 The corresponding compound **3** (0.20 mmol) was dissolved in $\text{CH}_2\text{Cl}_2/\text{MeOH}$ (9 mL, 1:2),
8 hydroxylamine (50% in water, 0.5 mL, 15 mmol) and NaOH (200 mg, 5 mmol) were added and the
9 reaction mixture was stirred at room temperature for 1 h. The solvent was removed, the residue was
10 dissolved in water and adjusted to pH 7–8 with acetic acid. The aqueous phase was extracted with
11 ethyl acetate (2 \times 50 mL), dried over Na_2SO_4 and concentrated in vacuum. The solid residue was
12 recrystallized from $\text{CH}_2\text{Cl}_2/n$ -hexane.

13 **N-Hydroxy-4-[1-methoxy-4-(4'-(3''-chloro-4'',5''-dimethoxyphenyl)oxazol-5'-yl)-2-phenoxy]b**
14 **utanamide (4a)**. Compound **4a** was obtained from **3a** (97 mg, 0.20 mmol), hydroxylamine (50% in
15 water, 0.5 mL, 15 mmol) and NaOH (200 mg, 5 mmol). Yield: 64 mg (0.14 mmol, 70%); colorless solid
16 of mp 171–172°C. $\nu_{\text{max}}(\text{ATR})/\text{cm}^{-1}$ 3101, 2942, 2868, 2843, 1655, 1593, 1566, 1516, 1492, 1463, 1441, 1401,
17 1364, 1328, 1258, 1242, 1228, 1206, 1179, 1168, 1141, 1117, 1100, 1073, 1052, 1024, 997, 941, 887, 866,
18 847, 808, 755, 710, 655, 625. ^1H NMR (300 MHz, CDCl_3): $\delta = 2.0$ – 2.2 (m, 2H), 2.4– 2.5 (m, 2H), 3.82 (s,
19 3H), 3.88 (s, 3H), 3.88 (s, 3H), 3.9– 4.0 (m, 5H), 6.90 (d, 1H, $J = 8.5$ Hz), 7.07 (s, 1H), 7.15 (s, 1H), 7.2– 7.3
20 (m, 3H), 7.89 ppm (s, 1H). ^{13}C NMR (75.5 MHz, CDCl_3): $\delta = 24.4, 30.5, 56.0, 56.2, 60.9, 68.4, 110.8,$
21 111.3, 111.5, 120.6, 121.0, 121.2, 128.3, 128.7, 132.4, 145.2, 145.8, 147.8, 149.4, 149.8, 153.9, 170.6 ppm.
22 m/z (%) 464 (4) [M^+], 462 (10) [M^+], 447 (27), 363 (32), 361 (100), 346 (19), 318 (10), 86 (12). Elemental
23 analysis calculated (%) for $\text{C}_{22}\text{H}_{23}\text{ClN}_2\text{O}_7$: C 57.09, H 5.01, N 6.05. Found: C 57.06, H 5.02, N 6.04.

24 **N-Hydroxy-5-[1-methoxy-4-(4'-(3''-chloro-4'',5''-dimethoxyphenyl)oxazol-5'-yl)-2-phenoxy]p**
25 **entanamide (4b)**. Compound **4b** was obtained from **3b** (90 mg, 0.18 mmol), hydroxylamine (50% in
26 water, 0.5 mL, 15 mmol) and NaOH (200 mg, 5 mmol). Yield: 62 mg (0.13 mmol, 72%); colorless solid
27 of mp 202°C. $\nu_{\text{max}}(\text{ATR})/\text{cm}^{-1}$ 3194, 2942, 2870, 2837, 1644, 1606, 1592, 1564, 1513, 1489, 1460, 1440,
28 1400, 1364, 1326, 1255, 1230, 1206, 1176, 1140, 1107, 1047, 1019, 996, 939, 895, 853, 807, 759, 711, 657,
29 628, 607. ^1H NMR (300 MHz, CDCl_3): $\delta = 1.7$ – 1.9 (m, 4H), 2.3– 2.4 (m, 2H), 3.82 (s, 3H), 3.88 (s, 3H),
30 3.9– 4.0 (m, 5H), 6.91 (d, 1H, $J = 8.4$ Hz), 7.04 (s, 1H), 7.1– 7.3 (m, 3H), 7.90 ppm (s, 1H). ^{13}C NMR (75.5
31 MHz, CDCl_3): $\delta = 21.5, 24.4, 26.4, 32.1, 55.9, 56.2, 60.9, 69.8, 110.2, 110.8, 111.3, 111.7, 119.9, 121.2,$
32 128.3, 128.8, 132.4, 145.1, 146.0, 148.1, 149.2, 149.4, 153.9, 170.2 ppm. m/z (%) 476 (3) [M^+], 461 (42), 363
33 (33), 361 (100), 346 (24), 318 (16), 240 (10), 100 (41), 44 (56). Elemental analysis calculated (%) for
34 $\text{C}_{23}\text{H}_{25}\text{ClN}_2\text{O}_7$: C 57.92, H 5.28, N 5.87. Found: C 57.90, H 5.26, N 5.86.

35 **N-Hydroxy-6-[1-methoxy-4-(4'-(3''-chloro-4'',5''-dimethoxyphenyl)oxazol-5'-yl)-2-phenoxy]h**
36 **exanamide (4c)**. Compound **4c** was obtained from **3c** (58 mg, 0.12 mmol), hydroxylamine (50% in
37 water, 0.5 mL, 15 mmol) and NaOH (200 mg, 5 mmol). Yield: 44 mg (0.09 mmol, 75%); colorless solid
38 of mp 189°C. $\nu_{\text{max}}(\text{ATR})/\text{cm}^{-1}$ 3180, 3120, 2997, 2939, 2865, 2837, 1652, 1595, 1567, 1513, 1491, 1464,
39 1435, 1399, 1363, 1327, 1305, 1257, 1228, 1206, 1192, 1175, 1141, 1110, 1074, 1049, 1017, 996, 951, 895,
40 870, 851, 823, 807, 777, 758, 729, 709, 657, 630. ^1H NMR (300 MHz, CDCl_3): $\delta = 1.4$ – 1.5 (m, 2H), 1.6– 1.7
41 (m, 2H), 1.7– 1.8 (m, 2H), 2.1– 2.2 (m, 2H), 3.8– 3.9 (m, 11H), 6.90 (d, 1H, $J = 8.4$ Hz), 7.04 (s, 1H), 7.15 (s,
42 1H), 7.21 (d, 1H, $J = 8.4$ Hz), 7.28 (s, 1H), 7.89 ppm (s, 1H). ^{13}C NMR (75.5 MHz, CDCl_3): $\delta = 24.9, 25.5,$
43 28.3, 32.8, 56.0, 56.2, 60.9, 68.9, 110.8, 111.3, 111.8, 119.9, 120.9, 121.3, 128.3, 129.0, 132.2, 145.0, 146.1,
44 148.4, 149.4, 150.0, 153.8, 170.9 ppm. m/z (%) 491 (5) [M^+], 489 (14) [M^+], 477 (23), 475 (72), 363 (23), 361
45 (100), 348 (13), 346 (36), 318 (23), 182 (13), 114 (45), 69 (51). Elemental analysis calculated (%) for
46 $\text{C}_{24}\text{H}_{27}\text{ClN}_2\text{O}_7$: C 58.72, H 5.54, N 5.71. Found: C 58.70, H 5.56, N 5.69.

47 **N-Hydroxy-4-[1-methoxy-4-(4'-(3''-bromo-4'',5''-dimethoxyphenyl)oxazol-5'-yl)-2-phenoxy]b**
48 **utanamide (4d)**. Compound **4d** was obtained from **3d** (100 mg, 0.19 mmol), hydroxylamine (50% in
49 water, 0.5 mL, 15 mmol) and NaOH (200 mg, 5 mmol). Yield: 86 mg (0.17 mmol, 90%); colorless solid
50 of mp 140– 141°C . $\nu_{\text{max}}(\text{ATR})/\text{cm}^{-1}$ 3192, 2934, 2837, 1639, 1592, 1559, 1513, 1486, 1463, 1440, 1400, 1362,
51 1255, 1229, 1179, 1140, 1107, 1076, 1041, 1021, 994, 954, 888, 856, 844, 806, 753, 733, 697, 657, 627. ^1H

1 NMR (300 MHz, CDCl₃): δ = 2.0-2.2 (m, 2 H), 2.4-2.5 (m, 2H), 3.82 (s, 3H), 3.87 (s, 3H), 3.9-4.0 (m, 5H),
2 6.91 (d, 1H, J = 8.5 Hz), 7.08 (s, 1H), 7.19 (s, 1H), 7.2-7.3 (m, 1H), 7.43 (s, 1H), 7.89 ppm (s, 1H). ¹³C
3 NMR (75.5 MHz, CDCl₃): δ = 24.4, 30.6, 56.0, 56.2, 60.7, 68.5, 111.3, 111.6, 117.6, 120.5, 121.1, 124.0,
4 129.4, 132.3, 145.9, 146.2, 147.8, 149.4, 149.8, 153.8, 170.5 ppm. m/z (%) 508 (7) [M⁺], 506 (8) [M⁺], 493
5 (17), 491 (20), 407 (66), 405 (67), 102 (26), 86 (32), 33 (100). Elemental analysis calculated (%) for
6 C₂₂H₂₃BrN₂O₇: C 52.08, H 4.57, N 5.52. Found: C 52.06, H 4.56, N 5.50.

7 **N-Hydroxy-5-[1-methoxy-4-(4'-(3''-bromo-4'',5''-dimethoxyphenyl)oxazol-5'-yl)-2-phenoxy]p**
8 **entanamide (4e)**. Compound **4e** was obtained from **3e** (110 mg, 0.21 mmol), hydroxylamine (50% in
9 water, 0.5 mL, 15 mmol) and NaOH (200 mg, 5 mmol). Yield: 74 mg (0.14 mmol, 67%); colorless solid
10 of mp 152-153°C. ν_{\max} (ATR)/cm⁻¹ 3186, 2940, 1641, 1593, 1563, 1515, 1487, 1401, 1361, 1327, 1257, 1231,
11 1181, 1162, 1143, 1106, 1074, 1040, 1022, 993, 950, 894, 858, 845, 802, 753, 700, 655, 628. ¹H NMR (300
12 MHz, CDCl₃): δ = 1.8-1.9 (m, 4 H), 2.3-2.5 (m, 2H), 3.82 (s, 3H), 3.87 (s, 3H), 3.9-4.0 (m, 5H), 6.90 (d,
13 1H, J = 8.5 Hz), 7.05 (s, 1H), 7.2-7.3 (m, 2H), 7.44 (s, 1H), 7.89 ppm (s, 1H). ¹³C NMR (75.5 MHz,
14 CDCl₃): δ = 24.4, 26.4, 32.1, 55.9, 56.2, 60.8, 69.8, 110.1, 111.3, 111.6, 117.6, 119.9, 121.2, 124.0, 129.5,
15 132.3, 146.0, 146.2, 148.1, 149.2, 149.4, 153.7, 170.3 ppm. m/z (%) 521 (5) [M⁺], 519 (5) [M⁺], 505 (24), 407
16 (100), 405 (95), 392 (24), 390 (24), 364 (12), 362 (13), 100 (93), 72 (67), 55 (54). Elemental analysis
17 calculated (%) for C₂₃H₂₅BrN₂O₇: C 52.99, H 4.83, N 5.37. Found: C 52.97, H 4.82, N 5.35.

18 **N-Hydroxy-6-[1-methoxy-4-(4'-(3''-bromo-4'',5''-dimethoxyphenyl)oxazol-5'-yl)-2-phenoxy]h**
19 **exanamide (4f)**. Compound **4f** was obtained from **3f** (80 mg, 0.15 mmol), hydroxylamine (50% in
20 water, 0.5 mL, 15 mmol) and NaOH (200 mg, 5 mmol). Yield: 75 mg (0.14 mmol, 93%); colorless solid
21 of mp 115-117°C. ν_{\max} (ATR)/cm⁻¹ 3190, 2938, 2865, 1647, 1591, 1558, 1512, 1485, 1463, 1400, 1362, 1325,
22 1254, 1229, 1203, 1176, 1139, 1107, 1042, 998, 939, 853, 807, 775, 753, 697, 658, 628. ¹H NMR (300 MHz,
23 CDCl₃): δ = 1.4-1.5 (m, 2H), 1.6-1.7 (m, 2H), 1.7-1.8 (m, 4H), 2.2-2.3 (m, 2H), 3.80 (s, 3H), 3.8-3.9 (m,
24 8H), 6.89 (d, 1H, J = 8.5 Hz), 7.05 (s, 1H), 7.2-7.3 (m, 2H), 7.43 (s, 1H), 7.89 ppm (s, 1H). ¹³C NMR (75.5
25 MHz, CDCl₃): δ = 25.0, 25.5, 28.3, 32.8, 56.0, 56.1, 60.8, 68.9, 111.2, 111.6, 111.7, 117.6, 119.9, 120.9,
26 124.1, 129.6, 132.0, 146.0, 146.1, 148.4, 149.4, 150.0, 153.7, 171.0 ppm. m/z (%) 536 (1) [M⁺], 534 (1) [M⁺],
27 521 (91), 519 (100), 407 (53), 405 (51), 392 (17), 390 (17), 364 (7), 362 (8), 282 (7), 265 (12), 243 (7), 194
28 (16), 167 (28), 114 (36), 69 (17), 44 (30). Elemental analysis calculated (%) for C₂₄H₂₇BrN₂O₇: C 53.84, H
29 5.08, N 5.23. Found: C 53.82, H 5.06, N 5.22.

30 **N-Hydroxy-4-[1-methoxy-4-(4'-(3'',4'',5''-trimethoxyphenyl)oxazol-5'-yl)-2-phenoxy]butanam**
31 **ide (4g)**. Compound **4g** was obtained from **3g** (119 mg, 0.25 mmol), hydroxylamine (50% in water,
32 0.5 mL, 15 mmol) and NaOH (200 mg, 5 mmol). Yield: 74 mg (0.16 mmol, 64%); colorless solid of mp
33 121-123°C. ν_{\max} (ATR)/cm⁻¹ 3194, 2935, 2837, 1658, 1583, 1515, 1454, 1415, 1373, 1256, 1238, 1173, 1123,
34 1020, 1002, 939, 884, 838, 813, 767, 734, 658, 628. ¹H NMR (300 MHz, CDCl₃) δ 2.0-2.2 (m, 2H), 2.3-2.4
35 (m, 2H), 3.76 (s, 6H), 3.85 (s, 3H), 3.9-4.0 (m, 5H), 4.15 (q, 2H, J = 7.1 Hz), 6.8-6.9 (m, 3H), 7.05 (s, 1H),
36 7.2-7.3 (m, 1H), 7.90 ppm (s, 1H). ¹³C NMR (75.5 MHz, CDCl₃): δ = 24.5, 30.2, 56.0, 56.2, 61.0, 68.2,
37 105.2, 110.0, 111.4, 120.4, 121.3, 127.8, 133.7, 145.5, 147.7, 149.3, 149.7, 153.3, 170.5 ppm. m/z (%) 458 (4)
38 [M⁺], 443 (100), 428 (26), 357 (98), 342 (62), 314 (17), 236 (16), 195 (18), 151 (12), 86 (22), 44 (29).
39 Elemental analysis calculated (%) for C₂₃H₂₆N₂O₈: C 60.26, H 5.72, N 6.11. Found: C 60.23, H 5.70, N
40 6.08.

41 **N-Hydroxy-5-[1-methoxy-4-(4'-(3'',4'',5''-trimethoxyphenyl)oxazol-5'-yl)-2-phenoxy]penta**
42 **namide (4h)**. Compound **4h** was obtained from **3h** (98 mg, 0.20 mmol), hydroxylamine (50% in water,
43 0.5 mL, 15 mmol) and NaOH (200 mg, 5 mmol). Yield: 72 mg (0.15 mmol, 76%); colorless solid of mp
44 118-120°C. ν_{\max} (ATR)/cm⁻¹ 3191, 2937, 2870, 2843, 1657, 1584, 1515, 1454, 1415, 1373, 1306, 1255, 1239,
45 1173, 1123, 1022, 838, 811, 768, 734, 658, 629. ¹H NMR (300 MHz, CDCl₃): δ = 1.8-1.9 (m, 4H), 2.2-2.3
46 (m, 2H), 3.78 (s, 6H), 3.8-3.9 (m, 5H), 3.94 (s, 3H), 6.8-6.9 (m, 3H), 7.02 (s, 1H), 7.2-7.3 (m, 1H), 7.90
47 ppm (s, 1H). ¹³C NMR (75.5 MHz, CDCl₃): δ = 24.0, 26.6, 32.0, 55.9, 56.2, 61.0, 69.5, 105.3, 110.4, 111.2,
48 119.9, 121.5, 127.9, 133.7, 137.8, 145.6, 148.0, 149.1, 149.3, 153.3, 170.1 ppm. m/z (%) 472 (3) [M⁺], 457
49 (100), 442 (10), 357 (73), 342 (34), 314 (11), 100 (17), 44 (12). Elemental analysis calculated (%) for
50 C₂₄H₂₈N₂O₈: C 61.01, H 5.97, N 5.93. Found: C 61.04, H 5.95, N 5.90.

51 **N-Hydroxy-6-[1-methoxy-4-(4'-(3'',4'',5''-trimethoxyphenyl)oxazol-5'-yl)-2-phenoxy]hexana**
52 **nide (4i)**. Compound **4i** was obtained from **3i** (73 mg, 0.15 mmol), hydroxylamine (50% in water, 0.5

1 mL, 15 mmol) and NaOH (200 mg, 5 mmol). Yield: 52 mg (0.11 mmol, 73%); colorless solid of mp
114-116°C. ν_{\max} (ATR)/cm⁻¹ 3211, 2936, 2870, 2837, 1651, 1584, 1515, 1455, 1414, 1372, 1331, 1306, 1255,
1238, 1173, 1122, 1019, 1001, 939, 892, 836, 810, 767, 732, 658, 628. ¹H NMR (300 MHz, CDCl₃): δ =
1.3-1.4 (m, 2H), 1.5-1.7 (m, 4H), 2.1-2.2 (m, 2H), 3.76 (s, 6H), 3.8-3.9 (m, 8H), 6.8-6.9 (m, 3H), 7.03 (s,
1H), 7.2-7.3 (m, 1H), 7.90 ppm (s, 1H). ¹³C NMR (75.5 MHz, CDCl₃): δ = 25.0, 25.4, 28.3, 32.8, 56.0, 56.1,
61.0, 68.8, 105.2, 111.5, 111.6, 119.8, 121.2, 127.9, 133.4, 137.6, 145.7, 148.2, 149.3, 149.8, 153.2, 171.0
ppm. *m/z* (%) 486 (18) [M⁺], 471 (100), 456 (17), 443 (11), 357 (48), 342 (38), 193 (17), 114 (13), 44 (21).
Elemental analysis calculated (%) for C₂₅H₃₀N₂O₈: C 61.72, H 6.22, N 5.76. Found: C 61.70, H 6.21, N
5.74.

10 4.6. Ester Hydrolysis of 3g to Carboxylic Acid 4j

11 **4-[1-Methoxy-4-(4'-(3'',4'',5''-trimethoxyphenyl)oxazol-5'-yl)-2-phenoxy]butyric acid (4j).**
12 Compound **3g** (119 mg, 0.25 mmol) was dissolved in MeOH (10 mL), aqueous NaOH (1 M, 10 mL)
13 was added and the reaction mixture was stirred at room temperature for 24 h. The solution was
14 acidified with aqueous HCl (1 M, to pH < 2) and the resulting precipitate was collected, washed with
15 water and dried in vacuum. Yield: 75 mg (0.17 mmol, 68%); colorless solid of mp 209-210°C.
16 ν_{\max} (ATR)/cm⁻¹ 3134, 2940, 2873, 2835, 2538, 1728, 1606, 1586, 1519, 1474, 1446, 1414, 1372, 1316, 1274,
17 1251, 1237, 1196, 1173, 1147, 1128, 1112, 1068, 1043, 1031, 1022, 1007, 962, 946, 883, 855, 840, 804, 769,
18 761, 736, 674, 654, 630, 623. ¹H NMR (300 MHz, CDCl₃): δ = 2.0-2.2 (m, 2H), 2.56 (t, 2H, *J* = 7.2 Hz), 3.76
19 (s, 6H), 3.86 (s, 3H), 3.87 (s, 3H), 3.98 (t, 1H, *J* = 6.3 Hz), 6.86 (d, 1H, *J* = 8.5 Hz), 6.88 (s, 2H), 7.12 (s,
20 1H), 7.22 (d, 1H, *J* = 8.5 Hz), 7.91 ppm (s, 1H). ¹³C NMR (75.5 MHz, CDCl₃): δ = 24.2, 30.2, 56.0, 56.1,
21 60.9, 67.8, 105.1, 111.6, 112.1, 120.5, 121.3, 127.6, 133.5, 137.9, 145.6, 148.2, 149.3, 150.1, 153.3, 177.0
22 ppm. *m/z* (ESI, %) 466.2 (27) [M⁺ + Na], 444.2 (100) [M⁺]. Elemental analysis calculated (%) for
23 C₂₃H₂₅NO₈: C 62.30, H 5.68, N 3.16. Found: C 62.26, H 5.65, N 3.08.

24 4.7. Biological Evaluations

25 4.7.1. Cell Lines and Culture Conditions

26 HT-29 (ACC-299), HCT-116 (ACC-581) and DLD-1 (ACC-278) colon carcinoma, MCF-7
27 (ACC-115) breast carcinoma, KB-V1 (ACC-149), 518A2 (Department of Radiotherapy and
28 Radiobiology, University Hospital Vienna) melanoma and Ea.Hy926 (ATCC no. CRL-2922) HUVEC
29 derived endothelial hybrid cells line were grown in Dulbecco's Modified Eagle Medium (DMEM;
30 Biochrom), high glucose supplemented with 10% (v/v) fetal bovine serum (FBS; Biochrom.) and 1%
31 (v/v) Antibiotic-Antimycotic solution (anti-anti; Thermo Scientific). HDFa human dermal fibroblasts
32 (ATCC: PCS-201-012™) were grown in DMEM supplemented with 10% FBS, 1% anti-anti and 2 mM
33 glutamine. The cells were incubated at 37 °C, 5% CO₂, 95% humidified atmosphere. By repeated
34 addition of topotecan or vinblastine at the maximum tolerated dose to the cell medium of MCF-7
35 and KB-V1 cells, the cells were rendered multidrug-resistant, indicated as MCF-7^{Topo} and KB-V1^{Vbl},
36 respectively. They were serially passaged following trypsinization by using 0.05% trypsin/0.02%
37 EDTA (Biochrom). Mycoplasma contamination was routinely monitored, and only mycoplasma-free
38 cultures were used.

39 4.7.2. MTT Assay

40 MTT [3-(4,5-dimethylthiazol-2-yl)-2,5-diphenyltetrazolium bromide] (ABCR) was used to
41 determine the cytotoxicity of test compounds as previously described [53]. Briefly, HDFa human
42 dermal fibroblasts and Ea.Hy926 endothelial hybrid cells (both 1 × 10⁵ cells/mL, 100 μL/well), 518A2
43 melanoma, KB-V1^{Vbl} cervix carcinoma, MCF-7^{Topo} breast carcinoma, HT-29, DLD-1 and HCT-116
44 colon carcinoma (all 5 × 10⁴ cells/mL, 100 μL/well) were grown in 96-well culture plates for 24 h.
45 Then, various concentrations of the test compounds were added and the cells incubated for 24-72 h
46 at 37 °C. After adding 12.5 μL of a 0.5% MTT solution in PBS (final concentration 0.05%) to cell
47 medium, microplates were incubated for 2 h and subsequently swiftly turned to discard the
48 medium. The precipitate of formazan crystals was then dissolved in a 10% solution of SDS in DMSO

1 containing 0.6% acetic acid. To ensure complete dissolution of formazan, microplates were
2 incubated for at least 4 h at 37 °C. Finally, the absorbance at $\lambda = 570$ nm (formazan) and 630 nm
3 (background) was measured using a microplate reader (Tecan F200). All experiments were carried
4 out in quadruplicate and the percentage of viable cells was calculated as the mean \pm SD with controls
5 set to 100%.

6 4.7.3. Tubulin Polymerization Assay

7 50 μ L of Brinkley's buffer 80 (BRB80) supplemented with 20% glycerol and 3 mM GTP was
8 given in a black 96-well half-area plate with clear bottom. Then, test compounds **4d-f** (final
9 concentration: 5 μ M, or 10 μ M) or vehicle (DMSO) were added. After adding 50 μ L tubulin in BRB80
10 (10 mg/mL) was pipetted in the wells and immediately placed in a pre-heated microplate reader
11 (Tecan). The polymerization was determined turbidimetrically at 37 °C by measuring the absorption
12 at 340 nm for 120 min in intervals of 5 min.

13 4.7.4. Immunofluorescence Staining of Microtubule Cytoskeleton

14 518A2 melanoma cells (5×10^4 cells/mL, 500 μ L/well) or Ea.Hy926 endothelial hybrid cells ($7.5 \times$
15 10^4 cells/mL, 500 μ L/well) were seeded in 24-well plates on small glass coverslips and grown for 24
16 h. Then, the cells were exposed to the test compounds for 24 h. After washing the cells once with
17 PBS, they were fixed in 3.7% formaldehyde in PBS (20 min, rt), and permeabilized and blocked in 1%
18 BSA and 0.1% triton X-100 in PBS (30 min, rt). Then, the cells were incubated with monoclonal
19 mouse anti-alpha-tubulin antibody (1 h, 37 °C). After washing the cells for three times with PBS, the
20 cells were exposed to the secondary anti-mouse 488 antibody conjugate (1 h, rt, in the dark). Then,
21 the cells were washed for three times with PBS and once with water. The glass coverslips were
22 mounted in 4-88 based mounting medium supplemented with 1 μ g/mL DAPI for counterstaining
23 the nuclei and 2.5% DABCO. Alterations of the microtubule were documented by a Zeiss Imager A1
24 AX10 fluorescence microscope (400 \times magnification).

25 4.7.5. HDAC Inhibition

26 The HDAC inhibitory potential of the novel compounds was determined by utilizing the
27 deacetylase activity of recombinant human HDAC1 (HDAC1 Inhibitor Screening Assay Kit; Cayman
28 Chemicals) or HDAC6 [HDAC6 Inhibitor Screening Kit (Fluorometric); Biovision] towards the
29 corresponding synthetic acetylated-peptide substrates resulting in the release of a fluorescent
30 product. The assays were performed according to manufacturer's description of the in commercial
31 available assay kits. The fluorescence intensity (HDAC1: $\lambda_{\text{ex}} = 352$ nm, $\lambda_{\text{em}} = 452$ nm; HDAC6: $\lambda_{\text{ex}} =$
32 380 nm, $\lambda_{\text{em}} = 510$ nm) as a measure of enzyme activity was measured at 37 °C with a microplate
33 reader (Tecan). The IC₅₀ values were derived from dose-response curves and are expressed as the
34 means \pm SD of two independent experiments.

35 4.7.6. Western Blot Analyses

36 For the microtubule acetylation blots, 518A2 melanoma cells (5×10^4 cells/mL, 3 mL/well) were
37 grown in 6-well plates for 24 h and then incubated with vehicle (DMSO), SAHA (10 μ M), or **4f** (4, 5,
38 and 6 μ M) for 24 h. After harvesting the cells by trypsination, they were pelleted by centrifugation
39 (300 \times g, 5 min) followed by cell lysis in 100 μ L lysis buffer (20 mM DTT, 200 μ M sodium vanadate,
40 50 mM Tris/HCl, 1% triton X-100, 150 mM NaCl, pH 7.4) for 10 min on ice. The cell lysates were
41 mixed with 100 μ L of 2 \times Laemmli buffer (125 mM Tris-HCl, 4% SDS, 20% glycerol, 10%
42 β -mercapto-ethanol, pH 6.8) and boiled (95 °C, 10 min). Equal amounts of total protein were
43 subjected to 10% SDS-polyacrylamide gel electrophoresis (SDS-PAGE) and transferred to
44 polyvinylidene difluoride membranes (PVDF, Carl Roth). For subsequent analysis of acetylated
45 protein and of alpha-tubulin which was used as a loading control, membranes were blocked and
46 incubated with primary antibody solutions in 5% bovine serum albumin in 1 \times TBS or 5% milk

1 powder in PBS, respectively. The protein bands were visualized by chemoluminescence (secondary
2 antibody-HRP conjugates, ECL detection system; Cell Signaling) using a LAS-3000 imager (Fujifilm).

3 For the cell cycle protein blots, 518A2 melanoma cells (2×10^6 cells/mL, 10 mL/well) were
4 grown in 10 cm dishes for 24 h and then incubated with **4d** (0.15–4 μ M) or SAHA (5 μ M) for 24 h.
5 After harvesting and lysing of the cells, western blotting was performed as described before [54]. For
6 subsequent analysis, the protein-loaded membranes were incubated with antibodies directed
7 against p21 (Abcam ab109199), p27 (Abcam ab109199), cyclin D1 (Cell Signaling 29225) and GADPH
8 (Santa Cruz sc25778) in 1:1000 dilutions. After incubation with horseradish peroxidase-coupled
9 anti-IgG antibodies (1:10,000; Amersham), the blot was developed using the Calvin-S developer
10 (Biostep) and the software SnapAndGo 1.8.1.

11 4.7.7. Immunofluorescence Staining of F-Actin

12 518A2 melanoma cells (5×10^4 cells/mL, 500 μ L/well) were seeded in 24-well plates on small
13 glass coverslips and grown for 24 h at 37 °C. Then, the cells were treated with **4d** (0.5 μ M), **4e** (1.5
14 μ M), **4f** (4 μ M), and vehicle (DMSO) for 24 h. After washing the cells once with PBS at 37 °C, they
15 were fixed with 3.7% formaldehyde solution in PBS (pH 7.0) for 10 min at room temperature. Then,
16 the cells were washed with PBS and permeabilized with 0.5% Triton X-100 in PBS for 5 min at room
17 temperature. After washing with PBS, the cells were incubated with 200 μ L of a 0.1 μ M Acti-stain™
18 488 phalloidin solution in PBS for 30 min at room temperature in the dark. Then, the cells were
19 washed three times with PBS and once with water, and the glass coverslips mounted in 4-88-based
20 mounting medium containing 1 μ g/mL DAPI for counterstaining the nuclei and 2.5% DABCO. The
21 effects on the actin cytoskeleton were documented by a Zeiss Imager A1 AX10 fluorescence
22 microscope (400 \times magnification).

23 4.7.8. Cell Cycle Analysis

24 518A2 melanoma cells (3 mL/well; 5×10^4 cells/mL) were grown on 6-well tissue culture plates
25 for 24 h. After treatment with **4d** (150, and 200 nM), **4e** (0.8, and 1 μ M), **4f** (2, and 3 μ M) or DMSO
26 (control) for another 24 h, cells were fixed (70% EtOH, 24 h, 4 °C), washed with PBS and incubated
27 with propidium iodide (PI; Carl Roth) staining solution (50 μ g/mL PI, 0.1% sodium citrate, 50 μ g/mL
28 RNase A in PBS) for 30 min at 37 °C. The fluorescence intensity of 10,000 single cells was measured
29 at $\lambda_{em} = 570$ nm ($\lambda_{ex} = 488$ nm laser source) with a Beckmann Coulter Cytomics FC 500 flow
30 cytometer. The percentages of cells in the different phases of the cell cycle (G1, S and G2/M phase)
31 were determined using the CXP Analysis software (Beckmann Coulter). The percentage of apoptotic
32 cells was derived from sub-G1 peaks.

33 4.7.9. In Vivo Toxicity

34 *In vivo* toxicity of **4d** was studied in nude mice (Harlan and Winkelmann, Borchon, Germany).
35 These experiments were carried out following the institutional guidelines. **4d** was formulated in 10%
36 Tween80/ 10% ethanol / 80% saline for administration. Mice were treated with 100 mg/kg body
37 weight (i.p.) or 200 mg/kg body weight (orally) of **4d** and then observed for two weeks. The body
38 weight of the mice was assessed daily under therapy.

39 4.8. In Silico Evaluation

40 4.8.1. Proteins and Compound Structures

41 The protein structures for tubulin, HDAC1, and HDAC6 used in the docking studies were
42 obtained from the Protein Data Bank (Table 7, PDB, www.rcsb.org, accessed 2018-03-06) [55]. One
43 representative per protein was selected for the docking studies based on the following criteria: The
44 protein should be co-crystallized with a ligand most similar to the ligands from which the studied
45 hybrid compounds **4d–f** were derived (combretastatin A-4 for tubulin and hydroxamic acids for
46 HDACs) [56]. Among these, the structures with the best resolutions were selected.

Table 7. Selection of PDB structures used for docking.

	PDB	Chain	Res.	Original ligand
Tubulin	5LYJ	A&B	2.4 Å	Combretastatin A-4
HDAC1	5ICN	B	3.3 Å	H4K16Hx
HDAC6	5EDU	A	2.8 Å	Trichostatin A

4.8.2. Initial Docking with LeadIT/FlexX

To generate initial predictions of binding positions, called docking poses, FlexX (included in LeadIT 2.2.0, which was kindly provided by BioSolveIT, www.biosolveit.de/LeadIT), was used [57]. The PDB structures were prepared as follows: For tubulin, chains A and B of 5LYJ, for HDAC1, chain B of 5ICN, and for HDAC6, chain A of 5EDU were chosen [47,50,51]. The binding pockets were defined with the co-crystallized ligands as a reference ligand, including all amino acids within a radius of 10 Å for the HDAC structures and 6.5 Å for tubulin. The metal coordination of the zinc ion in both HDAC structures was set to 'spherical' and zinc was defined as an essential pharmacophore for guided docking. All other settings for the receptor definition were used as default. The docking library contained compounds **4d–f** as well as the crystal structure's original ligand. For HDAC1 and HDAC6 vorinostat, a known HDAC inhibitor, was added to the library. The docking strategy, scoring and chemical parameters were kept as default. Only the maximum number of solutions per iteration and the maximum number of solutions per fragmentation were increased to 1000 steps each.

4.8.3. Pose Optimization with SeeSAR

Final pose optimization and affinity estimation was performed with SeeSAR 6.1, also kindly provided by BioSolveIT (www.biosolveit.de/SeeSAR). The best poses from the LeadIT docking were imported and were used for binding site definition. For each compound, 10 new poses were generated and all were evaluated with the built in HYDE scoring function [58]. The poses with the best estimated affinities were chosen for further analysis.

4.8.4. Additional Software Used

PyMOL was used to analyse, compare and visualize the binding pose predictions, as well as to create the 3D images [59].

Supplementary Materials: Supplementary materials can be found at www.mdpi.com/xxx/s1.

Author Contributions: Investigation, F.S., A.D. and T.M.; Compound preparation, B.B.; Docking, L.C.G. and A.V.; Writing-Original Draft Preparation, B.B.; Writing-Review & Editing, R.S. and M.H.; Supervision, R.S., A.V. and M.H.; Funding Acquisition, R.S., A.V. and M.H..

Funding: R.S. was funded by the Deutsche Forschungsgemeinschaft grant number Scho 402/12-1.

Conflicts of Interest: The authors declare no conflict of interest.

Abbreviations

CA-4	Combretastatin A-4
DMEM	Dulbecco's modified Eagle medium
EMT	Epithelial-to-mesenchymal transition
FBS	Fetal bovine serum
HDAC	Histone deacetylase
HDACi	HDAC inhibitor
HRP	Horseradish peroxidase
MDA	Microtubule disrupting agent
PI	Propidium iodide
ROS	Reactive oxygen species
SAHA	Suberoyl anilide hydroxamic acid

SAR	Structure activity relationship
SD	Standard deviation
VDA	Vascular-disrupting agents
ZBG	Zinc binding group

References

1. Ververis, K.; Hiong, A.; Karagiannis, T.C.; Licciardi, P.V. Histone deacetylase inhibitors (HDACs): multitargeted anticancer agents. *Biol. Targets Ther.* **2013**, *2013*, 47–60, DOI 10.2147/BTT.S29965.
2. Choi, J.-H.; Kwon, H.J.; Yoon, B.-I.; Kim, J.-H.; Ham, S.U.; Joo, H.J.; Kim, D.-Y. Expression profile of histone deacetylase 1 in gastric cancer tissues. *Cancer Sci.* **2001**, *92*, 1300–1304, DOI 10.1111/j.1349-7006.2001.tb02153.x.
3. Halkidou, K.; Gaughan, L.; Cook, S.; Leung, H.Y.; Neal, D.E.; Robson, C.N. Upregulation and nuclear recruitment of HDAC1 in hormone refractory prostate cancer. *The Prostate* **2004**, *59*, 177–189, DOI 10.1002/pros.20022.
4. Zhang, Z.; Yamashita, H.; Toyama, T.; Sugiura, H.; Omoto, Y.; Ando, Y.; Mita, K.; Hamaguchi, M.; Hayashi, S.; Iwase, H. HDAC6 expression is correlated with better survival in breast cancer. *Clin. Cancer Res.* **2004**, *10*, 6962–6968, DOI 10.1158/1078-0432.CCR-04-0455.
5. Zhu, P.; Martin, E.; Mengwasser, J.; Schlag, P.; Janssen, K.-P.; Göttlicher, M. Induction of HDAC2 expression upon loss of APC in colorectal tumorigenesis. *Cancer Cell* **2004**, *5*, 455–463, DOI 10.1016/S1535-6108(04)00114-X.
6. Wilson, A.J.; Byun, D.-S.; Popova, N.; Murray, L.B.; L'Italien, K.; Sowa, Y.; Arango, D.; Velcich, A.; Augenlicht, L.H.; Mariadason, J.M. Histone Deacetylase 3 (HDAC3) and other class I HDACs regulate colon cell maturation and p21 expression and are deregulated in human colon cancer. *J. Biol. Chem.* **2006**, *281*, 13548–13558, DOI 10.1074/jbc.M510023200.
7. Khan, O.; La Thangue, N.B. HDAC inhibitors in cancer biology: Emerging mechanisms and clinical applications. *Immunol. Cell Biol.* **2012**, *90*, 85–94, DOI 10.1038/icb.2011.100.
8. Bozorgi, A.H.A.; Zarghi, A. Search for the pharmacophore of histone deacetylase inhibitors using pharmacophore query and docking study. *Iran. J. Pharm. Res.* **2014**, *13*, 1165–1172.
9. Wang, J.; Sun, F.; Han, L.; Hou, X.; Pan, X.; Liu, R.; Tang, W.; Fang, H. Design, synthesis, and preliminary bioactivity studies of substituted purine hydroxamic acid derivatives as novel histone deacetylase (HDAC) inhibitors. *Med. Chem. Commun.* **2014**, *5*, 1887–1891, DOI 10.1039/c4md00203b.
10. Marks, P.A.; Breslow, R. Dimethyl sulfoxide to vorinostat: Development of this histone deacetylase inhibitor as an anticancer drug. *Nat. Biotechnol.* **2007**, *25*, 84–90, DOI 10.1038/nbt1272.
11. Marks, P.A. Discovery and development of SAHA as an anticancer agent. *Oncogene* **2007**, *26*, 1351–1356, DOI 10.1038/sj.onc.1210204.
12. Poole, R.M. Belinostat: First global approval. *Drugs* **2014**, *74*, 1543–1554, DOI 10.1007/s40265-014-0275-8.
13. Garnock-Jones, K.P. Panobinostat: First global approval. *Drugs* **2015**, *75*, 695–704, DOI 10.1007/s40265-015-0388-8.
14. Mottamal, M.; Zheng, S.; Huang, T.; Wang, G. Histone deacetylase inhibitors in clinical studies as templates for new anticancer agents. *Molecules* **2015**, *20*, 3898–3941, DOI 10.3390/molecules20033898.
15. Fantin, V.R.; Richon, V.M. Mechanisms of resistance to histone deacetylase inhibitors and their therapeutic implications. *Clin. Cancer Res.* **2007**, *13*, 7237–7242, DOI 10.1158/1078-0432.CCR-07-2114.
16. Kong, D.; Ahmad, A.; Bao, B.; Li, Y.; Banerjee, S.; Sarkar, F.H. Histone deacetylase inhibitors induce epithelial-to-mesenchymal transition in prostate cancer cells. *PLoS ONE* **2012**, *7*, e45045, DOI 10.1371/journal.pone.0045045.
17. Schobert, R.; Biersack, B. Multimodal HDAC inhibitors with improved anticancer activity. *Curr. Cancer Drug Targets* **2018**, *18*, 39–56, DOI 10.2174/1568009617666170206102613.
18. Negi, A.S.; Gautam, Y.; Alam, S.; Chanda, D.; Luqman, S.; Sarkar, J.; Khan, F.; Konwar, R. Natural antitubulin agents: Importance of 3,4,5-trimethoxyphenyl fragment. *Bioorg. Med. Chem.* **2015**, *23*, 373–389, DOI 10.1016/j.bmc.2014.12.027.
19. Bates, D.; Eastman, A. Microtubule destabilising agents: Far more than just antimetabolic anticancer drugs: MDA mechanisms of action. *Br. J. Clin. Pharmacol.* **2017**, *83*, 255–268, DOI 10.1111/bcp.13126.

- 1 20. Kim, J.H.; Yoon, E.-K.; Chung, H.-J.; Park, S.-Y.; Hong, K.-M.; Lee, C.-H.; Lee, Y.-S.; Choi, K.; Yang, Y.; Kim,
2 K.; Kim, I.H. P53 acetylation enhances taxol-induced apoptosis in human cancer cells. *Apoptosis* **2013**, *18*,
3 110–120, DOI 10.1007/s10495-012-0772-8.
- 4 21. Zuco, V.; De Cesare, M.; Cincinelli, R.; Nannei, R.; Pisano, C.; Zaffaroni, N.; Zunino, F. Synergistic
5 antitumor effects of novel HDAC inhibitors and paclitaxel in vitro and in vivo. *PLoS ONE* **2011**, *6*, e29085,
6 DOI 10.1371/journal.pone.0029085.
- 7 22. Chobaninan, N.H.; Greenberg, V.L.; Gass, J.M.; Desimone, C.P.; Van Nagell, J.R.; Zimmer, T.G. Histone
8 deacetylase inhibitors enhance paclitaxel-induced cell death in ovarian cancer cell lines independent of
9 p53 status. *Anticancer Res.* **2004**, *24*, 539–546.
- 10 23. Zhang, X.; Zhang, J.; Tong, L.; Luo, Y.; Su, M.; Zang, Y.; Li, J.; Lu, W.; Chen, Y. The discovery of
11 colchicine-SAHA hybrids as a new class of antitumor agents. *Bioorg. Med. Chem.* **2013**, *21*, 3240–3244, DOI
12 10.1016/j.bmc.2013.03.049.
- 13 24. Zhang, X.; Kong, Y.; Zhang, J.; Su, M.; Zhou, Y.; Zang, Y.; Li, J.; Chen, Y.; Fang, Y.; Zhang, X.; Lu, W.
14 Design, synthesis and biological evaluation of colchicine derivatives as novel tubulin and histone
15 deacetylase dual inhibitors. *Eur. J. Med. Chem.* **2015**, *95*, 127–135, DOI 10.1016/j.ejmech.2015.03.035.
- 16 25. Yang, Z.; Wang, T.; Wang, F.; Niu, T.; Liu, Z.; Chen, X.; Long, C.; Tang, M.; Cao, D.; Wang, X.; Xiang, W.;
17 Yi, Y.; Ma, L.; You, J.; Chen, L. Discovery of selective histone deacetylase 6 inhibitors using the quinazoline
18 as the cap for the treatment of cancer. *J. Med. Chem.* **2016**, *59*, 1455–1470, DOI
19 10.1021/acs.jmedchem.5b01342.
- 20 26. Wang, L.; Woods, K.W.; Li, Q.; Barr, K.J.; McCroskey, R.W.; Hannick, S.M.; Gherke, L.; Credo, R.B.; Hui,
21 Y.-H.; Marsh, K.; Warner, R.; Lee, J.Y.; Zielinski-Mozng, N.; Frost, D.; Rosenberg, S.H.; Sham, H.L. Potent,
22 orally active heterocycle-based combretastatin A-4 analogues: Synthesis, structure–activity relationship,
23 pharmacokinetics, and in vivo antitumor activity evaluation. *J. Med. Chem.* **2002**, *45*, 1697–1711, DOI
24 10.1021/jm010523x.
- 25 27. Schobert, R.; Biersack, B.; Dietrich, A.; Effenberger, K.; Knauer, S.; Mueller, T.
26 4-(3-Halo/Amino-4,5-dimethoxyphenyl)-5-aryloxazoles and -N-methylimidazoles that are cytotoxic
27 against combretastatin A resistant tumor cells and vascular disrupting in a cisplatin resistant germ cell
28 tumor model. *J. Med. Chem.* **2010**, *53*, 6595–6602, DOI 10.1021/jm100345r.
- 29 28. Atuegbu, A.; Solas, D.; Hurt, C.; Kitaygorodskyy, A. Anti-HIV compounds. WO2016100391 (A1).
- 30 29. Greene, L.M.; Wang, S.; O’Boyle, N.M.; Bright, S.A.; Reid, J.E.; Kelly, P.; Meegan, M.J.; Zisterer, D.M.
31 Combretazet-3 a novel synthetic cis-stable combretastatin A-4-azetidinone hybrid with enhanced stability
32 and therapeutic efficacy in colon cancer. *Oncol. Rep.* **2013**, *29*, 2451–2458, DOI 10.3892/or.2013.2379.
- 33 30. Huber, S.; Wege, A.K.; Bernhardt, G.; Buschauer, A.; Brockhoff, G. Topotecan-induced ABCG2 expression
34 in MCF-7 cells is associated with decreased CD24 and EpCAM expression and a loss of tumorigenicity:
35 CD24/EpCAM and tumorigenicity of MCF-7 cells. *Cytometry A* **2015**, *87*, 707–716, DOI
36 10.1002/cyto.a.22675.
- 37 31. Forgue-Lafitte, M.-E.; Coudray, A.-M.; Bréant, B.; Mešter, J. Proliferation of the human colon carcinoma
38 cell line HT29: Autocrine growth and deregulated expression of the c-Myc oncogene. *Cancer Res.* **1989**, *49*,
39 6566–6571.
- 40 32. Sutherland, R.L.; Hall, R.E.; Taylor, I.W. Cell proliferation kinetics of MCF-7 human mammary carcinoma
41 cells in culture and effects of tamoxifen on exponentially growing and plateau-phase cells. *Cancer Res.*
42 **1983**, *43*, 3998–4006.
- 43 33. Mahal, K.; Biersack, B.; Caysa, H.; Schobert, R.; Müller, T. Combretastatin A-4 derived imidazoles show
44 cytotoxic, antivascular, and antimetastatic effects based on cytoskeletal reorganisation. *Invest. New Drugs*
45 **2015**, *33*, 541–554, DOI 10.1007/s10637-015-0215-9.
- 46 34. Mahal, K.; Schrufer, S.; Steinemann, G.; Rausch, F.; Schobert, R.; Biersack, B.; Höpfner, M. Biological
47 evaluation of 4,5-diarylimidazoles with hydroxamic acid appendages as novel dual mode anticancer
48 agents. *Cancer Chemother. Pharmacol.* **2015**, *75*, 691–700, DOI 10.1007/s00280-015-2685-z.
- 49 35. Aldana-Masangkay, G.I.; Sakamoto, K.M. The role of HDAC6 in cancer. *J. Biomed. Biotechnol.* **2011**, *2011*, ID
50 875824, DOI 10.1155/2011/875824.
- 51 36. Ropero, S.; Esteller, M. The role of histone deacetylases (HDACs) in human cancer. *Mol. Oncol.* **2007**, *1*,
52 19–25, DOI 10.1016/j.molonc.2007.01.001.
- 53 37. Xu, W.S.; Parmigiani, R.B.; Marks, P.A. Histone deacetylase inhibitors: Molecular mechanisms of action.
54 *Oncogene* **2007**, *26*, 5541–5552, DOI 10.1038/sj.onc.1210620.

- 1 38. Steinemann, G.; Dittmer, A.; Kuzyniak, W.; Hoffmann, B.; Schrader, M.; Schobert, R.; Biersack, B.;
2 Nitzsche, B.; Höpfner, M. Animacroxam, a novel dual-mode compound targeting histone deacetylases
3 and cytoskeletal integrity of testicular germ cell cancer cells. *Mol. Cancer Ther.* **2017**, *16*, 2364–2374, DOI
4 10.1158/1535-7163.MCT-17-0293.
- 5 39. Tojkander, S.; Gateva, G.; Lappalainen, P. Actin stress fibers - assembly, dynamics and biological roles. *J.*
6 *Cell Sci.* **2012**, *125*, 1855–1864, DOI 10.1242/jcs.098087.
- 7 40. Kanthou, C.; Tozer, G.M. The tumor vascular targeting agent combretastatin A-4-phosphate induces
8 reorganization of the actin cytoskeleton and early membrane blebbing in human endothelial cells. *Blood*
9 **2002**, *99*, 2060–2069, DOI 10.1182/blood.V99.6.2060.
- 10 41. Mahal, K.; Resch, M.; Ficner, R.; Schobert, R.; Biersack, B.; Mueller, T. Effects of the
11 tumor-vasculature-disrupting agent verubulin and two heteroaryl analogues on cancer cells, endothelial
12 cells, and blood vessels. *ChemMedChem* **2014**, *9*, 847–854, DOI 10.1002/cmdc.201300531.
- 13 42. Mahal, K.; Biersack, B.; Schobert, R. New Oxazole-bridged combretastatin A-4 analogues as potential
14 vascular-disrupting agents. *Int. J. Clin. Pharmacol. Ther.* **2013**, *51*, 41–43, DOI 10.5414/CP51041.
- 15 43. Kim, Y.B.; Ki, S.W.; Yosnida, M.; Horinouchi, S. Mechanism of cell cycle arrest caused by histone
16 deacetylase inhibitors in human carcinoma cells. *J. Antibiot. (Tokyo)* **2000**, *53*, 1191–1200, DOI
17 10.7164/antibiotics.53.1191.
- 18 44. Finzer, P.; Kuntzen, C.; Soto, U.; zur Hausen, H.; Rösl, F. Inhibitors of histone deacetylase arrest cell cycle
19 and induce apoptosis in cervical carcinoma cells circumventing human papillomavirus oncogene
20 expression. *Oncogene* **2001**, *20*, 4768–4776, DOI 10.1038/sj.onc.1204652.
- 21 45. Kanthou, C.; Greco, O.; Stratford, A.; Cook, I.; Knight, R.; Benzakour, O.; Tozer, G. The tubulin-binding
22 agent combretastatin A-4-phosphate arrests endothelial cells in mitosis and induces mitotic cell death. *Am.*
23 *J. Pathol.* **2004**, *165*, 1401–1411, DOI 10.1016/S0002-9440(10)63398-6.
- 24 46. Halperin, I.; Ma, B.; Wolfson, H.; Nussinov, R. Principles of docking: An overview of search algorithms
25 and a guide to scoring functions. *Proteins Struct. Funct. Genet.* **2002**, *47*, 409–443, DOI 10.1002/prot.10115.
- 26 47. Gaspari, R.; Prota, A.E.; Bargsten, K.; Cavalli, A.; Steinmetz, M.O. Structural basis of cis- and
27 trans-combretastatin binding to tubulin. *Chem* **2017**, *2*, 102–113, DOI 10.1016/j.chempr.2016.12.005.
- 28 48. Schärfer, C.; Schulz-Gasch, T.; Ehrlich, H.-C.; Guba, W.; Rarey, M.; Stahl, M. Torsion angle preferences in
29 druglike chemical space: A comprehensive guide. *J. Med. Chem.* **2013**, *56*, 2016–2028, DOI
30 10.1021/jm3016816.
- 31 49. Guba, W.; Meyder, A.; Rarey, M.; Hert, J. Torsion library reloaded: A new version of expert-derived
32 SMARTS rules for assessing conformations of small molecules. *J. Chem. Inf. Model.* **2016**, *56*, 1–5, DOI
33 10.1021/acs.jcim.5b00522.
- 34 50. Hai, Y.; Christianson, D.W. Histone deacetylase 6 structure and molecular basis of catalysis and inhibition.
35 *Nat. Chem. Biol.* **2016**, *12*, 741–747, DOI 10.1038/nchembio.2134.
- 36 51. Watson, P.J.; Millard, C.J.; Riley, A.M.; Robertson, N.S.; Wright, L.C.; Godage, H.Y.; Cowley, S.M.;
37 Jamieson, A.G.; Potter, B.V.L.; Schwabe, J.W.R. Insights into the activation mechanism of class I HDAC
38 complexes by inositol phosphates. *Nat. Commun.* **2016**, *7*, 11262, DOI 10.1038/ncomms11262.
- 39 52. Mahal, K.; Kahlen, P.; Biersack, B.; Schobert, R. 4-(1-Ethyl-4-anisyl-imidazol-5-yl)-N-hydroxycinnamide –
40 A new pleiotropic HDAC inhibitor targeting cancer cell signalling and cytoskeletal organisation. *Exp. Cell*
41 *Res.* **2015**, *336*, 263–275, DOI 10.1016/j.yexcr.2015.06.008.
- 42 53. Mosmann, T. Rapid colorimetric assay for cellular growth and survival: Application to proliferation and
43 cytotoxicity assays. *J. Immunol. Methods* **1983**, *65*, 55–63, DOI 10.1016/0022-1759(83)90303-4.
- 44 54. Höpfner, M.; Sutter, A.P.; Huether, A.; Schuppan, D.; Zeitz, M.; Scherübl, H. Targeting the epidermal
45 growth factor receptor by gefitinib for treatment of hepatocellular carcinoma. *J. Hepatol.* **2004**, *41*,
46 1008–1016, DOI
- 47 55. Berman, H.M.M.; Westbrook, J.; Feng, Z.; Gilliland, G.; Bhat, T.N.; Weissig, H.; Shindyalov, I.N.; Bourne,
48 P.E. The protein data bank. *Nucleic Acids Res.* **2000**, *28*, 235–242.
- 49 56. Schmitt, F.; Gold, M.; Begemann, G.; Andronache, I.; Biersack, B.; Schobert, R. Fluoro and pentafluorothio
50 analogs of the antitumoral curcuminoid EF24 with superior antiangiogenic and vascular-disruptive
51 effects. *Bioorg. Med. Chem.* **2017**, *25*, 4894–4903, DOI 10.1016/j.bmc.2017.07.039.
- 52 57. Rarey, M.; Wefing, S.; Lengauer, T. Placement of medium-sized molecular fragments into active sites of
53 proteins. *J. Comput. Aided Mol. Des.* **1996**, *10*, 41–54, DOI 10.1007/BF00124464.

- 1 58. Schneider, N.; Lange, G.; Hindle, S.; Klein, R.; Rarey, M. A consistent description of HYdrogen bond and
2 DEhydration energies in protein–ligand complexes: Methods behind the HYDE scoring function. *J.*
3 *Comput. Aided Mol. Des.* **2013**, *27*, 15–29, DOI 10.1007/s10822-012-9626-2.
- 4 59. DeLano, W. Pymol: An open-source molecular graphics tool. *CCP4 Newsl. Protein Crystallogr.* **2002**, *40*,
5 44–53.



6 © 2018 by the authors. Submitted for possible open access publication under the terms
7 and conditions of the Creative Commons Attribution (CC BY) license
8 (<http://creativecommons.org/licenses/by/4.0/>).

-Supporting Information-

Oxazole-bridged combretastatin A-4 derivatives with alkyl hydroxamate side chains: Structure activity relationship studies of new inhibitors of HDAC and/or tubulin function

Florian Schmitt¹, **Lisa Chiara Gosch**^{2,3}, **Alexandra Dittmer**², **Thomas Mueller**⁴, **Rainer Schobert**¹,
Bernhard Biersack^{1,*}, **Andrea Volkamer**³, and **Michael Höpfner**²

¹ Department of Chemistry, University of Bayreuth, Universitaetsstrasse 30, 95447 Bayreuth, Germany;
florian1.schmitt@uni-bayreuth.de, rainer.schobert@uni-bayreuth.de

² Institute of Physiology, Charité – Universitätsmedizin Berlin, Charitéplatz 1, 10117 Berlin, Germany; lisa-
chiara.gosch@charite.de, michael.hoepfner@charite.de

³ In Silico Toxicology Group, Institute of Physiology, Charité – Universitätsmedizin Berlin, Charitéplatz 1,
10117 Berlin, Germany; andrea.volkamer@charite.de

⁴ Klinik für Innere Medizin IV, Universitätsklinikum Halle (Saale), Ernst-Grube-Str. 40, 06120 Halle, Germany;
thomas.mueller@medizin.uni-halle.de

* Correspondence: bernhard.biersack@yahoo.com; Tel.: +49-921-55-2673

Table of content

Material and Methods.....	S2
DCFH-DA assay.....	S2
Immuofluorescence staining of acetylated alpha-tubulin.....	S2
Wound healing assay.....	S2
Results	S3
Effect on the intracellular ROS levels.....	S3
Effect on the microtubule cytoskeleton.....	S4
Effect on the acetylation of alpha-tubulin.....	S4
Effect on migratory activity.....	S5

Material and Methods.

DCFH-DA assay.

The assay was performed as previously described. Briefly, 518A2 melanoma cells (1×10^5 cells/mL, 100 μ L/well) were grown in a black 96-well plate for 24 h. Then, the cell medium was exchanged for serum-free DMEM supplemented with 20 μ M DCFH-DA and incubated for 30 min at 37 °C. After washing the cells twice with 100 μ L PBS, the cells were treated with the test compounds 4d-f (10 μ M), and vehicle (DMSO) in serum-free DMEM for 1 h at 37 °C. Then, the cells were washed twice with 100 μ L PBS and subsequently placed in a microplate reader (TECAN). The DCF-fluorescence ($\lambda_{ex} = 485$ nm, $\lambda_{em} = 535$ nm) as a measure of ROS production was determined and that of vehicle treated controls set to 100%. Values exceeding 100% indicate a drug-induced ROS generation. The values of six independent assays were depicted as the means \pm SD.

Immuofluorescence staining of acetylated alpha-tubulin.

518A2 melanoma cells (5×10^4 cells/mL, 500 μ L/well) were grown on glass coverslips in 24-well plates for 24 h. Then, the cells were treated with 4f (4 μ M), SAHA (10 μ M), or vehicle (DMSO) for 24 h. After washing the cells with PBS, they were fixed in 3.7% formaldehyde in PBS (20 min, rt) followed by blocking and permeabilization in TBS supplemented with 5% BSA and 0.1% triton X-100 (30 min, rt). Then the cells were incubated with monoclonal rabbit anti-acetyl-alpha-tubulin antibody (2 h, 37 °C). After washing the cells for three times with PBS, they were incubated with a secondary anti-rabbit 488 antibody conjugate in the dark (2 h, rt). Then, the cells were washing again for three times with PBS and once with water. The glass coverslips were mounted in 4-88 based mounting medium containing 1 μ g/mL DAPI and 2.5% DABCO. Pictures were taken by using a Zeiss Imager A1 AX10 fluorescence microscope (400 \times magnification).

Wound healing assay.

518A2 melanoma cells (1×10^5 cells/mL, 500 μ L/well) were grown in 24-well plates for 24 h so that the cells have arranged in a sub-confluent monolayer. Then, a strip of cells was scraped off by using a 100 μ L pipette tip. The medium containing the detached cells was aspirated and exchanged for new medium. Then, the cells were treated with vehicle (DMSO), **4d** (0.2 μ M), **4e** (1.2 μ M), and **4f** (3.8 μ M) and wound re-closure was documented subsequently and 24 h after application by using a light microscope (Zeiss Axiovert 135, 100 \times magnification). The open image area after 24 h (%) compared to that at 0 h was quantified from three independent experiments by using the imageJ 1.50i software. The significance of results was assessed by Student's t-test ($p < 0.01$ for controls versus treated cells).

Results

Effect on the intracellular ROS levels.

Elevated levels of reactive oxygen species (ROS) are known to trigger apoptosis and reverse chemoresistance in tumors. Several approved chemotherapeutics exert their effect by direct or indirect promotion of ROS production which results in the induction of apoptosis. HDACi like SAHA are known to induce apoptosis by increased intracellular levels of ROS. Hence, the effect of **4d-f** on the intracellular ROS levels was tested in 518A2 melanoma cells using the DCFH-DA assay. In fact, the intracellular ROS levels were distinctly increased to levels exceeding 190% when compared to untreated controls which were set to 100% (**4d**: 241% \pm 17; **4e**: 230 \pm 31; **4f**: 198 \pm 24). As already observed for anti-proliferative activity the ability to elevate ROS levels decreases with increasing linker length.

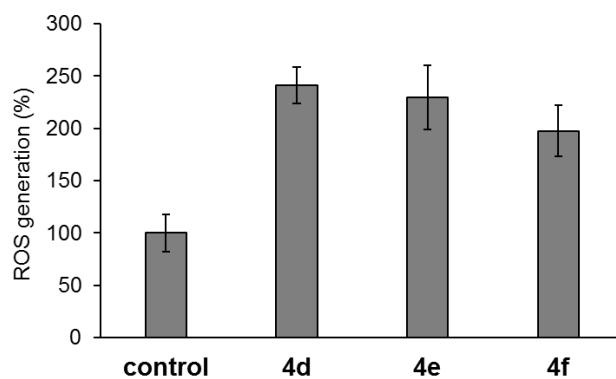


Figure S1. Effect of the test compounds **4d-f** (10 μ M) on the intracellular ROS levels in 518A2 melanoma cells after 1 h incubation as determined by DCFH-DA assay. Values are the means \pm SD of six independent experiments with vehicle treated control cells set to 100% ROS production. Significant deviations from the vehicle treated control cells were determined using a t-test. The p-value was < 0.05 for compound **4d-f**.

Effect on the microtubule cytoskeleton.

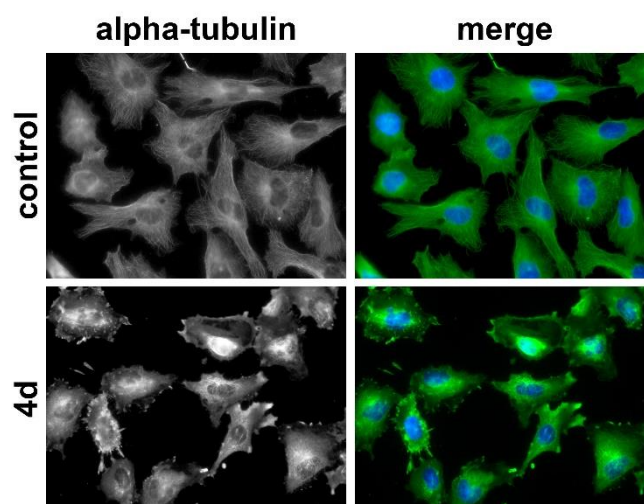


Figure S2. Effect of **4d** (0.2 μ M), or vehicle (DMSO) on the organization of microtubule cytoskeleton in Ea.Hy926 endothelial hybrid cells after 24 h incubation. Nuclei were counterstained with DAPI (merge, blue); alpha-tubulin (green). Pictures are representative of two independent experiments (400 \times magnification).

Effect on the acetylation of alpha-tubulin.

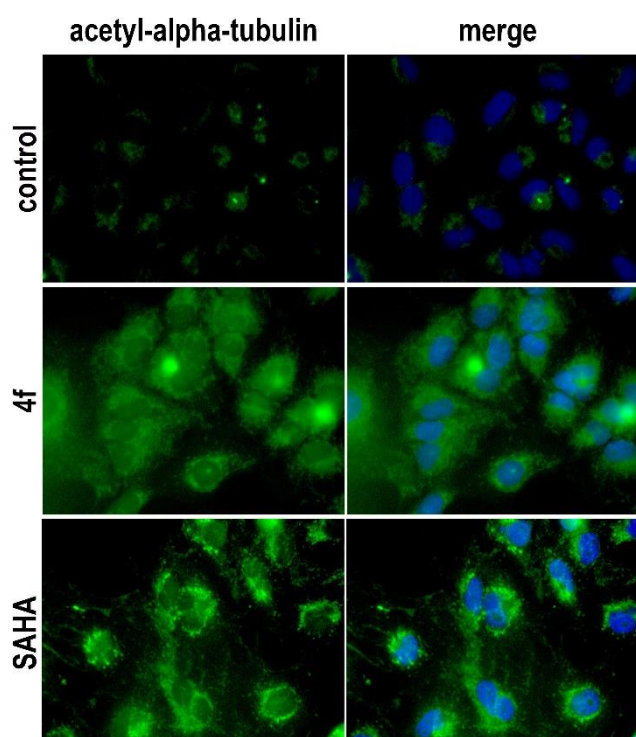


Figure S3. Increasingly acetylated microtubules (acetyl-alpha-tubulin; green) in 518A2 melanoma cells after 24 h treatment with vehicle (control; DMSO), **4f** (4 μ M), and SAHA (10 μ M) as visualized by immunofluorescence microscopy (400 \times magnification). Nuclei were counterstained with DAPI (merge, blue).

Effect on migratory activity.

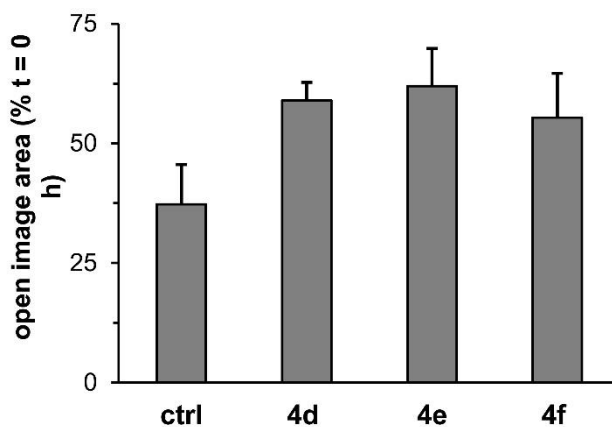


Figure S4. Inhibitory effect of **4d** (0.2 μ M), **4e** (1.2 μ M) and **4f** (3.8 μ M) on the cell migration of 518A2 melanoma cells as determined by wound-healing assays. Values are the means \pm SD of at least three independent experiments. Control cells were treated with DMSO only. Significant deviations from the vehicle treated control cells were determined using a t-test. The p-value was < 0.05 for compound **4d-f**.

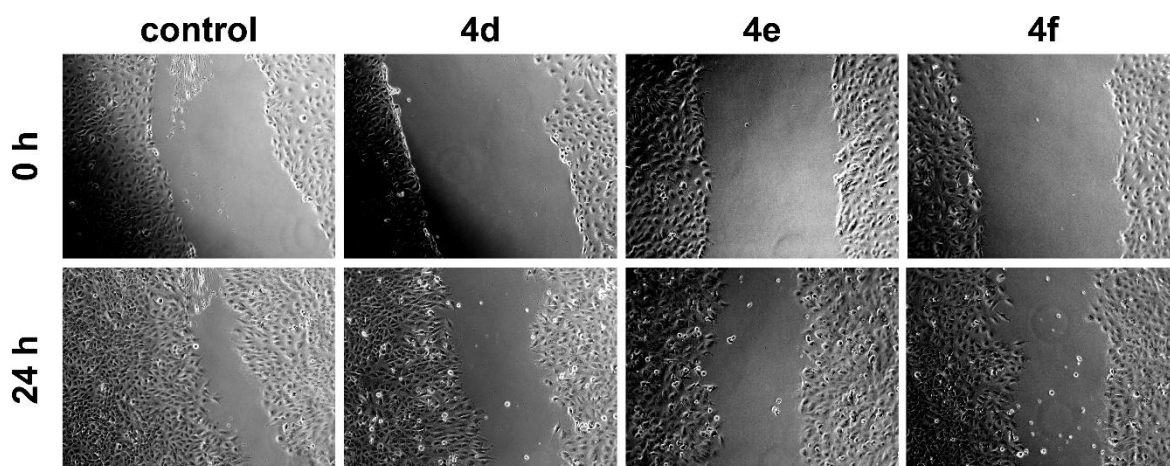


Figure S5. Inhibitory effect of **4d** (0.2 μ M), **4e** (1.2 μ M), **4f** (3.8 μ M) on cell migration of 518A2 melanoma cells. Pictures are representative of at least three independent experiments. Control cells were treated with DMSO only

6 Liste weiterer Publikationen im Rahmen der Dissertation

Synthesis, stereochemical assignment, and bioactivity of the *Penicillium* metabolites penicillenols B₁ and B₂.

Karl Kempf, Florian Schmitt, Ursula Bilitewski, Rainer Schobert

Tetrahedron 71 (2015) 5064-5068.

Tetrahedron 71 (2015) 5064–5068



Contents lists available at ScienceDirect

Tetrahedron

journal homepage: www.elsevier.com/locate/tet



Synthesis, stereochemical assignment, and bioactivity of the *Penicillium* metabolites penicillenols B₁ and B₂



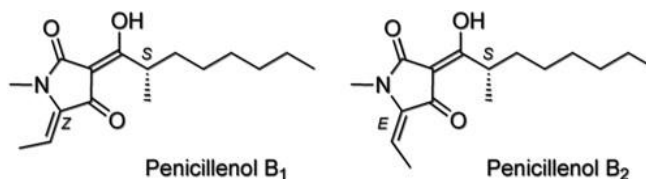
Karl Kempf^a, Florian Schmitt^a, Ursula Bilitewski^b, Rainer Schobert^{a,*}

^aOrganic Chemistry Laboratory, University Bayreuth, Universitaetsstr. 30, D-95440 Bayreuth, Germany

^bHelmholtz Centre for Infection Research, Inhoffenstrasse 7, 38124 Braunschweig, Germany

Abstract

The *Penicillium* metabolites penicillenols B₁ and B₂ were synthesised for the first time by elimination of a mesylated penicillenol A precursor as obtained from an L-threonine derived tetramic acid. The



(*Z,S*)- and (*E,S*)-configured diastereomers were identical to the natural compounds as to NMR spectra and optical rotations. Both isomers showed antiproliferative effects against cancer and endothelial cell lines and penicillenol B₁ was also notably antibiotic against *Staphylococcus aureus*.

[Abstract and graphical abstract reprinted with permission from Elsevier]

Copyright © 2015 Elsevier Inc.

Improved anticancer and antiparasitic activity of new lawsone Mannich bases

Katharina Mahal, Aamir Ahmad, Florian Schmitt, Julia Lockhauserbäumer, Kathrin Starz, Rohan Pradhan, Subhash Padhye, Fazlul H. Sarkar, Waleed S. Koko, Rainer Schobert, Klaus Ersfeld, Bernhard Biersack

European Journal of Medicinal Chemistry 126 (2017) 421-431.

European Journal of Medicinal Chemistry 126 (2017) 421–431



Contents lists available at ScienceDirect

European Journal of Medicinal Chemistry

journal homepage: <http://www.elsevier.com/locate/ejmech>



Research paper

Improved anticancer and antiparasitic activity of new lawsone Mannich bases



Katharina Mahal ^{a,1}, Aamir Ahmad ^{b,1}, Florian Schmitt ^a, Julia Lockhauserbäumer ^c, Kathrin Starz ^c, Rohan Pradhan ^d, Subhash Padhye ^d, Fazlul H. Sarkar ^b, Waleed S. Koko ^{e,f}, Rainer Schobert ^a, Klaus Ersfeld ^c, Bernhard Biersack ^{a,*}

^a Organic Chemistry Laboratory, University of Bayreuth, Universitaetsstrasse 30, 95440 Bayreuth, Germany

^b Karmanos Cancer Institute, Dept. of Pathology, Wayne State University, Detroit 48201, USA

^c Laboratory of Molecular Parasitology, Department of Genetics, University of Bayreuth, 95440 Bayreuth, Germany

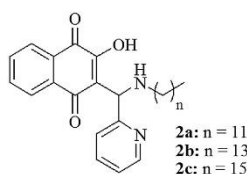
^d Department of Chemistry, Abeda Inamdar Senior College, Pune 411001, India

^e Department of Microbiology and Parasitology, Medicinal and Aromatic Plants Research Institute, National Centre for Research, Khartoum, Sudan

^f College of Science and Arts (Ar Rass), Qassim University, Buraidah, Saudi Arabia

Abstract

Substituted lawsone Mannich bases **2a-e**, **3a-e** and **4a-e** were prepared and tested for their biological activities. The new fatty alkyl substituted compounds **2a-c** exhibited strong and selective growth inhibitory activities in the low one-digit micromolar and sub-micromolar range



- anticancer active (PC-3, BxPC-3, KB-V1/Vbl cells)
- antiparasitic (*T. b. brucei*, *E. histolytica*)



T. b. brucei cell rounding

against a panel of human cancer cell lines associated with ROS formation. In addition, compounds **2a-c** revealed sub-micromolar anti-trypanosomal activities against parasitic *Trypanosoma brucei brucei* cells via deformation of the microtubule cytoskeleton. The N-hexadecyl compound **2c** was also highly active against locally isolated *Entamoeba histolytica* parasite samples exceeding the activity of metronidazole.

[Abstract and graphical abstract reprinted with permission from Elsevier]

Copyright © 2016 Elsevier Inc.

Effects of histidin-2-ylidene vs. imidazol-2-ylidene ligands on the anticancer and antivascular activity of complexes of ruthenium, iridium, platinum, and gold.

Florian Schmitt, Kate Donnelly, Julienne K. Muenzner, Tobias Rehm, Vojtech Novohradsky, Viktor Brabec, Jana Kasparkova, Martin Albrecht, Rainer Schobert, Thomas Mueller.

Journal of Inorganic Biochemistry 163 (2016) 221-228.

Journal of Inorganic Biochemistry xxx (2016) xxx-xxx



Contents lists available at ScienceDirect

Journal of Inorganic Biochemistry

journal homepage: www.elsevier.com/locate/jinorgbio



Effects of histidin-2-ylidene vs. imidazol-2-ylidene ligands on the anticancer and antivascular activity of complexes of ruthenium, iridium, platinum, and gold

Florian Schmitt^a, Kate Donnelly^b, Julienne K. Muenzner^a, Tobias Rehm^a, Vojtech Novohradsky^c, Viktor Brabec^c, Jana Kasparkova^d, Martin Albrecht^{b,1}, Rainer Schobert^{a,*}, Thomas Mueller^e

^a Organic Chemistry Laboratory, University of Bayreuth, Universitätsstraße 30, 95447 Bayreuth, Germany

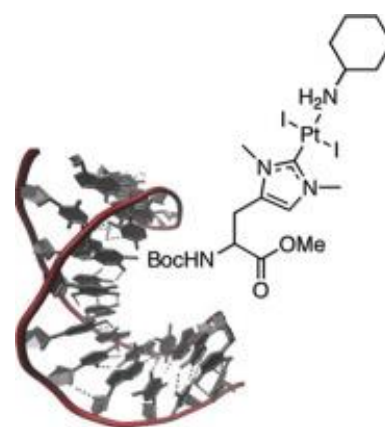
^b School of Chemistry and Chemical Biology, University College Dublin, Belfield, Dublin 4, Ireland

^c Institute of Biophysics, Academy of Sciences of the Czech Republic, CZ-61265 Brno, Czech Republic

^d Department of Biophysics, Faculty of Science, Palacky University, 17. listopadu 12, CZ-77146 Olomouc, Czech Republic

^e Department of Internal Medicine IV, Oncology/Hematology, Martin-Luther-University Halle-Wittenberg, 06120 Halle-Saale, Germany

Couples of N-heterocyclic carbene complexes of ruthenium, iridium, platinum, and gold, each differing only in the carbene ligand being either 1,3-dimethylimidazol-2-ylidene (IM) or 1,3-dimethyl-N-boc-O-methylhistidin-2-ylidene (HIS), were assessed for their antiproliferative effect on seven cancer cell lines, their interaction with DNA, their cell cycle interference, and their vascular disrupting properties. In MTT [3-(4,5-dimethylthiazol-2-yl)-2,5-diphenyltetrazolium bromide] assays only the platinum complexes were cytotoxic at single-digit micromolar IC₅₀ concentrations with the (HIS)Pt complex being on average twice as active as the (IM)Pt complex. The former was highly efficacious against cisplatin-resistant HT-29 colon carcinoma cells where the latter had no effect. Both Pt complexes were accumulated by cancer cells and bound to double-helical DNA equally well. Only the (HIS)Pt complex modified the electrophoretic mobility of circular DNA in vitro due to the HIS ligand causing greater morphological changes to the DNA. Both platinum complexes induced accumulation of 518A2 melanoma cells in G2/M and S phase of the cell cycle. A disruption of blood vessels in the chorioallantoic membrane of fertilized chicken eggs was observed for both platinum complexes and the (IM)gold complex. The (HIS)platinum complex was as active as cisplatin in tumor xenografted mice while being tolerated better. We found that the HIS ligand may augment the cytotoxicity of certain antitumoral metal fragments in two ways: by acting as a transmembrane carrier increasing the cellular accumulation of the complex, and by initiating a pronounced distortion and unwinding of DNA. We identified a new



(HIS)platinum complex which was highly cytotoxic against cancer cells including cisplatin-resistant ones.

[Abstract and graphical abstract reprinted with permission from Elsevier]

Copyright © 2016 Elsevier Inc.

Fluoro and pentafluorothio analogs of the antitumoral curcuminoid EF24 with superior antiangiogenic and vascular-disruptive effects

Florian Schmitt, Madeleine Gold, Gerrit Begemann, Ion C. Andronache, Bernhard Biersack, Rainer Schobert

Bioorganic & Medicinal Chemistry 25 (2017) 4894-4903.

Bioorganic & Medicinal Chemistry 25 (2017) 4894-4903



Contents lists available at ScienceDirect

Bioorganic & Medicinal Chemistry

journal homepage: www.elsevier.com/locate/bmc



Fluoro and pentafluorothio analogs of the antitumoral curcuminoid EF24 with superior antiangiogenic and vascular-disruptive effects



Florian Schmitt^a, Madeleine Gold^a, Gerrit Begemann^b, Ion Andronache^c, Bernhard Biersack^a, Rainer Schobert^{a,*}

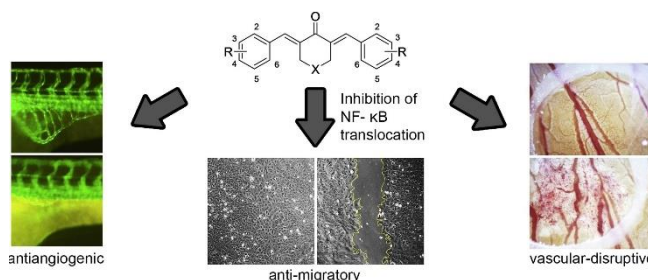
^aOrganic Chemistry Laboratory, University of Bayreuth, Universitaetsstrasse 30, 95447 Bayreuth, Germany

^bDevelopmental Biology, University of Bayreuth, Universitaetsstrasse 30, 95447 Bayreuth, Germany

^cUniversity of Bucharest, Research Center for Integrated Analysis and Territorial Management, 4-12, Regina Elisabeta Avenue, Bucharest, 3rd district, 030018, Romania

Abstract:

A series of 14 analogs of the curcuminoid EF24, (3*E*,5*E*)-3,5-bis[(2-fluorophenyl)methylene]-4-piperidinone, bearing fluorine or pentafluorothio substituents, were prepared and tested for antiproliferative, vascular-disruptive, and antiangiogenic activity, as well as for their



influence on other cancer-relevant targets. They proved antiproliferative against eight cancer cell lines with IC₅₀ values in the low single-digit micromolar to triple-digit nanomolar range. Like EF24, the hexafluoro **3c** and **3d** and bis(pentafluorothio) **4f** derivatives arrested HT-29 colon carcinoma cells in G2/M phase of the cell cycle, yet inhibited angiogenesis, e.g. in zebrafish larvae, to a much greater extent. The antimigratory effects in 518A2 melanoma cells of **3c**, its regioisomer **3d**, and of **4f**, originate from an inhibition of NF-κB translocation. Moreover, **3c** and **3d** showed potential as vascular-disruptive agents in chorioallantoic/vitelline membrane (CA/VM) assays.

[Abstract and graphical abstract reprinted with permission from Elsevier]

Copyright © 2017 Elsevier Inc.

Halogenated bis(methoxy-benzylidene)-4-piperidone curcuminoids with improved anticancer activity

Florian Schmitt, Dharmalingam Subramaniam, Shrikant Anant, Subhash Padhye,
Gerrit Begemann, Rainer Schobert, Bernhard Biersack

ChemMedChem 2018, doi: 10.1002/cmdc.201800135

ChemMedChem

10.1002/cmdc.201800135

WILEY-VCH

FULL PAPER

Halogenated bis(methoxy-benzylidene)-4-piperidone curcuminoids with improved anticancer activity

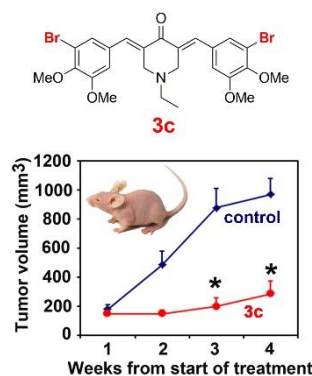
Florian Schmitt,^[a] Dharmalingam Subramaniam,^[b] Shrikant Anant,^[b] Subhash Padhye,^[b] Gerrit Begemann,^[c] Rainer Schobert,^[a] Bernhard Biersack*^[a]

[a] F. Schmitt, Prof. Dr. R. Schobert, Dr. B. Biersack
Department of Chemistry
University of Bayreuth
Universitätsstraße 30, 95440 Bayreuth (Germany)
E-mail: bernhard.biersack@yahoo.de

[b] Prof. Dr. D. Subramaniam, Prof. Dr. S. Anant, Prof. Dr. S. Padhye
University of Kansas Medical Center
3901 Rainbow Boulevard, Kansas City 66160 (USA)

[c] Prof. Dr. G. Begemann
Developmental Biology
University of Bayreuth
Universitätsstraße 30, 95440 Bayreuth (Germany)

Abstract: A series of readily available curcuminoids **3a-f** with halogenated bis(4-methoxy/4,5-dimethoxybenzylidene)-4-piperidone structure was prepared and analyzed for their cytotoxic impact on eight human cancer cell lines of five different entities. The known 3,4,5-trimethoxybenzylidene curcuminoid **2a** and the new bis-(3-bromophenyl)- and bis-(3,5-dibromophenyl)-derivatives **3c** and **3d** proved more strongly antiproliferative than the known curcuminoid EF24 against six of these cell lines. Compounds **2a** and **3c** caused a distinct increase of reactive oxygen species, which eventually elicited apoptosis in 518A2 melanoma cells. **2a** arrested 518A2 melanoma cells in G1 phase of the cell cycle and had no effect on the expression of prometastatic matrix metalloproteinases MMP-2 and MMP-9, whereas **3c** led to an accumulation of 518A2 cells in G2/M phase and to a down-regulation of the MMP-2 expression. In addition, **2a** and **3c** treatment resulted in significant inhibition of colony formation in HCT-116 cells. Both **2a** and **3c** showed antiangiogenic activity, e.g. by inhibiting the formation of subintestinal veins (SIV) in zebrafish embryos. **3c** was also well-tolerated by mice and inhibited the growth of HCT-116 colon cancer xenografts.



[Abstract reprinted with permission from 10.1002/cmdc.201800135.]

Copyright © 2018 WILEY-VCH Verlag GmbH & Co. KGaA, Weinheim

7 Danksagung

Mein besonderer Dank gilt Prof. Dr. Rainer Schobert sowohl bezüglich der interessanten Themenstellung als auch für die Diskussionsbereitschaft, die Unterstützung und wissenschaftliche Förderung während meiner Promotion.

Über dies möchte ich Dr. Biersack danken für die vielen Diskussionen und Tipps bei der Arbeit an diversen Projekten, sowie für die Synthese eines Großteils der im Rahmen dieser Arbeit untersuchten Verbindungen.

Ein Dankeschön geht auch an Prof. Dr. Albrecht, seine Mitarbeiter und Tobias Rehm für die Synthese der NHC-Komplexe. Weiterhin möchte ich mich bei Dr. Thomas Müller und Prof. Dr. Michael Höpfner sowie ihren Mitarbeitern für die gute Zusammenarbeit und Unterstützung bei diversen Projekten danken. Auch Prof. Dr. Brabec und seinen Mitarbeitern gilt mein Dank für ihre Studien bezüglich der DNA-Bindung und zelluläre Aufnahme diverser Verbindungen. Für die überaus gute Kooperation möchte ich mich auch bei Dr. Ion C. Andronache bedanken.

Bedanken möchte ich mich auch bei Prof. Dr. Gerrit Begemann und seinen Mitarbeitern für die Möglichkeit die *in vivo* Assays am Zebrafischembryo unter Verwendung seiner Ressourcen und Mitbenutzung sämtlicher Geräte durchführen zu können. Auch Prof. Dr. Olaf Stemmann, Prof. Dr. Andreas Möglich, Prof. Dr. Frank Hahn, und Prof. Dr. Klaus Ersfeld, sowie ihren Mitarbeitern möchte ich für die Mitnutzung ihrer Geräte, die fachliche Unterstützung und ihre Hilfsbereitschaft danken.

Ein ganz besonderes Dankeschön geht auch an meine Arbeitskollegen der OCI:

Dr. Thomas Schmalz, Dr. Ulrike Lacher, und Silvia Kastner möchte ich für die Hilfe bei organisatorischen, technischen, bürokratischen und auch bei privaten Angelegenheiten danken. All den ehemaligen und aktuellen Doktoranden am Lehrstuhl möchte ich für die gute Atmosphäre, wissenschaftlichen Ratschläge und Unterstützung danken.

Besonders möchte ich mich bei allen ehemaligen und aktuellen Biochemikerkollegen aus dem S1-Labor, Dr. Katharina Mahal, Dr. Julienne Münzner, Matthias Rothmund und Madeleine Gold für die angenehme Arbeitsatmosphäre, die gute Zusammenarbeit und Unterstützung bedanken. Die vielen fachlichen Diskussionen, Tipps und Ratschläge haben mir bei meiner Arbeit enorm geholfen. Weiterhin möchte ich auch allen Praktikanten und Masteranden danken, die ich während meiner Promotion betreuen durfte, und deren Unterstützung mir bei meiner

Danksagung

Arbeit geholfen hat.

Ein herzliches Dankeschön gilt auch meiner Familie, die mich nicht nur während des Studiums, sondern auch während meiner Promotion immer unterstützt haben und für mich da waren. Meiner Frau Angela und meinen Kindern Noah und Matilda danke ich ganz besonders für ihre Unterstützung.

8 Eidesstattliche Versicherung und Erklärungen des Verfassers

(§ 8 Satz 2 Nr. 3 PromO Fakultät)

Hiermit versichere ich eidesstattlich, dass ich die Arbeit selbstständig verfasst und keine anderen als die von mir angegebenen Quellen und Hilfsmittel benutzt habe (vgl. Art. 64 Abs. 1 Satz 6 BayHSchG).

(§ 8 Satz 2 Nr. 3 PromO Fakultät)

Hiermit erkläre ich, dass ich die Dissertation nicht bereits zur Erlangung eines akademischen Grades eingereicht habe und dass ich nicht bereits diese oder eine gleichartige Doktorprüfung endgültig nicht bestanden habe.

(§ 8 Satz 2 Nr. 4 PromO Fakultät)

Hiermit erkläre ich, dass ich Hilfe von gewerblichen Promotionsberatern bzw. –vermittlern oder ähnlichen Dienstleistern weder bisher in Anspruch genommen habe noch künftig in Anspruch nehmen werde.

(§ 8 Satz 2 Nr. 7 PromO Fakultät)

Hiermit erkläre ich mein Einverständnis, dass die elektronische Fassung der Dissertation unter Wahrung meiner Urheberrechte und des Datenschutzes einer gesonderten Überprüfung unterzogen werden kann.

(§ 8 Satz 2 Nr. 8 PromO Fakultät)

Hiermit erkläre ich mein Einverständnis, dass bei Verdacht wissenschaftlichen Fehlverhaltens Ermittlungen durch universitätsinterne Organe der wissenschaftlichen Selbstkontrolle stattfinden können.

.....

Ort, Datum,

Unterschrift (Florian Schmitt)